Till Cremer

Ionic Liquid Bulk and Interface Properties

Electronic Interaction, Molecular Orientation and Growth Characteristics

Springer

Springer Theses

Recognizing Outstanding Ph.D. Research

Aims and Scope

The series "Springer Theses" brings together a selection of the very best Ph.D. theses from around the world and across the physical sciences. Nominated and endorsed by two recognized specialists, each published volume has been selected for its scientific excellence and the high impact of its contents for the pertinent field of research. For greater accessibility to non-specialists, the published versions include an extended introduction, as well as a foreword by the student's supervisor explaining the special relevance of the work for the field. As a whole, the series will provide a valuable resource both for newcomers to the research fields described, and for other scientists seeking detailed background information on special questions. Finally, it provides an accredited documentation of the valuable contributions made by today's younger generation of scientists.

Theses are accepted into the series by invited nomination only and must fulfill all of the following criteria

- They must be written in good English.
- The topic should fall within the confines of Chemistry, Physics, Earth Sciences, Engineering and related interdisciplinary fields such as Materials, Nanoscience, Chemical Engineering, Complex Systems and Biophysics.
- The work reported in the thesis must represent a significant scientific advance.
- If the thesis includes previously published material, permission to reproduce this must be gained from the respective copyright holder.
- They must have been examined and passed during the 12 months prior to nomination.
- Each thesis should include a foreword by the supervisor outlining the significance of its content.
- The theses should have a clearly defined structure including an introduction accessible to scientists not expert in that particular field.

Till Cremer

Ionic Liquid Bulk and Interface Properties

Electronic Interaction, Molecular
Orientation and Growth
Characteristics

Doctoral Thesis accepted by
the University of Erlangen-Nuremberg, Germany

Springer

Author
Dr. Till Cremer
Department of Chemistry
   and Chemical Biology
Harvard University
Cambridge, MA
USA

Supervisor
Prof. Dr. Hans-Peter Steinrück
Lehrstuhl für Physikalische Chemie II
Universität Erlangen-Nürnberg
Erlangen
Germany

Parts of this thesis have been published in the following journal articles:

1. Schmidt, M., Cubillas, A. M., Taccardi, N., Euser, T. G., Cremer, T., Maier, F., Steinrück, H.-P., Russell, P. S. R., Wasserscheid, P., Etzold, B. J. M. (2013): Chemical and (photo)-catalytical transformations in photonic crystal fibers. *ChemCatChem*, 5, 641–650

2. Deyko, A., Cremer, T., Rietzler, F., Perkin, S., Crowhurst, L., Welton, T., Steinrück, H.-P., Maier, F. (2013): On the interfacial behaviour of thin ionic liquids films on mica. *Journal of Physical Chemistry C*, 117, 5101–5111

3. Cremer, T., Wibmer, L., Krick Calderón, S., Deyko, A., Maier, F., Steinrück, H.-P. (2012): Interfaces of ionic liquids and transition metal surfaces–adsorption, growth, and thermal reactions of ultrathin $[C_1C_1Im][Tf_2N]$ films on metallic and oxidized Ni(111) surfaces. *Physical Chemistry Chemical Physics*, 14, 5153–5163

4. Cremer, T., Stark, M., Deyko, A., Steinrück, H.-P., Maier, F. (2011): Liquid/ solid interface of ultrathin ionic liquid films: $[C_1C_1Im][Tf_2N]$ and $[C_8C_1Im]$ $[Tf_2N]$ on Au(111). *Langmuir*, 27, 3662–3671.

5. Steinrück, H.-P., Libuda, J., Wasserscheid, P., Cremer, T., Kolbeck, C., Laurin, M., Maier, F., Sobota, M., Schulz, P. S., Stark, M. (2011): Surface science and model catalysis with ionic liquid-modified materials. *Advanced Materials*, 23, 2571–2587.

6. Cremer, T., Kolbeck, C., Lovelock, K. R. J., Paape, N., Wölfel, R., Schulz, P. S., Wasserscheid, P., Weber, H., Thar, J., Kirchner, B., Maier, F., Steinrück, H.-P. (2010): Towards a molecular understanding of cation–anion interactions—probing the electronic structure of imidazolium ionic liquids by NMR spectroscopy, X-ray photoelectron spectroscopy and theoretical calculations. *Chemistry-a European Journal*, 16, 9018–9033.

7. Kolbeck, C., Lehmann, J., Lovelock, K. R. J., Cremer, T., Paape, N., Wasserscheid, P., Fröba, A. P., Maier, F., Steinrück, H.-P. (2010): Density and surface tension of ionic liquids. *Journal of Physical Chemistry B*, 114, 17025–17036.

8. Maier, F., Cremer, T., Kolbeck, C., Lovelock, K. R. J., Paape, N., Schulz, P. S., Wasserscheid, P., Steinrück, H.-P. (2010): Insights into the surface composition and enrichment effects of ionic liquids and ionic liquid mixtures. *Physical Chemistry Chemical Physics*, 12, 1905–1915.

9. Kolbeck, C., Paape, N., Cremer, T., Schulz, P. S., Maier, F., Steinrück, H.-P., Wasserscheid, P. (2010): Ligand effects on the surface composition of Rh-containing ionic liquid solutions used in hydroformylation catalysis. *Chemistry-a European Journal*, 16, 12083–12087.

10. Kolbeck, C., Cremer, T., Lovelock, K. R. J., Paape, N., Schulz, P. S., Wasserscheid, P., Maier, F., Steinrück, H.-P. (2009): Influence of different anions on the surface composition of ionic liquids studied using ARXPS. *Journal of Physical Chemistry B*, 113, 8682–8688.

11. Lovelock, K. R. J., Kolbeck, C., Cremer, T., Paape, N., Schulz, P. S., Wasserscheid, P., Maier, F., Steinrück, H.-P. (2009): Influence of different substituents on the surface composition of ionic liquids studied using ARXPS. *Journal of Physical Chemistry B*, 113, 2854–2864.

12. Cremer, T., Killian, M., Gottfried, J. M., Paape, N., Wasserscheid, P., Maier, F., Steinrück, H.-P. (2008): Physical vapor deposition of [EMIM] [Tf$_2$N]: a new approach to the modification of surface properties with ultrathin ionic liquid films. *ChemPhysChem*, 9, 2185–2190.

Supervisor's Foreword

In recent years, Ionic liquids (ILs)—organic salts with a low melting point close to room temperature—received strongly increasing scientific attention. Their structural diversity results into nearly unlimited possibilities to combine cations and anions with different properties. Consequently, the physico-chemical properties of ILs (e.g., liquid range, polarity, coordination behaviour, viscosity, density, heat capacity, etc.) can be tuned over a wide range, and thus, ILs can be adapted to specific applications. Based on the promising properties of ILs, various potential application areas have been explored, ranging from catalysis, electrochemistry, green chemistry to green engineering or analytics, to name a few.

While research activities initially solely concentrated on the bulk properties of ILs, nowadays the importance of the interface of an IL with its environment (solid, liquid or gaseous) has been recognized for a large number of application areas. Consequently, surface and interface properties, such as surface tension and wettability or heat and mass transport characteristics, receive more and more attention. Due to the unbalanced forces resulting from the non-isotropic environment, the chemical composition of the near-surface region and the molecular arrangement at the surface can be very different from that in the bulk. The same holds true for the liquid/solid interface with the support material, where specific support—IL interactions come into play. From these considerations, it is evident that investigations of the surface and interface properties of ionic liquids, at an atomic level accuracy, are of the same pivotal importance as for solids. Starting in 2005, it was realized that, due to their low vapour pressure (typically $<10^{-9}$ mbar at room temperature), the bulk and surface properties of ILs can also be investigated using the well-developed techniques of classical surface science under ultra-high vacuum (UHV) conditions. In the meantime, this new field of "Ionic Liquid Surface and Interface Science" has established itself as an important discipline in ongoing IL research and many surface science techniques have successfully contributed to an increasingly detailed understanding not only of the IL/vacuum interface, but also of IL bulk properties. This allows determining surface- and interface-related properties of ILs with the same atomic level accuracy as for solid surfaces and conventional adsorbate systems. A particularly useful method is X-ray photoelectron spectroscopy (XPS), also denoted as electron spectroscopy for chemical analysis (ESCA), which allows for the determination of the chemical composition of the surface and

the surface-near bulk and is also sensitive to the chemical environment and the oxidation state of the analysed atoms.

The Ph.D. thesis of Till Cremer addresses several important and fundamental aspects of the bulk and interface properties of ionic liquids using a surface science approach. By combining angle-resolved X-ray photoelectron spectroscopy with physical vapour deposition of ionic liquids, an approach he pioneered, Till Cremer presents a number of fundamental contributions to the new field of "Ionic Liquid Surface and Interface Science". The highlights are his results concerning anion/cation interactions and the growth of ultrathin layers of ionic liquids on various substrates in the context of supported ionic liquid catalysis. His results significantly contributed to the present level of understanding in the field. Accordingly, he is author and coauthor of twelve publications on the topic in high-ranked journals, which have been extremely well received by the research community and beyond.

Till Cremer performed his Ph.D. thesis at the Chair of Physical Chemistry II of the Universität Erlangen-Nürnberg. At the Chair, all research groups focus on surface and interface science employing a wide range of spectroscopic and microscopic methods including synchrotron-radiation based techniques. The main research interests are (1) the development of new materials with novel electronic, geometric and chemical properties, (2) the investigation of elementary steps of surface reactions and (3) the development and construction of advanced scientific apparatus. The investigations aim at a fundamental physical and chemical understanding of all mechanisms and processes involved, at an atomic level. The Ph.D. thesis of Till Cremer was embedded in the Cluster-of-Excellence "*Engineering of Advanced Materials*" granted to the Universität Erlangen-Nürnberg and in the Priority Programm SPP 1191 "*Ionic Liquids*" of the German Research Foundation (DFG), both of which provided a perfect research environment through strong co-operation partners in chemistry and chemical engineering, experimentally as well as theoretically. In particular, the fruitful collaborations with Prof. Peter Wasserscheid (U Erlangen-Nürnberg) and Prof. Barbara Kirchner (U Leipzig) should be mentioned.

April 2013   Prof. Dr. Hans-Peter Steinrück
Erlangen, Germany

Acknowledgments

I would like to express my appreciation to many people who have given me help and support towards the completion of this thesis, only some of whom can be mentioned here.

I am particularly grateful to my principal supervisor, Prof. Hans-Peter Steinrück, for the support and encouragement, his advice, and his unsurpassed knowledge of surface science. I am grateful for the opportunity I had working in his laboratories and for the stimulating environment he provided me with. I am equally indebted to my second supervisor, Dr. Florian Maier, whose guidance, support and unconventional thinking have been invaluable.

I would also like to acknowledge Prof. Peter Wasserscheid and his group members for the fruitful in-house collaboration and stimulating discussions. Likewise, I am grateful to Prof. Barbara Kirchner and Henry Weber for the DFT calculations.

Apart from my fellow colleagues, I acknowledge my office partners, especially Dr. Regine Streber, Dr. Christian Papp, Dr. Alexey Deyko, Florian Rietzler and Inga Niedermaier. Also, Michael Stark, Leonie Wibmer and Sandra Krick Calderon are thanked for their experimental contributions. Special recognition is given to Dr. Claudia Kolbeck for her very uncomplicated nature and sharing of the apparatus.

I am most appreciative to the technical staff in our institute who were always helpful and open to questions and problems. Friedhold Wölfel and his co-workers are thanked for their craftsmanship. Of particular significance, Hans-Peter Bäumler and Bernd Kress have been invaluable, not only for solving technical problems but also for their kindness, friendship and personal support given me.

Last but not least, I would like to thank Rob Lynch for his editorial assistance. My family and especially Nicole Lynch, have given me their unequivocal support throughout, as always, for which my mere expression of thanks does not suffice.

Contents

Chapter 1
Introduction and Motivation

Ionic liquids (ILs) are a new class of materials, which have attracted vast scientific and industrial interest over the last decade [1]. They are salt melts comprised solely of ions and exhibit very low melting points compared to classical molten salts. The term "IL" is commonly used when the melting point is equal to or lower than 100 °C, while "RTIL" specifically refers to ILs with melting points lower than or equal to room temperature (RT). The low melting points of ILs are achieved by the chemical structure of the ions, which is characterized by low charge density and low molecular symmetry. A few common IL-forming anions and cations are portrayed in Fig. 1.1. The resulting manifold low-energy conformations prevent the formation of a stable crystal lattice, thus leading to low melting points [1, 2]. Attracted by their structural diversity and unique profile of physico-chemical properties (e.g., extremely low volatility, unusual solvation and miscibility properties, electroconductivity) [3–5], many research groups have studied this new class of materials. Possible applications range from green chemistry [6, 7], catalysis [8, 9] and electrochemistry [10] to analytics [11] and separation technologies [12], for all of which a brief overview and a few promising examples shall be given in the following.

In chemical synthesis ILs are used as green solvents because of their very low vapour pressure. This low volatility helps to considerably reduce waste and pollution compared to conventional organic solvents and allows for facilitated product separation in reaction processes [4]. Furthermore, ILs can have co-catalytic effects in homogenous catalysis leading to considerable changes in product distribution and in stereoselectivity [8, 9]. In electrochemistry (i.e., electrodeposition, batteries and solar cells) ILs show very promising results due their non-volatile character and wide electrochemical window [13, 14]. For separation technologies and sensor applications, ILs are capable of enhancing device performance while they currently revolutionize the field of gas chromatography when employed as stationary phase [11, 15]. In engineering, ILs are tested as lubricants, gas scavengers and for gas separation technologies [16, 17]. Certain ILs are even found to provide corrosion protection to metal alloys [18]. From the above-mentioned examples it

Cations

1,3-dialkyl-imidazolium	tetraalkyl-ammonium	tetraalkyl-phosphonium	N,N-dialkyl-pyrrolidinium	N-alkyl-pyridinium
$[C_nC_mIm]^+$	$[N_{nnnm}]^+$	$[P_{nnnm}]^+$	$[C_nC_mPyr]^+$	$[C_nPy]^+$

Anions

dicyanamide	tetrafluoroborate	alkyl-sulfate	bis(trifluoromethyl-sulfonyl)imide	tris(pentafluoroehtyl)-trifluorophosphate
$[DCA]^-$	$[BF_4]^-$	$[C_nOSO_3]^-$	$[Tf_2N]^-$	$[FAP]^-$
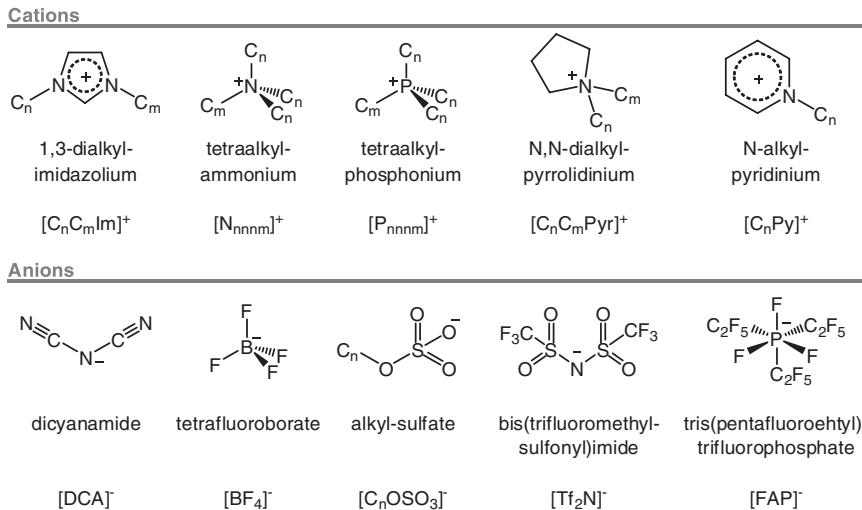
Fig. 1.1 Exemplary selection of a few typical cations and anions of which ILs can be composed. The most intensely investigated combination of ions where the largest experimental and theoretical data set is available are imidazolium-based cations paired with the bis(trifluoromethylsulfonyl)imide ($[Tf_2N]^-$) anion

becomes clear that the eminent issues that need to be addressed to understand and improve these novel applications/processes mainly lie in the IL interface regions, namely the IL/gas and the IL/solid interface.

The main motivation for the work conducted in the framework of this thesis stems from applications in heterogeneous catalysis, where ILs have led to completely new catalyst concepts such as the "Supported Ionic Liquid Phase" (SILP) and "Solid Catalyst with Ionic Liquid Layer" (SCILL) technologies, as illustrated in Fig. 1.2 [19–23]. In the SILP system a porous inert support material is coated with a thin IL layer that has a homogenous catalyst dissolved in it. This concept unifies the advantages of highly product- and stereo-selective homogenous catalysis and the continuous flow reactor design known from heterogeneous catalysis. In SCILL systems the catalyst material is impregnated with an IL layer. As a consequence enhanced selectivity, product distribution and yields may be observed. This is achieved by specific interactions of the IL with reactive sites of the heterogeneous catalyst particles or by solubility and mass transport changes when reactants and products diffuse through the IL to/from the catalyst surface [24, 25].

Figure 1.3 shows an overview over the aspects relevant for the performance of the catalyst concepts introduced in the above paragraph. Due to the above mentioned low volatility of IL's, a surface science approach, i.e., defined surface structures, ultra-clean conditions, ultra-high vacuum (UHV) environment, can be used to model and understand these systems on a fundamental level. As can be seen from Fig. 1.3, important aspects for tuning the catalyst performance are found in
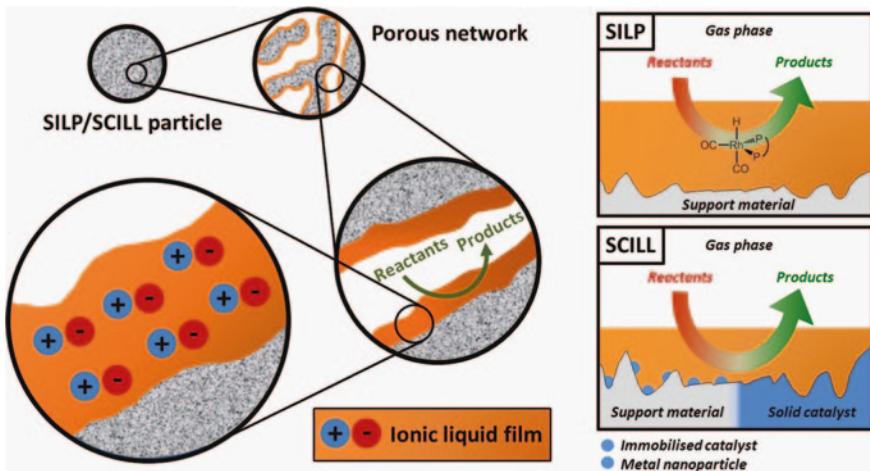
Fig. 1.2 Schematic representation of the SILP and SCILL catalyst concepts, adapted from Ref. [26]. For details, see text
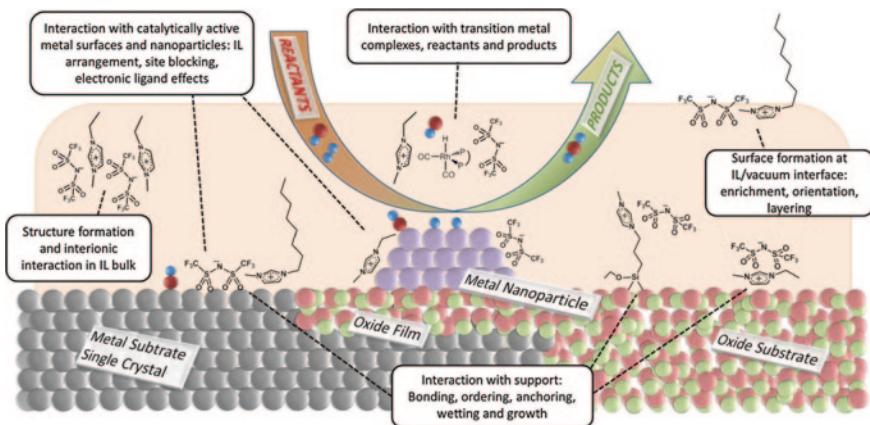
Fig. 1.3 Illustration of the aspects relevant for SILP and SCILL performance and surface science approaches used to model the SILP and SCILL catalysis concepts. The surface structure of the IL film can be analysed by ARXPS, whereas electronic interactions in the IL bulk can be investigated using geometries in which 7–9 nm of the liquid are probed. The IL/solid interface can be accessed by investigating ultrathin IL films deposited by physical vapour deposition on the selected substrate

all regions of the IL film. At the IL/gas interface, for example, surface formation and preferential arrangement of the ion can influence properties such as gas solubility and mass transport across the interface. In the SILP concept enrichment of the catalyst in the surface near region is desired to avoid diffusion-limited reaction rates. With respect to IL bulk structure formation, interactions between the IL ions

but also with other species dissolved therein, are of fundamental interest. Finally, the IL/solid interface is accountable for properties such as surface wetting, ligand effects and interfacial arrangement of the ions.

Due to the above-mentioned multitude of possible applications, where the IL/gas interface is of importance, this topic has seen increasing research focus over the last years and has been examined by multiple surface-sensitive spectroscopic methods such as sum-frequency generation (SFG), X-ray reflectivity and neutron reflectometry [27–29]. In addition, owing to the sufficiently low vapour pressure of IL's, a whole arsenal of UHV-based surface sensitive methods can be used to examine the IL/vacuum interface. The include photoelectron spectroscopy (PES), low energy ion scattering (LEIS), secondary ion mass spectrometry (SIMS), (high resolution) electron energy loss spectroscopy ((HR)EELS) and direct recoil spectroscopy (DRS), to name only a few [30–33]. Amongst all these techniques, angle-resolved XPS is one of the most powerful tools: It allows the investigation of the surface electronic structure, elemental composition and enrichment effects [34, 35]. By addressing the IL/vacuum interface by means of XPS, our group has previously made important contributions aiding to understand SILP systems on a fundamental level [36–39].

In this thesis, in addition to further expanding our knowledge of the IL/vacuum interface, an attempt was made to move on and investigate other domains relevant to SCILL and SILP catalysis. As evident from Fig. 1.3 IL bulk properties such as ion–ion interactions and structure formation are of utmost interest. The physico-chemical properties of bulk ILs have been under intense investigation for over two decades, leading to a reputable body of knowledge. However, open questions remain and it is shown in this thesis that XPS can greatly contribute to understanding the electronic structure and ion–ion interactions in the IL bulk.

With regard to the IL/solid interface, increasing efforts have been made in the past few years to investigate systems, where the bulk IL is in contact with the solid. However, information on the IL/solid interface of thin IL films on a substrate of interest, is still scarce and the small number of corresponding fundamental studies reflects the infancy of this research area. It has been shown that, despite their very low vapour pressure at room temperature, a large variety of ILs can be evaporated without decomposition by heating in vacuum [40, 41]. Several recent experimental and theoretical studies addressed the volatility of a large number of aprotic ionic liquids [40, 42–44]. Gas phase measurements showed that a thermally evaporated IL beam mainly consists of isolated ion pairs, with no larger clusters or single ions being observed [40, 43]. Based on these findings, an IL-based physical vapour deposition (PVD) process was recently developed by our group [45]. This technique allows in situ deposition of thin IL films on support materials under ultra-clean conditions, not only enabling us to investigate the IL-solid interface but also providing a tool to fabricate novel hybrid materials [46].

In this work, by using mainly XPS, a variety of issues of fundamental interest (illustrated in Fig. 1.3) were addressed with respect to IL bulk, IL/vacuum and IL/

solid interface properties. In each chapter a separate introductory and experimental section is provided to give a deeper insight into the aspects relevant to each subject. This thesis is organized such that the introduction (this chapter) is followed by the fundamentals of the applied surface science techniques and the experimental setup (Chap. 2). Chapter 3 encompasses the studies performed on macroscopically thick IL films, and in Chaps. 4 and 5 the results obtained on IL thin films deposited on different support materials are compiled.

In Sect. 3.1, the ion–ion interactions of ILs were investigated to gain a fundamental understanding of the electronic structure of and the specific interactions within the ionic liquid. By combining XPS, nuclear magnetic resonance (NMR) spectroscopy and density functional theory (DFT) calculations, an assortment of imidazolium-based ILs was analysed. Coulomb and hydrogen-bonding contributions were scrutinized and experimental evidence was found for charge transfer effects. In Sect. 3.2 the IL/vacuum interface of a variety of imidazolium-based ILs was investigated. It was found in a previous study, that alkyl chains attached to either the cation or the anion are enhanced in the surface layer, while oligo(ethyleneglycol)ether (PEG) chains of similar length are randomly oriented even at the immediate IL/vacuum interface [38]. Herein, the effect of anion structure on the surface enhancement of an octyl chain attached to the imidazolium ring was investigated. Thereby a strong anion size-dependency on the alkyl enhancement was observed, exhibiting reduced surface enrichment with increasing anion size. For very small anions such as chloride a very efficient chain enhancement takes place which in magnitude is comparable to that of highly ordered systems such as thiolate self-assembled monolayers (SAM) on Au(111).

In Sect. 4.1 ultrathin IL films were deposited on an Au(111) single crystal. The aim of this study was to gain fundamental insights into the electronic interaction between the IL and the metal support, the molecular arrangement of the IL at the surface and the growth characteristics of the resulting IL films. Three different ILs were deposited on the Au(111) surface and it was found that the charged moieties of anion and cation occupy the surface in equal amounts, i.e. they adsorb next to each other. Furthermore, it could be shown that the IL molecules show a ion-dependent chemical shift when in direct contact with the surface and that the ILs growth proceeds in a layer-by-layer fashion. In Sect. 4.2, a selected IL was deposited on a reactive Ni(111) surface. In analogy to the Au(111) experiments, electronic interaction, molecular arrangement and growth behaviour were analysed. While slightly different growth characteristics were observed, a strongly different interface arrangement of the IL was found for the IL/Ni(111) system. Moreover, the reactivity of the surface upon oxygen exposure was investigated for both IL-coated and pristine Ni(111). Finally, different IL growth behaviour was found when thin IL films were deposited on a native glass sample. There, after formation of a wetting layer, droplet formation occurred. The results from the IL/silicate interface are presented in Chap. 5, along with approaches to modify the surface such that more uniform IL coatings on glass can be achieved.

References

1. N.V. Plechkova, K.R. Seddon, Chem. Soc. Rev. **37**, 123 (2008)
2. P. Wasserscheid, W. Keim, Angew. Chem. Int. Ed. **39**, 3772 (2000)
3. K. Binnemans, Chem. Rev. **105**, 4148 (2005)
4. P. Wasserscheid, T. Welton, *Ionic Liquids in Synthesis*, 2nd edn. (Wiley-VCH, Weinheim, 2008)
5. H. Weingärtner, Angew. Chem. Int. Ed. **47**, 654 (2008)
6. C. Capello, U. Fischer, K. Hungerbuhler, Green Chem. **9**, 927 (2007)
7. M.J. Earle, K.R. Seddon, Pure Appl. Chem. **72**, 1391 (2000)
8. T. Welton, Coord. Chem. Rev. **248**, 2459 (2004)
9. T. Welton, Chem. Rev. **99**, 2071 (1999)
10. F. Endres, S.Z. El Abedin, Phys. Chem. Chem. Phys. **8**, 2101 (2006)
11. J.L. Anderson, D.W. Armstrong, G.T. Wei, Anal. Chem. **78**, 2892 (2006)
12. C. Jork, C. Kristen, D. Pieraccini, A. Stark, C. Chiappe, Y.A. Beste, W. Arlt, J. Chem. Thermodyn. **37**, 537 (2005)
13. B. Li, L.D. Wang, B.N. Kang, P. Wang, Y. Qiu, Sol. Energy Mater. Sol. Cells **90**, 549 (2006)
14. H.L. Liu, Y.S. Liu, J. Li, Phys. Chem. Chem. Phys. **12**, 1685 (2010)
15. P. Sun, D.W. Armstrong, Anal. Chim. Acta **661**, 1 (2010)
16. F. Zhou, Y. Liang, W. Liu, Chem. Soc. Rev. **38**, 2590 (2009)
17. S. Werner, M. Haumann, P. Wasserscheid, Ann. Rev. Chem. Biomol. Eng. **1**, 203 (2010)
18. M. Forsyth, W.C. Neil, P.C. Howlett, D.R. Macfarlane, B.R.W. Hinton, N. Rocher, T.F. Kemp, M.E. Smith, Appl. Mater. Interf. **2009**, 1 (1045)
19. A. Riisager, P. Wasserscheid, R. van Hal, R. Fehrmann, J. Catal. **219**, 452 (2003)
20. C.P. Mehnert, R.A. Cook, N.C. Dispenziere, M. Afeworki, J. Am. Chem. Soc. **124**, 12932 (2002)
21. Y.L. Gu, C. Ogawa, J. Kobayashi, Y. Mori, S. Kobayashi, Angw. Chem. Intl. Ed. **45**, 7217 (2006)
22. U. Kernchen, B. Etzold, W. Korth, A. Jess, Chem. Eng. Technol. **30**, 985 (2007)
23. Y. Gu, G. Li, Adv. Synt. Catal. **351**, 817 (2009)
24. J. Arras, E. Paki, C. Roth, J. Radnik, M. Lucas, P. Claus, J. Phys. Chem. C **114**, 10520 (2010)
25. J. Arras, M. Steffan, Y. Shayeghi, D. Ruppert, P. Claus, Green Chem. **11**, 716 (2009)
26. A. Riisager, R. Fehrmann, M. Haumann, P. Wasserscheid, Top. Catal. **40**, 91 (2006)
27. C. Aliaga, C.S. Santos, S. Baldelli, Phys. Chem. Chem. Phys. **9**, 3683 (2007)
28. E. Bowers, M.C. Vergara-Gutierrez, J.R.P. Webster, Langmuir **20**, 309 (2004)
29. E. Sloutskin, B.M. Ocko, L. Tamam, I. Kuzmenko, T. Gog, M. Deutsch, J. Am. Chem. Soc. **127**, 7796 (2005)
30. S. Krischok, M. Eremtchenko, M. Himmerlich, P. Lorenz, J. Uhlig, A. Neumann, R. Ottking, W.J.D. Beenken, O. Höfft, S. Bahr, V. Kempter, J.A. Schäfer, J. Phys. Chem. B **111**, 4801 (2007)
31. G. Law, P.R. Watson, A.J. Carmichael, K.R. Seddon, B. Seddon, Phys. Chem. Chem. Phys. **3**, 2879 (2001)
32. S. Caporali, U. Bardi, A. Lavacchi, J. Electron. Spectrosc. Rel. Phenom. **151**, 4 (2006)
33. E.F. Smith, F.J.M. Rutten, I.J. Villar-Garcia, D. Briggs, P. Licence, Langmuir **22**, 9386 (2006)
34. K.R.J. Lovelock, I.J. Villar-Garcia, F. Maier, H.-P. Steinrück, P. Licence, Chem. Rev. **110**, 5158 (2010)
35. H.-P. Steinrück, Surf. Sci. **604**, 481 (2010)
36. J.M. Gottfried, F. Maier, J. Rossa, D. Gerhard, P.S. Schulz, P. Wasserscheid, H.-P. Steinrück, Z. Phys, Chem. **220**, 1439 (2006)
37. C. Kolbeck, M. Killian, F. Maier, N. Paape, P. Wasserscheid, H.-P. Steinrück, Langmuir **24**, 9500 (2008)
38. K.R.J. Lovelock, C. Kolbeck, T. Cremer, N. Paape, P.S. Schulz, P. Wasserscheid, F. Maier, H.-P. Steinrück, J. Phys. Chem. B **113**, 2854 (2009)

39. F. Maier, J.M. Gottfried, J. Rossa, D. Gerhard, P.S. Schulz, W. Schwieger, P. Wasserscheid, H.-P. Steinrück, Angw. Chem. Intl. Ed **45**, 7778 (2006)
40. J.P. Armstrong, C. Hurst, R.G. Jones, P. Licence, K.R.J. Lovelock, C.J. Satterley, I.J. Villar-Garcia, Phys. Chem. Chem. Phys. **9**, 982 (2007)
41. M.J. Earle, J. Esperanca, M.A. Gilea, J.N.C. Lopes, L.P.N. Rebelo, J.W. Magee, K.R. Seddon, J.A. Widegren, Nature **439**, 831 (2006)
42. Y.U. Paulechka, D.H. Zaitsau, G.J. Kabo, A.A. Strechan, Thermochim. Acta **439**, 158 (2005)
43. D. Strasser, F. Goulay, M.S. Kelkar, E.J. Maginn, S.R. Leone, J. Phys. Chem. A **111**, 3191 (2007)
44. D.H. Zaitsau, G.J. Kabo, A.A. Strechan, Y.U. Paulechka, A. Tschersich, S.P. Verevkin, A. Heintz, J. Phys. Chem. A **110**, 7303 (2006)
45. T. Cremer, Diploma Thesis, Friedrich-Alexander University Erlangen-Nuremberg, 2008
46. F. Maier, T. Cremer, H.-P. Steinrück, P. Wasserscheid, Neuartige Hybridmaterialen, 2008, (pending patent application 10 2008 2015 2015.2000)

Chapter 2
Fundamentals and Techniques

2.1 X-Ray Photoelectron Spectroscopy (XPS)

Photoelectron spectroscopy makes use of the photoelectric effect, which was discovered in 1887 by Hertz and explained by Einstein in 1905 [1]. When a material is irradiated with light whose energy $h\nu$ exceeds the material's work function (usually a few electron volts, depending on the sample material), electrons are ejected from the material. The photoelectron leaves the sample with a defined kinetic energy E_{kin}, which can be measured with an energy dispersive electron analyser (e.g., a hemispherical analyser). Through knowledge of E_{kin} of the photoelectron, the binding energy (BE) E_B relative to the vacuum level can be calculated according to the Einstein equation:

$$E_B^V = h\nu - E_{kin} \tag{2.1}$$

While for gas phase species equation (2.1) is valid, for condensed matter the work functions of both the sample (ϕ_s, variable) and the electron analyser (ϕ_{spec}, constant) have to be considered as they influence E_{kin}, (see Scheme 2.1 for details). This reference problem is usually overcome by calibrating the spectrometer to the Fermi level of the (conducting) sample, which can be achieved by direct measurement of the Fermi level (for example in the case of Ni) or a characteristic signal of high intensity and narrow natural line width (such as the Au $4f_{7/2}$ level), leading to Eq. (2.2):

$$E_B^V = h\nu - E_{kin} - \phi_{spec} = h\nu - E_{kin}^{eff} \tag{2.2}$$

In the absence of such a defined reference level, other arbitrary internal reference levels can be defined, in most cases leading to less accurate absolute BE positions.

During the photoemission process, interactions of the photoelectrons with the surrounding matter can take place. Typical interactions are inelastic scattering, vibrational or other electronic excitations. A photoelectron may undergo multiple "energy loss events" leading to both lower kinetic energies of the primary electron and also the generation of secondary electrons, resulting in a superimposed

Scheme 2.1 Schematic
energy diagram for X-ray
photoelectron spectroscopy
[2–4]
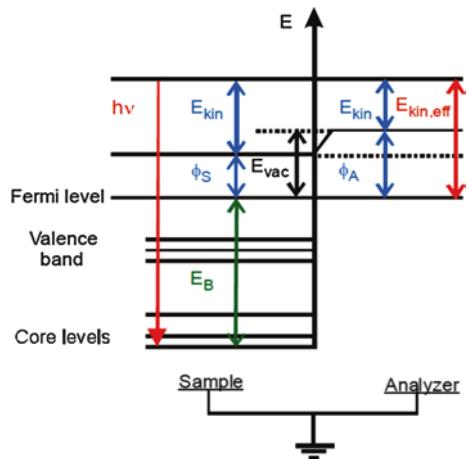
background signal. The spectral lines observed in a typical XP spectrum, however, are due to the discrete energy values of the core levels of the elements present in the sample, therefore making XPS an element specific technique. Furthermore, each core level has a constant excitation cross section at given hν, which allows for quantitative analysis, also leading to the expression "electron spectroscopy for chemical analysis" (ESCA). Quantitative analysis is possible when the transmission function of the electron analyser is known, which can be easily calibrated by using ILs such as $[C_2C_1Im][Tf_2N]$, due to the presence of a variety of different elements evenly distributed over the whole BE range probed by a standard x-ray gun. As signal and background intensity are dependent of a variety of parameters such as sample position (with respect to both x-ray gun and analyser), photon flux and detection angle, correction factors can be applied to compensate for intensity variations and therefore allow for quantitative comparison of spectra taken at different detection angles (see below) [5]. A typical XPS survey spectrum of a clean Au(111) single crystal and an ionic liquid, in this case $[C_8C_1Im][Tf_2N]$, is shown in Fig. 2.1.

Although the core electrons of an atom are not directly involved in a chemical bond, they are still influenced by the chemical surrounding of the atom. Consequently, the BE depends on the chemical state of a compound, leading to a chemical shift of the core level signal, which can amount to BE shifts of several eV. Typically, this effect can be divided into so-called initial state and final state effects. The terms initial and final state refer to the respective energies in the photoemission process resulting in the measured BE [2]:
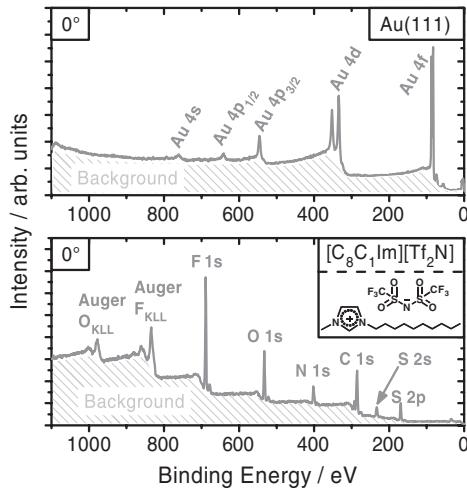
$$E_B = E_f^{N-1} - E_i^N \tag{2.3}$$

with:

E_i^N Energy of the initial state with N electrons
E_f^{N-1} Energy of the final state with N − 1 electrons.

A typical initial state effect is given by a permanent partial charge at the emitting atom, for example through chemical bonding to another atom. When this atom

Fig. 2.1 XPS survey scans
of an Au(111) single crystal
and the IL [C$_8$C$_1$Im][Tf$_2$N]

is probed, the kinetic energy of the emitted photoelectron is higher for a negative and lower for a positive partial charge, due to higher/lower Coulomb interactions. A typical final state effect is a more efficient screening of the core hole or more efficient relaxation by surrounding electrons. Such more effective screening leads to a higher kinetic energy of the photoelectron as the positive core hole is not interacting as strongly with the emitted photoelectron, resulting in a lower BE value. Another feature in XP spectra is the appearance of "shake off" and "shake up" satellites, which can also be assigned to the subgroup of final state effects. A more detailed description of these phenomena can be found in References [2, 3, 6]. Furthermore, an excited core hole created in the photoemission process can undergo an Auger decay resulting in an Auger electron with a characteristic kinetic energy independent of the incident photon energy. Therefore, Auger peaks are a common (but often undesired) feature in an XP spectrum, as can be seen in Fig. 2.1.

The excited photoelectrons have a very high cross section with condensed matter, which makes XPS an inherently surface sensitive method. Due to inelastic scattering processes described above fewer electrons from deeper layers can leave the sample surface without undergoing some kind of energy loss process. The mean distance an electron can travel without an inelastic scattering event is given by the inelastic mean free path λ, which is a function of the kinetic energy of the respective electron and also depends on the nature (atomic number and density) of the material it passes through. For the organic materials and the kinetic energies used in this study λ is estimated to be 2–3 nm [7, 8]. The maximum information depth of 6–9 nm can be calculated from Eq. (2.4), where the signal intensity I_0 is damped to I_d when covered by an overlayer of a certain thickness d.

$$I_d = I_0 \cdot e^{-d/\lambda} \cdot \cos \vartheta \qquad (2.4)$$

with ϑ: electron take-off angle with respect to the surface normal.

Equation (2.4) can also be used to estimate the film thickness and to analyse the growth behaviour of a compound deposited on top of a support material. For strict layer-by-layer growth a polygon-like behaviour along the exponential line should be observed, as until completion of one closed layer (with a defined thickness given by the dimensions of the deposit), a linear decrease should be observed until the next layer starts to grow (see Ref. [9] for details). Further information on the growth behaviour can be extracted when measuring in an angle-resolved XPS (ARXPS) setup. In ARXPS the surface sensitivity can be enhanced by the cosine of the electron take-off angle relative to the surface normal, as depicted in Scheme 2.2. By comparing the signal damping in normal and grazing emission, the growth behaviour can be analysed in such a way, that it is even possible to distinguish between Frank-van-der-Meerve (layer-by-layer growth) and Stranski–Krastanov (2D-wetting layer followed by island growth) growth mechanisms, which will be shown in this thesis (see Chaps. 4 and 5).

However, ARXPS is not only advantageous for the determination of the growth behaviour deposits. In fact, it is a very powerful tool for the investigation of surface enrichment effects within the top most layers of a compound, which is achieved by comparing the relative normal and grazing emission intensities of the species (i.e., an element or parts of a molecule) present in the topmost layers of the sample. If the grazing emission intensity of a certain species A is increased at the expense of another species B compared to the XPS intensities under normal emission geometry, it can be concluded that A is enriched at the surface. This is elucidated in Fig. 2.2, where the enrichment of the C_{10} alkyl chain of $[C_{10}C_1Im][Tf_2N]$ is compared to the non-enriched oligo(etherglycol) chains of $[Me(EG)_3C_1Im][Tf_2N]$ [10].
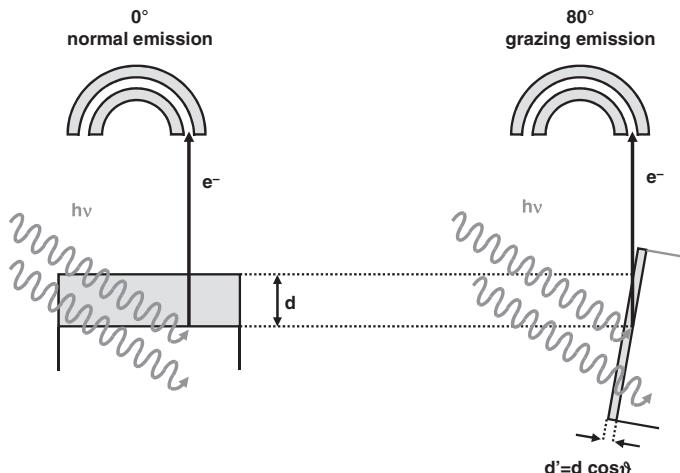
Scheme 2.2 Illustration of the ARXPS setup. The information depth d' results from the cosine of the tilt angle with respect to the surface normal, therefore at 80° the surface sensitivity of XPS can be enhanced by a factor of six
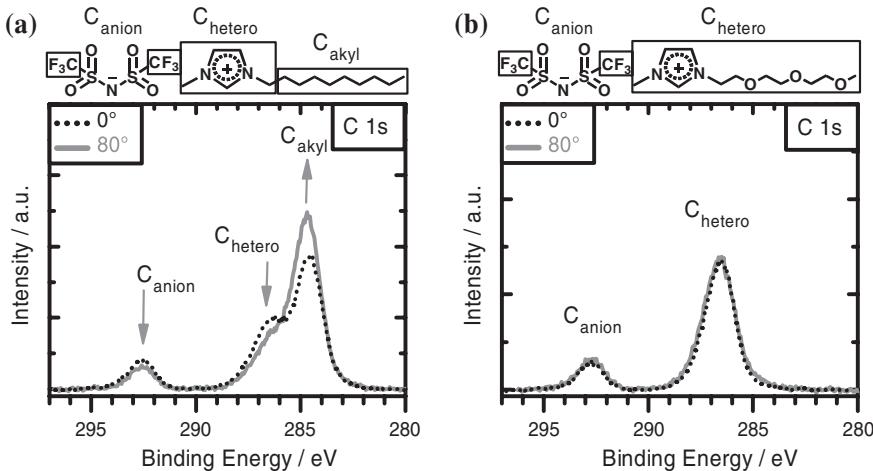
Fig. 2.2 Comparison of ARXP spectra of **a** $[C_{10}C_1Im][Tf_2N]$ and **b** $[Me(EG)_3C_1Im][Tf_2N]$. In **a** an unambiguous increase of C_{alkyl} and a concomitant decrease of C_{anion} and C_{hetero} is observed in 80° emission. For **b**, however, no relative changes are observed. For a detailed assignment of spectral features in the C 1s region, see Sect. 2.2, for a more detailed discussion of the surface structure of $[C_nC_1Im][Tf_2N]$ ILs, see Ref. [10] and Sect. 3.2. Note, that the 80° emission data have been normalized using a geometry factor to allow for visual comparison, see Ref. [5] for details

2.2 Ionic Liquids

As already mentioned in the Introduction, ILs are a new class of materials with unique physico-chemical properties. The concept of molten salts, however, has been around for a long time and it has been shown that in some well-established industrial processes (vanadia-based catalysts for sulphuric acid production and flue gas cleaning, see Ref. [11] and references therein) the heterogeneous catalyst is in fact a molten salt under reaction conditions. Also, in aluminium smelters, a eutectic mixture of alumina (Al_2O_3) and Kryolithe ($Na_3[AlF_6]$) is used as the electrolyte from which metallic Al is cathodically deposited. However, examples for the use of molten salts are rare and usually require high energy input (due to the high melting points). In addition, high temperature salt melts are usually strongly corrosive and thus extremely hazardous and difficult to handle. While the first representative of a room temperature IL (RTIL) was synthesized and characterized almost 100 years ago by Paul Walden [12], it was not until the late second half of the twentieth century that the potential of these materials was recognized and the term "Ionic Liquid" was coined. While the early generation of ILs still had numerous disadvantageous properties such as air- and water-sensitivity, research efforts by Wilkes led to the development of easy-to-handle air- and water-stable ILs [13, 14].

After this, as ILs became readily available to a lot of fields, IL research progressed into new realms. Already after a few years a broad range of IL-based

research fields had developed, which is mainly due to the fact that because of the diversity of possible IL structures an almost unlimited number of different ILs can be synthesized [15]. This led to the terms "task-specific" ILs and "designer solvents" and accounts for the fact that by changing the chemical structure of an IL the physico-chemical properties can be adjusted according to the boundary conditions given by the desired application. An overview of a few common cations and anions that ILs can be composed of is shown in Fig. 1.1.

Although the structural diversity has enormous and exciting potential for future applications, it is also disadvantageous from a fundamental point of view. The physico-chemical properties of ILs can be tuned in such a wide range and are therefore so manifold that so far quite often a thorough understanding of the structure-performance relationship is lacking and systematic trends have yet to be developed. However, in the fields of fundamental IL research addressing the physico-chemical properties of ILs there is one IL, namely $[C_nC_1Im][Tf_2N]$, which could be considered the "guinea pig" of IL research, being by far the best-investigated IL system. Also in this thesis, mainly imidazolium-based ILs are investigated; in Chap. 3 $[C_8C_1Im]^+$-based cations are paired with different anions, while $[C_nC_1Im][Tf_2N]$ is, apart from one pyrrolidinium IL, exclusively used in Chaps. 4 and 5. An overview of the ILs used in this thesis is given in Table 2.1. As the imidazolium cation and the $[Tf_2N]^-$ anion are mainly used, some important fundamental properties of these two ions shall be reviewed followed by a brief description of their "bulk" XP spectra.

Starting with the imidazolium cation, the most striking feature in its chemical structure is the aromatic ring system, where the positive charge is delocalized leading to a relatively low average charge density. This property is of fundamental relevance for forming an IL, as it prevents build-up of a stable crystal lattice by allowing multiple low energy conformations. Delocalized positively charged moieties are found for a variety of other cations. Another structural motif leading to reduced melting points is found in systems, where the positive centre is surrounded by bulky alkyl substituents (i.e. $[NR_4]^+$) and is thus sterically inaccessible by the anion. For the imidazolium cation, alkyl chains of usually different length (usually one methyl group (m = 1) and one alkyl chain with $1 \leq n \leq 10$) are attached to the two nitrogen atoms. The positive charge does not penetrate very far into the alkyl chain, resulting in a rather neutral part of the ion (see also Sect. 3.1 for a detailed discussion). While generally distinct alterations in the physico-chemical properties of an IL can be achieved by changing the ion backbone, i.e., the cationic headgroup/charged moiety of the cation and by changing the anion, fine tuning of the resultant IL is usually achieved by changing the length of the alkyl chains attached to the ionic part of the cation [16]. In a further step, functional groups can be introduced into these side chains leading to even more structural diversity and higher abundance of individually tuneable properties.

For imidazolium-based ILs, three main intermolecular interaction modes with the counter ion (or other species such as dissolved molecules or surface atoms in contact with the IL) can be identified: Coulombic, dispersive and hydrogen-bonding interactions. Coulombic interactions are long range interactions that fall

Table 2.1 Overview of al ILs investigated in this thesis

Label	Structure	Name	Chapter #
[C$_8$C$_1$Im]Cl		1-methyl-3-octyl-imidazolium chloride	3
[C$_8$C$_1$Im]Br		1-methyl-3-octyl-imidazolium bromide	3
[C$_8$C$_1$Im]I		1-methyl-3-octyl-imidazolium iodide	3
[C$_8$C$_1$Im][NO$_3$]		1-methyl-3-octyl-imidazolium nitrate	3
[C$_8$C$_1$Im][BF$_4$]		1-methyl-3-octyl-imidazolium tetrafluoroborate	3
[C$_8$C$_1$Im][PF$_6$]		1-methyl-3-octyl-imidazolium hexafluorophosphate	3
[C$_8$C$_1$Im][TfO]		1-methyl-3-octyl-imidazolium trifluoromethylsulfonate	3
[C$_8$C$_1$Im][Tf$_2$N]		1-methyl-3-octyl-imidazolium bis[(trifluoromethyl)sulfonyl]imide	3, 4
[C$_8$C$_1$Im][Pf$_2$N]		1-methyl-3-octyl-imidazolium bis[(pentafluoroethyl)sulfonyl]imide	3
[C$_8$C$_1$Im][FAP]		1-methyl-3-octyl-imidazolium tris(pentafluoroethyl)-trifluorophosphate	3
[C$_8$C$_1$C$_1$Im]Br		1,2-methyl-3-octyl-imidazolium bromide	3

(continued)

Table 2.1 (continued)

Label	Structure	Name	Chapter #
[C$_8$C$_1$C$_1$Im] [Tf$_2$N]		1,2-methyl-3-oc-tylimidazolium bis[(trifluoromethyl) sulfonyl]imide	3
[C$_4$C$_1$Pyrr] [Tf$_2$N]		1-Butyl-1-methylpyrrolidinium bis[(trifluoromethyl) sulfonyl]imide	4
[C$_1$C$_1$Im][Tf$_2$N]		1,3-dimethylimidazolium bis[(trifluoromethyl) sulfonyl]imide	4, 5
[C$_2$C$_1$Im][Tf$_2$N]		1-ethyl-3-methyl-imidazolium bis[(trifluoromethyl) sulfonyl]imide	5

Displayed are their label used throughout this thesis, their chemical structure, IUPAC name, and the chapter in which the respective IL is investigated

off with 1/r, leading to some kind of long range order, even in the liquid phase of ILs. Dispersive forces are of much shorter range and taper off with 1/r^6, yet, theoretical calculations show that dispersive interactions play a crucial role for the liquidity of ILs as they create more shallow energy potential curves compared to solid salts such as NaCl [17]. The dispersive interactions discussed here actually address dispersive forces within the charged regions of the molecules, as they are usually large and have a strongly delocalized excess charge. Contributions through dispersive forces by the alkyl chains—usually referred to as van der Waals interactions—have to be taken into account, too; however, these interactions eventually lead to increased melting points. Therefore, the influence of alkyl chain length on the melting point of the IL has to be subdivided into two parts, namely the symmetry breaking region ranging from C$_2$–C$_8$ where decreased melting points are observed, and the hydrophobic region $\geq$C$_{10}$, where melting points are drastically increased due to increasing dispersive forces between the alkyl chains [18]. While imidazolium-ILs with short alkyl chains (n < 4) have a homogenous structure with alternating ions, it was shown that for longer alkyl chains domains develop where non-polar alkyl chains and charged headgroups segregate and create micro-heterogeneities [19]. This concept holds true for all ILs containing longer aliphatic carbon chains. A similar trend is observed for the IL/vacuum (and the IL/air) interface, where for n $\geq$ 4 an alkyl-dominated surface layer develops, as has been shown in a recent XPS study performed by our group [10]. Therein, it could be shown that for [C$_n$C$_1$Im][Tf$_2$N] (with $1 \leq n \leq 16$) stronger surface enrichment of the alkyl chain is found with increasing alkyl chain length (see Fig. 3.14 in Sect. 3.2). Hydrogen bonds have—as the name implies—a localized bond-like structure and have to be considered in imidazolium ILs because the proton in

the C_2 position of the imidazolium ring exhibits a certain acidity ($pK_a \sim 24$ for $[C_1C_1Im]^+$ [20], compared to ~16 for EtOH and >40 for butane). A measure for the hydrogen bond donor ability of the cation is given by the Kamlet-Taft parameter α. Nonetheless, the extent to which hydrogen bonding can take place also depends on the nature of the anion, i.e., its hydrogen bond basicity (Kamlet-Taft parameter β), which is closely related to the availability of localized electron lone pairs and therefore increases with decreasing strength of the conjugate acid of the anion. Further aspects dealing with electrostatic and hydrogen-bonding forces in imidazolium ILs are discussed in more detail in Chap. 3.

The $[Tf_2N]^-$ anion with its very bulky yet highly flexible low symmetry structure (apart from one conformer with C_2 symmetry, all other structures have C_1 symmetry) has the negative charge distributed fairly evenly over the whole $[O_2S$-N-$SO_2]$ moiety of the molecule, with slightly less charge density at the electron-withdrawing CF_3 groups [21]. Furthermore, access to the $[S$–N–$S]^-$ centre is hindered due to steric shielding by the surrounding triflate groups [22]. There are a number of low energy conformations leading to a variety of almost energetically degenerate conformations at room temperature, which help to prevent the formation of a stable crystal lattice, eventually leading to reduced melting points. Broadly speaking it can be said that $[Tf_2N]^-$-based ILs are rather hydrophobic, chemically inert and thermally stable, and are therefore most widely used [22]. In XPS, as derived from our own experience, $[Tf_2N]^-$-based ILs exhibit relatively few X-ray radiation-induced decomposition effects compared to other anions such as $[BF_4]^-$ or $[FAP]^-$. Also, no water adsorption on the IL surface or in the IL bulk is observed during XPS, which can be the case for strongly hydrophilic ILs such as $[C_nC_mIm]Cl$. Furthermore, $[Tf_2N]^-$ ILs can be evaporated under UHV conditions well below their decomposition temperature and are therefore ideal candidates for the IL-PVD process used in the thin films experiments presented in Chaps. 4 and 5.

At this point, it seems relevant to discuss the spectral features that a prototypical IL used throughout this thesis, namely $[C_8C_1Im][Tf_2N]$, gives rise to in XPS. In Fig. 2.3 a survey scan of $[C_8C_1Im][Tf_2N]$ is shown, along with the detailed core level spectra of all IL-related signals. The F 1s, O 1s and S 2p regions only show anion-related signals with BE values of ~689, 532 and 169 eV, respectively. The asymmetric structure of the S 2p peak is due to the 2:1 spin–orbit splitting inherent to 2p orbitals, in the case of sulphur amounting to a peak separation of 1.2 eV. The C 1s and N 1s regions, however, contain multiple signals that can be assigned to both cation and anion and are therefore of utmost value when analysing the surface structure with regard to enrichment effects. More specifically, in the N 1s region two signals with a ratio of 2:1 are observed. The 402 eV feature is attributed to the two imidazolium nitrogens (exhibiting identical BE values irrespective of their slightly different chemical environment) and is therefore labelled N_{cation}. The peak around 399 eV originates from the imidic nitrogen of the anion and is accordingly named N_{anion}. For the C 1s region a more complicated structure is observed which shall be discussed in more detail in the following paragraph.

For $[C_8C_1Im][Tf_2N]$ three main features can be clearly distinguished in the C 1s region with BE values of ~293, 287 and 285 eV. Due to the chemical structure of
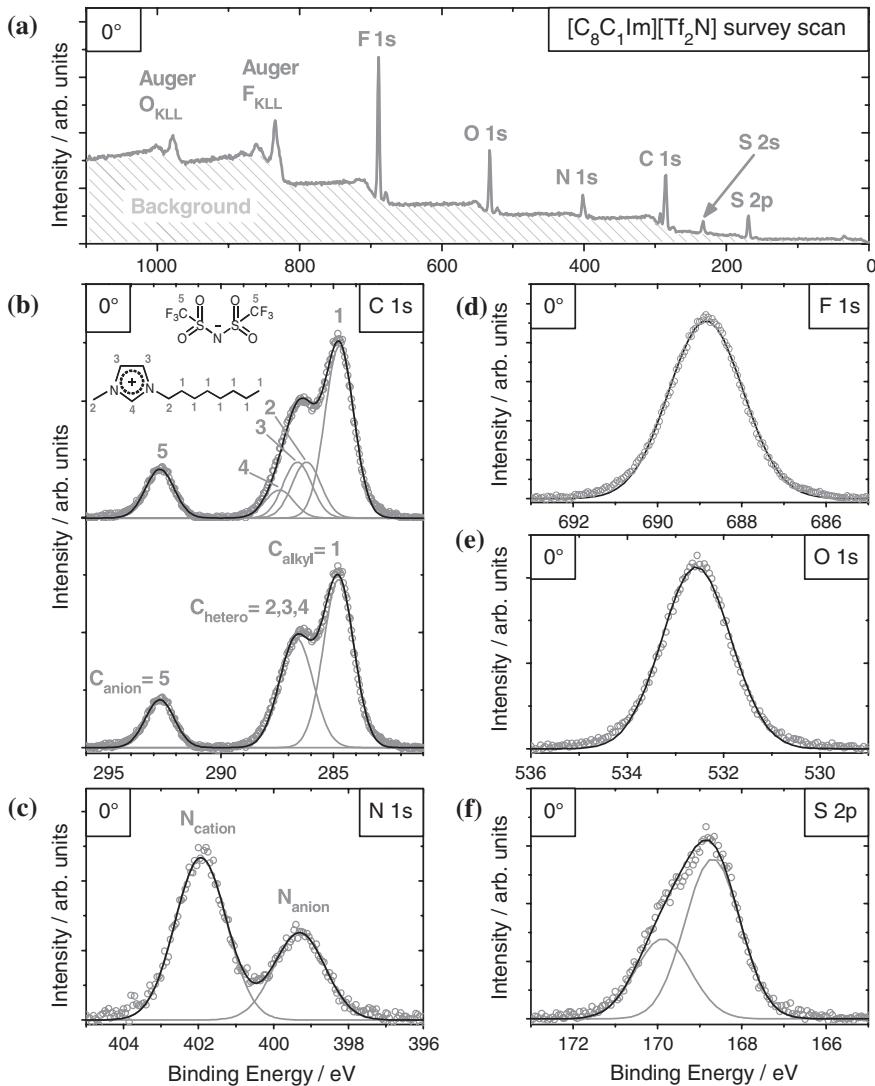
Fig. 2.3 Overview over XP survey (**a**) and core level spectra of $[C_8C_1Im][Tf_2N]$. In the C 1s region (**b**) two different fitting procedures are shown. The upper spectrum is fitted according to Ref. [23], while the latter portrays the fitting protocol used in this thesis (for details, please see text). In the C 1s spectrum three main features can be seen which correspond to aliphatic carbon (~285 eV; C_{alkyl}), carbon atoms bonded to nitrogen atoms (~287 eV; C_{hetero}) and the CF_3 groups of the anion (~293 eV; C_{anion}). In the N 1s region (**c**), two peaks are observed, of which the high BE signal corresponds to the two cationic nitrogen atoms (~402 eV, N_{cation}), while the low BE signal is attributed to the imidic nitrogen of the anion (~399 eV; N_{anion}). The F(~689 eV), O(~532 eV) and S(~169 eV) atoms (**d**–**f**) of the anion are all chemically equivalent and give rise to one single signal, whereas the S 2p signal is spin orbit split by 1.2 eV

the $[C_8C_1Im]^+$ cation four chemically non-equivalent carbon species are present (species 1–4, see Fig. 2.3). An additional carbon species is derived from the anion, resulting in five chemically different species (shown in the fit analysis of the upper C 1s spectrum of Fig. 2.3b). Due to the limited energy resolution all carbon species of the imidazolium ring bonded to nitrogen atoms give rise to the feature observed at ~287 eV. As is illustrated in the lower spectrum of Fig. 2.3b, we therefore coalesce these three species (2–4) into one carbon signal (slightly broader, see experimental section for details), labelled C_{hetero}. The high-BE feature is assigned to the CF_3 groups of the anion (5) and is accordingly called C_{anion}. The signal at ~285 eV originating from the aliphatic carbons (1) of the alkyl chain is named C_{alkyl}.

With this procedure an unambiguous assignment of all IL-related signals is achieved and will be used as presented here throughout this thesis. The subsumption of all C_{hetero} into one peak does not only allow for a very intuitive interpretation of ARXPS results but also yields a highly reliable quantitative analysis, which is partly due to the fact that the amount of fit constraints are reduced to a minimum.

2.3   The UHV Apparatus

The aim of this chapter is to introduce the reader to the UHV apparatus used in this thesis. The general setup of the chamber is explained and new additions and alteration made to the chamber are briefly discussed.

ESCALAB 200: The ESCALAB 200 system is a standard UHV chamber composed of an analysis chamber, a preparation chamber and a sample transfer system through which samples can be introduced into the UHV system. To the preparation chamber are fitted a sputter gun for sample cleaning by Ar^+ ion bombardment, an IL evaporator system and a quartz-crystal microbalance (QCM) for IL flux control. Furthermore, low energy electron diffraction (LEED) optics and a gas dosing system are attached. The analysis chamber is equipped with a concentric hemispherical electron energy analyser (CHA) for measuring the kinetic energy of the photoelectrons and a non-monochromatised dual anode X-ray gun generating either Al-K_α (hν = 1486.6 eV) or Mg–K_α (hν = 1253.4 eV) radiation. Furthermore, a UV lamp and an electron gun are attached for UP and Auger spectroscopy, while a quadrupole mass spectrometer allows for detection of desorbing species during heating or photon-induced desorption from the sample surface. The setup of the chamber is depicted in Scheme 2.3.

The general setup of the chamber in its original (analysis and load lock chamber) and modified (preparation chamber upgrade) state has been thoroughly discussed elsewhere [24, 25]. In the course of this thesis a few major modifications were made. Firstly, the old ESCALAB 200 MK II CHA was replaced by a new VG SCIENTA R3000 analyser. In addition, the former X-ray gun was replaced by a SPECS XR50 featuring an additional water-cooled shroud to minimize heat transfer from the x-ray anode to the sample surface. For IL thin film preparation a detachable IL evaporator system was installed, allowing for IL exchange and separate
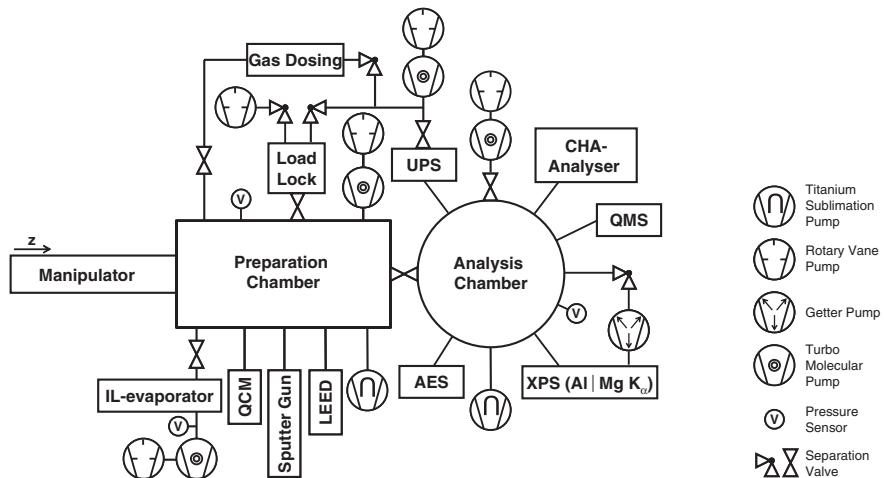
Scheme 2.3   Diagram of the ESCALAB 200 spectrometer in its current state

baking of the evaporator unit. Finally, a new sample holder system was designed and installed meeting the specific needs for both the current and future IL research planned in our group. While the new CHA was characterized elsewhere [26], both the evaporator unit and the sample holder system will be reviewed below.

IL Evaporator: Compared to standard thermal evaporator systems, an IL evaporator has to meet a number of specific criteria to provide the desired performance. The most important aspects are that (i) the evaporator can be installed in a way, that the IL will not drip out, (ii) creeping of the IL inside the evaporator is avoided, (iii) the evaporator unit can be cooled during bake-out, as the IL evaporation temperature is in the range of the bake-out temperatures (~160 °C), (iv) the evaporator unit can be attached and removed without venting the chamber. The above-mentioned criteria were satisfactorily met by choosing a setup as is displayed in Fig. 2.4.

For the evaporator unit a commercially available TECTRA WKC3 high temperature Knudsen cell was chosen, which has a cooling shroud and a tight-fitting shutter assembly. The shutter assembly was slightly modified by inserting an additional aperture to avoid excessive creeping of the IL within the evaporator. Detailed drawings and measurements of the evaporator unit as well as the modified parts can be found in the Appendix, Sect. A.1.1. Using a separate pumping unit and pressure sensor, a gate valve and a z-transfer on which the evaporator is mounted, the whole setup can be separated from the main chamber. This setup allows for separate baking of the evaporator (at moderate baking temperature ≤120 °C) and fast IL refill/exchange. Temperature control is achieved by a type-K thermocouple linked to a EUROTHERM 2261 PID controller. The evaporation rates are monitored using a QCM mounted on a rotatable feedthrough which can be pivoted directly into the IL beam.
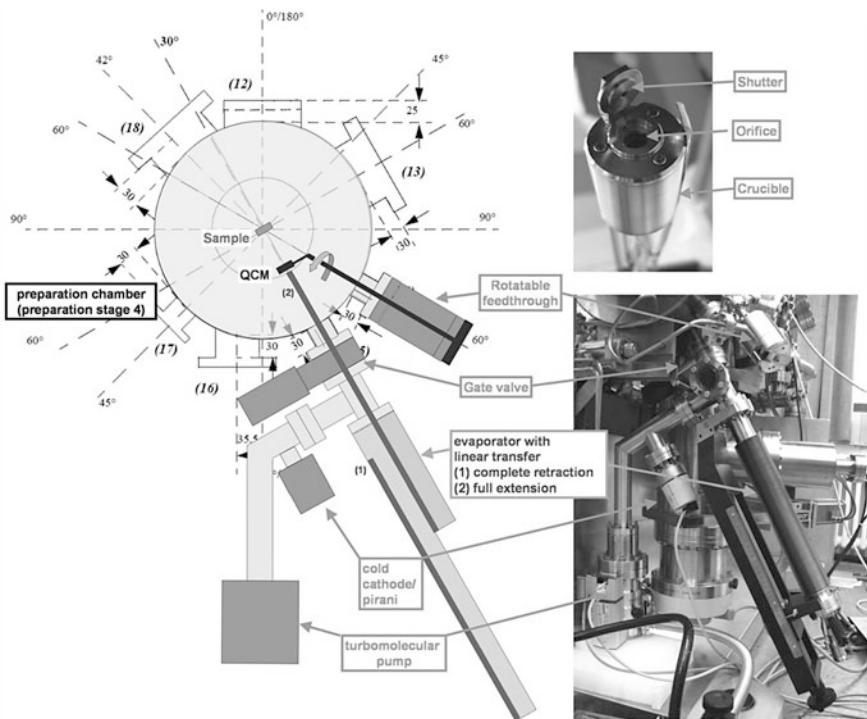
Fig. 2.4 Sketch and photo of the IL evaporator setup. With this setup the evaporator can be detached from the chamber, for refilling or change of IL. Furthermore, the IL can be introduced to the chamber after bake-out, which is a crucial point as the IL evaporation temperature lies in the range of the bake-out temperature

Sample Holder System: Certain improvements to the old sample holder system were necessary to successfully pursue future research goals. Regarding the old sample holder system, three main disadvantages occurred when using it for the IL research conducted in this work. Firstly, the absence of reliable temperature reading (thermo couple only mounted on the side of the manipulator head) directly on the sample was found to be a major drawback, as it is necessary to both accurately determine the IL temperature when heating or cooling the sample but also when annealing the single crystals used for the thin film experiments. A further disadvantage of the former system was that the sample was positioned rather loosely in the sample holder. Therefore, when tilting the sample to 80°, tipping of the sample sometime occurred leading to erroneous sample positions and reduced signal intensities. To summarize, the main requirements for a new sample holder system were found to be (i) reliable and fast sample transfer paired with a firm and reproducible sample position in the manipulator, (ii) stable and accurate temperature reading directly on the sample, (iii) the option to install a three electrode setup to be able to perform in situ electrochemistry in future projects, and (iv) the possibility to efficiently cool (good
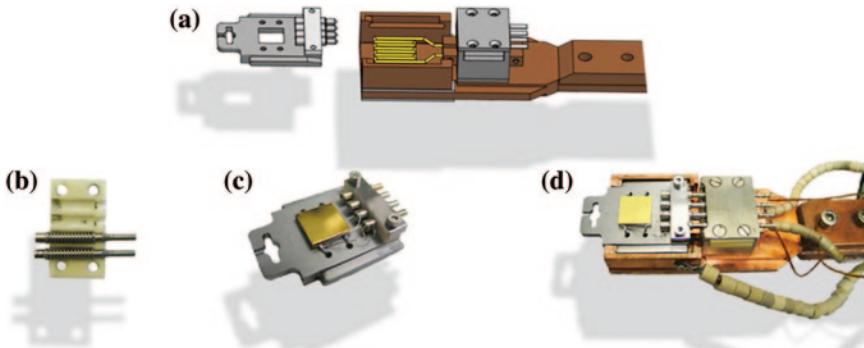
Fig. 2.5 Sketch (**a**) and pictures (**b**–**d**) of the sample holder system. The pins on the sample holder and the spring-loaded counter-notches (**b**) fitted to the manipulator head are made of type K thermocouple material. Once inserted into the manipulator, the springs push the sample holder back into its locked position (**c**), which guarantees both good electrical contact as well as firm and accurate mechanical interlock

thermal contact to LN_2 cooling of manipulator) and heat (both heating filament and electron bombardment for high-temperature annealing) the sample. After assessing the requirements a completely new design of sample holder, manipulator head and transfer system was developed. In the sample holder setup presented in Fig. 2.5 all of these requirements are met satisfactorily. By using the pin-shaped spring contact two major issues—firm mechanical interlock and both thermocouple and electric connection of the sample—could be solved at once. The sample transfer system offers an easy yet reliable and robust transfer mechanism. Compared to the former sample holder system cooling is much more efficient, resulting in sample temperatures as low as 90 K (using liquid nitrogen as cooling agent) as compared to 130 K achieved with the old sample holder. Also, electron beam heating works much more reliably with the new sample holder system, where in first tests with a Ni(111) single crystal temperatures of ~1200 K could be achieved easily. The detailed construction drawings are compiled in the Appendix section, Sect. A.1.2.

2.4 Experimental Aspects

Throughout this thesis a variety of different sample preparation methods as well as different analysis methods and UHV components were used. Therefore, specific experimental aspects are provided in the corresponding sections. In addition, a few fundamental experimental aspects will be discussed to give the reader a basic insight into the methods employed.

Ionic Liquids: In this work a variety of ILs were used, therefore an overview of all ILs studied is given in Table 2.1. [C_8C_1Im][Tf_2N], [C_8C_1Im][Pf_2N], [C_8C_1Im]Cl, [C_2C_1Im][Tf_2N], and [C_1C_1Im][Tf_2N] were synthesized under

ultra-clean conditions by Natalia Paape in the laboratories of Peter Wasserscheid. $[C_8C_1Im]I$ was provided by Alasdair Taylor from the Licence group at University of Nottingham, while $[C_8C_1Im][NO_3]$ was synthesized by Ralf Lungwitz from the Spange group at University of Chemnitz. The above-mentioned ILs were synthesized under the premise of utmost purity and characterized by a variety of spectroscopic methods, including NMR spectroscopy, Karl-Fischer titration, thermal gravimetric analysis (TGA), and density and viscosity measurements. The ILs $[C_8C_1Im][FAP]$, $[C_8C_1C_1Im][Tf_2N]$ and $[C_8C_1C_1Im]Br$ were kindly given by Merck, while $[C_8C_1Im]Br$ and $[C_8C_1Im][PF_6]$ were purchased therefrom. $[C_8C_1Im][BF_4]$ and $[C_8C_1Im][TfO]$ where purchased from Sigma-Aldrich, whereas $[C_4C_1Pyrr][Tf_2N]$ was purchased from IoLiTec. The Merck-ILs were synthesized in small batches, also enforcing ultra-clean standards [27]. The ILs from Sigma Aldrich had specified purities of >95 % for $[C_8C_1Im][BF_4]$ and >97 % for $[C_8C_1Im][TfO]$, while the IoLiTec IL was specified as >99 % pure. All ILs were used as obtained.

Sample Preparation: In the following a brief introduction to the standard sample preparation procedures is given. Detailed aspects or specific preparation steps for particular experiments are provided within the corresponding chapters.

Ionic liquid films: Macroscopically thick IL films (thickness ~0.1 mm) were prepared by depositing the corresponding IL onto a planar gold foil, which had previously been treated with acetone and isopropanol in an ultrasonic bath, and had been stored in an oven at 70 °C for drying [28]. In the load lock chamber of the XPS apparatus the IL samples were carefully degassed at a pressure of ~1×10^{-6} mbar to remove residual water and other possible volatile impurities [5].

Single crystal surfaces: The Au(111) and Ni(111) single crystals were both purchased from MATECK GmbH, with specified purities of 99.999 and 99.99 %, respectively. Both crystals were polished on one side and aligned to the (111) plane to better than 0.1°. They were both of square shape with dimensions of $11 \times 11 \times 2$ mm^3, with spark-eroded holes along two sides allowing for sample mounting with Ta wires as is shown in Fig. 2.5 and Ref. [26]. For the Au(111) single crystal sample preparation was performed by sputtering the sample with 600 V Ar$^+$ ions followed by annealing to 800–900 K for 5 min. The Ni(111) was sputtered with 1 kV Ar$^+$ ions and heated to 1100–1200 K for about 1 min. To avoid surface segregation of sulphur during the cooling process, the Ni(111) sample was additionally cooled with LN$_2$. Surface cleanliness was checked with XPS, while long range order of the surface was monitored with LEED, where for Au(111) the typical $(23 \times \sqrt{3})$ "herringbone" superstructure was observed. For clean Ni(111) very sharp (1×1) reflexes without superstructure were observed.

Suprasil glass samples: Suprasil 300 fused silica samples were kindly provided by M. Scharrer from the MPI Erlangen. They were obtained from HERAEUS as 1 mm thick disks of d = 25 mm and fitted to the sample holder by cutting down to dimensions of 15×12 mm^2. This was followed by thorough cleaning with acetone and isopropanol in an ultrasonic bath and storing in an oven at 70 °C until further use. All subsequent surface modifications carried out are specifically

discussed in Chap. 5. For mounting the samples on a sample holder, tantalum strips were used as is shown in Ref. [26].

Thin film preparation: IL thin film deposition was achieved by thermal evaporation of the respective IL using the evaporator setup discussed above. After degassing the empty evaporator crucible at 1200 K, the IL was introduced into a pyrolytic boron nitride (PBN) crucible and fitted to the evaporator. The evaporator unit was slowly pumped down with open shutter followed by moderate baking (T $\leq$ 120 °C) while simultaneously "cooling" the crucible with 60 °C hot water. After bake-out the evaporator was held at 380 K for at least 4 h to degas the IL, again with the shutter opened. During IL deposition the temperature was set between 420 and 440 K, depending on IL and desired evaporation rate (see Sect. 4.2 for details). Deposition rates were estimated using the attenuation (damping) of the Au 4f XPS signal of the Au(111) single crystal. Consistency of the deposition rate was regularly monitored with QCM measurements.

XPS measurements and data evaluation: General aspects relevant for all studies of this thesis are discussed in the following, while procedures only relevant to individual chapters are discussed therein.

XPS measurements: XP spectra were taken with a VG Escalab 200 spectrometer using non-monochromatised Al-K$_\alpha$ radiation (hν = 1486.6 eV). For the core-level spectra pass energies were set to low enough values (depending on which analyser was used, as will be specified in the respective chapters), so that the resulting overall resolution of ~0.9 eV was given mainly by the natural line width of the non-monochromatised Al-K$_\alpha$ radiation. At the kinetic energies used (800–1400 eV) the inelastic mean free path (IMFP) of photoelectrons in organic compounds is in the range 2–3 nm [8]. Therefore, measurements at 0° average over several ion layers of the near-surface region (information depth, ID: 5–9 nm, depending on the kinetic energy), while for 80° emission the surface sensitivity is enhanced by a factor of six resulting in an information depth of around 1–1.5 nm, with the majority of the signal originating from within the first molecular layer.

Data evaluation: For the two different CHA analysers slightly different data analysis procedures were used. For the old analyser, the spectra were directly imported into Origin 7.5 and fitted using Gaussian functions after linear background subtraction. For the new R3000 analyser, the raw data were analysed with the Casa XPS software, where for peak fitting a combination of Gaussian and Lorentzian lineshape at a ratio of 70:30 was used, leading to slightly better fits without affecting the quantitative analysis; indeed, within the margins of error, both methods provided identical results for quantitative analysis done in this thesis. For $[C_8C_1Im]^+$ ILs the C 1s spectra were fitted with the constraint of full width half-maximum, fwhm(C_{hetero}) = 1.11 × fwhm(C_{alkyl}), in accordance with previously published results [10]. In some case, as will be specified were it applies, it was necessary to account for slight charging phenomena ($\pm$ 0.15 eV), which have been observed and discussed previously [29]. Therefore, the spectra were shifted in a way that BE(C_{alkyl}) = 285.0 eV. Please see Sect. 3.1 for a detailed discussion. For film thickness calculations a constant value of 3 nm for

the IMFP of the recorded photoelectrons was assumed for systems where the kinetic energy of the photoelectron is ~1200 eV (Au 4f and Si 2p), according to Ref. [8]. For kinetic energies well below 1000 eV (such as the Ni2p signal, E_{kin} ~640 eV), however, the IMFP value of 3 nm was adjusted by dividing by a factor of 1.83 (as estimated from IMFP calculations for organic materials for 1200 and 650 eV, see Ref. [7]), which provided reliable results.

References

 1. A. Einstein, Ann. Phys. **322**, 132 (1905)
 2. S. Hüfner, *Photoelectron Spectroscopy* (Springer-Verlag, Berlin Heidelberg New York, 1995)
 3. M. Henzler, W. Göpel, *Oberflächenphysik des Festkörpers* (Teubner, Stuttgart, 1994)
 4. G. Ertl, J. Küppers, *Low Energy Electrons and Surface Chemistry* (VCH, Weinheim, 1985)
 5. C. Kolbeck, M. Killian, F. Maier, N. Paape, P. Wasserscheid, H.-P. Steinrück, Langmuir **24**, 9500 (2008)
 6. D. Briggs, M.P. Seah, *Practical Surface Analysis* (Springer-Verlag, Berlin, 1990)
 7. S. Tanuma, C.J. Powell, D.R. Penn, Surf. Interf. Anal. **21**, 165 (1994)
 8. R.F. Roberts, D.L. Allara, C.A. Pryde, D.N.E. Buchanan, N.D. Hobbins, Surf. Interf. Anal. **2**, 5 (1980)
 9. D.C. Jackson, T.E. Gallon, A. Chambers, Surf. Sci. **36**, 381 (1973)
10. K.R.J. Lovelock, C. Kolbeck, T. Cremer, N. Paape, P.S. Schulz, P. Wasserscheid, F. Maier, H.-P. Steinrück, J. Phys. Chem. B **113**, 2854 (2009)
11. S. Boghosian, R. Fehrmann, N.J. Bjerrum, G.N. Papatheodorou, J. Catal. **119**, 121 (1989)
12. P. Walden, Bull. Acad. Impér. Sci. St. Pétersbourg **8**, 405 (1914)
13. J.S. Wilkes, J.A. Levisky, R.A. Wilson, C.L. Hussey, Inorg. Chem. **21**, 1263 (1982)
14. J. Wilkes, Chem. Commun. **13**, 965 (1992)
15. A.E. Visser, R.P. Swatloski, W.M. Reichert, R. Mayton, S. Sheff, A. Wierzbicki, J.H. Davis, R.D. Rogers, Chem. Commun. **37**, 135 (2001)
16. P. Wasserscheid, W. Keim, Angew. Chem. Int. Ed. **39**, 3772 (2000)
17. S. Zahn, F. Uhlig, J. Thar, C. Spickermann, B. Kirchner, Angew. Chem. Int. Ed. **47**, 3639 (2008)
18. N.V. Plechkova, K.R. Seddon, Chem. Soc. Rev. **37**, 123 (2008)
19. J.N.C. Lopes, A.A.H. Padua, J. Phys. Chem. B **110**, 3330 (2006)
20. T.L. Amyes, S.T. Diver, J.P. Richard, F.M. Rivas, K. Toth, J. Am. Chem. Soc. **126**, 4366 (2004)
21. P. Nockemann, B. Thijs, S. Pittois, J. Thoen, C. Glorieux, K. Van Hecke, L. Van Meervelt, B. Kirchner, K. Binnemans, J. Phys. Chem. B **110**, 20978 (2006)
22. P. Wasserscheid, T. Welton, *Ionic liquids in synthesis*, 2nd edn. (Wiley-VCH, Weinheim, 2008)
23. O. Höfft, S. Bahr, M. Himmerlich, S. Krischok, J.A. Schäfer, V. Kempter, Langmuir **22**, 7120 (2006)
24. M. Probst, PhD Thesis, Friedrich-Alexander-University Erlangen-Nuremberg, 2003
25. F. Grellner, PhD Thesis, Friedrich-Alexander-University Erlangen-Nuremberg, 1993
26. M. Stark, Master Thesis, Friedrich-Alexander-University Erlangen-Nuremberg, 2010
27. Personal Communication, M. Watermann, Merck KGaA, Darmstadt, 2009
28. T. Cremer, Diploma Thesis, Friedrich-Alexander University Erlangen-Nuremberg, 2008
29. E.F. Smith, F.J.M. Rutten, I.J. Villar-Garcia, D. Briggs, P. Licence, Langmuir **22**, 9386 (2006)

Chapter 3
Pure Ionic Liquid Systems

In this chapter macroscopically thick IL films were investigated with regards to their bulk electronic structure and their surface composition. The (AR) XP spectra of ten $[C_8C_1Im]^+$-based ILs were analysed while the anion was systematically varied. In Sect. 3.1 the bulk electronic structure and ion–ion interactions are examined, whereas Sect. 3.2 deals with the surface structure of these systems.

3.1 Electronic Structure and Interionic Interactions in $[C_8C_1Im]^+$-Based Ionic Liquids

The results presented in this chapter where performed in a joint collaboration with the groups of B. Kirchner (Leipzig) and P. Wasserscheid (Erlangen) within the DFG priority program SPP 1191 "Ionic Liquids" and were published in the following article [1]:

Towards a Molecular Understanding of Cation–Anion Interactions—Probing the Electronic Structure of Imidazolium Ionic Liquids by NMR Spectroscopy, X-ray Photoelectron Spectroscopy and Theoretical Calculations [1].

As mentioned in the introductory chapters, ILs have been labelled "designer solvents" for the exciting prospect of tailoring their physical properties by using the appropriate cations and anions as building blocks, thereby combining their individual properties to obtain the desired IL. It has indeed been shown that trends for groups of compounds exist, which—to a certain extent—makes it feasible to predict the physical and chemical properties for a chosen combination of cation and anion [2, 3]. However, the simple picture of superimposing properties of the individual ions does not hold true. Anion and cation will always interact in a specific way leading to a unique combination with specific properties. In order to evaluate the predictive power and the uncertainties of this "superposition" approach, one has to understand the nature of different interactions between cation and anion the respective IL. In this chapter the interactions between the IL ions were investigated

to gain a thorough understanding of ILs and their interionic structure formation and interaction mechanisms. Therefore, ten $[C_8C_1Im]^+$-based ILs with anions Cl^-, Br^-, I^-, $[NO_3]^-$, $[BF_4]^-$, $[TfO]^-$, $[PF_6]^-$, $[Tf_2N]^-$, $[Pf_2N]^-$, and $[FAP]^-$ and two $[C_8C_1C_1Im]^+$-based ILs with anions Br^- and $[Tf_2N]^-$ were characterized using a combination of XP and NMR spectroscopies, and theoretical calculations. While ^{1}H-NMR spectroscopy was found to specifically probe the hydrogen bond interactions between cation and anion, the XPS measurements provided first direct experimental evidence for cation/anion charge transfer phenomena in ionic liquids as a function of the ionic liquid's anion. These charge transfer effects have been found to be surprisingly similar for $[C_8C_1Im]^+$ and $[C_8C_1C_1Im]^+$ salts of the same anion, which in combination with the theoretical calculations leads to the conclusion that hydrogen bonding (H-bonding) and charge transfer occur independently from each other. They are both more pronounced for small and more strongly coordinating anions and greatly reduced in the case of large and weakly coordinating anions.

3.1.1 General Considerations

Apart from coulomb forces, dispersive and inductive interactions as well as H-bonding type interactions play a considerable role in ILs [4, 5]. In particular for the intensively studied class of imidazolium-based ILs, many groups have tried to qualitatively (and in some cases also quantitatively) correlate interactions between the ions with the physico-chemical properties of the IL [6–13]. Due to the IL's ionic nature, coulombic interactions are expected to play a pronounced role. Commonly, the excess charges of the ions are considered to be integer values, i.e., $+1e$ for the imidazolium cation; within the last years a number of molecular dynamic (MD) simulations have been successfully carried out applying IL force fields with the constraint of integer-charged imidazolium cations and anions [14–16]. However, it was also shown that modified force fields with reduced (i.e., non-integer or fractional) charges on the ions can considerably improve the MD results [17, 18]; for details see the excellent review by Maginn [19]. When introducing such "effective charges" in computational chemistry, one might ask whether the value of this effective charge of a certain ion is a "real" quantity implying some charge transfer between anion and cation or whether it should be considered as a MD simulation parameter taking many-body effects (e.g., polarization) into account [7, 18, 20, 21]. An indication of "real" fractional charges is provided by density functional theory (DFT) calculations. By applying a natural bond orbital (NBO) analysis of isolated ion pairs in their calculations, Hunt and co-workers observed a pronounced partial charge transfer between $[C_4C_1Im]^+$ and its counter-ion Cl^- [7]. Similar charge transfer effects were already observed in DFT calculations of Na^+/Cl^- ion pairs [22]. A first step towards experimental evidence for non-integer charges was made by Tokuda et al., who introduced the parameter "effective ionic concentration", C_{eff}, in their combined electrochemical impedance and NMR measurements. C_{eff} was proposed to be dominantly related to the

coulombic forces in the IL and to depend particularly on the nature of the anion and the chain length [23]. However, it not only includes contributions from effective ionic charges but also takes ion aggregation (or dissociativity) into account, as discussed in the concept of ionicity [24]. To the best of our knowledge a direct experimental proof of "reduced" or "effective" ionic charges in the case of ILs has not yet been reported.

A major point in the context of intermolecular forces in imidazolium-based ILs is the elucidation of H-bonding effects [25]. These mainly occur at the proton bound in C^2 and also—to a smaller extent—at the protons in C^4 and C^5 position in the imidazolium ring (see Scheme 3.1). H-bonding has been proposed to be of crucial importance for the melting point as well as the viscosity of ILs [11, 13, 26, 27]. While early experiments from Elaiwi et al. [26] and Avent et al. [27] indicate that less H-bonding leads to a reduction in melting point and viscosity, more recent IR results and DFT calculations from the Ludwig group point towards a reverse trend [11, 13]. In recent years, a large number of studies concerning H-bonding in ILs have been carried out, mostly by NMR spectroscopy [8–10, 28, 29]. Lungwitz et al. correlated the Kamlet-Taft parameters α and β, which are well-known indicators for the H-bonding abilities of compounds, to ^{1}H-NMR shifts of the proton bound to C^2. Their studies indicated that anion-dependent differential ^{1}H-NMR shifts are a direct measure of the strength of H-bonding in imidazolium-based ILs [8, 9]. Most NMR-studies mentioned above were carried out for ILs diluted in organic solvents, which can have a considerable influence on the NMR-shifts [27]. However, ILs of sufficiently low viscosity can also be studied in undiluted pure form by NMR spectroscopy, thus ruling out additional solvent interactions that may complicate the interpretation of the obtained spectra [30].

Finally, apart from coulombic and H-bonding interactions, dispersion and induction forces also significantly contribute to the specific interactions between anion and cation [4]. From ab initio calculations, considerable differences between ILs and classical molten salts were found due to different dispersive and inductive contributions, which is claimed to be one reason for the reduced melting points and viscosities of ILs [4].
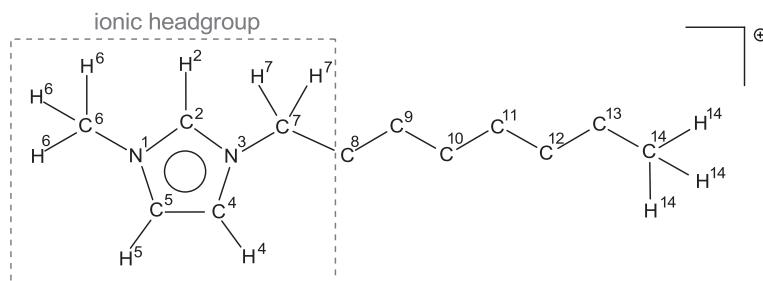
Scheme 3.1 Labelled structure of the $[C_8C_1Im]^+$ cation. The labelling method is the same as used by Hunt et al. [21]. Carbon atoms attached to the ring of the ionic head group (C^2, C^4–C^7) are referred to in the text as "C_{hetero}" and C^8–C^{14} as "C_{alkyl}". Additionally, hydrogen atoms relevant for this work are added for sake of clarity

Interactions between IL ions are closely related to their electronic structure. A powerful experimental method in this respect is photoelectron spectroscopy (PES), which provides direct access to the electronic structure of a compound. Traditionally applied to solid surfaces, PES of ILs has only emerged during the last few years. Due to the very low vapour pressure of aprotic ILs (usually $<10^{-10}$ mbar at RT), PES is highly suitable for probing their electronic structure UHV conditions [31–33]. By means of ultra-violet photoelectron spectroscopy (UPS) [34–36] and inverse photoelectron spectroscopy (IPES) [36] occupied and unoccupied valence states are directly accessible. In combination with theory, the density of valence states ascribed to the cation and the anion have been successfully investigated [34–36]. Moreover, using XPS, core levels can be studied [34, 35, 37–47]. In terms of electronic structure, XPS can be used to identify and quantify the different chemical environments of one specific element by analysing the so-called chemical shifts [48]. The BE of a certain core level is a function of the chemical environment of the atom, i.e., the oxidation state and the nature of the neighbouring atoms. In a simplified picture, the same core level of a given atom exhibits a higher BE if it is positively charged compared to a more negatively charged one. However, up to now, most XPS studies of pure ILs have concentrated on the surface composition and molecular orientation of the ions [38, 40, 42, 44, 49–51], while few have addressed the electronic structure in terms of ion–ion interactions [52].

To gain a more detailed understanding of the specific interactions within imidazolium-based ILs, a systematic XPS and NMR study in combination with theoretical calculations is presented here. Pure ILs carrying the same cation, 1-methyl-3-octyl-imidazolium ($[C_8C_1Im]^+$), but ten different anions have been investigated (an overview of all ILs investigated in this study is given in Table 2.1). The $[C_8C_1Im]^+$ cation was chosen because it is a well-investigated system, and also because its XP spectrum shows features important for referencing of spectra. As mentioned in the introduction, the $[C_8C_1Im]^+$ cation consists of a positively charged head group, i.e., the imidazolium ring, and a neutral aliphatic tail. This pronounced asymmetry of the cation is one reason for the low melting point of all ILs investigated here [53]. The anions were selected due to the fact that they form room temperature ILs with the $[C_8C_1Im]^+$ cation, cover different sizes (ranging from Cl^- to $[FAP]^-$), basicities, shapes (from spherical to elongated anions) and coordination abilities (from strongly coordinating halides to weakly coordinating anions with perfluoroalkyl groups), and are free of aliphatic chains to avoid pronounced dispersive interactions with the chains of the cation. Moreover, the selected anions do not contain atoms that interfere with XPS and NMR signals from the cation and thus could hamper an unambiguous interpretation of the spectra. In addition, two ILs with the cation $[C_8C_1C_1Im]^+$ (methylated at the C^2-position) were compared to their non-methylated homologues.

Altogether, it is shown in this study that (i) the nature of the anion has a strong influence on the positive charge of the imidazolium ring, (ii) the absolute value of the positive charge on the imidazolium ring is hardly influenced by hydrogen bonding interactions between anion and cation, and, (iii) the nature of the anion presumably modifies the degree of hybridisation in the imidazolium ring in case of the $[C_8C_1Im]^+$ ILs.

3.1.2 Experimental Aspects

XPS measurements: IL films (thickness ~0.2 mm) were prepared as described in Sect. 2.4. XP spectra were taken with a VG Escalab 200 MK II CHA using non-monochromatised Al-K$_\alpha$ radiation (hν = 1486.6 eV). All core level spectra were recorded at a pass energy of 20 eV, resulting in an overall resolution of ~0.9 eV, and at normal emission (0° with respect to the surface normal). Due to the inelastic mean free path of about 3 nm of photoelectrons in organic compounds at the kinetic energies used (~1080 eV for N 1s and ~1200 eV for C 1s), measurements at 0° average over several ion layers of the near-surface region (information depth, ID: ~9 nm). Hence, the measured BEs represent the electronic states of the corresponding ions in the bulk of the IL. The spectra were fitted using Gaussian functions after linear background subtraction and fit constraints as discussed in the experimental section in Chap. 2. To allow for comparison of relative BE positions of different ILs, all spectra were shifted so that the peak position of C$_{alkyl}$ was at 285.0 eV (for a detailed discussion, please see the results section). This procedure was necessary to account for slight charging phenomena ($\pm$0.15 eV), which have been observed and discussed previously [38]. The unshifted C 1s spectra are shown in Fig. 3.3a.

NMR measurements: ^{1}H- and ^{13}C-NMR measurements were performed by the Wasserscheid group using a Jeol ECX 400 MHz spectrometer. The ILs were carefully degassed at 10^{-3} mbar and then introduced into a standard NMR tube with a d^6-DMSO-inset as external standard and reference. All spectra were recorded without additional solvent making this set of data a valuable NMR reference for a large set of pure [C$_8$C$_1$Im]$^+$-based ILs. Chemical shifts were referenced to DMSO with 2.50 and 39.51 ppm for ^{1}H- and ^{13}C-spectra, respectively [54]. For the measurement of the methylated IL [C$_8$C$_1$C$_1$Im]Br, which is solid at room temperature, a liquid 5:1 mixture of [C$_8$C$_1$Im]Br and [C$_8$C$_1$C$_1$Im]Br was measured.

Computational methods: All calculations were performed by the Kirchner group. The models used are isolated ion pairs in the gas-phase. For all compounds, methods and basis sets applied the structures were always optimized. In most cases, more than one geometrical configuration of the anion relative to the cation was considered. All calculations from the Kirchner group were performed with the Turbomole 5.10 program package [55] using density functional theory in combination with the dispersion corrected BLYP [56, 57] -D [58] functional. This choice of functional and dispersion correction has been shown to perform well for ionic liquid ion pairs [59, 60]. The TZVPP basis set was employed as implemented in the Turbomole 5.10 program package; all calculations were combined with the resolution of identity technique calculations [55]. To obtain atomic charges, a natural population analysis (NPA) was carried out with the aid of the Turbomole 5.10 implementation [61]. In order to avoid ambiguities in charge assignment to individual atoms, a sum of charges over characteristic groups of the molecules (e.g., CH$_2$ and CH$_3$ groups) is given. Orbitals were calculated with the Turbomole 5.10 program package. The isosurface value for all orbitals was set to 0.02.

The GAUSSIAN03 program was employed for the NBO analysis under application of the TZVP basis set [62, 63]. The NBO analysis was carried out using the BLYP functional without the resolution of identity approximation.

Mass density measurements: After extensive degassing for at least 4 h at a reduced pressure of 10^{-2} mbar at 40 °C, the mass densities of all samples were measured at room temperature (20 °C) by weighing a defined volume of the IL (at least, 0.100 mL) on a chemical balance (for $[C_8C_1Im][BF_4]$, $[C_8C_1Im][TfO]$, $[C_8C_1Im][Tf_2N]$, $[C_8C_1Im][Pf_2N]$, $[C_8C_1Im][FAP]$). With this method, a relative error in mass density $d\rho/\rho$ values below 1.5 % was achieved. For the relatively viscous ILs ($[C_8C_1Im]Cl$, $[C_8C_1Im]Br$ and $[C_8C_1Im]I$) and also for $[C_8C_1Im][PF_6]$, density measurements were performed at a 0.02 % accuracy level using the vibrating tube method [64].

Sample purity and radiation damage: Using XPS, elemental identification is possible, meaning that XPS can be used to detect the presence of surface contaminants, such as silicone or hydrocarbon impurities, that cannot be detected with other techniques such as NMR [38–42, 64, 65]. All ILs used in this study were found to be free of such surface active contaminants. Also, no signs of halide contamination or other bulk impurities were observed using ARXPS for all ILs studied herein. Thus, in situ cleaning methods such as argon sputtering were not necessary [40, 41].

It should be noted that extended exposure to X-rays during XPS can lead to spectral changes. Damage affecting the N 1s region of $[C_8C_1Im][BF_4]$ under X-ray irradiation has previously been observed [65]. Similar damage over time under X-ray irradiation was observed for all ILs investigated herein, most commonly in the N 1s region at BE lower than that of the imidazolium nitrogen, suggesting the presence of a non-charged decomposition product (see Fig. 3.1) [65]. The most significant damage occurred for $[C_8C_1Im][BF_4]$ and $[C_8C_1Im][FAP]$, both of which contain significant amounts of fluorine; samples could be studied for a minimum of 4 h with our standard non-monochromatised X-ray source (power

Fig. 3.1 XP spectra of N 1s for $[C_8C_1Im][BF_4]$ recorded under 0° emission, for different irradiation times. The X-ray power was 150 W ($I = 10$ mA, $U = 15$ kV)
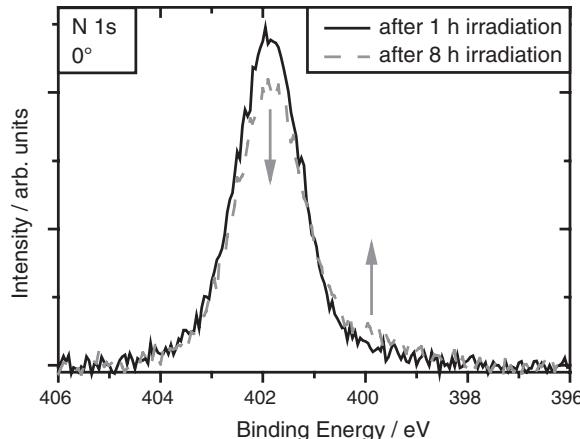
150 W) before significant and observable (5 % of the total N 1s intensity) damage occurred. Spectra reported here were collected at much lower X-ray exposure times than 4 h. No significant damage was observed over 12 h irradiation time for $[C_8C_1Im][PF_6]$ in XPS, suggesting no obvious trend for sample decomposition.

3.1.3 Results and Discussion

#### 3.1.3.1 XPS Measurements and Computational Results

Given that this study focuses on the influence of the anion on the electronic structure of the imidazolium ring of the cation, only the C 1s and N 1s spectra (i.e. the regions, where a direct comparison between different ILs can be made) are discussed. The XPS intensities of all ILs agree within the margins of error with the nominal IL compositions confirming the high purity of the samples. Values for the elemental composition and BE values for all relevant core levels of all ILs are provided in the Appendix in Tables A2 and A3, respectively.

As mentioned in Sect. 3.1.2, direct comparison of absolute BE values is not possible due to minor charging effects in the range of ± 0.15 eV, which have been observed for all ILs (see Fig. 3.3a and Table A3). Slight charging of IL films during XPS was first observed and discussed by Smith et al. [38]. Consequently, it is difficult to determine absolute BE values in particular as no reference level (such as a Fermi edge) is available. To account for the resulting slight variations in BE and to allow for a comparison of different ILs, one can choose a specific carbon atom as internal reference. Smith et al. arbitrarily chose the BE position of the C^2 carbon as internal reference. However, this approach proved to be impracticable for the present study, because the imidazolium ring interacts electronically with the anion (as will be shown in the following). Therefore, we used the aliphatic carbon signal C_{alkyl} of the octyl chain, which is present in all ILs studied herein, as internal reference. After fitting the C 1s spectra, the C_{alkyl} BE position was set to (the arbitrarily chosen position of) 285.0 eV, the value commonly used in XPS for adventitious hydrocarbon [66]. It should be mentioned at this point that the absolute calibration of the energy scale does not have an impact on the conclusions drawn from this data.

The use of C_{alkyl} as a reliable internal BE reference is justified by the following reasons: (i) the aliphatic chain is expected to be least susceptible to chemical shifts induced by electronic interaction with the anion due to the lack of coulombic interactions of the anion with the neutral alkyl chain. It has even been shown that polar and non-polar regions are formed in long-chained ILs, with the alkyl chains being on average separated from the ionic moieties [67, 68]; (ii) the ionic moieties (the charged imidazolium ring and the anion) most likely exhibit the strongest interactions as suggested by other groups [7, 10, 69]; (iii) in an extended study of a series of $[C_nC_1Im][Tf_2N]$ ILs with varying alkyl chain lengths it was found that the XPS peak separation Δ(BE) of the two different sets of cationic carbon atoms,

C_{hetero} and C_{alkyl}, remains unchanged for chains longer than C_8. This means that from C_8 onwards the BE of C_{alkyl} is independent of the electronic structure and environment of the charged imidazolium ring, as is illustrated in Fig. 3.2a [41].

This is further corroborated by calculations of a series of $[C_nC_1Im]Cl$ (n = 1–8) showing the rapid decay of the positive charge with increasing chain length saturating around n = 8: In Fig. 3.2b the average NPA charge, as deduced by natural population analysis, per CH_x group (x = 2, 3) of the alkyl chain and the NPA charge on the terminal CH_3 group of the alkyl chain are plotted as a function of chain length. (iv) For the octyl chain, as shown in Fig. 3.2c for the three calculated $[C_8C_1Im]X$ ion pairs, the NPA charges on the (CH_2) units exhibit a fast drop to zero as a function of distance from the imidazolium ring, irrespective of the counter anion. The exponential decay length is in the order of one C–C bond length, proving that the positive charge on the imidazolium ring does not significantly impact on longer alkyl chains. (v) Finally, for practical reasons, the position of the dominant C_{alkyl} peak in the C 1s region can be determined with a high accuracy of better than 0.02 eV in our XPS measurements.
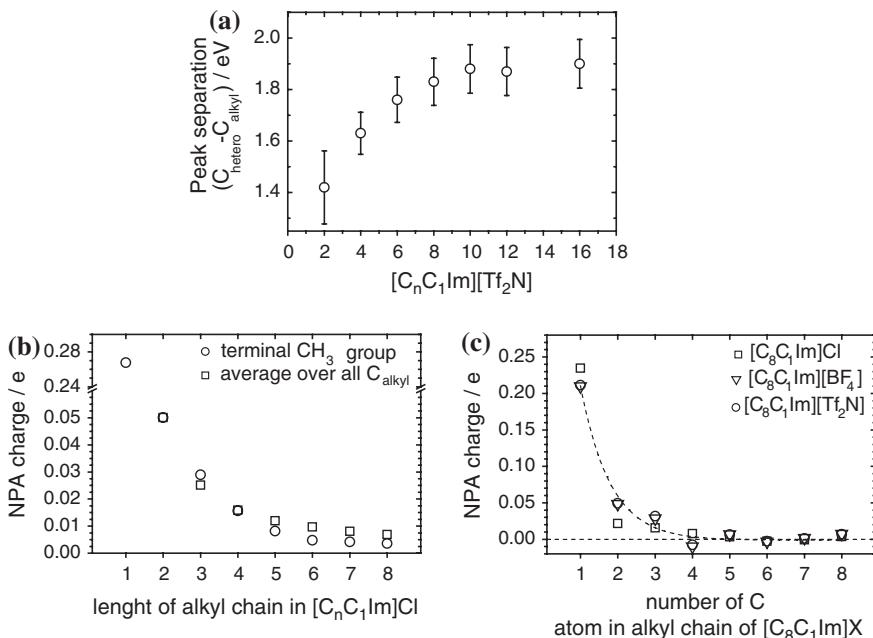

Fig. 3.2 **a** BE peak separation between C_{hetero} and C_{alkyl} for $[C_nC_1Im][Tf_2N]$ as a function of chain length. It can be clearly seen that for $n \geq 8$ saturation of $\Delta(BE)$ takes place indicating that the electronic structure of the alkyl chain is not further influenced by the charged fraction of the cation; **b** NPA charge of terminal CH_3 group (*squares*) and averaged NPA charge per CH_x unit of the alkyl chain (*circles*) of $[C_nC_1Im]Cl$ (where n = 1–8) as a function of chain length; **c** NPA charges on the (CH_2) moieties and on the terminal CH_3 group of the octyl chain as a function of position and anion ($[C_8C_1Im]Cl$ *squares*; $[C_8C_1Im][BF_4]$ *triangles*, $[C_8C_1Im][Tf_2N]$ *circles*). The *dashed line* is an exponential fit to the mean values

$[C_8C_1Im]^+$-based ILs

The unshifted and BE-referenced C 1s spectra of all $[C_8C_1Im]^+$-based ILs are displayed in Fig. 3.3a and b, respectively. Common to all ILs is the dominant C_{alkyl} peak at 285.0 eV, which arises from the seven carbon atoms of the alkyl chain (see fit analysis in Table A3 in the Appendix section). The second feature in the C 1s region is the peak/shoulder at 1.44–2.04 eV higher BE than the C_{alkyl} peak. As mentioned in the introduction, this signal corresponds to the five carbon atoms bound to the nitrogen atoms of the imidazolium ring. Further carbon signals at higher BE are observed for $[C_8C_1Im][Tf_2N]$ (peak at 293.0 eV), $[C_8C_1Im][Pf_2N]$ (peaks at 293.6 and 291.0 eV) and $[C_8C_1Im][FAP]$ (peaks at 293.3 and 291.0 eV). They correspond to the perfluorated carbon atoms of the anions with specific local electronic environments (see also Table A3 in the Appendix).

Figure 3.4a shows a close-up of the cation-related C 1s signals focusing on the region including only C_{alkyl} and C_{hetero}. Inspection of this figure and of the fit results in Table A3 reveals that the C_{hetero} peak is subject to a differential shift with respect to the C_{alkyl} peak, depending on the nature of the anion. The shift follows a clear trend, from small peak separation $BE(C_{hetero})–BE(C_{alkyl})$ of 1.44 eV for the smallest, most basic and most coordinating anion (Cl^-) to a considerably larger value of 2.04 eV for the much larger, least basic and least coordinating $[FAP]^-$ anion. The corresponding N 1s spectra are displayed in Fig. 3.4b. For all ILs a symmetric peak is observed around 402 eV, which corresponds to the two nitrogen atoms of the imidazolium ring; these nitrogen atoms are indistinguishable with XPS [38, 39, 41, 42, 44]. Two of the ILs, $[C_8C_1Im][Tf_2N]$ and $[C_8C_1Im][Pf_2N]$, contain nitrogen in the anion and, therefore, show an extra N 1s peak at 399.6 eV. The exact BE of the peak at ~402 eV depends on the nature of the anion and follows the trend observed for C_{hetero} in the C 1s region (see Fig. 3.4a). In particular, the differential BE shifts of the imidazolium ring signals observed for the series of ILs are more or less identical for both the C 1s and N 1s region. This is evident from Fig. 3.4c,

Fig. 3.3 C 1s core level spectra of the ten $[C_8C_1Im]^+$ ILs investigated. **a** shows the unshifted spectra, while in **b** the BE scale is referenced to $BE(C_{alkyl}) = 285.0$ eV
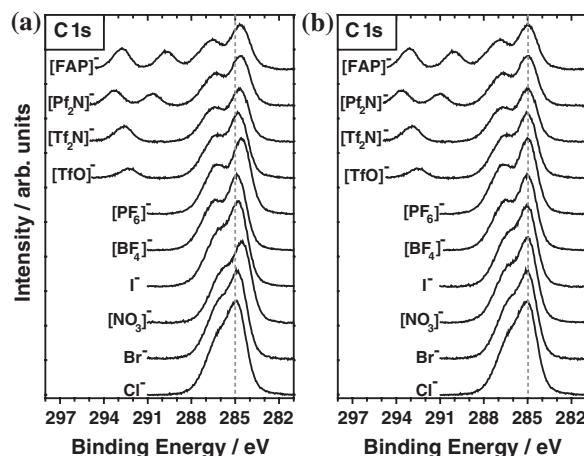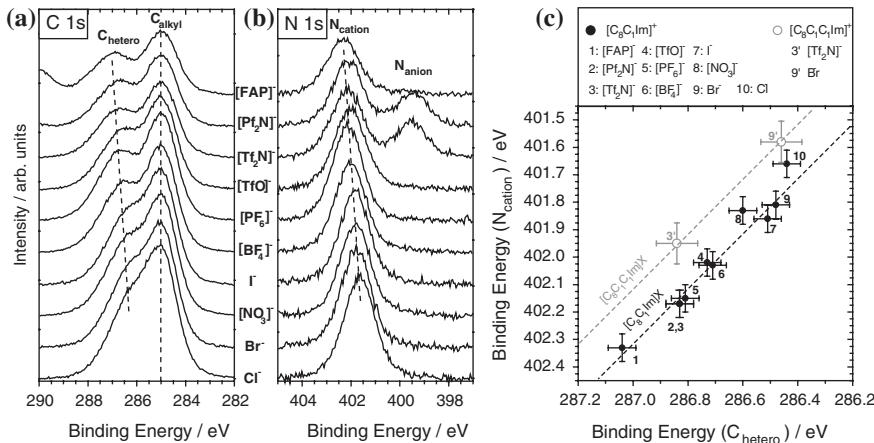
Fig. 3.4 **a** and **b** Detailed XP spectra of the C 1s (**a**) and N 1s (**b**) region for all $[C_8C_1Im]^+$ ILs (the *dashed lines* are visual guides for the BE changes of the imidazolium ring signals). **c** Correlation of BE positions for C_{hetero} and N_{cation} for the ten $[C_8C_1Im]^+$ ILs (*filled*) and the two $[C_8C_1C_1Im]^+$ ILs (*hollow*). *Dashed lines* with slope 1 are indicated for both groups

where a linear relation between the C_{hetero} 1s and N 1s BE shifts with slope 1 is observed. This observation provides strong evidence that the shifts discussed above are genuine physical observables and not artefacts of the fitting procedure.

The observed differential shifts indicate that the nature of the anion must have an effect on the electronic structure of the imidazolium ring. In particular, for the smallest and most coordinating anions, the ring signals have the lowest BE and, vice versa, the highest BE values are measured for the largest and least coordinating anions. In Fig. 3.5a and b the position of the C 1s and N 1s signals of the imidazolium ring are plotted against the IL molecular volume (for exact values of mass density and molecular volume, please see Table 3.2 in Sect. 3.2), demonstrating this general trend. From the smallest, most basic and most coordinating anion Cl^- up to the medium sized, weakly coordinating $[PF_6]^-$ anion the shift towards higher BE is nearly linear. Interestingly, for the three ILs containing $[PF_6]^-$, $[Tf_2N]^-$ and $[Pf_2N]^-$ (circles) the BE values are nearly constant, despite strong differences in molecular volume. This indicates that the coordination properties (all three anions are similarly very weakly coordinating) have the main effect on the BE shift. Apart from the size of the anion, other parameters describing the coordination behaviour of the ILs were correlated with the observed anion dependent BE shifts. As is shown in Fig. 3.5c and will be discussed in detail later, the observed BE shifts exhibit a linear relationship with the Kamlet-Taft parameter β, which is a measure for the hydrogen bond acceptor basicity of the IL anion [8, 70].

Before discussing the origin of the XPS shifts of the ionic head group of the imidazolium ion, the contributions from intermolecular H-bonding interactions will be elucidated below.
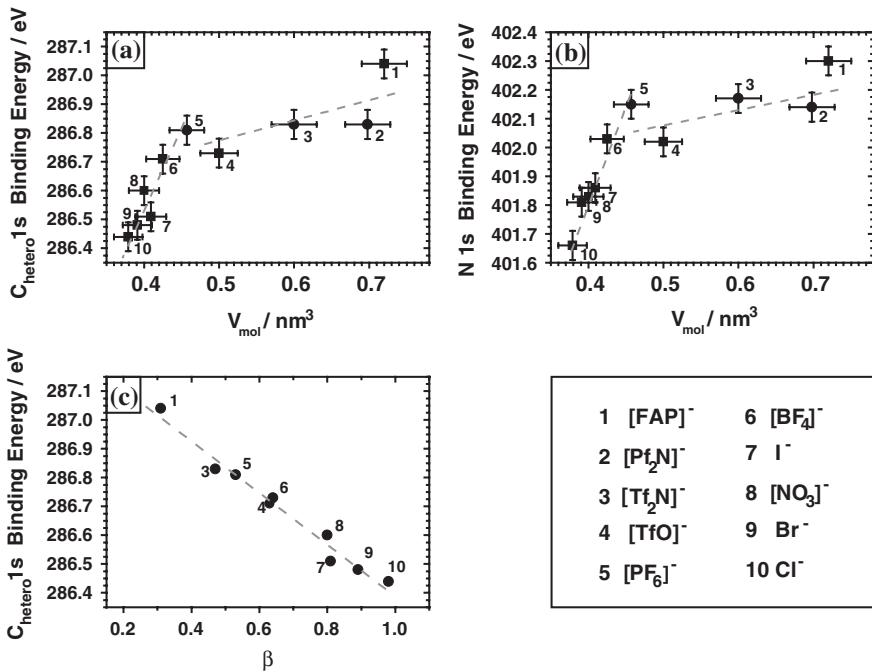
Fig. 3.5 **a** and **b** Correlation of BE values of C_{hetero} 1s (**a**), and N_{cation} 1s (**b**) of the ten $[C_8C_1Im]^+$-based ILs with molecular volume. Differentiation into *squares* and *circles* relate to discussion in the text. **c** Correlation of C_{hetero} 1s BE with Kamlet-Taft parameter β (values for $[C_8C_1Im]Cl$, $[C_8C_1Im]Br$ and $[C_8C_1Im][FAP]$ are unpublished data from the Spange group, remaining values from Ref. [70])

$[C_8C_1C_1Im]^+$-based ILs

Apart from coulomb forces, H-bonding interactions between cation and anion play a major role in imidazolium-based ILs [8, 9]; they are mediated through the hydrogen atoms at the C^2, C^4, and C^5 position (see also Scheme 3.1) with the hydrogen atom at C^2 contributing strongest (see also next section) [6, 13, 26, 27, 69]. To study the possible influence of H-bonding on the C_{hetero} 1s BE discussed in the preceding paragraph, two representative ILs, namely $[C_8C_1C_1Im]Br$ and $[C_8C_1C_1Im][Tf_2N]$, in which a methyl group in C^2-position replaces the most acidic proton, were measured. Consequently, hydrogen bonding between anion and cation is strongly reduced in these two ILs compared to the non-methylated homologues $[C_8C_1Im]Br$ and $[C_8C_1Im][Tf_2N]$ [6, 71, 72].

In Fig. 3.6, the C 1s and N 1s spectra of the methylated ILs $[C_8C_1C_1Im][Tf_2N]$ (first row) and $[C_8C_1C_1Im]Br$ (second row) are displayed (black dots); for the C 1s region the spectra of the corresponding $[C_8C_1Im]^+$ ILs are superimposed open circles). The BE of the N 1s signal from the methylated imidazolium ring exhibits an anion dependent difference of 0.41 eV (Fig. 3.6, right column), which is
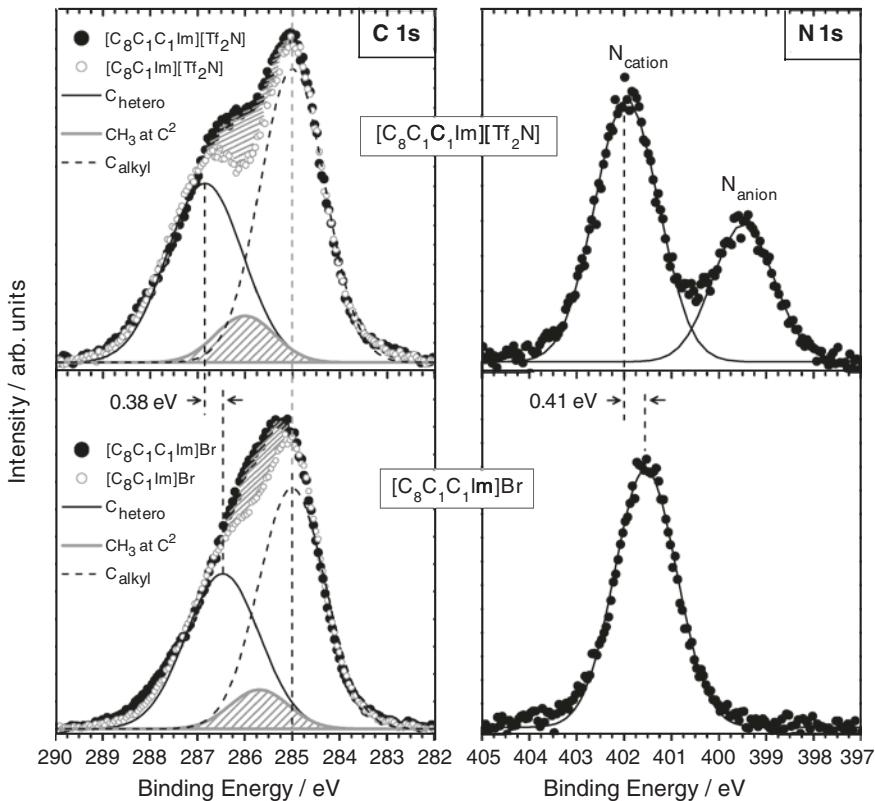
Fig. 3.6 Analysis of C 1s and N 1s spectra of $[C_8C_1C_1Im][Tf_2N]$ and $[C_8C_1C_1Im]Br$. The grey-shaded fit curve corresponds to the additional methyl group in C^2 position. The C 1s spectra of the two corresponding $[C_8C_1Im]^+$ ILs (*open circles*) are overlaid for comparison and illustration of the C^2-methyl contribution

within the margins of error very close to the differential N 1s shift of 0.36 eV for the non-methylated homologues $[C_8C_1Im][Tf_2N]$ and $[C_8C_1Im]Br$ (Fig. 3.4c and Table A3); only the absolute value of the N 1s BE for the $[C_8C_1C_1Im]^+$ ILs is smaller by 0.2 eV (see also Fig. 3.4c). In the C 1s spectra of both $[C_8C_1C_1Im]^+$ ILs the signal of the additional CH_3-group, with its BE between C_{hetero} and C_{alkyl}, is superimposed making the data interpretation not as straight forward as in the N 1s region. Nevertheless, the BE positions of C_{hetero} for both $[C_8C_1C_1Im]^+$ ILs can unambiguously be derived by fitting as shown in Fig. 3.6 (left column), and also by simple subtraction techniques (see Fig. A1 in the Appendix). Independent of the presence of the methyl group in the C^2 position, the BE values of C_{hetero} for the Br^- as well as the $[Tf_2N]^-$ ILs are identical within ± 0.05 eV. This data demonstrates that the observed anion dependent differential XPS shifts of the imidazolium ring signals are rather independent of the strength of the H-bonding between anion and cation.

Interpretation of anion dependent differential XPS shifts of imidazolium ring signals

In general, variations in the local electron density at a particular atom contribute to shifts in the corresponding core levels in XPS, the so-called chemical shifts. As a common trend, an increase in electron density at the atom under investigation (e.g., induced by electron transfer due to reduction or by bonding to an electron-donating neighbour atom) leads to a lowering of the measured core level BE, whereas a decrease in electron density (e.g., due to oxidation processes or due to bonding to an electron-withdrawing atom) increases the measured BE. In particular, good correlation between XPS shifts and (semi)empirical charges on the atoms (e.g., described by oxidation states or Pauling charges) can be found, as already pointed out by the pioneering work of Siegbahn et al. [73]. For an accurate calculation of chemical shifts using ab initio methods, the discrimination between initial state effects (i.e., changes of the ground state) and final state effects (due to the specific response of the remaining electrons to screen the generated core hole during the photoemission process) is required, which is not straightforward at all. Fortunately, initial and final state effects in most cases result in BE shifts in the same direction [48, 74], which leads to the general observation that an INCREASE in electron density at an atom yields a core-level shift towards LOWER BEs (and vice versa).

Hence, we propose that the observed anion-dependent XPS shifts of the cationic head group are attributed to some kind of charge transfer between the anion and the cation. Such charge transfer is expected to be smallest (probably close to zero) for the large and weakly coordinating anions, where anion and cation are most separated and local charge densities are so small that charge transfer is improbable. In this case excess charges very close to the integer values of $+1e$ for the cation and $-1e$ for the anion are expected. Thus, the observed highest BE values of the ring signals for the large and weakly coordinating anions indicate a situation where no charge transfer occurs. For the smaller and more strongly coordinating anions, which are closer to the imidazolium ring, the much more localized charge is transferred from the anion to the cation, leading to a less positively charged ring and in turn to lower XPS BEs. As a consequence of the overall charge neutrality, the negative excess charge of the anion must also deviate from the formal value of $-1e$ in the ILs. Hence, small and strongly coordinating anions (such as the halides and $[NO_3]^-$) carry less negative charge compared to the large anions $[Tf_2N]^-$ and $[FAP]^-$. The degree of the ionic character of the ILs in a chemical meaning is thus affected by the choice of combination of anion and cation (the term "ionicity" will be avoided here because it is commonly used to describe transport properties and degree of association of anion and cation [24]). The saturation effect seen in Fig. 3.5a and b for the anions larger than $[BF_4]^-$ indicates that the charge transfer reaches values close to zero above a certain size of the weakly coordinating anions.

While in Fig. 3.5a and b the molecular volume was chosen as an easily quantifiable parameter to correlate the amount of charge transfer between anion and cation, it is obvious that specific interaction parameters, such as coordination characteristics of the molecules (e.g., shapes, terminal groups, etc.), will also play an important role. Accordingly, a much better correlation of the differential BE shift

is found with the Kamlet-Taft parameter β (Fig. 3.5c), as it is a measure of the H-bonding acceptor ability of an ILs anion, which directly relates to the anion's coordination strength and charge localization [8, 70]. The dipolarity/polarisability parameter π^* also reflects the coordination ability of a given anion; however this value incorporates contributions from both the anion and cation as has been shown recently by Lungwitz et al. [70].

Counter-ion dependent shifts of XPS core levels have been observed before in ionic crystals, but no clear statement on their origin has been made [75–77]. However, these data show similar trends to that observed in our study, i.e., shift of the respective cation core levels to higher BE for larger and less basic anions. Unfortunately, the question of reference level is not easy to handle for those earlier described inorganic salts in comparison to our well-adapted internal referencing method using the cation's octyl chains. Therefore, we refrain from a quantitative and detailed comparison of these previous studies on solid salts with our findings.

To corroborate our interpretation of the anion dependent XPS shifts as a measure for the charge transfer between ions, detailed quantum chemical calculations on the representative ILs $[C_8C_1Im]X$ and $[C_8C_1C_1Im]X$ (X = Cl^-, Br^-, $[BF_4]^-$, $[Tf_2N]^-$) in form of gas-phase ion pairs were performed. For the non-methylated $[C_8C_1Im]^+$ ILs, the in-plane configurations (i.e., the anion in-plane of the imidazolium ring in front of the C^2 position) were found to be energetically favoured. However, on-top configurations (i.e., the anion located above the ring plane in close proximity to the C^2–H^2 bond) were found to lie only at slightly higher energies and, thus, were also considered [12, 78]. Especially for the larger and less-strongly coordinating $[Tf_2N]^-$ anion the on-top configuration is energetically degenerate, i.e. has the same energy, or is even slightly favoured compared to the in-plane configuration. In case of the methylated $[C_8C_1C_1Im]^+$ ILs, only on-top configurations were found to be energetically stable. These low-energy conformers agree well with results from comparable imidazolium ion pair calculations conducted by Hunt and coworkers [7]. A detailed discussion of ion-pair geometries and total energy of different conformers is beyond the scope of this investigation, where we restrict ourselves to the aspects directly related to our experimental findings.

In Table 3.1 the sums over partial charges for different moieties of $[C_8C_1Im]X$ and $[C_8C_1C_1Im]X$ ion pairs (X = Cl^-, Br^-, $[BF_4]^-$, $[Tf_2N]^-$) as well as the isolated $[C_8C_1Im]^+$ cation (labelled as "monomer" in Table 3.1) are given as derived by natural population analysis ("NPA charges"). It is evident that the overall excess charges of the cation and anion are non-integer and smaller than 1 in all cases except for the isolated $[C_8C_1Im]^+$ cation, where the charge +1e is imposed by boundary conditions. Thus, charge transfer between anion and cation is clearly indicated by the NPA analysis. Most of the positive charge on the cation is located at the atoms of the ionic head group (labelled R' in Table 3.1) being fairly equally distributed over the imidazolium ring R and both the adjacent methyl (C^6) and methylene (C^7) groups bonded to the nitrogen atoms of the ring (note that R' comprises the atoms C_{hetero} and N_{cation} measured in XPS). The two different in-plane and on-top conformers of the $[C_8C_1Im]X$ ILs show only minor deviations in charging of R'. Only for $[Tf_2N]^-$ is the difference somewhat larger, which could be related to the higher degree of

Table 3.1 NPA charge distribution in units of the elementary charge e summed over chemical groups for selected ion pairs
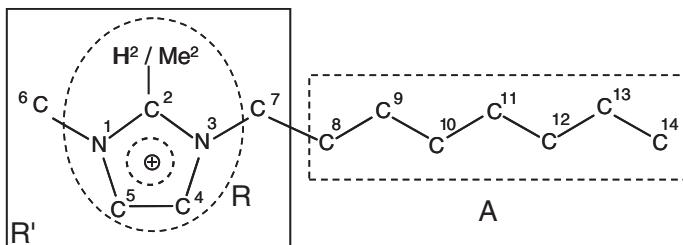
(a) Labelling of groups in the $[C_8C_1Im]^+$ and $[C_8C_1C_1Im]^+$ cations

(b) $[C_8C_1Im]^+$	Monomer	$[C_8C_1Im]X$ for in-plane/on-top configuration			
Group\anion	–	$[Cl]^-$	$[Br]^-$	$[BF_4]^-$	$[Tf_2N]^-$
Cation (= −anion)	1	0.811/0.791	0.824/0.803	0.940/0.964	0.936/0.972
Ionic head group R'	0.920	0.762/0.742	0.772/0.751	0.860/0.906	0.850/0.913
Imidazolium ring R	0.388	0.265/0.269	0.272/0.272	0.359/0.384	0.353/0.394
$(CH_3)^6$	0.293	0.263/0.260	0.266/0.263	0.291/0.285	0.286/0.281
$(CH_2)^7$	0.239	0.235/0.214	0.234/0.217	0.210/0.236	0.211/0.238
Alkyl rest A	0.080	0.049/0.049	0.052/0.052	0.080/0.058	0.086/0.059

(c) $[C_8C_1C_1Im]^+$	Monomer	$[C_8C_1C_1Im]X$ for on-top configuration			
Group\anion	–	$[Cl]^-$	$[Br]^-$	$[BF_4]^-$	$[Tf_2N]^-$
Cation (= −anion)	1	0.838	0.893	0.966	0.970
Ionic head group R'	0.925	0.787	0.833	0.927	0.927
Imidazolium ring R	0.311	0.258	0.292	0.320	0.306
$(CH_3)^6$	0.284	0.256	0.262	0.270	0.278
$(CH_2)^7$	0.233	0.209	0.207	0.246	0.250
Me^2	0.097	0.064	0.071	0.090	0.093
Alkyl rest A	0.075	0.051	0.060	0.039	0.043

flexibility of the $[Tf_2N]^-$ anion compared to the more spherical anions. The insensitivity of the excess charge to the different in-plane/on-top geometries is particularly surprising for the strongly coordinating anions Cl^- and Br^- because of the different method of orbital interaction (to be detailed in the next section). In short, for the in-plane configuration the charge transfer between the halide anion and the cation occurs mainly under strong participation of σ-type MOs of the cation located at the C^2 position and the p atomic orbitals of the anion (i.e., a H-bonding type interaction) whereas, for the on-top configuration, anion and cation mainly interact through π-orbitals of the imidazolium ring (i.e., a more p-π type bonding interaction). Nevertheless, both geometries with their individual charge transfer mechanisms yield similar net charges of R'. These findings are in line with earlier results for $[C_4C_1Im]Cl$ [21]. The RELATIVE distribution of the excess charge on the groups of the cation is similar for all anions and resembles the intrinsic charge distribution of

the monomer (see Table 3.1). However, the ABSOLUTE values of the NPA charges are significantly affected by the anion. Whereas the small, basic and strongly coordinating anions Cl^- and Br^- yield the smallest values for the charges on the ionic head group R' (e.g., a mean value of 0.76e in both configurations), the positive charge is considerably increased by $+0.12e$ for the larger, less basic and more weakly coordinating $[BF_4]^-$ and $[Tf_2N]^-$. The highest value for the positive charge on R' of 0.91e is found for $[Tf_2N]^-$ in the energetically favoured on-top configuration (coming close to the nominal value of 1). Hence, the measured increase in XPS BEs of C_{hetero} and N_{cation}—the R' atoms that are accessible by means of XPS—with increasing anion size (decreasing basicity) is indeed directly reflected by an increase in positive charge on the ionic head group, as was proposed above. To our knowledge this is the first time that inter-ionic charge transfer phenomena found for ILs in theory can be directly related to experimentally observable chemical shifts in XPS.

Moreover, the calculations clearly show that the anion-dependent charging of the ionic head group takes place independently of the methylation at C^2. In particular for the ILs investigated in XPS, the on-top configuration NPA charges on R' of the non-methylated ILs $[C_8C_1Im]Br$ (0.75e) and $[C_8C_1Im][Tf_2N]$ (0.91e) ILs and their methylated counterparts $[C_8C_1C_1Im]Br$ (0.83e) and $[C_8C_1C_1Im][Tf_2N]$ (0.93e) reveal a common increase of at least $+0.1e$ of the ionic head group when the small and basic Br^- is replaced by the larger and less basic $[Tf_2N]^-$ anion. This is in good agreement with the measured BE shifts of C_{hetero} and N_{cation} shown in Fig. 3.6. As is also indicated in Table 3.1 the additional methyl group at C^2 of $[C_8C_1C_1Im]^+$ ILs has only minimal contribution (about 0.07e, only weakly anion dependent) to the total positive charge of the ionic head group. The positive NPA charges of this methyl group are thus considerably smaller than the NPA charges on the N-CH_3 and the N-CH_2 carbon atoms but larger than the NPA charges on methylene groups in the octyl chain (which are rather neutral, see Fig. 3.2c). This explains the C 1s peak position of the methyl group between the C_{hetero} and the C_{alkyl} position found by our XPS analysis (see Fig. 3.6).

The different degree of charge transfer that is presumably responsible for the observed XPS shifts of the cationic head group is directly reflected by the degree of mixing of molecular orbitals between cation and anion. In Fig. 3.7 the three highest occupied orbitals (HOMO) and the lowest unoccupied MO (LUMO) of three ion pairs $[C_8C_1Im]Cl$, $[C_8C_1Im][BF_4]$ and $[C_8C_1Im][Tf_2N]$ in the low-energy in-plane configurations are shown. In the case of the smallest and most basic Cl^- a pronounced mixing of the Cl 2p atomic orbitals with molecular orbitals from the imidazolium cation is found. For the HOMO of the $[C_8C_1Im]Cl$ ion pair, which is dominated by the p states of Cl^-, and for the LUMO dominated by the cation, considerable density of states is present at both the imidazolium ring and the Cl^- anion. Mixing of orbitals becomes, however, more evident for the lower lying HOMO-2, which has a pronounced σ-type bond character and exhibits strong interaction between the Cl 2p states and states localized at the -N^1-C^2H–N^3- unit of the imidazolium ring. As was stated earlier [21], it is this HOMO-2 orbital that is important for the H-bond formation between the cation and the Cl^- anion. For the on-top configuration of $[C_8C_1Im]Cl$ the LUMO, HOMO, HOMO-2 and HOMO-3 MOs show pronounced orbital mixing between the Cl 2p states and the cationic head group, as evident from Fig. 3.8.
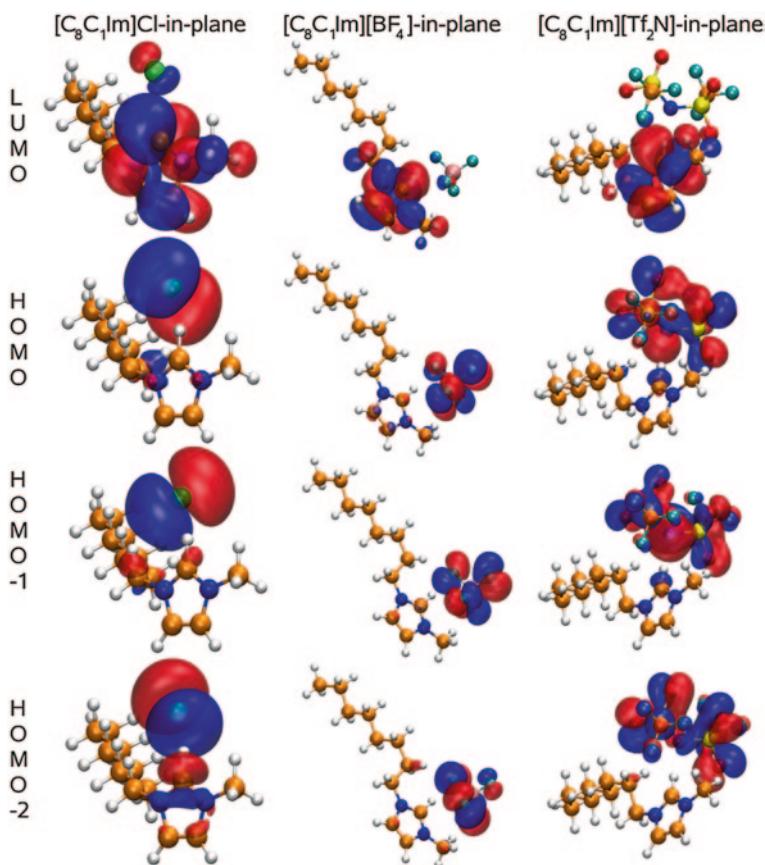
Fig. 3.7 Frontier orbitals of $[C_8C_1Im]X$ ($X = Cl^-$, $[BF_4]^-$, $[Tf_2N]^-$) in in-plane configuration (isosurface value 0.02 for all orbitals)

Upon replacement of Cl^- by the much larger and less basic $[BF_4]^-$ and $[Tf_2N]^-$ anions, no comparable strong mixing of orbitals could be detected for the in-plane configuration as is shown in Fig. 3.7. The character of MOs of the ion pairs for the in-plane configuration (Fig. 3.7) is mainly given by either the MOs of the cation or MOs of the anion. As depicted in Fig. 3.8 for the on-top configuration of $[C_8C_1Im][BF_4]$ and $[C_8C_1Im][Tf_2N]$, only some minor orbital mixing is observed in the HOMO-3 for $[C_8C_1Im][BF_4]$ and in the HOMO-1 of $[C_8C_1Im][Tf_2N]$, which accounts for the slightly reduced charges in these ILs.

Furthermore, the frontier orbitals of $[C_8C_1C_1Im]Cl$ in on-top configuration were calculated and compared to the on-top conformers of $[C_8C_1Im]Cl$; Fig. 3.9 demonstrates that $[C_8C_1C_1Im]Cl$ on-top shows the same pronounced orbital mixing as it was observed for $[C_8C_1Im]Cl$ on-top, which further corroborates our interpretation of results.
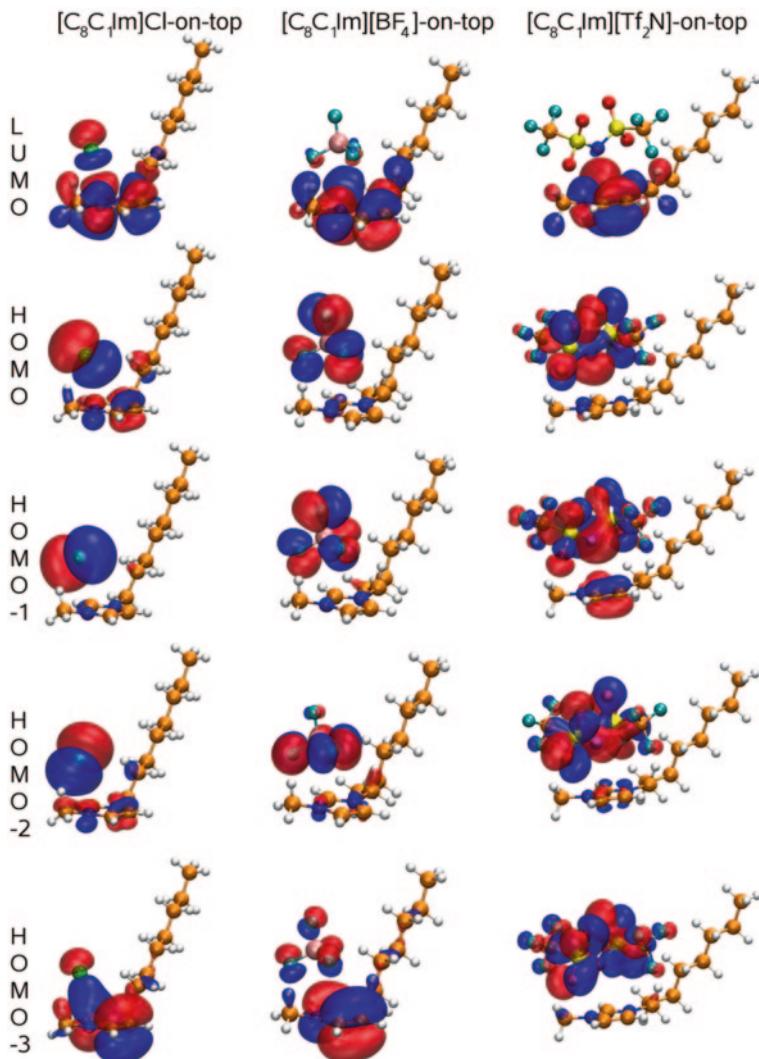
Fig. 3.8 Molecular orbitals of [C$_8$C$_1$Im]X (X = Cl$^-$, [BF$_4$]$^-$, [Tf$_2$N]$^-$) in on-top configuration (isosurface value 0.02 for all orbitals)

As an intermediate summary, our experimental XPS results in combination with quantum chemical calculations clearly indicate a strong electronic interaction between anion and cation for small, basic and strongly coordinating anions. This interaction leads to a partial charge transfer between anion and cation and, as a consequence, to effective charges considerably smaller than 1. The amount of charge transfer decreases with increasing anion size and decreasing basicity, i.e. with decreasing coordination strength. For the anions [PF$_6$]$^-$, [TfO]$^-$, [Tf$_2$N]$^-$, [Pf$_2$N]$^-$, [FAP]$^-$, which are all of low basicity and coordination strength, charge

Fig. 3.9 Comparison of [C$_8$C$_1$C$_1$Im]Cl and [C$_8$C$_1$Im]Cl on-top configurations of the LUMO and HOMO-3 orbitals, where the most pronounced orbital mixing is observed. It becomes evident that introducing the additional methyl group in C^2 position does not largely affect the electronic structure in the frontier orbitals
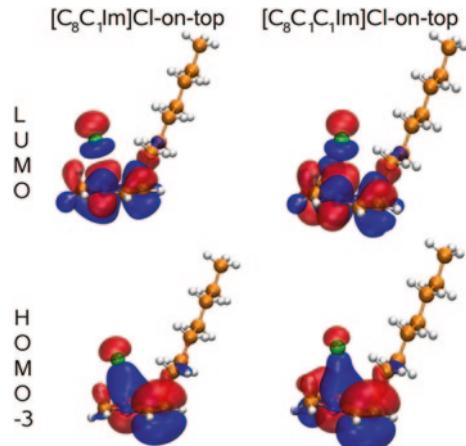
transfer between anion and cation is very small (<0.1 e) leading to charge values close to the ideal values ±1e. We believe that these findings are crucial for the understanding of ionicity and polarity of ILs in general. Moreover, correct charges assigned in MD simulations are most important to obtain correct interaction potentials, especially for coulombic interactions.

As emphasized in the introduction, in addition to coulombic interactions, hydrogen bonding type interactions also play an important role for the physicochemical properties of ILs. Thus, to obtain complementary information on the molecular interactions between anion and cation, ^{1}H- and ^{13}C-NMR spectroscopy measurements on the ten [C$_8$C$_1$Im]$^+$-based ILs were carried out, and the results were compared to the XPS findings.

3.1.3.2 ^{1}H- and ^{13}C-NMR Spectra of the [C$_8$C$_1$Im]$^+$-Based ILs

To rule out any influence of solvents, ^{1}H- and ^{13}C-NMR spectra of the neat ILs were recorded. For all ILs, the signals arising from the ring protons (H^2, H^4, H^5) and the corresponding carbon atoms (C^2, C^4, C^5) of the cation (labelled in Scheme 3.1) are shown in Fig. 3.10a and c, respectively. Both the ^{1}H- and ^{13}C-NMR spectra show anion-dependent shifts.

^{1}H-NMR of [C$_8$C$_1$Im]X ILs

Focusing first on the ^{1}H-NMR signals of the imidazolium ring in Fig. 3.10a, all peaks shift towards lower ppm values when going from small, basic and strongly coordinating anions to larger, less basic and weakly coordinating anions. Our data agree well with previously published ^{1}H-NMR data by Tokuda et al., who investigated neat [C$_4$C$_1$Im]$^+$ salts carrying [TfO]$^-$, [Tf$_2$N]$^-$, [Pf$_2$N]$^-$, [BF$_4$]$^-$ and [PF$_6$]$^-$ counterions [10]. The NMR shift is largest for the H^2 proton (from 9.9 ppm for Cl$^-$ to 7.4 ppm for [FAP]$^-$) and slightly smaller for the H^4/H^5 signals
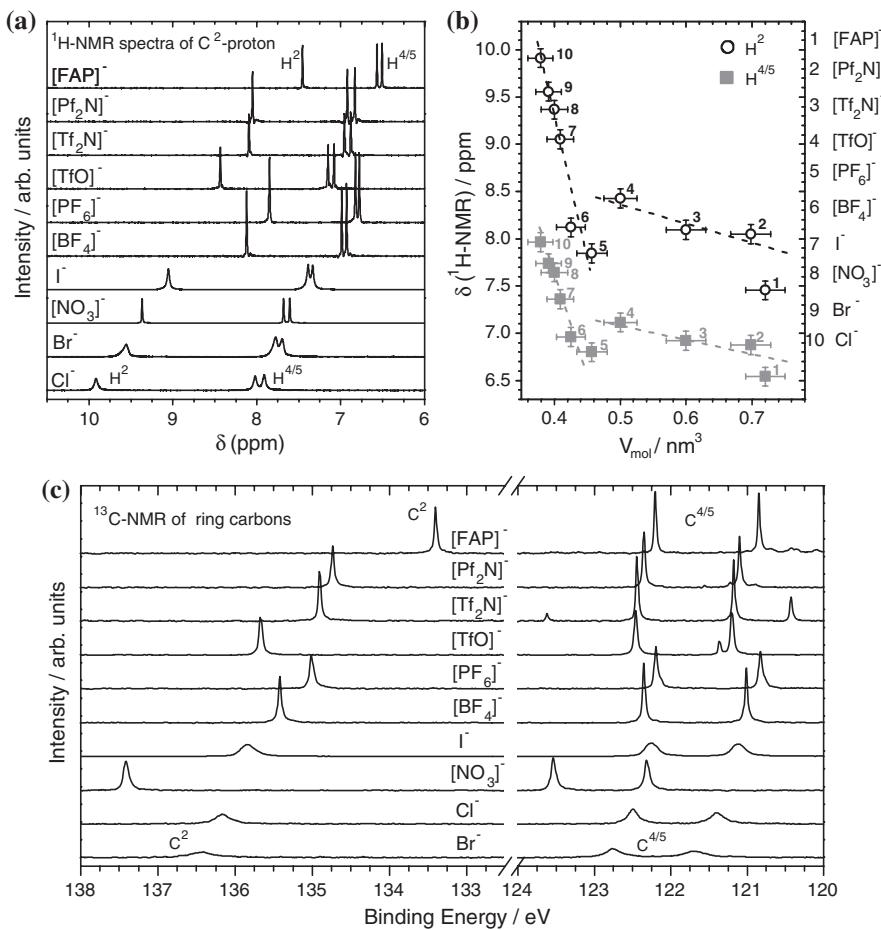
Fig. 3.10 a ^{1}H-NMR spectra of H^2 and H$^{4/5}$ of [C$_8$C$_1$Im]X. **b** Correlation of ^{1}H-NMR resonances of H^2 (*open circles*) and H$^{4/5}$ (*solid squares*, values are for mid position for H^4/H^5) with molecular volume (*dashed lines* are guides to the eye). **c** ^{13}C-NMR-spectra of C^2 and C$^{4/5}$ of [C$_8$C$_1$Im]X; the spectra are offset for sake of clarity in the order of increasing molecular volume

(from 7.9 ppm for Cl$^-$ to 6.5 ppm for [FAP]$^-$). The correlation of the NMR shifts with the size of the anion is shown in Fig. 3.10b, where ^{1}H-NMR positions of the ring protons are plotted against IL molecular volume. The data reveal a similar overall trend as the chemical shifts in XPS (Fig. 3.5): with increasing molecular volume, a steep decrease in ppm shifts from Cl$^-$ to about [BF$_4$]$^-$/[PF$_6$]$^-$ is measured, followed by a plateau-like behaviour for the larger anions (dashed lines in Fig. 3.10b). Again, it should be mentioned that anion size is a rough, but easily accessible parameter which seems to give a good correlation as long as anions with a spherical charge distribution are considered. Also, as evident from Fig. 3.11, a good overall correlation of the ^{1}H-NMR shifts is found with the ILs'
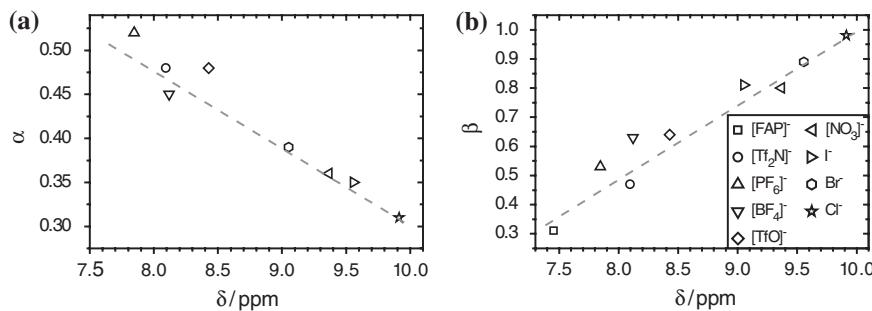
Fig. 3.11 Correlation of ^{1}H-NMR resonance of the H^2 proton with the Kamlet-Taft parameters α (**a**) and β (**b**). α and β values are taken from Ref. [70], apart from the values for [C$_8$C$_1$Im]Cl, [C$_8$C$_1$Im]Br and [C$_8$C$_1$Im][FAP](only β), which are unpublished data from the Spange group

Kamlet-Taft parameters α and β, which represent the hydrogen bond donor and acceptor capability of the IL, respectively [8].

Such anion-dependent ^{1}H-NMR shifts have been commonly interpreted as a measure for the extent of H-bonding in imidazolium ILs or as a measure of the extent of π-stacking of the imidazolium rings [27, 28, 72, 79]. Increased π-stacking—as is predicted for an increasing concentration of ILs diluted in common solvents—generally leads to a shift towards lower ppm values [27]. In our case of pure ILs it appears unlikely that the very large and weakly coordinating anions [Pf$_2$N]$^-$ and [FAP]$^-$ show a higher degree of association to the imidazolium cations and, thus, a better π-stacking, as compared to the small halides. Lungwitz and Spange observed an analogous anion-dependent H^2 shift for a series of [C$_4$C$_1$Im]$^+$-based IL solutions with the ILs sufficiently diluted in CD$_2$Cl$_2$ to ensure that the ILs are present as ion pairs [8, 9]. The measured NMR shifts were unambiguously identified as a measure for H-bonding-type interactions between the anion and the cation because of their good correlation with corresponding Kamlet-Taft parameters α and β of the ILs as probed by solvatochromic dyes. According to the interpretation of the Spange group, the interaction with small and strongly coordinating anions leads to a weakening of the C–H bond at the C^2 position, and thus, to a proton resonance which is closer to that of an acidic proton. Comparing the data from Lungwitz with our measurements, the trend of the ^{1}H-NMR signals of the H^2-proton with the different anions is similar; however, in our case of the pure ILs absolute values for the ppm positions are about 0.5 ppm smaller, which is attributed to the influence of the solvent. The above-mentioned interpretation is adapted for the observed anion-dependent ^{1}H-NMR shifts, which are accordingly attributed to changes in the magnetic shielding constant at H^2 and (to a lesser extent) at H$^{4/5}$. Shifts towards higher ppm are usually due to less pronounced shielding of the protons, indicating stronger H-bonding and vice versa. This is in line with the qualitative picture of diamagnetic shielding in NMR: the lower the electron density at the location of the ^{1}H-nucleus (as is the case of pronounced hydrogen bonding), the weaker the local shielding of the external magnetic field resulting in higher ppm shifts (it is important to note that

quantification of NMR shifts is very complicated—particularly in case of delocalized π-electron systems—and many theoretical approaches have been employed in the past to ascribe for the different effects, see Ref. [80]). As the concentration of the ILs is not varied in our case and the structure of the $[C_8C_1Im]^+$ cation remains virtually unchanged in our series, it is not expected that variations in π-stacking have a strong influence on the observed ^{1}H-shifts. Nevertheless, it is interesting to note that $[C_8C_1Im][BF_4]$ and $[C_8C_1Im][PF_6]$ are to some extent outliers in the series exhibiting smaller shifts than expected from their molecular volume (see Fig. 3.10b) which might be attributed to the fact that for these anions very low basicity and coordination strength is combined with relatively small molecular volume compared to the larger fluorinated anions in this study.

^{13}C-NMR of $[C_8C_1Im]X$ ILs

In the hydrogen bonding scheme described above, smaller and more strongly coordinating anions lead to a more pronounced loss in electron density at the position of the ring protons and consequently to high ppm shifts in ^{1}H-NMR. Thus, one might expect that the neighbouring carbon atoms C^2, C^4, and C^5 simultaneously gain in electron density. This assumption is supported by the anion dependent C 1s and N 1s XPS shifts of the imidazolium ring, which indicate an increase in electron density within the ring for the small anions as compared to the large and weakly coordinating anions. As a consequence, if electron density was the sole contribution to signal shifts, the ^{13}C-NMR signals of the ring carbon atoms should shift towards Lower ppm with decreasing size of the anion, due to a higher shielding within the imidazolium ring (see also the discussion on charge density and ^{13}C NMR for typical aromatic compounds given by Wiberg et al. [81]). In Fig. 3.10c the ^{13}C-NMR data of the ring carbon atoms of all $[C_8C_1Im]^+$ ILs are shown. Overall, the ^{13}C-NMR signals of the imidazolium ring are approximately constant within the whole series and changes are very small. The differential shifts of the C^2 signal amounts to ± 1.5 ppm around 135 ppm, and those of the C^4/C^5 signals to ± 0.5 ppm around 122.5 ppm, being therefore in the range of typical heteroaromatic compounds, and are more or less independent of the anion (only $[C_8C_1Im][NO_3]$ seems to be an outlier with larger shifts of the ring carbon atoms). Consequently, ^{13}C-NMR seems to be rather insensitive to the influence of the anion. Nonetheless, a small trend is observed: for smaller anions the ^{13}C-NMR signals slightly shifts towards higher ppm (most pronounced at C^2), meaning that ^{1}H- and ^{13}C-NMR signals exhibit "parallel" shifts for the C^2-H^2 group of the ring, as seen in Fig. 3.10c, which contradicts the mere consideration of electron density in the case of ^{13}C-NMR spectra. It seems that some compensating effects are present, such as changes in the ring current, hybridization re-arrangements accompanied by anisotropy changes etc., which are known to have an impact on local shielding constants in ^{13}C-NMR. In particular, it has been shown for monocyclic aromatic compounds that it is the degree of p_z occupancy for sp^2-hybridized ring carbon atoms rather than the local charge density that affects the ^{13}C-NMR shifts [81]. It is therefore assumed that the different degree of orbital mixing (see also Fig. 3.7 and the discussion in the preceding section) has a direct impact on the ^{13}C-NMR shifts.

If this assumption was correct one should expect anion-dependent hybridisation changes in the imidazolium ring. For that reason we performed an NBO analysis of selective bonds within the imidazolium ring using natural resonance theory (NRT) [62]. Here, NBO values of one and two describe classical single and double bonds, respectively, whereas values close to 1.5 in the aromatic compound benzene would correspond to a typical delocalized aromatic bond. In view of the fact that the effect of the different anions on the NBO values is rather small, we compare the isolated $[C_8C_1Im]^+$ cation (representing the most extreme case, where a coordinating anion is absent) with $[C_8C_1Im]Cl$, the most strongly coordinating anion in our series (NBO averaged for in-plane and on-top configuration).

From Fig. 3.12 it becomes evident that for the "weakly coordinating anion" (i.e. the isolated cation) the ring bonds exhibit a pronounced aromatic bond character with a rather delocalized π-system (NBOs vary from 1.39 for the N^1-C^2-N^3 bonds, 1.26 for the N^1-C^5/N^3-C^4 bonds to 1.55 for the C^4-C^5 bond)). For the strongly coordinating Cl^- ion, the ring bonds of the cation resemble more an Arduengo carbene with a double bond at C^4–C^5 (1.79) whereas the N^1–C^5 and N^3–C^4 bonds exhibit single bond character (1.10). The reduced NBO value for the C^2-H^2-bond (0.97, 0.94 for the in-plane-configuration) is a clear indication for the H-bonding of the H^2 proton with the coordinating Cl^- anion as already discussed in the context of ^{1}H-NMR, see also Ref. [21]. An illustration of the proposed interactions and changes in hybridization (representative for the in-plane configurations) is given in Scheme 3.2, where both the degree of H-bonding as well as slight changes in hybridization and aromaticity of the system are depicted. This interaction scheme is also supported by the work of Fumino et al., who find a significant weakening in the C^2-H^2 vibrational bands for the rather strongly coordinating anion $[NO_3]^-$ as compared to $[BF_4]^-$ [11, 13].

Our interpretation is supported by the ^{13}C-NMR chemical shifts for the classical imidazolium compound $[C_1C_1Im]Cl$ (C^2 resonance at 135 ppm) and the corresponding extreme case of complete proton abstraction, an Arduengo carbene (C^2 resonance at 213.7 ppm) [82]. For the carbene, changes in hybridization, and thus, changes in shielding constant, lead to a strong increase in chemical shift despite the fact that the electron density at the C^2 position is obviously enhanced. Although our results from the NBO analysis point in the right direction, further theoretical investigations would be helpful to elucidate details regarding the

Fig. 3.12 NBO values of selected ring bonds in the isolated $[C_8C_1Im]^+$ cation (first value) and in the $[C_8C_1Im]Cl$ ion pair (second value, average of in-plane and on-top configuration)
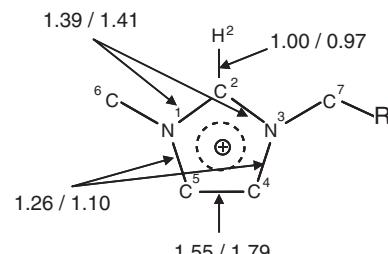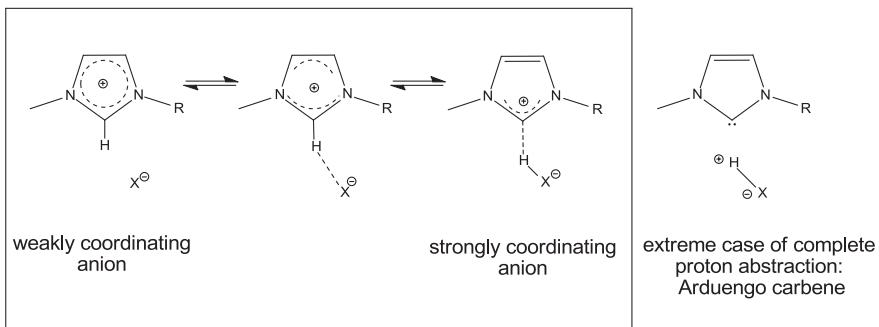
Scheme 3.2 Interaction scheme of the imidazolium ring with anions of increasing (from *left* to *right*) coordination strength

electronic structure of the imidazolium ring as a function of the anion, especially for the larger, less basic and therefore least coordinating representatives.

NMR results from [C$_8$C$_1$C$_1$Im]X ILs

To consolidate our interpretation of ^{1}H- and ^{13}C-NMR shifts of [C$_8$C$_1$Im]X ILs, a comparison was made with the C^2-methylated ILs [C$_8$C$_1$C$_1$Im]Br and [C$_8$C$_1$C$_1$Im][Tf$_2$N]. [C$_8$C$_1$C$_1$Im]Br is solid at room temperature, and therefore could not be measured in pure form. To circumvent the use of a solvent which could possibly lead to undesired shifts in the NMR spectrum, a liquid 5:1 mixture of [C$_8$C$_1$Im]Br:[C$_8$C$_1$C$_1$Im]Br was investigated, the ^{1}H- and ^{13}C-NMR spectra of which are shown in Fig. 3.13. From the ^{13}C-NMR measurements it can be seen that the peak assigned to C^2 undergoes a clear downfield shift of about 8 ppm towards higher values upon methylation, which is a general feature in aromatic systems, when a proton is substituted with a methyl group [83]. This shift is commonly assigned to a change in electron current at the ^{13}C nucleus resulting from the different bonding environment (exchange of s-type (H) with sp^3-type (C) orbital). In contrast, the C$^{4/5}$ signals undergo a high field shift of ~1.5 ppm, which can be assigned to the molecular changes due to methylation. However, this shift could also be related to the slight high field shifts observed for the H$^{4/5}$ protons in ^{1}H-NMR. Whereas in the spectra of [C$_8$C$_1$C$_1$Im]Br and [C$_8$C$_1$C$_1$Im][Tf$_2$N] no H^2 peak is present, the H$^{4/5}$ peaks are subject to a subtle high field shift of about 0.2 ppm for both ILs indicating less pronounced (or at least no enhanced) H-bonding through H$^{4/5}$. This means that upon methylation of the C^2 position the main H-bonding interaction is indeed eliminated and to no extent compensated by the H$^{4/5}$ protons.

Our results from NMR and the NBO analysis show that the interaction between anions and the imidazolium cations via hydrogen bonding type interactions is strongly altered by the nature of the anion. Small and more basic anions exhibit pronounced hydrogen bonding with the hydrogen atoms of the ring (particularly with H^2) as compared to the larger and less basic anions. Moreover, the electronic structure of the imidazolium ring in terms of charge distribution is modified by the coordination ability of the anion, where large anions lead to a more
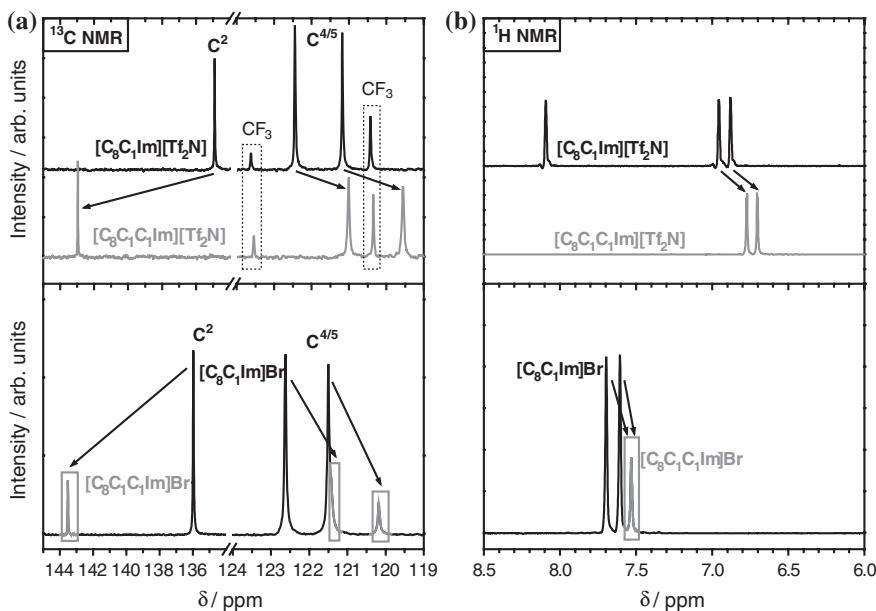
Fig. 3.13 Imidazolium ring signals in **a** ^{13}C- and **b** ^{1}H-NMR of $[C_8C_1Im][Tf_2N]$ (*black curves*) and $[C_8C_1C_1Im][Tf_2N]$ (*grey curves*) (*top row*) and of the 5:1 mixture of $[C_8C_1Im]Br:[C_8C_1C_1Im]Br$ (*bottom black curve*, with $[C_8C_1C_1Im]Br$ contributions in *grey*) are compared (signals originating from the $[Tf_2N]^-$ anion in this region are indicated by *dotted boxes*). The differential ppm shifts due to methylation at C^2 are marked by *arrows*

aromatic character of the π-system of the ring; this is in contrast to small anions, which give rise to a more carbene-like bond structure of the imidazolium ring. Importantly, we find no evidence that the presence or absence of intermolecular hydrogen bonds considerably influences the absolute value of the net charge transfer between anion and cation; this is deduced from XPS results and DFT calculations in combination with NMR data for the methylated and non-methylated ILs.

3.1.4 Summary

In this systematic XPS, NMR and theoretical study ten $[C_8C_1Im]^+$ and two $[C_8C_1C_1Im]^+$ ILs were investigated. In XPS, an anion-dependent shift of the C 1s and N 1s levels originating from the head group of the imidazolium cation towards higher BE is found for larger, less basic and weakly coordinating anions. This shift is interpreted as a measure for the net positive charge on the ionic moiety of the cation, i.e., the imidazolium ring with the adjacent methyl and methylene groups. The charge transfer between anion and cation is unambiguously related to the nature of the anion: for spherical anions a linear correlation of the BE shift with IL molecular volume is observed, whereas for the more asymmetric large anions carrying perfluoralkyl groups,

the BE shift exhibits only minor changes with increasing size. Overall, a linear correlation with the hydrogen bond acceptor basicity of the anion—characterized by the corresponding Tamlet-Kraft parameter β—is found, which indicates that the interionic charge transfer is closely related to the anion's coordination strength and, thus, to the localization of the negative excess charge in the anion. These findings are corroborated by DFT calculations on isolated $[C_8C_1Im]X$ ion pairs, which show that a net charge transfer via orbital mixing of anion and cation occurs for all energetically favourable conformations (i.e. the, "on-top" and "in-plane" configurations). The positive excess charge on the ionic head group of the cation varies from $+0.75$ e for $[C_8C_1Im]Cl$ up to of $+0.91$ e for $[C_8C_1Im][Tf_2N]$, coming close to the nominal value of $+1.0$ e. The calculations also show that for less basic and less strongly coordinating anions, the on-top configuration is energetically favoured; this also holds true for $[C_8C_1C_1Im]X$ ILs, where the most acidic proton in 2-position is substituted by a neutral methyl group. Despite the considerably lower contribution of hydrogen bond type interactions in the methylated $[C_8C_1C_1Im]X$ ILs (deduced from natural bond order (NBO) analysis and ^{1}H-NMR), the anion-dependent charge transfer is nearly identical to that for the non-methylated homologue ILs (deduced by natural population analysis of atomic charges (NPA) and XPS). Thus, the anion-dependent charge transfer cannot solely be mediated through pronounced H-bonding but is most likely dominated by the degree of orbital mixing of anion and cation. This contribution is strongly dependent on the proximity of the ions; hence, the local charge distributions play a crucial role.

Apart from coulombic interactions related to the charged ions, an understanding of the role of hydrogen bonding type interactions is essential for ILs. The analysis of the ^{1}H-NMR-spectra of pure ILs, where additional solvent interactions can be ruled out, reveals that the increasing size of the anion, accompanied by gradual reduction in anion basicity, leads to a reduction in H-bonding, which is in line with findings from other groups measuring ILs in organic solvents. The ^{13}C-NMR signals of the imidazolium ring are only weakly influenced by the nature of the anion. However, a small shift of the signal assigned to the C^2 carbon reflects an anion-dependent change of electronic structure within the ring, which is likely related to a modification of ring hybridisation, an argument also supported by the NBO analysis.

In this study an important contribution was made towards a detailed understanding of intermolecular interactions in ionic liquids, which can be transferred to other liquid systems where comparable interactions play an important role. The insights obtained from this study also provide a better understanding and interpretation of force field parameters (e.g., effective charges) used in molecular dynamics simulations.

3.2 Surface Composition of $[C_8C_1Im]^+$ Ionic Liquids

The results presented in this chapter are based on the following publications [50, 51]:
Influence of Different Anions on the Surface Composition of Ionic Liquids Studied Using ARXPS [50]

Insights into the Surface Composition and Enrichment Effects of Ionic Liquids and Ionic Liquid Mixtures [51]

Using the ten [C$_8$C$_1$Im]$^+$ ILs investigated in the previous section, we employed ARXPS in this study to examine the influence of different anions on the surface composition of these ILs. Within the first molecular layer, for all ILs an enrichment of the octyl chain was found at the expense of the charged moieties of the cation and the anions, which arrange in a sublayer. The aliphatic alkyl chains show the most pronounced surface enrichment for the smallest anions, while the effect decreases with increasing size of the anion. In a collaborative effort, UPS and MIES results for [C$_8$C$_1$Im]Cl and [C$_8$C$_1$Im][Tf$_2$N] were related to the ARXPS measurements, leading to the conclusion that for small anions the surface is solely terminated by densely packed alkyl chains, while for larger anions ionic groups are still present at the interface.

3.2.1 General Considerations

As mentioned in Chap. 1, an understanding of the nature of the IL/gas and IL/vacuum interface is of fundamental interest for a variety of IL-based applications such as sensors and gas chromatography [84, 85], or nanoparticle synthesis [86, 87]. For the SILP and SCILL approaches the IL/gas interface is vital because transport of reactants is directly influenced by the interaction of gaseous molecules with the IL ions at the surface. Furthermore, an understanding of the IL/vacuum interface at a molecular level is crucial in order to explain fundamental macroscopic surface properties such as surface tension [88]. For the IL/vacuum (or IL/gas) interface, the composition and molecular arrangement at the surface will be different to that of the bulk due to the unbalanced forces, which are present as a result of the non-isotropic environment.

Based on the very low vapour pressure of aprotic ILs [31, 32, 33] ultra-high vacuum (UHV) conditions have been applied to investigate IL surfaces using XPS [34, 35, 37–47], metastable impact electron spectroscopy (MIES) [34, 35], high resolution electron energy loss spectroscopy (HREELS) [34], low energy ion scattering (LEIS) [37], and direct recoil spectroscopy (DRS) [89, 90]. Other surface sensitive methods without UHV requirements such as sum frequency generation (SFG) [91–97], X-ray and neutron reflectometry [96, 98, 99], surface tension measurements [88, 97, 100], grazing incidence X-ray diffraction [101] and simulations have also been applied [68, 102, 103]. Most of these surface studies have mainly concentrated on non-functionalized imidazolium-containing ILs [104], and only few surface investigations of functionalized ILs have been reported [40, 41, 47, 95].

The discussion on IL surface structure often involves two different but interrelated aspects: surface composition and molecular orientation at the surface. Surface composition involves the identification of the molecules present in the near-surface region and whether there is enhancement of certain ions (or parts of ions) and depletion of other ions (or parts of ions) with respect to the

bulk composition. This identification becomes even more important when small amounts of surface-active impurities are present in the IL [39–42, 65]. Molecular orientation at the surface concerns detailed ordering and geometry effects of the ions (or part of the ions) present at the surface.

With regard to surface composition, a consensus has been established that both cations and anions are present in the surface region of a wide range of pure imidazolium ILs, particularly those ILs containing shorter alkyl chains such as $[C_2C_1Im]^+$ [34, 37, 41]. For ILs containing longer aliphatic alkyl chains (i.e. C_4H_9 or longer) it has been shown that more alkyl carbon is present in the near-surface region than non-alkyl parts of either the charged imidazolium ring or of the anion [44, 68, 92, 97, 102]. As illustrated in Fig. 3.14 and also Fig. 2.2 in Sect. 2.1, using ARXPS, our group recently investigated the influence of different substituents on the surface composition of $[Tf_2N]^-$-based imidazolium ILs [41]. The degree of surface enrichment of aliphatic alkyl carbon chains gradually increases in $[C_nC_1Im][Tf_2N]$ ILs (n = 2–16) with increasing chain length, as observed by Lockett et al. for $[C_nC_1Im][BF_4]$ (where n = 4–8) also using ARXPS [44]. Moreover, it was found that aliphatic alkyl chains seem to generally dominate the composition at the outer surface of pure ILs, independent of whether the chains
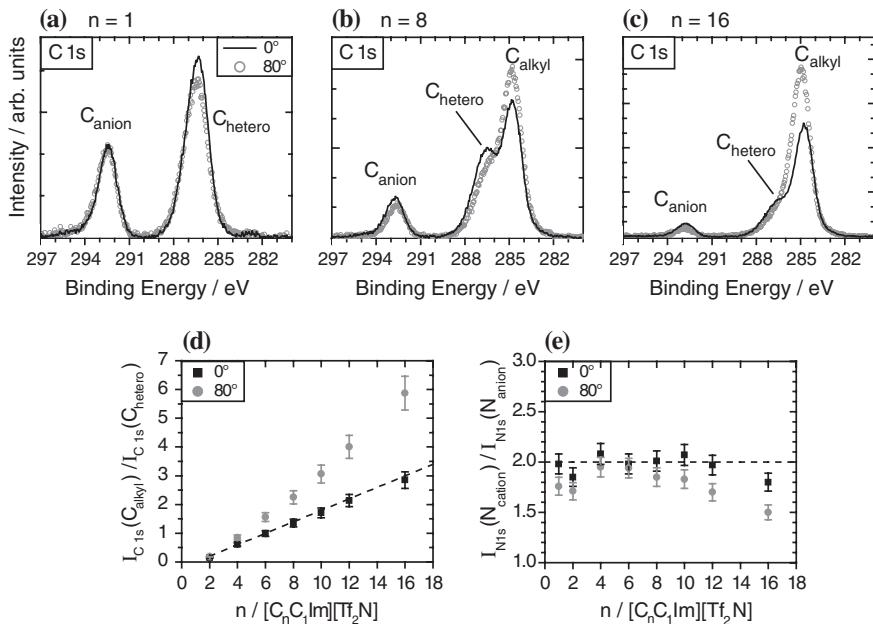
Fig. 3.14 **a–c** C 1s XP spectra of $[C_nC_1Im][Tf_2N]$ (n = 1, 8 16), recorded under 0° (*black*) and 80° (*grey circles*) electron emission angle, with respect to the surface normal. The intensity ratios for C_{alkyl} : C_{hetero}, and N_{cation} : N_{anion} of $[C_nC_1Im][Tf_2N]$ recorded at different electron emission angles as a function of chain length are shown in (**d**) and (**e**), respectively. A line for the nominal ratios (*dashed line*) is also added. For a detailed discussion, please see Ref. [41]

are attached to the cation or the anion, as demonstrated for $[C_2C_1Im][C_8OSO_3]$ [41]. These findings were confirmed by Baldelli et al. using SFG [97]. When the aliphatic chains are substituted by functional groups with the potential of intra- and intermolecular attractive interactions (such as ether moieties), the surface composition is found to be similar to the IL bulk (see also Fig. 2.2) [41].

In contrast to results on surface composition of ILs, there is more uncertainty concerning preferential molecular orientation of ions in the near-surface region. This uncertainty is partly related to different experimental techniques and their variation in sensitivity to orientation effects at the outer surface [104]. Particular focus has surrounded the orientation of the imidazolium ring of the cation and the longer alkyl chain of the cation. It has been shown that the alkyl chain is oriented approximately along the surface normal with a chain density lower (at least for larger anions) than that of archetypal thiolate self-assembled monolayers on Au (111) [68, 96, 102]. In different studies the imidazolium ring has been found to be either perpendicular or parallel to the surface normal [104]. The location of the anion relative to the cation has been addressed by only a few systematic surface studies employing ILs with the same cation but different anions. Using SFG, Rivera-Rubero et al. found for nine different anions with $[C_4C_1Im]^+$ that the imidazolium ring lay parallel to the surface plane and the butyl chain projects into the gas phase, independent of the anion identity [105]. Jeon et al. found using SFG and X-ray reflectivity that, for $[C_4C_1Im]X$ (where $X^- = I^-$, $[BF_4]^-$ and $[PF_6]^-$), the loosely-packed butyl chains were projected towards the gas/liquid interface whereas the tightly-packed charged cores (i.e. imidazolium cores and anions) were in contact with the neighbouring IL molecules in the bulk [96]. From their results these authors also suggested that I^- was located beneath the imidazolium core (i.e. the charged ring) whereas $[BF_4]^-$ and $[PF_6]^-$ were located alongside. Conclusions on surface orientation have also been made based on the macroscopic property surface tension [94, 106]. Lockett et al. successfully used synchrotron radiation to investigate the mutual location of ionic head groups in different ILs [107]. Apart from pure ILs only few surface studies of more complex IL systems such as of IL solutions [42, 43, 49] and IL mixtures [108] have been reported.

In order to obtain a better understanding of the factors that determine the IL surface structure this ARXPS investigation addresses the influence of the anion on the composition of the near-surface region of ten $[C_8C_1Im]X$ ILs. We have chosen $[C_8C_1Im]^+$ as the common cation for three reasons. Firstly, there are a broad range of ILs with this cation with very different anions available that are liquid at room temperature [31]. Secondly, these ILs can be prepared with surface contamination below XPS detection limits. Thirdly, surface enrichment of the octyl chain was already thoroughly studied for $[C_8C_1Im][Tf_2N]$ in previous work on the influence of substituents on the IL surface composition [41]. The anions X^- under investigation are very different in chemical nature, and include anions such as halides, $[NO_3]^-$, $[BF_4]^-$, $[PF_6]^-$, $[TfO]^-$ and also more complex anions containing perfluoroalkyl groups such as $[Tf_2N]^-$, $[Pf_2N]^-$ or $[FAP]^-$. The anions were chosen to cover different sizes (ranging from Cl^- to $[FAP]^-$), shapes (from spherical to elongated anions), and coordination abilities (from strongly coordinating

halides to weakly coordinating anions with perfluoroalkyl groups). Many of the anions studied here are commonly used in IL applications. Certain anions (e.g., $[MeOSO_3]^-$, $[OcOSO_3]^-$, $[B(CN)_4]^-$) were deliberately excluded from this ARXPS study, since they exhibit XPS carbon signals that strongly overlap with carbon signals from the $[C_8C_1Im]^+$ cation [1]. In this investigation it is demonstrated that the different anions have a considerable effect on the degree of surface enrichment of the octyl chains. The anion location is also commented upon for all ILs. The ILs studied herein are shown in Table 2.1, while some of their physical properties are listed in Table 3.1.

3.2.2 Experimental Aspects

XPS measurements: As already described in the experimental section and elsewhere [41], the thin IL films were prepared by deposition of the corresponding IL onto a planar Au foil in air, introduced into the UHV system, followed by careful degassing in the sample transfer chamber. ARXP spectra were recorded under polar angles of 0° (normal emission), 70°, and 80° (grazing emission), corresponding to an information depth of 7–9, 2–3, and 1.0–1.5 nm, respectively. A preferential increase in core level intensity with increasing detection angle and, thus, with increasing surface sensitivity, indicates a higher concentration of this element in the topmost layers as compared to the "bulk measurement" at 0° emission.

Usually, the Au $4f_{7/2}$ signal is employed as a reference for the reported BE; however, ILs have been shown to charge, even for low viscosity ILs [41]. Under the experimental conditions of the XPS setup in use, peak positions were reproduced with variations of about ± 0.15 eV [41]. To facilitate visual comparison of IL spectra, we used an internal standard for the BE scale, where the C 1s signal of the octyl chain of the common $[C_8C_1Im]^+$ cation was set to 285.0 eV. Please see the Sect. 3.1 for a detailed discussion of the referencing procedure.

For C 1s spectra of ILs with perfluoroalkyl group-containing anions ($[C_8C_1Im]$ [TfO], $[C_8C_1Im][Tf_2N]$, $[C_8C_1Im][Pf_2N]$, and $[C_8C_1Im][FAP]$) a three point linear background subtraction was applied; for all other spectra a two point linear background subtraction was used. All peaks were fitted using Gaussian lineshapes. As discussed earlier in the experimental section, when using a non-monochromatised Al-K_α source as in this study, it is best to fit C 1s peaks arising from the cation with two components only, C_{alkyl} and C_{hetero} [41]. These peaks are labelled as 1 and 2, respectively, in the chemical structure given in Fig. 3.16. This procedure provides reliable results, employing only one empirically derived constraint for the FWHM values of peaks 1 and 2, namely $fwhm(C_{hetero}) = 1.11 \times fwhm(C_{alkyl})$. Applying this constraint was found to give good fits for all $[C_8C_1Im]X$ ILs, and has previously given good fits for a range of non-functionalized and functionalized ILs [41].

From the areas under the fitted peaks, and by taking into account the sensitivity factors for the different elements, quantitative information can be obtained on the stoichiometry of the near-surface region. The atomic sensitivity factors (ASFs) used for C 1s,

N 1s, O 1s, F 1s, S 2p spectra are those reported previously [41]; additional ASFs for Cl 2p, Br 3d, I 3d$_{5/2}$, B 1s, P 2p were determined as described by Kolbeck et al. [40]. All ASF values for the corresponding elements are given in Tables A1 and A2.

Mass density, sample purity and radiation damage: All aspects relevant for this study were already discussed previously. Please refer to Sect. 3.1 for details.

3.2.3 Results and Discussion

Figure 3.15 shows survey scans for $[C_8C_1Im]Cl$, $[C_8C_1Im][BF_4]$ and $[C_8C_1Im]$ [Pf$_2$N]. These three ILs were chosen as case studies to explain the results. $[C_8C_1Im][BF_4]$ was studied using ARXPS by Lockett et al., thus providing a relevant opportunity for comparison [44]. As noted in Sect. 3.1, XPS signals were observed for all expected elements with no indication of impurities (above the limits of XPS detection, ~1 %). For all elements, a table containing quantitative analysis of all spectra (taken at 0, 70, and 80°) is given in the Appendix, Table A1. Comparison between the BE positions for both the C$_{hetero}$ and the anion elements is given in Table A3 in the Appendix.

Fig. 3.15 XP survey scan spectra of **a** $[C_8C_1Im]Cl$, **b** $[C_8C_1Im][BF_4]$, **c** $[C_8C_1Im]$ [Pf$_2$N], recorded under 0° emission
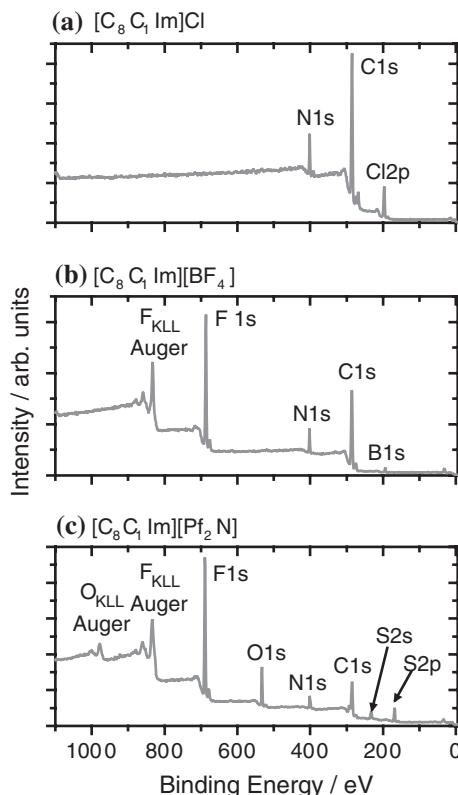
As already established in the previous chapter, the C 1s region for all ten [C_8C_1Im]X ILs studied contain 12 carbon atoms from the imidazolium cation, which were decomposed into two types: C_{alkyl} and C_{hetero}, in the structure in Fig. 3.16 labelled as 1 and 2, respectively [41]. C_{hetero} is located at a higher BE (~286.4 to 287.0 eV) than C_{alkyl} (285.0 eV) due to the C–N bond(s) to the more electronegative nitrogen atoms of the imidazolium ring [1]. The procedure for determining the relative amounts of C_{alkyl} and C_{hetero} has been explained previously for [C_8C_1Im][Tf_2N] [41]. The BE peak separation for C_{alkyl} and C_{hetero} is dependent on the nature of the anion, which was discussed in detail in Sect. 3.1 and in Ref. [1]. In Fig. 3.16a–f the C 1s region is shown for [C_8C_1Im]Cl, [C_8C_1Im][BF_4] and [C_8C_1Im][Pf_2N] at 0° and 80°, along with fitted components. At 0° the measured intensity ratios C_{alkyl}/C_{hetero} for all three ILs approximately match the nominal ratio, 7:5 = 1.4, as shown in Fig. 3.16g, suggesting that within the probing depth of 7–9 nm there is a homogeneous distribution of alkyl chains and imidazolium rings. At 80° and, thus, a probing depth of 1.0–1.5 nm, the intensity of the C_{hetero} component decreases relative to the intensity of the C_{alkyl} component, indicating that there are more alkyl carbons

Fig. 3.16 ARXP spectra of the C 1s region: [C_8C_1Im]Cl at **a** 0° and **d** 80°, [C_8C_1Im][BF_4] at **b** 0° and **e** 80°, [C_8C_1Im] [Pf_2N] at **c** 0° and **f** 80°. **g** Ratio of the C_{alkyl}/C_{hetero} intensities for [C_8C_1Im]Cl, [C_8C_1Im][BF_4] and [C_8C_1Im] [Pf_2N] as a function of emission angle
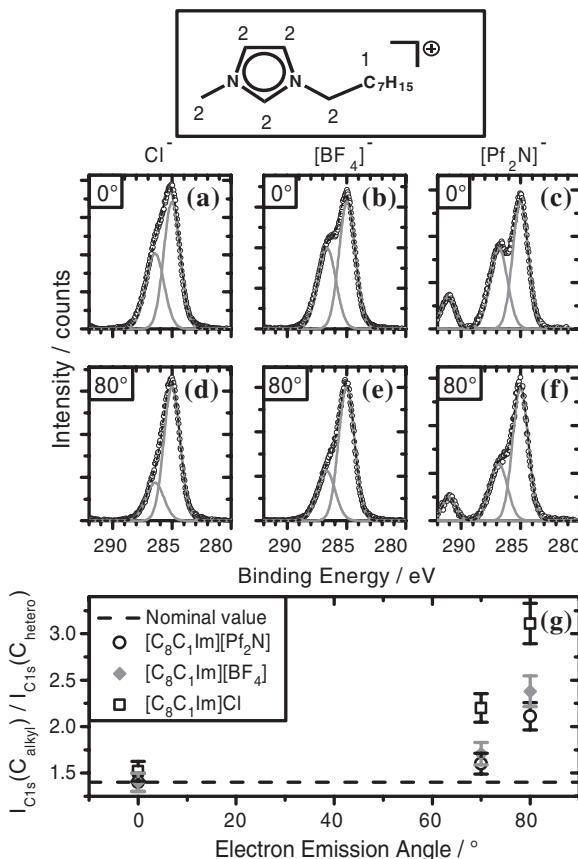
present in the near-surface region than ring carbon atoms. The intensity ratio C_{alkyl}/C_{hetero} at 80° follows the trend: 3.1 for $[C_8C_1Im]Cl$ > 2.4 for $[C_8C_1Im][BF_4]$ > 2.1 for $[C_8C_1Im][Pf_2N]$, as shown in Fig. 3.16g. This trend scales with the size of the anions: most alkyl chains are present for the smallest anion Cl⁻ whereas for the much larger $[Pf_2N]^-$ the surface enrichment of alkyl carbon relative to ring carbon is less pronounced. For all nine ILs studied, the ratio C_{alkyl}/C_{hetero} measured at 80° follows this trend: Cl⁻ ~ Br⁻ > I⁻ > $[PF_6]^-$ ~ $[BF_4]^-$ ~ $[TfO]^-$ > $[Tf_2N]^-$ > $[Pf_2N]^-$ > $[FAP]^-$ (see Table 3.1).

    In order to quantify this observation, the molar volume M/ρ or the molecular volume $M/\rho/N_A$ is used, where M, ρ, N_A are the molar mass, the mass density at room temperature and the Avogadro constant, respectively. It has previously been shown that many key physicochemical properties of ILs can be directly related to molecular volumes [109]; molecular volumes are not only available from measurements but can also be predicted from calculations [3]. The values for molecular volumes of the ILs studied herein, given in Table 3.2, are determined from our own liquid density measurements [110].

    Figure 3.17 shows the intensity ratio C_{alkyl}/C_{hetero} for all ten ILs at 0° and 80° (70° are omitted here), plotted against the molecular volume of the ILs. The error bars for the intensity ratios are ±7 %, representing a conservative estimation for the mean error for all data sets and fitting procedures; the error in the molecular volumes is given by the density measurements (±1.5 %). At 0° (I.D. 7–9 nm) the surface composition of all ten primary ILs investigated was approximately the same as the nominal composition (see also Appendix, Table A2), suggesting that the average of the first seven to nine nanometres corresponds to a homogeneous distribution of cations and anions. The largest enhancement for alkyl carbon is

Table 3.2 Quantitative analysis of the XP spectra of $[C_8C_1Im]X$ for the carbon atoms of the cation

IL	Ratios I(C_alkyl)/I(C_hetero) at			ᵃLiquid density ρ/g cm⁻³	ᵃIL molecular volume/nm³
	0°	70°	80°		
$[C_8C_1Im]Cl$	1.52	2.20	3.11	1.009	0.380
$[C_8C_1Im]Br$	1.47	1.96	3.06	1.169	0.390
$[C_8C_1Im]I$	1.47	2.01	2.74	1.305	0.410
$[C_8C_1Im][NO_3]$	1.49	2.11	3.28	1.065	0.401
$[C_8C_1Im][BF_4]$	1.40	1.71	2.38	1.099	0.426
$[C_8C_1Im][PF_6]$	1.39	1.68	2.35	1.235	0.458
$[C_8C_1Im][TfO]$	1.37	1.69	2.40	1.142	0.501
$[C_8C_1Im][Tf_2N]$	1.36	1.63	2.25	1.311	0.603
$[C_8C_1Im][Pf_2N]$	1.40	1.60	2.11	1.396	0.685
$[C_8C_1Im][FAP]$	1.36	1.66	2.01	1.497	0.711

The experimentally determined ratios of C_{alkyl} relative to C_{hetero} are given; the experimental values are derived from XP spectra taken at 0°, 70° and 80°. Nominal ratio C_{alkyl}/C_{hetero} is 7:5 = 1.4:1. In addition, liquid density values and molecular volumes (determined using liquid density) are shown
ᵃValues taken from Ref. [110]
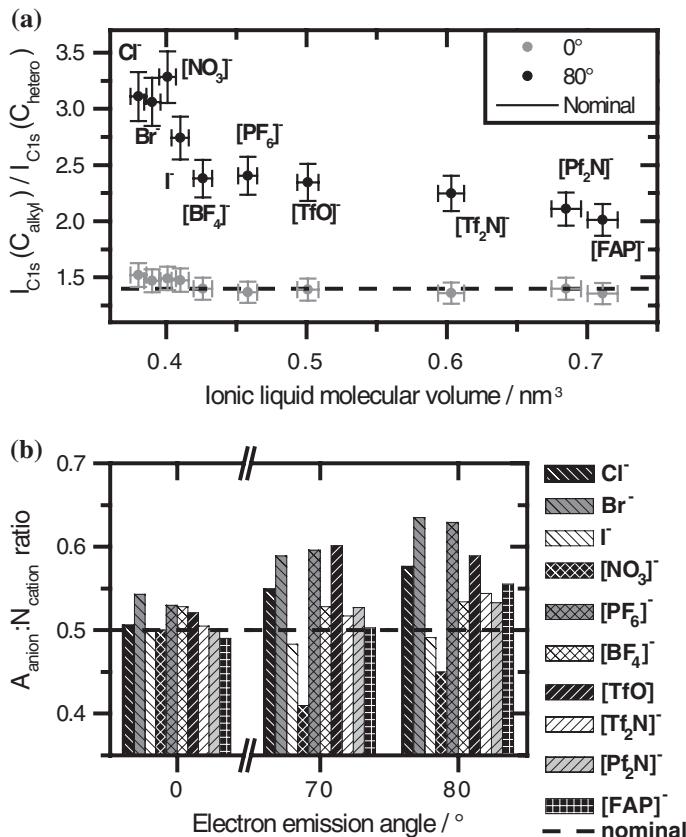
Fig. 3.17 **a** Ratio of the intensities for C_{alkyl}/C_{hetero} for $[C_8C_1Im]X$, recorded under $0°$ (*grey circles*) and $80°$ (*black circles*) emission, against ionic liquid molecular volume (calculated using liquid densities). A line for the nominal ratio (*dashed line*) is also added. **b** Ratios of the intensities $A_{anion}{:}N_{cation}$ for $[C_8C_1Im]X$ (where X = anion, A = element selected from anion X) at different electron emission angles

observed for the smallest anion, Cl^-, and the smallest enhancement is observed for the largest anion, $[FAP]^-$. The amount of enhancement observed is thus clearly correlated with the size of the anion. However, the change in surface enhancement of C_{alkyl} from chloride to iodide (i.e. the halides) is relatively large for a relatively small change in molecular volume. Conversely, the change in surface enhancement of C_{alkyl} from $[BF_4]^-$ to $[FAP]^-$ is relatively small for a relatively large change in molecular volume. To explain the influence of the anion on the degree of octyl chain surface enrichment (which is related to the mean orientation of the cation at the surface) it is proposed that mainly the size of the anion and the strength of the interaction between the charged groups determines how densely packed and well oriented the surface layer is. Therefore, in the case of $[C_8C_1Im]Cl$, the small size of a ion pair allows for a dense packing of the alkyl chains (leading to some

kind of self-assembly due to dispersive interactions of the alkyl chains), therefore leading to a strong enhancement. It should be noted that the surface enrichment of the octyl chains in the case of $[NO_3]^-$ is at least as pronounced as for the smaller Cl^- which might be related to a specific interaction of the planar $[NO_3]^-$ anion with the imidazolium ring, allowing for a well ordered surface structure. For the larger anions, the packing density decreases and the ionic region becomes more diffuse, leading to a loss in order and also reduced enrichment of the octyl chains at the surface. Once the lateral distance between alkyl chains exceeds a certain value, no dispersive interactions are possible and a remarkable drop in alkyl surface enhancement should be observed. Figure 3.17a indeed shows a plateau-like behaviour for ILs from $[BF_4]^-$ onwards.

In order to draw a full picture of the surface composition, anion-related signals were also investigated. Figure 3.17b shows the intensity ratio for one central atom from the anion, labelled A, and the two nitrogen atoms from the imidazolium ring (representing the centre of the polar head group of the cation); the nominal ratio is 0.5 for all ILs studied. Selections for the central atom A of the corresponding anion are Cl, Br, I (halides), N ($[NO_3]^-$, $[Tf_2N]^-$ and $[Pf_2N]^-$), B ($[BF_4]^-$), P ($[PF_6]^-$ and $[FAP]^-$), S ($[TfO]^-$). The signal-to-noise level for the measured ratios is quite low because most excitation cross-sections of elements A are quite small. Additionally, for 70° and 80° measurements, damping of A and N 1s signals by surface alkyl carbon atoms occurs. Overall, the total error bars are estimated to ±10 %. For seven of the ten ILs the A:N intensity ratio shows a weak increase with increasing surface sensitivity. This observation leads to the tentative conclusion that for all the ILs shown the mean centre of the anion in the near-surface region is located nearly at the same (or even slightly shorter) distance from the outer surface as compared to the imidazolium ring, irrespective of the nature of the anion. Jeon et al. have proposed that, using SFG and X-ray reflectivity for $[C_4C_1Im]I$, the anion is located beneath the imidazolium ring [96]. There is no evidence from our data to suggest that the iodide anion, or any other anion, is preferentially located beneath the imidazolium ring; such a scenario would lead to significant damping of the anion signal relative to the cation signal at grazing emission. Jeon et al. also proposed, for $[C_4C_1Im][BF_4]$ and $[C_4C_1Im][PF_6]$, that the anion is located at the same level as the imidazolium ring; this conclusion fits well with the data presented here [96].

A comparison can be directly made between the results obtained herein and by Lockett et al. for $[C_8C_1Im][BF_4]$ [44]. Both experiments show an increase in the amount of C_{alkyl} at increasing surface sensitivity. A smaller ratio, and consequently lower enhancement, was observed by Lockett et al. at 80° emission (about 1.9 as opposed to 2.3 obtained in this work) [44]. This difference is likely due to different fitting procedures employed (fitting either three or one peak for C_{hetero}) and/or different acceptance angles of the corresponding electron analyser.

As noted elsewhere, ARXPS is not very sensitive to detailed geometry effects such as molecular orientation but is instructive for determining depth distribution of certain elements, i.e. the surface composition [41]. Since the systems investigated are liquids, and therefore the surface is mobile and fluid, the data recorded represent an average of the true situation at any time. In the most surface sensitive geometry at

80°, with an information depth of 1–1.5 nm, 65 % of the XPS intensity arises from the first 0.3–0.5 nm, which is below the size of most of the IL ions studied herein. This high surface sensitivity allows one to derive information on the surface composition and to speculate on the arrangement of the molecules in the topmost layer. For all of the ILs in this study, the outer surface is dominated by the presence of alkyl carbon atoms compared to the ILs' nominal composition. The strong implication therefore is that the topmost IL layer consists of cations oriented to a certain degree with the octyl chains preferentially protruding into the vacuum. The corresponding imidazolium rings (i.e. the charged cation head groups) are located below this aliphatic carbon overlayer and at the same (or a slightly larger, see Fig. 3.17b) distance from the outer surface than the centre of the anions (which is expected to coincide roughly with the centre of negative charge).

For the halide ILs, and in particular [C_8C_1Im]Cl, this layered model, as schematically shown in Fig. 3.18, fits our data particularly well, assuming the head groups of the cations and the anions form a confined "ionic sublayer". The degree of packing and, therefore, the density of the polar groups depend on the size of the anions, and, most likely, on the strength of interaction between anion and imidazolium ring: highly coordinating anions such as Cl^- bond more strongly to the imidazolium ring than anions such as [Tf_2N]$^-$ and [FAP]$^-$ [7]. The ionic region is therefore more
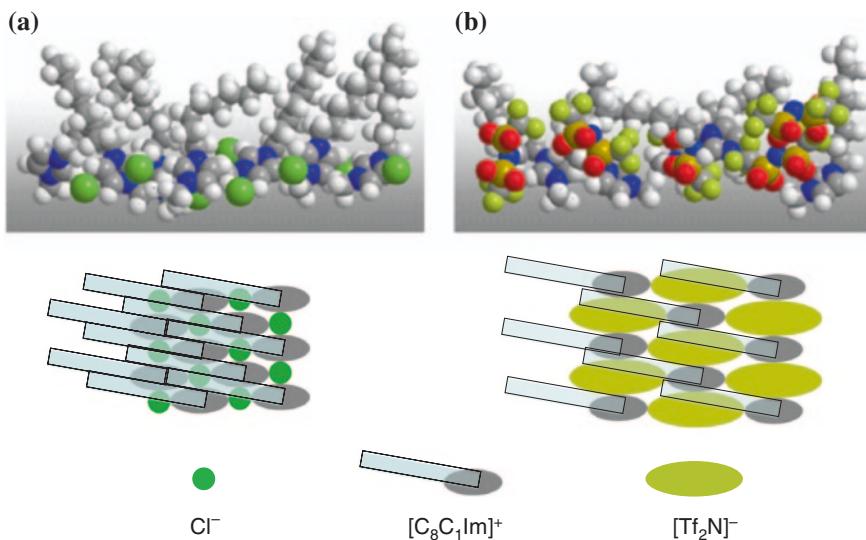
Fig. 3.18 Proposed model of the highly ordered IL-vacuum interface for [C_8C_1Im]Cl (**a**) compared to the [C_8C_1Im][Tf_2N] interface (**b**). For **a** the first molecular layer consists of a well-defined layer of octyl chains protruding to the vacuum with the ionic parts of the cation and the chloride anions buried underneath with no direct contact with the vacuum. For the larger anions such as [Tf_2N]$^-$, the first molecular layer is considerably less ordered so that (at least) the CF_3 groups of the anion still protrude to the vacuum (for details, see text). *Below* are *top-view models* illustrating how the size of the anion influences the packing density (and therefore the amount of alkyl enhancement) of the alkyl chains

ordered and compact for the smaller anions, imposing a dense packing of the aliphatic chains by attractive vdWs interactions between the aliphatic chains in the ILs similar to the situation for alkyl-thiolate self-assembled monolayers adsorbed on surfaces such as Au(111) [111, 112]. In fact, when comparing the damping achieved by the octyl chains in $[C_8C_1Im]Cl$ with C_8-thiol SAMS on an Au(111) substrate, similar values are obtained leading to the conclusion that indeed, for very small anions Cl^-, Br^- and $[NO_3]^-$, a highly associated and oriented alkyl overlayer may be present. For alkyl SAMs on Au(111) a S···S distance of 0.5 nm is found, which is close to the C_8···C_8 chain distance of ~ 0.6 nm for $[C_8C_1Im]Cl$ estimated from the IL molecular volume of $[C_1C_1Im][Cl]$. For the larger anions the interaction between the charged groups (i.e., the imidazolium ring and the anion) is weaker. Within the first molecular layer, the ionic parts of the molecules are consequently not as well confined as for the halides. The resultant higher disorder, and simply the fact that larger anions demand more lateral space in one "unit cell" of ion pairs, results in a reduction in vdWs interactions and in a loss of order for the aliphatic chains. This is shown in Fig. 3.18, where a top-view scheme is presented in which the $[C_8C_1Im]^+$ cation forms an idealised, confined surface structure with both a small spherical and a large, bulky anion, resulting in a highly confined alkyl chain structure for the small anion and an open structure with high degrees of freedom for the alkyl chains in the case of the large anion. It must also be noted that the specific chemical moieties of the anions may orient themselves; for example, the perfluoroalkyl groups of $[Tf_2N]^-$, $[Pf_2N]^-$ and $[FAP]^-$ have been shown to be located closer to the surface than other parts of the anion [41, 113]. Such competing orientation effects are also expected to lead to a loss in surface enrichment of alkyl chains.

Considering the complexity of the system, the proposed model, especially the scheme for larger anions presented in Fig. 3.18 is probably not the only one which is consistent with the experimental findings. As an alternative, one could envisage, for example, inhomogeneous lateral arrangements, with islands of highly oriented alkyl chains, separated by non-ordered regions, the size of which depends on the size of the anion. While we cannot unequivocally rule out such arrangements, our model seems to be the most simple and plausible.

Further evidence for the proposed models discussed here comes from complementary PES work by the Krischok group (TU Ilmenau), who performed UPS and metastable impact electron spectroscopy (MIES) measurements of $[C_nC_1Im]Cl$ (n = 2, 4, 6, 8) [114], and $[C_nC_1Im][Tf_2N]$ [115]. While UPS is a standard tool to investigate the VB structure of compounds, but exhibits slightly higher surface sensitivity than valence band XPS, in MIES only the outermost surface atoms are probed. This ultimate surface sensitivity is achieved by the energy transfer from a metastable excited He* ion to the most proximate surface atom resulting in a "photoelectron". From the MIES data it becomes evident from the absence of a Cl 3p contribution, that for $[C_8C_1Im]Cl$ the outer surface is solely alkyl-terminated, suggesting the existence of a highly confined alkyl overlayer. In contrast, it is found for $[C_8C_1Im][Tf_2N]$ that contributions from both the anion and the cationic head group are still observed in MIES and are therefore present at the outermost surface, further corroborating the models proposed in Fig. 3.18.

3.2.4 Summary

As an extension of previous work on the influence of functionalized and non-function-alized chain substituents on the surface composition of imidazolium-based $[Tf_2N]^-$ ILs, the influence of the anion was systematically investigated here. Also, this study was conducted as an extension to the results presented in Sect. 3.1 addressing the electronic properties of $[C_8C_1Im]^+$ ILs. Thereby, the same ten $[C_8C_1Im]^+$ ILs with anions covering different sizes (ranging from Cl^- to $[FAP]^-$), shapes (from spherical to elongated anions) and coordination abilities (from strongly coordinating halides to weakly coordinating anions with perfluoroalkyl chains) were investigated using ARXPS.

All ILs were free from surface contaminations and no significant beam damage occurred over the time-scale of the ARXPS experiments reported here. At an emission angle of 0°, i.e., for an information depth of 7–9 nm, the measured compositions of all ILs correspond to the nominal stoichiometry, suggesting that on average anions and cations are homogeneously distributed within this region. At 80°, i.e., an information depth of 1.0–1.5 nm, the concomitant rise in C 1s intensity of aliphatic carbon at the expense of all other IL signals unambiguously proves surface enrichment of the octyl chains in the first molecular layer. This enrichment decreases with increasing anion size: it is most pronounced for Cl^- and Br^- and is considerably less distinctive for the larger anions $[Pf_2N]^-$ and $[FAP]^-$. In contrast, no significant surface segregation effects of the anions relative to the imidazolium rings (i.e., the positively charged head group of the cation) occur in the first molecular layer. In other words this observation means that the ionic cation head groups and the anions are located at about the same distance from the outer IL surface, forming a more or less confined polar layer; the IL surface is terminated by the octyl chains to a different degree, depending on anion size. To explain the influence of the anion on the degree of octyl chain surface enrichment (which is related to the mean orientation of the cation at the surface) we propose that mainly the small size of the anion and the strength of the interaction between the polar groups lead to the formation of a densely packed, well oriented surface layer, e.g., in the case of $[C_8C_1Im]Cl$. For the larger anions, the packing density decreases and the ionic region becomes more diffuse, leading to a loss in order and also a reduced enrichment of the octyl chains at the surface.

Based on the fundamental knowledge attained in this chapter the subsequent chapter deals with ultrathin IL films deposited on metal substrates, focusing on aspects such as IL arrangement at the solid interface, surface wetting and subsequent IL growth behaviour, and also scrutinising the electronic interaction of the adsorbate with the solid.

References

1. T. Cremer, C. Kolbeck, K.R.J. Lovelock, N. Paape, R. Wölfel, P.S. Schulz, P. Wasserscheid, H. Weber, J. Thar, B. Kirchner, F. Maier, H.-P. Steinrück, Chem. Eur. J. **16**, 9018 (2010)
2. I. Krossing, J.M. Slattery, C. Daguenet, P.J. Dyson, A. Oleinikova, H. Weingärtner, J. Am. Chem. Soc. **128**, 13427 (2006)

3. U.P.R.M. Preiss, J.M. Slattery, I. Krossing, Ind. Eng. Chem. Res. **48**, 2290 (2009)

4. S. Zahn, F. Uhlig, J. Thar, C. Spickermann, B. Kirchner, Angew. Chem. Int. Ed. **47**, 3639 (2008)

5. J. Thar, M. Brehm, A.P. Seitsonen, B. Kirchner, J. Phys. Chem. B **113**, 15129 (2009)

6. P.A. Hunt, J. Phys. Chem. B **111**, 4844 (2007)

7. P.A. Hunt, I.R. Gould, B. Kirchner, Austr. J. Chem. **60**, 9 (2007)

8. R. Lungwitz, M. Friedrich, W. Linert, S. Spange, New J. Chem. **32**, 1493 (2008)

9. R. Lungwitz, S. Spange, New J. Chem. **32**, 392 (2008)

10. H. Tokuda, S. Tsuzuki, M. Susan, K. Hayamizu, M. Watanabe, J. Phys. Chem. B **110**, 19593 (2006)

11. K. Fumino, A. Wulf, R. Ludwig, Angw. Chem. Intl. Ed. **47**, 8731 (2008)

12. S. Zahn, G. Bruns, J. Thar, B. Kirchner, Phys. Chem. Chem. Phys. **10**, 6921 (2008)

13. K. Fumino, A. Wulf, R. Ludwig, Phys. Chem. Chem. Phys. **11**, 8790 (2009)

14. J.N.C. Lopes, A.A.H. Padua, J. Phys. Chem. B **110**, 19586 (2006)

15. J.N.C. Lopes, J. Deschamps, A.A.H. Padua, J. Phys. Chem. B **108**, 2038 (2004)

16. T. Koddermann, D. Paschek, R. Ludwig, ChemPhysChem **8**, 2464 (2007)

17. B.L. Bhargava, S. Balasubramanian, J. Chem. Phys. **127**, 114510 (2007)

18. T.I. Morrow, E.J. Maginn, J. Phys. Chem. B **106**, 12807 (2002)

19. E.J. Maginn, J. Phys.: Condens. Matter **21**, 373101 (2009)

20. T.G.A. Youngs, C. Hardacre, ChemPhysChem **9**, 1548 (2008)

21. P.A. Hunt, B. Kirchner, T. Welton, Chem. Eur. J. **12**, 6762 (2006)

22. H. Boroudjerdi, Y.W. Kim, A. Naji, R.R. Netz, X. Schlagberger, A. Serr, Phys. Rep. **416**, 129 (2005)

23. H. Tokuda, K. Hayamizu, K. Ishii, M. Susan, M. Watanabe, J. Phys. Chem. B **109**, 6103 (2005)

24. D.R. MacFarlane, M. Forsyth, E.I. Izgorodina, A.P. Abbott, G. Annat, K. Fraser, Phys. Chem. Chem. Phys. **11**, 4962 (2009)

25. V. Kempter, B. Kirchner, J. Mol. Struct. **972**, 22 (2010)

26. A. Elaiwi, P.B. Hitchcock, K.R. Seddon, N. Srinivasan, Y.M. Tan, T. Welton, J.A. Zora, J. Chem. Soc., Dalton Trans. **21**, 3467 (1995)

27. A.G. Avent, P.A. Chaloner, M.P. Day, K.R. Seddon, T. Welton, J. Chem. Soc. Dalton Trans. **23**, 3405 (1994)

28. D. Bankmann, R. Giernoth, Prog. Nucl. Magn. Reson. Spectrosc. **51**, 63 (2007)

29. J. Palomar, V.R. Ferro, M.A. Gilarranz, J.J. Rodriguez, J. Phys. Chem. B **111**, 168 (2007)

30. R. Giernoth, D. Bankmann, N. Schlorer, Green Chem. **7**, 279 (2005)

31. J.P. Armstrong, C. Hurst, R.G. Jones, P. Licence, K.R.J. Lovelock, C.J. Satterley, I.J. Villar-Garcia, Phys. Chem. Chem. Phys. **9**, 982 (2007)

32. D.H. Zaitsau, G.J. Kabo, A.A. Strechan, Y.U. Paulechka, A. Tschersich, S.P. Verevkin, A. Heintz, J. Phys. Chem. A **110**, 7303 (2006)

33. J.P. Leal, J. Esperanca, M.E.M. da Piedade, J.N.C. Lopes, L.P.N. Rebelo, K.R. Seddon, J. Phys. Chem. A **111**, 6176 (2007)

34. S. Krischok, M. Eremtchenko, M. Himmerlich, P. Lorenz, J. Uhlig, A. Neumann, R. Ottking, W.J.D. Beenken, O. Höfft, S. Bahr, V. Kempter, J.A. Schäfer, J. Phys. Chem. B **111**, 4801 (2007)

35. O. Höfft, S. Bahr, M. Himmerlich, S. Krischok, J.A. Schäfer, V. Kempter, Langmuir **22**, 7120 (2006)

36. T. Nishi, T. Iwahashi, H. Yamane, Y. Ouchi, K. Kanai, K. Seki, Chem. Phys. Lett. **455**, 213 (2008)

37. S. Caporali, U. Bardi, A. Lavacchi, J. Electron. Spectrosc. Rel. Phenom. **151**, 4 (2006)

38. E.F. Smith, F.J.M. Rutten, I.J. Villar-Garcia, D. Briggs, P. Licence, Langmuir **22**, 9386 (2006)

39. J.M. Gottfried, F. Maier, J. Rossa, D. Gerhard, P.S. Schulz, P. Wasserscheid, H.-P. Steinrück, Z. Phys, Chem. **220**, 1439 (2006)

40. C. Kolbeck, M. Killian, F. Maier, N. Paape, P. Wasserscheid, H.-P. Steinrück, Langmuir **24**, 9500 (2008)

41. K.R.J. Lovelock, C. Kolbeck, T. Cremer, N. Paape, P.S. Schulz, P. Wasserscheid, F. Maier, H.-P. Steinrück, J. Phys. Chem. B **113**, 2854 (2009)
42. E.F. Smith, I.J. Villar Garcia, D. Briggs, P. Licence, Chem. Commun. **45**, 5633 (2005)
43. D.S. Silvester, T.L. Broder, L. Aldous, C. Hardacre, A. Crossley, R.G. Compton, Analyst **132**, 196 (2007)
44. V. Lockett, R. Sedev, C. Bassell, J. Ralston, Phys. Chem. Chem. Phys. **10**, 1330 (2008)
45. T. Cremer, M. Killian, J.M. Gottfried, N. Paape, P. Wasserscheid, F. Maier, H.-P. Steinrück, ChemPhysChem **9**, 2185 (2008)
46. Q.H. Zhang, S.M. Liu, Z.P. Li, J. Li, Z.J. Chen, R.F. Wang, L.J. Lu, Y.Q. Deng, Chem. Eur. J. **15**, 765 (2009)
47. N. Paape, W. Wei, A. Bosmann, C. Kolbeck, F. Maier, H.-P. Steinrück, P. Wasserscheid, P.S. Schulz, Chem. Commun. **33**, 3867 (2008)
48. I. Lindgren, J. Electron. Spectrosc. Rel. Phenom. **137**, 59 (2004)
49. F. Maier, J.M. Gottfried, J. Rossa, D. Gerhard, P.S. Schulz, W. Schwieger, P. Wasserscheid, H.-P. Steinrück, Angw. Chem. Intl. Ed **45**, 7778 (2006)
50. C. Kolbeck, T. Cremer, K.R.J. Lovelock, N. Paape, P.S. Schulz, P. Wasserscheid, F. Maier, H.-P. Steinrück, J. Phys. Chem. B. **113**, 8682 (2009)
51. F. Maier, T. Cremer, C. Kolbeck, K.R.J. Lovelock, N. Paape, P.S. Schulz, P. Wasserscheid, H.-P. Steinrück, Phys. Chem. Chem. Phys. **12**, 1905 (2010)
52. S. Krischok, R. Ottking, W.J.D. Beenken, M. Himmerlich, P. Lorenz, O. Höfft, S. Bahr, V. Kempter, J.A. Schäfer, Z. Phys. Chem. **220**, 1407 (2006)
53. N.V. Plechkova, K.R. Seddon, Chem. Soc. Rev. **37**, 123 (2008)
54. Bruker-Almanac, Bruker BioSpin (2009), (http//www.bruker.com)
55. R. Ahlrichs, M. Bar, M. Haser, H. Horn, C. Kolmel, Chem. Phys. Lett. **162**, 165 (1989)
56. A.D. Becke, Phys. Rev. A **38**, 3098 (1988)
57. C. Lee, W. Yang, R.G. Parr, Phys. Rev. B **37**, 785 (1988)
58. S. Grimme, J. Comput. Chem. **27**, 1787 (2006)
59. E.I. Izgorodina, U.L. Bernard, D.R. MacFarlane, J. Phys. Chem. A **113**, 7064 (2009)
60. S. Zahn, B. Kirchner, J. Phys. Chem. A **112**, 8430 (2008)
61. A.E. Reed, R.B. Weinstock, F. Weinhold, J. Chem. Phys. **83**, 735 (1985)
62. A.E. Reed, L.A. Curtiss, F. Weinhold, Chem. Rev. **88**, 899 (1988)
63. M.J. Frisch, *Gaussian 94 (rev. C.2)*. (Gaussian Inc., Wallingford, 2004)
64. A.P. Fröba, H. Kremer, A. Leipertz, J. Phys. Chem. B **112**, 12420 (2008)
65. K.R.J. Lovelock, E.F. Smith, A. Deyko, I.J. Villar-Garcia, P. Licence, R.G. Jones, Chem. Commun. **46**, 4866 (2007)
66. NIST, X-ray Photoelectron Spectroscopy Database, Version 3.5, (National Institute of Standards and Technology, Gaithersburg, 2003). (http://srdata.nist.gov/xps/NIST)
67. J.N.C. Lopes, A.A.H. Padua, J. Phys. Chem. B. **110**, 3330 (2006)
68. W. Jiang, Y.T. Wang, T.Y. Yan, G.A. Voth, J. Phys. Chem. C **112**, 1132 (2008)
69. K. Fumino, A. Wulf, R. Ludwig, Angew. Chem. Int. Ed. **47**, 3830 (2008)
70. R. Lungwitz, V. Strehmel, S. Spange, New J. Chem. **34**, 1135 (2010)
71. A. Wulf, K. Fumino, R. Ludwig, Angew. Chem. Int. Ed. **49**, 449 (2010)
72. P. Bonhote, A.P. Dias, N. Papageorgiou, K. Kalyanasundaram, M. Grätzel, Inorg. Chem. **35**, 1168 (1996)
73. U. Gelius, P.F. Heden, J. Hedman, B.J. Lindberg, R. Marine, R. Nordberg, C. Nordling, K. Siegbahn, Phys. Scr. **2**, 70 (1970)
74. W.F. Egelhoff Jr, Surf. Sci. Rep. **6**, 253 (1987)
75. P.H. Citrin, T.D. Thomas, J. Chem. Phys. **57**, 4446 (1972)
76. J.M. Benson, I. Novak, A.W. Potts, J. Phys. B: At. Mol. Phys. **20**, 6257 (1987)
77. S.P. Kowalczyk, F.R. Feely, L. Ley, R.A. Pollack, D.A. Shirley, Phys. Rev. B **9**, 3573 (1974)
78. B. Kirchner, *Topics in Current Chemistry*, vol. 290. (Springer, New York, 2010)
79. P.A.Z. Suarez, S. Einloft, J.E.L. Dullius, R.F. d. Souza, J. Dupont, J. Chim. Phys. Phys. Chim. Biol. **95**, 1626 (1998)
80. T. Heine, C. Corminboeuf, G. Seifert, Chem. Rev. **105**, 3889 (2005)

81. K.B. Wiberg, J.D. Hammer, T.A. Keith, K. Zilm, J. Phys. Chem. A **103**, 21 (1999)
82. A.J. Arduengo, D.A. Dixon, K.K. Kumashiro, C. Lee, W.P. Power, K.W. Zilm, J. Am. Chem. Soc. **116**, 6361 (2002)
83. M. Hesse, H. Meier, B. Zeeh, in *Spectroscopic Methods in Organic Chemistry*, 2nd ed. (Thieme, Stuttgart, New York, 2007)
84. J.L. Anderson, D.W. Armstrong, G.T. Wei, Anal. Chem. **78**, 2892 (2006)
85. P. Sun, D.W. Armstrong, Anal. Chim. Acta **661**, 1 (2010)
86. J. Dupont, J.D. Scholten, Chem. Soc. Rev. **39**, 1780 (2010)
87. O. Höfft, F. Endres, Phys. Chem. Chem. Phys. **13**, 13472 (2011)
88. P.J. Carvalho, M.G. Freire, I.M. Marrucho, A.J. Queimada, J.A.P. Coutinho, J. Chem. Eng. Data **53**, 1346 (2008)
89. G. Law, P.R. Watson, A.J. Carmichael, K.R. Seddon, B. Seddon, Phys. Chem. Chem. Phys. **3**, 2879 (2001)
90. T.J. Gannon, G. Law, P.R. Watson, A.J. Carmichael, K.R. Seddon, Langmuir **15**, 8429 (1999)
91. C.S. Santos, S. Baldelli, J. Phys. Chem. B **111**, 4715 (2007)
92. T. Iimori, T. Iwahashi, K. Kanai, K. Seki, J.H. Sung, D. Kim, H.O. Hamaguchi, Y. Ouchi, J. Phys. Chem. B **111**, 4860 (2007)
93. C. Aliaga, S. Baldelli, J. Phys. Chem. B **111**, 9733 (2007)
94. C.S. Santos, S. Baldelli, J. Phys. Chem. C **112**, 11459 (2008)
95. C. Aliaga, G.A. Baker, S. Baldelli, J. Phys. Chem. B **112**, 1676 (2008)
96. Y. Jeon, J. Sung, W. Bu, D. Vaknin, Y. Ouchi, D. Kim, J. Phys. Chem. C **112**, 19649 (2008)
97. C.S. Santos, S. Baldelli, J. Phys. Chem. B **113**, 923 (2009)
98. J. Bowers, M.C. Vergara-Gutierrez, J.R.P. Webster, Langmuir **20**, 309 (2004)
99. E. Solutskin, B.M. Ocko, L. Taman, I. Kuzmenko, T. Gog, M. Deutsch, J. Am. Chem. Soc. **127**, 7796 (2005)
100. V. Halka, R. Tsekov, W. Freyland, Phys. Chem. Chem. Phys. **7**, 2038 (2005)
101. Y.F. Yano, H. Yamada, Anal. Sci. **24**, 1269 (2008)
102. R.M. Lynden-Bell, M. Del Popolo, Phys. Chem. Chem. Phys. **8**, 949 (2006)
103. W. Jiang, T.Y. Yan, Y.T. Wang, G.A. Voth, J. Phys. Chem. B **112**, 3121 (2008)
104. C. Aliaga, C.S. Santos, S. Baldelli, Phys. Chem. Chem. Phys. **9**, 3683 (2007)
105. S. Rivera-Rubero, S. Baldelli, J. Phys. Chem. B **110**, 4756 (2006)
106. G. Law, P.R. Watson, Chem. Phys. Lett. **345**, 1 (2001)
107. V. Lockett, R. Sedev, S. Harmer, J. Ralston, M. Horne, T. Rodopoulos, Phys. Chem. Chem. Phys. **12**, 13816 (2010)
108. F. Bresme, M. Gonzalez-Melchor, J. Alejandre, J. Phys. Condens. Matter **17**, 3301 (2005)
109. J.M. Slattery, C. Daguenet, P.J. Dyson, T.J.S. Schubert, I. Krossing, Angew. Chem. Int. Ed. **46**, 5384 (2007)
110. C. Kolbeck, J. Lehmann, K.R.J. Lovelock, T. Cremer, N. Paape, P. Wasserscheid, A.P. Fröba, F. Maier, H.-P. Steinrück, J. Phys. Chem. B **114**, 17025 (2010)
111. F. Schreiber, J. Phys. Condens. Matter **16**, 881 (2004)
112. D.P. Woodruff, Phys. Chem. Chem. Phys. **10**, 7211 (2008)
113. T. Iwahashi, T. Miyamae, K. Kanai, K. Seki, D. Kim, Y. Ouchi, J. Phys. Chem. B **112**, 11936 (2008)
114. A. Ulbrich, M. Reinmöller, W.J.D. Beenken, S. Krischok, Chem. Phys. Chem. **13**, 1718 (2012)
115. M. Reinmöller, A. Ulbrich, T. Ikari, J. Preiss, O. Höfft, F. Endres, S. Krischok, W.J.D. Beenken, Phys. Chem. Chem. Phys. **13**, 19526 (2011)

Chapter 4
Ionic Liquid/Metal Interfaces

The content of this chapter is based on the following publications [1, 2]:

The Liquid/Solid Interface of Ultrathin Ionic Liquid Films: [C₁C₁Im][Tf₂N] and [C₈C₁Im][Tf₂N] on Au(111) [1].
Ultrathin Layers of the Ionic Liquid [C₁C₁Im][Tf₂N] on Ni(111)—Growth, Interfacial Arrangement and Reactivity [2].

The previous chapter addressed both bulk- (Sect. 3.1) and surface-related (Sect. 3.2) IL properties. The IL/solid interface is the third main subject investigated in this thesis. Compared to the previous aspects of IL research, the IL/solid interface is the least explored, as reflected by the small number of fundamental studies available. To gain detailed information on the electronic interaction between IL and support material, and to determine properties such as growth behaviour and molecular arrangement at the surface, ultrathin IL films can be deposited in ultrahigh vacuum by IL-PVD, see Chap. 2. The resulting films with thicknesses of only a few nanometres, or even in the sub-monolayer regime, allow direct access to the unadulterated (i.e., not affected by bulk IL on top of the interface layer) IL/solid interface by surface-sensitive spectroscopic methods such as ARXPS. In this chapter, ultrathin IL films were produced by IL-PVD on two different metal supports, namely the (111)-faceted surfaces of Au and Ni single crystals. Questions related to arrangement of the IL ions at the solid interface, surface wetting and subsequent IL growth behaviour, as well as electronic interaction between adsorbate and solid, were addressed. In the first study, three different ILs deposited on an Au(111) surface were investigated using ARXPS. Later, IL films prepared on a more reactive system, namely a Ni(111) surface, were examined, also with respect to the interaction of the IL with oxygen-precovered and oxidized Ni surfaces. Furthermore, surface reactivity of IL-precovered Ni(111) with oxygen was investigated to gain fundamental insights into aspects related to surface passivation of reactive surfaces after IL-impregnation.

4.1 General Considerations

Bulk properties of ILs have been extensively studied over the last two decades [3, 4]. More recently, the interfaces of ILs with other media such as the liquid/liquid, liquid/gas and liquid/vacuum have attracted considerable attention (for a detailed discussion and references, please see Chap. 1 and Sect. 3.2). The IL/solid interface, however, has only very recently become the focus of research activities, despite its importance in many practical applications: For all liquid/solid interface-controlled processes, a detailed understanding of the chemical structure, coordination behaviour, reactivity, stability and also phase transitions of ILs at the solid surfaces is of pivotal relevance. Examples are engineering [5], analytical chemistry [6, 7] nanoparticle synthesis [8, 9], nanocomposites [10], and solar cells [11, 12]. Additionally, ILs are extensively used in electrochemical and battery research (both as electrolytes and as modifier of the electrode) [13]. There, interfacial effects such as electric double layer (EDL) formation, adsorption and deposition at the electrodes, and charge transfer processes at the electrode–electrolyte interface are important issues for enhancing device performance. As an example, for the electrodeposition of Si and Ge from IL solutions, solvation layers at the electrochemically polarized interface play a crucial role [14]. Finally, certain ILs are found to provide corrosion protection for metal alloys [15]. An understanding of the interaction between IL and the alloy surface, as well as the chemical nature of the resulting film, will allow for a more controlled design of ILs in the production of uniform protective films or advanced lubricants. With respect to advanced catalytic materials, two new concepts, namely "Supported Ionic Liquid Phase" (SILP) catalysis [16, 17] and the "Solid Catalyst with Ionic Liquid Layer" (SCILL) system [18, 19], have been developed and were discussed in Chap. 1. A modification of the SCILL system not mentioned thus far, is, to render an air-sensitive catalyst easier to handle at ambient conditions by a protective IL layer. This concept was introduced by the Wasserscheid group, who coated Raney-nickel with IL and observed a reduction in pyrophoric character, while the catalytic activity remained mainly unchanged [20]. While the importance of the IL/gas interface and of IL bulk properties was highlighted in the previous chapter, it is stressed again here that the IL/solid interface considerably contributes to the overall properties of these catalytic systems [21]. Therefore, the presently small number of fundamental studies addressing the IL/solid interface does not reflect the importance of this research area but epitomises its infancy.

Various methods have been applied for the investigation of the IL/solid interface buried under a macroscopically thick IL film. It has been shown by atomic force microscopy (AFM) that in the vicinity of single crystal surfaces such as Au(111), mica, and graphite, ordered IL layers are formed, with the degree of layer ordering strongly dependent on the chemical structure of the IL and the nature of the solid surface [22]. Thereby, a rather strong interaction between the Au(111) surface and $[C_4C_1Pyrr][Tf_2N]$ is observed, as compared to, for example, $[C_2C_1Im][Tf_2N]$ [14, 22]. The increased layer penetration forces of the AFM tip in distance-force-measurements at the IL-metal interface are tentatively assigned to a stronger interaction

of the Au(111) surface with the more localized charge at the pyrrolidinium cation, as opposed to the delocalized charge in case of imidazolium ILs. In a current study using AFM, STM and electrochemical impedance spectroscopy, an anion-enriched interface layer is proposed for positive surface potential, while a cation-enriched surface layer is observed for open circuit potential (OCP) and also for negative potentials [23]. Some of these conclusions are corroborated by X-ray reflectivity studies [24, 25], where Mezger et al. deduced a vertical bi-layer structure on the polar Sapphire(0001) surface. Also, various theoretical investigations addressing the IL/solid interface of bulk ILs yield similar results, i.e., ordered layers in the vicinity of the interface [26–33]. With respect to the IL layer directly at the IL/solid interface, SFG measurements by the Conboy [34, 35], Baldelli [11, 36–40] and Ouchi [41] groups revealed that the IL ions exhibit distinct geometries and seem to be well-ordered at the interface. Furthermore, some of these studies showed that at the electrified IL/metal interface preferential ionic adsorption and charge-dependent reorientation can occur. Further evidence for well-ordered interface layers is provided by in situ STM measurements by the Freyland group and Su et al. who find ordered interface structures but also rearrangement of the IL at the surface depending on the applied electrochemical potential [42–44]. Very recently, alternating anion-cation layering between mica surfaces was reported, which strongly depends on the chemical nature of the IL [45].

A different approach to obtain a better understanding of the IL/solid interface is to investigate thin IL layers with thicknesses in the order of only several nanometres or even in the sub-monolayer regime. In AFM studies of thin IL films drop-cast onto various support materials Bovio et al. found solid-like structures on oxide supports and a more liquid-like behaviour on highly ordered pyrolytic graphite (HOPG) [30, 46]. As mentioned in Chap. 2 it has been shown by Earle et al. that—despite their very low (nearly negligible at room temperature) vapour pressure—a number of aprotic ILs can be evaporated without decomposition by heating in vacuum. In an extended TPD study Armstrong et al. found that the IL vapour consists of neutral ion pairs (NIPs) [47]. Based on these findings our group recently established a process denoted as physical vapour deposition of ILs (IL-PVD) that allows access to the IL/solid interface by means of surface sensitive techniques [48]. This IL-PVD approach opens up an entire new field of UHV-based IL research: well-established methods for in situ sample preparation under ultra-clean conditions can be applied and extremely well-defined systems can be investigated. When studying these ultrathin IL layers by ARXPS, detailed information on the initial stages of IL growth, wetting behaviour, the arrangement of the ions at the IL/solid interface, and the electronic interactions between IL and support can be derived. In a preliminary study (see also Sect. 5.3.1), the IL/glass interface was investigated and a bilayer structure was found for low coverages within the first IL adsorption layer. IL growth was found to proceed in a Stranski–Krastanov-like manner, where the completion of one wetting layer is followed by 3D island growth for higher coverages [49]. In recent infrared-reflection–absorption-spectroscopy (IRAS) studies Sobota et al. used the IL-PVD approach to investigate thin $[C_4C_1Im][Tf_2N]$ layers on a well-defined Al_2O_3 support and

on catalytically active model systems containing Pd and Pt nanoparticles. They found distinct orientations of the ions at the Al_2O_3 surface and deduced preferential adsorption sites (step-edges for Pd, (111) facets for Pt) and ligand effects (in case of Pt) resulting from specific electronic interactions between the IL and the catalytically active nanoparticles [50–52]. Finally, first STM investigations on IL-PVD films for an IL/Au(111) interface by the Behm group show a low degree of lateral ordering of $[C_4C_1Pyrr][FAP]$ [53], while in a recent Å-resolution X-ray study a checkerboard arrangement is proposed for Langmuir films of the same IL on mercury [54].

The consecutive discussion of experimental aspects is followed by the results section, in which first thin IL films of three different ILs deposited on an Au(111) single crystal are presented. Later, the experiments on thin IL films deposited on a Ni(111) substrate are discussed before the findings on IL/metal interfaces are summarized leading over to Chap. 5, where IL-PVD was used to investigate the nature of the IL/glass interface.

4.2   Experimental Aspects

Single Cystals: The Au(111) single crystal with a size of $11 \times 11 \times 2$ mm^3 was purchased from MaTecK (Ch.Nr. 0807289, purity 99.999 %, one side polished and aligned to the (111) plane to better than 0.1°). It was mounted on a Mo sample holder and fixed with two Ta wires. Surface preparation was performed by sputtering with 600 eV Ar$^+$ ions, followed by annealing at ~800 K. Sample cleanliness was checked by XPS, while long range surface order was verified with LEED, in which the typical $(23 \times \sqrt{3})$ herringbone reconstruction was observed. The substrate temperature during IL deposition and XPS was between 290 and 320 K (RT and slightly above).

The Ni(111) single crystal with a size of $11 \times 11 \times 2$ mm^3 was purchased from MaTecK (Ch.Nr. 10072815, purity 99.99 %, one side polished and aligned to the (111) plane better than 0.1°). The crystal was mounted on a Mo sample holder with two Ta wires. Surface preparation was performed by sputtering with 1 keV Ar$^+$ ions, followed by annealing at ~1100 K on a LN_2 cooled manipulator (LN_2 cooling is vital for sample preparation as fast cooling rates are necessary after annealing of the crystal to avoid surface segregation of impurities). Sample cleanliness and long range surface order were checked by XPS and LEED, respectively. The substrate temperature during IL deposition was 220 ± 20 K, during XPS as low as 160 K.

Ionic liquid Thin Films: Two ILs, $[C_1C_1Im][Tf_2N]$ and $[C_8C_1Im][Tf_2N]$, were synthesized under ultra-clean conditions, according to previous publications [55], and $[C_4C_1Pyrr][Tf_2N]$ was purchased from IoLiTec and used without further purification. IL films were prepared by thermal evaporation of the IL using a modified high-temperature Knudsen cell for organic materials (TECTRA WKC3), see Chap. 2. The temperature of the crucible was regulated by a EUROTHERM 2261 controller with

an accuracy of ± 1 K using a type-K thermocouple. For evaporation, approximately 1 mL of the corresponding IL was placed in a PBN crucible fitted to the evaporator. This setup was mounted to the UHV system and—to avoid bubbling of the IL—slowly evacuated to UHV followed by baking of the evaporator unit (~120 °C). Prior to evaporation, the IL was further degassed and purified by keeping the sample ~30 K below the evaporation temperature for several hours at a base pressure of ~1×10^{-9} mbar. The evaporation temperatures were 420 K for [C$_8$C$_1$Im][Tf$_2$N], 440 K for [C$_4$C$_1$Pyrr][Tf$_2$N] and 420–440 K [C$_1$C$_1$Im][Tf$_2$N], depending on the deposition rate. The evaporation rates were monitored by QCM measurements in order to guarantee constant IL fluxes (found to be constant for all experiments apart from [C$_1$C$_1$Im][Tf$_2$N] on Au(111)). Film thicknesses d were determined by analysis of the damping of the substrate Au 4f levels by rearranging Eq. (2.4) to

$$d = ln \left({I_0}/{I_d} \right) \cdot \lambda \cdot \cos \vartheta \tag{4.1}$$

The film thickness is given in monolayers (ML), where 1 ML of IL is referred to as one closed layer of ION PAIRS, vertically arranged on top of each other; possible arrangements of the ion pairs which are consistent with this definition, are illustrated in Scheme 4.1a. According to this definition one closed layer of ions covering the surface in a checkerboard arrangement, as shown in Scheme 4.1b, corresponds to a coverage of 0.5 ML.

The height h of 1 ML is approximated from the IL bulk molecular volume V_m, using

$$h = \sqrt[3]{V_m} = \sqrt[3]{\frac{M/N_A}{\rho}} \tag{4.2}$$
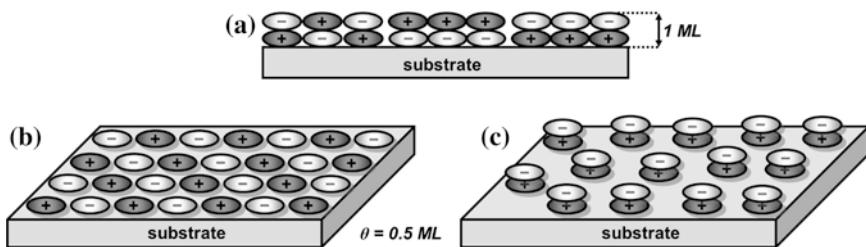
Scheme 4.1 **a** Schematic illustration of the arrangement of ion pairs in the first ML of IL deposited on an Au(111) substrate; according to Ref. [49]. Note that the definition of 1 ML is independent of possible arrangements of the IL ions at the surface which can be, e.g., alternating/disordered (*left*) or in a layered geometry with the cations (*middle*) or the anions (*right*) preferentially adsorbed at the surface. **b** Closed layer of alternating cations and anions in a checkerboard-like arrangement, corresponding to a coverage of 0.5 ML. **c** Nominal coverage of 0.5 ML for a case, where a bilayer structure is preferred. Here, the surface is fully covered at a coverage of 1 ML

Table 4.1 Molar mass (M), mass density (ρ; at $T = 298.15$ K), molecular volume (V_m), ion pair height (h_{ML}) and enthalpy of vaporisation (ΔH_{vap}), for all ILs evaporated in this thesis ([C$_2$C$_1$Im] [Tf$_2$N] is used in Chap. 5)

Ionic liquid	M/g mol^{-1}	ρ/g cm^{-3}	V_m/g mol^{-1}	h_{ML}/nm	ΔH_{vap}/kJ mol^{-1}
[C$_1$C$_1$Im][Tf$_2$N]	377.29	1.567	0.400	0.73	n. a.
[C$_8$C$_1$Im][Tf$_2$N]	475.47	1.311	0.603	0.84	149 ± 2[a]
[C$_4$C$_1$Pyrr][Tf$_2$N]	422.41	1.394	0.503	0.80	152 ± 3[b]
[C$_2$C$_1$Im][Tf$_2$N]	391.31	1.518	0.428	0.75	134 ± 2[a]

[a]Value taken from Ref. [47]; [b]Value taken from Ref. [56]

The respective values for molar mass M, mass density ρ and molecular volume V_{mol} are taken from Ref. [57], and are summarized in Table 4.1 along with the experimental ΔH_{vap} values, from Refs. [47, 56].

X-ray induced beam damage effects play a crucial role when studying ILs [58, 59]. This is particularly the case for ultrathin IL films as will be shown in Sect. 4.3.1.5). Therefore, each IL film was freshly prepared on the Au(111) surface and measured only for about 1 h, in order to minimize radiation-induced changes. After each measurement, the IL film was completely removed by ion sputtering, the Au(111) surface was restored by annealing, and a new IL film was deposited. The same procedure was followed for the experiments conducted on Ni(111).

IL Growth Analysis: The growth mode of a deposited material on a substrate can be determined by analysis of the attenuation of a substrate-derived signal, in our case the Au 4f and Ni 2p$_{3/2}$ peak intensity. For this study, IMFP values of $\lambda = 1.6$ and 3 nm were used for Ni 2p$_{3/2}$ and Au 4f electrons, respectively (kinetic energies of 630 eV for Ni 2p$_{3/2}$ and 1400 eV for Au 4f), as has been reported for organic materials of densities similar to [C$_n$C$_1$Im] [Tf$_2$N] (uncertainty in λ ± 10 %) [60]. In case of ideal two-dimensional growth, also denoted as layer-by-layer growth (i.e., the full completion of a layer is achieved before a new layer starts to grow on top), the substrate signal is expected to decrease with increasing amount of IL in a sectionwise linear fashion from the start of a new layer up to its completion [61, 67]. With increasing number of the layers the absolute value of the (negative) slope of these sections decreases. The intensity decrease of the Ni 2p$_{3/2}$ signal after completion of successive layers, $I_{d(n)}$, follows an exponential decay, as given in Eq. (4.3).

$$\frac{I_{d(n)}}{I_0} = \exp\left(\frac{d(n)}{\lambda(E_{kin}).cos\vartheta}\right) \qquad (4.3)$$

with I_0 being the Ni 2p$_{3/2}$ intensity measured for the clean surface, $d(n)$ the total film thickness of n completed layers, ϑ the emission angle with respect to the surface normal, and $\lambda(E_{kin})$ the inelastic mean free path of the respective substrate signal electrons. The ultimate proof for two-dimensional growth is obtained, when the data derived from a fit of the data to Equation (4.3) at one angle (e.g., 0°) can be used to predict the behaviour at other angles (e.g., 80° in our case) [1]. This latter approach can also be used, when the number of data points or the signal to-noise-ratio of the substrate signals are not good enough to differentiate a sectionwise

linear decrease for perfect layer-by-layer growth from an overall continuous expo-
nential decrease: if the deposition time dependence at 80° can be reproduced with
the same set of parameters used for the 0° data, taking only the cosine of 80° into
account, this is a clear indication for layer-by-layer growth, as will be discussed in
more detail in the results section. A less pronounced decay of the substrate signals
in grazing emission compared to the damping calculated from Equation (4.3) then
indicates a deviation from perfect layer-by-layer growth. One should note here that
for high emission angles and strong damping some deviations from Equation (4.3)
are expected due to neglecting elastic scattering effects [68].

Furthermore, the increase of the IL signals can be used to further analyse the
growth behaviour, according to Equation (4.4)

$$\frac{I_{d(n)}}{I_\infty} = 1 - \exp\left(\frac{d(n)}{\lambda(E_{kin}).cos\vartheta}\right) \tag{4.4}$$

with I_∞ being the IL signal intensity of an infinitely thick IL layer, $d(n)$ the total
film thickness of n completed layers, ϑ the emission angle with respect to the sur-
face normal, and $\lambda(E_{kin})$ the inelastic mean free paths of corresponding IL-related
core level electrons.

XPS measurements and Data Analysis: XP spectra were measured with the
VG Scienta R3000 electron analyser and non-monochromatized Al-K_α radiation
(hν = 1486.6 eV) generated by the VG Escalab 200 X-ray source at a power of
150 W (U = 15 kV, I = 10 mA) in case of the Au(111) experiments. For Ni(111)
the new Specs XR 50 x-ray gun was used at a power of ~240 W (U = 12.5 kV,
I = 19 mA). Survey spectra were taken with a pass energy of 200 eV, while all
detailed core level spectra were recorded with a pass energy of 100 eV, result-
ing in an overall resolution of ~0.9 eV. Due to the inelastic mean free path of about
1.6–3 nm of photoelectrons in organic compounds [60, 62] at the kinetic energies
used (~600–1300 eV), measurements at 0° emission average over several layers of
the near-surface region (information depth, ID: 5–9 nm, depending on the kinetic
energy); at 80° emission approximately the first 1–1.5 nm of the sample are probed.
As the Au 4f and Ni 2p$_{3/2}$ signals were used for thickness determination according to
Eq. (4.1), different IMFP values of 3 nm (Au) and 1.6 nm (Ni) were used due to the
largely different kinetic energy of the respective photoelectrons, according to Refs.
[60, 62]. For the ultrathin films on Au(111) all BEs (apart from macroscopically
thick films, see below) reported are referenced to the Au 4f$_{7/2}$ signal at 83.85 eV,
while for the Ni(111) experiments all spectra are referenced to the Fermi edge.
The BEs for the macroscopically thick IL films are reported as measured due to the
absence of a reference level. In contrast to earlier publications by our group [49, 55,
56, 58, 63–67], the spectra were analysed using the software CasaXPS, employing
a symmetric pseudo-Voigt function with a G:L ratio of 70:30. Compared to ear-
lier fitting procedures using the multi-peak fitting tool of Origin 7.5, where only a
Gaussian lineshape was available, the pseudo-Voigt function leads to somewhat
better fits, but does not affect the quantitative analysis (differences are well below
the margins of error). The C 1s spectra of [C$_8$C$_1$Im][Tf$_2$N] and [C$_4$C$_1$Pyrr][Tf$_2$N]

were fitted with the constraints that fwhm(C_{hetero}) is equal to $1.11 \times$ fwhm(C_{alkyl}) and $0.92 \times$ fwhm(C_{alkyl}), respectively. When fitting the N 1s region, the constraint of equal fwhm values for both signals was used. For IL-related F 1s, O 1s, N 1s and S 2p regions a 2-point linear background subtraction was used, whereas for the C 1s region a 3-point linear background subtraction was applied. The Au 4f and Ni $2p_{3/2}$ regions were analysed using a Shirley background subtraction and numerical integration. To compare the thin film data of the Au(111) experiments to that of a macroscopically thick film, a droplet of about 0.1 mL of IL was deposited onto the Au(111) crystal under ambient conditions and then introduced into the UHV system. For preparation of a macroscopically thick film on clean Ni(111), a small amount of about 0.1 mL of IL, degassed and stored for several hours under UHV conditions, was directly deposited onto the freshly prepared Ni(111) crystal within the UHV system to avoid re-contamination of the Ni(111) surface.

4.3 Results and Discussion

4.3.1 The Ionic Liquid/Gold Interface

Besides serving as a model system from which fundamental insights into the IL/metal interface can be gained, the IL/Au interface is actually application-relevant as it is of importance to research fields such as nanoparticle synthesis and electrochemistry [8, 68, 69]. By investigating a model system, where usually only relatively weak physisorption takes place, first insights into the initial stages of IL growth, electronic interactions and molecular arrangement at the interface can be studied without risk of complicated side effects such as coadsorption of residual gas molecules or reaction/decomposition of the adsorbed IL molecules at the surface. Furthermore, it allows for investigation of radiation-induced changes of the thin IL films.

In this chapter, the adsorbate/substrate interaction, the molecular arrangement and orientation, and the growth behaviour of three imidazolium-based ILs ([C_1C_1Im][Tf_2N], [C_8C_1Im][Tf_2N] and [C_4C_1Pyrr][Tf_2N]) on Au(111) is investigated. In particular, it is shown that (i) anions and cations within the first adsorption layer are adsorbed next to each other, in direct contact with the substrate, (ii) indications for formation of a rather well-ordered interface IL layer (checkerboard arrangement) are found for [C_1C_1Im][Tf_2N], (iii) a reorientation of the octyl chain takes place upon formation of the first closed layer of [C_8C_1Im][Tf_2N], and that (iv) the IL layers grow in a layer-by-layer fashion up to a thickness of at least 9 nm. Furthermore, radiation induced decomposition processes are discussed.
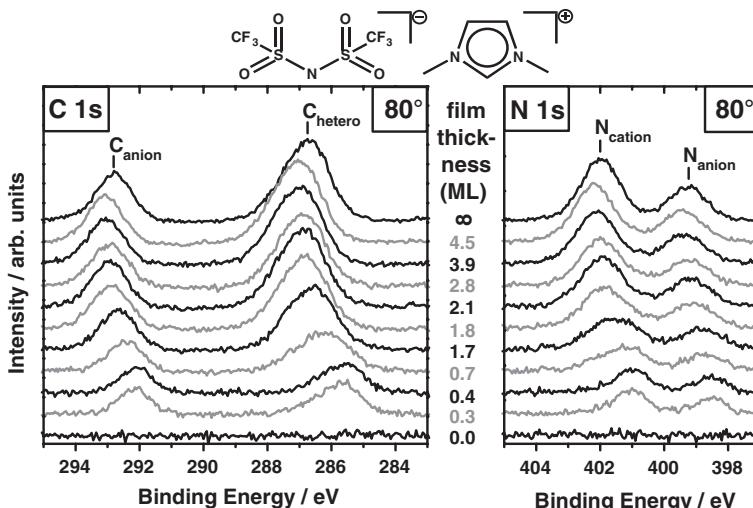
4.3.1.1 [C_1C_1Im][Tf_2N] on Au(111)

[C_1C_1Im][Tf_2N] was chosen as a first example to study the adsorption of ultrathin IL films on Au(111) for several reasons: (1) it consists only of polar head groups (the

charged moieties) and, thus, no influence of additional neutral alkyl chains is possible; (2) various distinct adsorption geometries in the first molecular layer should be distinguishable by ARXPS (e.g., the planar imidazolium ring parallel or perpendicular to the surface, the elongated $[Tf_2N]^-$ anion in a *cis*- or a *trans*-configuration); and (3) all core levels can be easily attributed to either the cation or the anion.

In the thick reference film (topmost spectrum in Fig. 4.1) the cation exhibits one XPS signal in the N 1s region at a BE of 402.0 eV, originating from the two equivalent imidazolium nitrogen atoms (denoted as "N_{cation}"). In the C 1s region one peak at 286.8 eV is observed, which is assigned to the five carbon atoms bonded to the imidazolium nitrogen atoms (denoted as "C_{hetero}", according to earlier work, see Ref. [55]). The anion leads to a distinct N 1s signal from the imide nitrogen at around 399.3 eV ("N_{anion}") and a C 1s signal from the two equivalent CF_3 groups at 292.8 eV ("C_{anion}"). As a consequence, the N 1s and the C 1s regions allow for the analysis of both cations and anions and is therefore of utmost importance because, from direct comparison of intensity changes and differential BE changes, information on the electronic interaction between surface and adsorbate and also on adsorption geometries can be derived. Other XPS signals are observed for all IL related atoms such as O, S and F, which, however, will not be discussed in the following.

In Fig. 4.1 the C 1s and N 1s spectra of ultrathin $[C_1C_1Im][Tf_2N]$ films of increasing thickness are displayed along with the already mentioned manually deposited macroscopically thick reference film (topmost spectra in Fig. 4.1); furthermore, the C 1s and N 1s regions of the clean gold substrate before deposition are included (bottom spectra). All spectra in Fig. 4.1 were recorded in surface

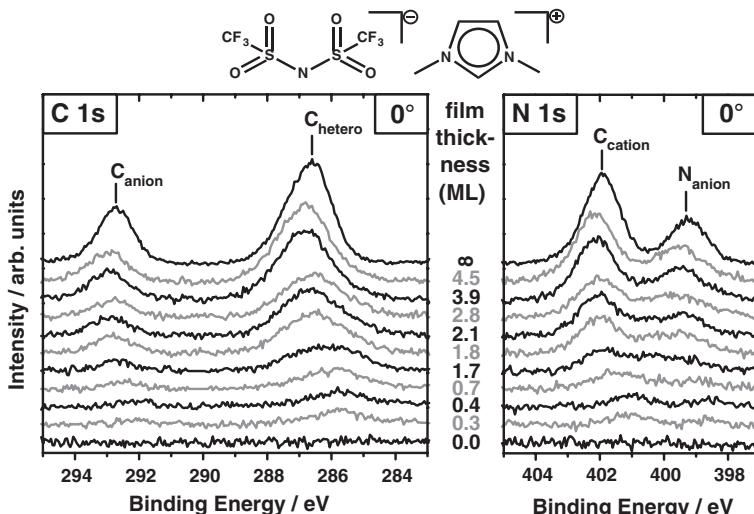**Fig. 4.1** Waterfall plots of PVD films of $[C_1C_1Im][Tf_2N]$ on Au(111) with different thicknesses, starting from the clean Au(111) substrate up to macroscopic films. Depicted are the C 1s and N 1s core level spectra for 80° emission. Please see text for details

sensitive geometry at 80° emission angle. The spectra for the more bulk sensitive geometry at 0° emission are shown in Fig. 4.2 and exhibit very similar spectral characteristics in terms of BE positions and peak shape. However, the signal-to-noise ratio is lower in 0° emission; moreover, radiation damage effects are more pronounced for the 0° spectra, because these spectra were recorded after measuring the 80° spectra and thus at a higher accumulated X-ray dose (see Sect. 4.3.1.5). Consequently, for the analysis of the IL/Au(111) interface we mainly focus on the 80° spectra.

With increasing film thickness the N_{cation}, N_{anion}, C_{anion} and C_{hetero} peaks in Fig. 4.1 initially reveal constant BEs, up to a coverage of 0.4 ML (note that throughout this study the coverage of 1 ML corresponds to one closed layer of vertically arranged IL ion pairs according to Eq. (4.2) and Scheme 4.1). All peaks are clearly shifted by around 1 eV towards lower BE compared to the reference spectra of the thick film, with the exact value of the shift depending on the particular peak.

For film thicknesses above 0.5 ML a nearly parallel shift of the IL peaks towards higher BEs is observed, until a maximum value is reached at a final coverage of 4.5 ML. The total BE shifts range from 0.9 to 1.4 eV, depending on the respective peak. The detailed analysis reveals that, with respect to the thickest deposited IL film (4.5 ML), anion-related signals shift less (1.00 ± 0.02 eV for C_{anion} 1s and 0.88 ± 0.02 eV N_{anion} 1s) than the cation signals (1.40 eV ± 0.02 eV for C_{hetero} 1s and 1.21 ± 0.02 eV for N_{cation} 1s), as is also detailed in Table 4.2. The BE changes are most pronounced for film thicknesses between 0.4 and 2.1 ML. In this coverage regime also, the signal shapes change for both 0° and 80°

Fig. 4.2 Waterfall plots of PVD films of [C_1C_1Im][Tf_2N] on Au(111) with different thicknesses, starting from the clean Au(111) substrate up to macroscopic films. Depicted are the C 1s and N 1s core level spectra for 0° emission

Table 4.2 Comparison of BE values of different (4.5 and 80 ML PVD and ex-situ deposited macroscopically thick) $[C_1C_1Im][Tf_2N]$ films with the 0.4 ML PVD film; Δ-values in brackets are the resulting differential shifts. For details, see text

System	Binding energy position/eV			
	C_{hetero}	C_{anion}	N_{cation}	N_{anion}
Thick, evaporated (4.5 ML)[a]	287.08	293.09	402.19	399.44
sub-ML (0.4 ML)	285.68 ($\Delta = 1.40$)	292.09 ($\Delta = 1.00$)	400.98 ($\Delta = 1.21$)	398.56 ($\Delta = 0.88$)
Thick, evaporated (60 ML)[b]	287.08	293.07	402.29	399.56
sub-ML (0.4 ML)	285.68 ($\Delta = 1.40$)	292.09 ($\Delta = 0.98$)	400.98 ($\Delta = 1.31$)	398.56 ($\Delta = 1.00$)
Thick layer ex-situ	286.81	292.81	401.99	399.28
sub-ML (0.4 ML)	285.68 ($\Delta = 1.13$)	292.09 ($\Delta = 0.72$)	400.98 ($\Delta = 1.01$)	398.56 ($\Delta = 0.72$)

[a]Used as BE reference in text and Ref. [1]; [b]Film thickness of 60 nm was estimated from deposition rate

spectra. All peaks are broadened and slightly asymmetric, seen best for the 0.7 ML spectra in Fig. 4.1. Similar findings are also observed up to 4.5 ML coverage in the 0° spectra, where due to the increased information depth the Au/IL interface layer still contributes to the XP signal (see also Fig. 4.2).

As is evident from Fig. 4.1 and Table 4.2, the BE positions for the in situ deposited films do not converge to the values of the ex situ prepared reference film, but to higher values. For the thickest in situ deposited film (4.5 ML) all IL signals exhibit an about 0.2–0.3 eV higher BE than observed for the thick reference film. This difference persists for even higher coverages (thickest film deposited by means of PVD was ~60 nm, where C 1s BE positions are within 0.02 eV identical to the 4.5 ML film, whereas N 1s signals are again shifted to higher BE by ~0.1 eV, see Table 4.2). One possible explanation for the observed different BE positions of evaporated and manually deposited films is the presence of different work functions (surface potentials) at the Au(111)/IL interface due to unavoidable contamination of the Au(111) surface in case of the ex-situ prepared films. In this case, thick IL films prepared in situ by IL-PVD would eventually display different BE positions than the ex-situ prepared thick film.

For very thin IL films, it is evident that the XPS peaks of the sub-0.5 ML films exhibit narrow peak widths, which are comparable to the fwhm values of IL films above 2 ML thickness (measured at 80°) and of the reference IL, but are shifted towards lower BE by about 1 eV. These chemical shifts are attributed to the interaction of both the cations and the anions with the Au(111) surface. Assuming that anions and cations in the first layer are alternately adsorbed next to each other (as schematically depicted in Scheme 4.1b), a coverage of 0.5 ML would correspond to a closed IL film on the surface; its nominal height would be the mean height of cations and anions ions (i.e., 0.36 nm). The observed chemical shifts (i.e., lower BEs) of the various core levels of the ions in contact with the substrate may be due to a bonding mechanism (initial state effect), which could involve charge transfer between substrate and IL. Another possibility is a more efficient screening of the

excited IL core hole in the vicinity of the gold surface (final state effect). Both scenarios result in lower BE values, and have been observed for adsorption of neutral molecules such as benzene or methanol on metal surfaces, with similar magnitudes as found here [70, 71].

Increasing the coverage above 0.5 ML leads to the already mentioned broadening of the XP spectra. This observation is attributed to the superposition of signals from the IL ions in direct contact with the gold surface (at lower BE) and IL molecules adsorbed on top of these interface ions, which display a higher BE. In the coverage range between 0.5 and 2.0 ML, the peak broadening should be most pronounced. This is shown in Fig. 4.1, where the peak broadening for 0.7 ML and the 1.7 ML films is clearly observed. With further film thickness increase, the peaks originating from the interface IL layer are subject to pronounced signal damping, and the "bulk" IL characteristics become dominating. Note that for this scenario, a layer-by-layer growth is assumed. Evidence for this assumption comes from the quantitative analysis of decrease of the Au 4f intensities at 0° and 80° emission, which will be discussed in Sect. 4.3.1.4.

Additional information on the arrangement of the IL ions at the Au(111) interface can be derived from the quantitative analysis of the XP spectra; the composition (i.e., stoichiometry derived from the C 1s and N 1s signals of the cations and anions in Fig. 4.1) is summarized in Table 4.3. For thin films below 0.5 ML, the contribution of the C_{anion} signal measured at 80° corresponds to the stoichiometric value (± 0.1), while F is noticeably enhanced. The cation signals C_{hetero} and N_{cation}, however, are considerably smaller. Since cations and anions are deposited as neutral ion pairs, i.e. in equal amounts, on the gold surface [47], the deviations from the nominal composition indicate an arrangement of the anion and the cation in an adsorption geometry where the anion is located slightly above the cation, and thus, the cation signals are damped by inelastic scattering. Table 4.4 shows the respective anion-to-cation-ratios which further highlight the observed anion signal enhancement. To understand the observed attenuation of the cation signals, an arrangement of cations and anions adsorbed next to each other on the surface is considered, with the imidazolium ring parallel to surface; the anions are bound via the SO_2 groups in *cis*-conformation and the CF_3 groups point towards the vacuum

Table 4.3 Elemental composition for several $[C_1C_1Im][Tf_2N]$ films below 0.5 ML thickness, determined under 80° emission, and the elemental composition derived for a thick, macroscopic film; also given are the nominal values (the intensities are normalized to $3N + 7C + 6F = 16$ atoms in total)

Signal	Coverage			Nominal value
	0.3 ML	0.4 ML	Thick	
N_{cation}	1.4	1.3	1.8	2.0
N_{anion}	0.8	0.8	1.0	1.0
C_{anion}	1.9	2.2	2.1	2.0
C_{hetero}	3.5	3.3	4.5	5.0
F	8.4	8.5	6.7	6.0

Table 4.4 Anion-to-cation ratios for sub-0.5 ML and thick reference $[C_1C_1Im][Tf_2N]$ films, along with the nominal value. Deviations to higher values indicate surface enrichment of anion-related signals CF_3 and N_{anion}

System investigated	C_{anion}/C_{hetero}	N_{anion}/N_{cation}
0.3 ML	0.60	0.63
0.4 ML	0.66	0.62
Thick film on Au(111)[a]	0.47	0.55
Nominal	0.40	0.50

[a]Macroscopically thick, ex-situ deposited $[C_1C_1Im][Tf_2N]$ film

(see Scheme 4.2). At a coverage of 0.5 ML, the gold surface is fully covered with anions and cations in direct contact with the underlying gold (see above). From Scheme 4.2, it is evident that the mean distance of the flat-lying imidazolium ring from the surface is significantly smaller than that of the anion.

In particular, the CF_3 groups of the $[Tf_2N]^-$ anion are located above the level of the imidazolium ring of the cation, and also N_{anion} is estimated to be somewhat higher than the imidazolium ring, due to the slightly enhanced N_{anion}/N_{cation} ratio. This explains why ARXPS signals from these parts of the anion are more intense in 80° emission whereas the corresponding cation signals are reduced in intensity due to damping. Since this qualitative analysis is not very sensitive to the detailed geometry, a situation where the cation is even partly covered by parts of the $[Tf_2N]^-$ would also be in agreement with our findings.

Some additional support for the adsorption geometry proposed in Scheme 4.2 comes from the different chemical shifts observed for the anions and cations within the first adsorption layer. In a simplified picture these shifts should decrease with increasing distance of the respective atoms from the surface. Hence, the anion-related species located further away from the Au surface, namely the nitrogen and the CF_3-groups, should be subject to reduced screening, which is indeed observed: The shift of the cation-related signals, N_{cation} and C_{hetero}, is larger (1.20–1.40 eV) than that of the anion-related signals N_{anion} and C_{anion} (0.9–1.0 eV).
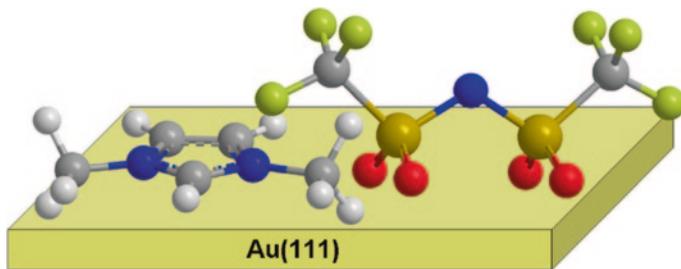
Scheme 4.2   Three-dimensional drawing of anion and cation of $[C_1C_1Im][Tf_2N]$ in the proposed adsorption geometry on Au(111), for films below 0.5 ML coverage. Note that most atoms of the anion are considerably further away from the surface (i.e. closer to the vacuum side) than the cation, which leads to a damping of the cation signals at an electron emission angle of 80°

There are some recent studies in the literature addressing the adsorption behaviour of [Tf$_2$N]$^-$-based ILs. For [C$_4$C$_1$Im][Tf$_2$N] thin films on a well-defined Al$_2$O$_3$ oxide model surface, Sobota et al. [50] derived information on the molecular orientation from infrared reflection absorption spectroscopy (IRAS). They proposed that the cation is preferentially oriented parallel to the surface and that the anion is adsorbed in a *cis*-conformation similar to the one shown in Scheme 4.2. In our own ARXPS work on [C$_2$C$_1$Im][Tf$_2$N] deposited on a native glass substrate a *cis*-configuration of the anions was also proposed in the sub-ML regime [49]. Interestingly, a double layer (sandwich) adsorption geometry was proposed, in which the anion is located on top of the cation and not in direct contact with the surface, see also Chap. 5. For the [C$_1$C$_1$Im][Tf$_2$N] thin films on Ni(111) discussed in Sect. 4.3.2, a similar sandwich arrangement is found for very low coverages ≤0.4 ML, while a structure of alternating cation and anion layers was deduced for thick IL layers on a polar sapphire surface from an high-energy X-ray reflectivity study [25]. For [C$_1$C$_1$Im][Tf$_2$N] on Au(111) such a bilayer structure can definitely be ruled out in the initial growth phase.

It should be noted that density functional theory calculations of isolated [C$_2$C$_1$Im][Tf$_2$N] ion pairs show that the *trans*-conformer is energetically favoured by only about 10 kJ/mol relative to the *cis*-conformer, meaning that at RT both conformers should be present in (nearly) equal amounts [72]. However, a linear *trans*-type adsorption geometry of the [Tf$_2$N]$^-$ anion would lead to more stoichiometric relative intensities in ARXPS on the Au(111) surface, which is clearly not observed. Additional support for the *cis*-configuration comes from the known non-coordinating behaviour of CF$_3$ groups, which makes the preferential orientation of these groups towards the vacuum very likely. This behaviour has been found for the IL/vacuum interface of macroscopically thick IL films [55, 66].

At coverages above 0.5 ML, the relative intensities of the different core levels change towards the nominal values of the bulk film. Especially in 80°, the corresponding nominal bulk values are reached as soon as the first (half)layer in direct contact with the gold surface is completely damped by the overlaying film. This situation is reached when the film thickness exceeds 2 ML, which corresponds to about 1.5 nm (information depth at 80°: 1.0–1.5 nm).

In summary, our findings clearly indicate that for molecules directly adsorbed at (and in contact with) the gold surface, pronounced orientation effects take place. For the sub 0.5 ML films, the imidazolium rings of [C$_1$C$_1$Im][Tf$_2$N] are adsorbed parallel to the surface and the anions are bonded to the surface in *cis*-conformation via the oxygen atoms, with the CF$_3$ groups pointing towards the vacuum. At coverages larger than one layer of molecules (i.e., half a layer of ion pairs), this high degree of order is lifted and the additional molecules tend to adsorb with a more random orientation on top of the confined interface layer.
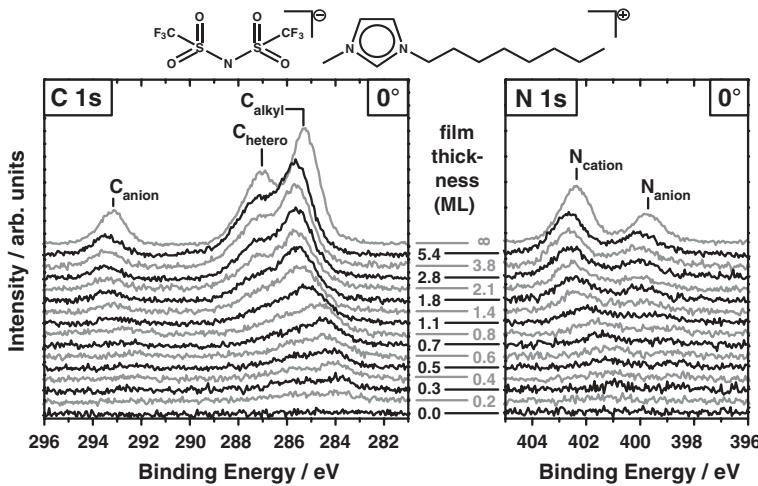
4.3.1.2 [C$_8$C$_1$Im][Tf$_2$N] on Au(111)

It was shown in Sect. 3.2 and in previous publications by our group that the composition of the IL/vacuum interface of a given IL is drastically influenced by the

length of the alkyl chain attached to the N^1 position of the imidazolium ring [55, 66]. Hence, we moved on to study the influence of the alkyl chain on the adsorption behaviour and molecular orientation at the IL/substrate interface. Therefore, ultrathin films of $[C_8C_1Im][Tf_2N]$ were deposited on Au(111). Compared to $[C_1C_1Im][Tf_2N]$ discussed above, one methyl substituent of the imidazolium ring is replaced by a $-C_8H_{17}$ chain, which introduces an additional C_{alkyl} feature to the XP spectra (for details, please see Chaps. 2 and 3).

In Fig. 4.3 the 80° emission C 1s and N 1s spectra of ultrathin $[C_8C_1Im][Tf_2N]$ films of increasing thickness are displayed along with a manually deposited macroscopically thick reference film (topmost spectra) and the spectra of the clean gold substrate (bottom spectra). The corresponding 0° emission spectra are shown in Fig. 4.4. The main difference to the spectra for $[C_1C_1Im][Tf_2N]$ is the prominent additional carbon signal at 285.5 eV (reference spectrum) in the C 1s region, which is attributed to the seven alkyl carbon atoms in the octyl chain of the cation (denoted "C_{alkyl}") [55]. Similar to $[C_1C_1Im][Tf_2N]$, all C 1s and N 1s signals are shifted to lower BE for coverages below 0.5 ML. With increasing coverage, the peak positions start to shift towards higher BE until they reach a maximum value (analogous to our findings for $[C_1C_1Im][Tf_2N]$, this peak shift can be observed up to higher coverages in the 0° measurements, see Fig. 4.4). The total shifts from the 0.2 ML film to the 5 ML film range from 1.3 to 1.8 eV, depending on the particular core level, and are thus slightly higher than for $[C_1C_1Im][Tf_2N]$, see Table 4.5. The BE values of the spectra of the thick reference film are again about 0.3 eV lower than for the thickest IL-PVD film, in accordance with observations made for $[C_1C_1Im][Tf_2N]$.
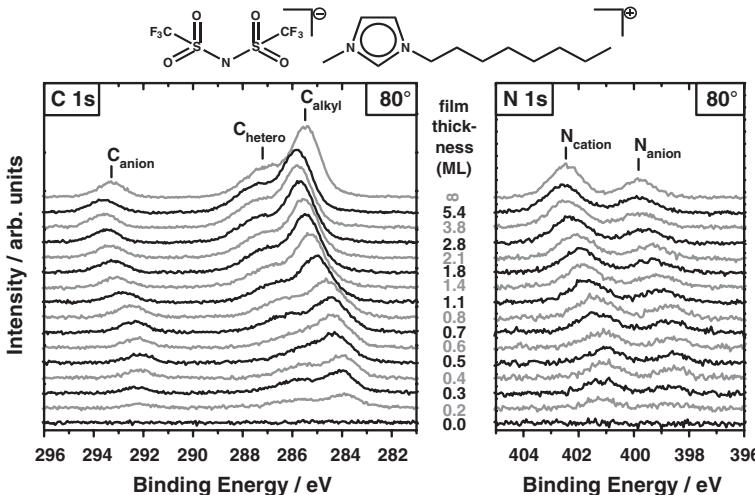
Fig. 4.3 Waterfall plots of PVD films of $[C_8C_1Im][Tf_2N]$ on Au(111) with different thicknesses, starting from the clean substrate up to macroscopic films. Depicted are the C 1s and N 1s core level spectra for 80° emission. For details, see text

Fig. 4.4 Waterfall plots of PVD films of $[C_8C_1Im][Tf_2N]$ on Au(111) with different thicknesses, starting from the clean Au(111) substrate up to macroscopic films. Depicted are the C 1s and N 1s core level spectra for 0° emission

In analogy to the results for $[C_1C_1Im][Tf_2N]$, we propose that the constant BEs for the core levels of $[C_8C_1Im][Tf_2N]$ films up to 0.5 ML are due to the formation of a closed IL (half)layer with cations and anions adsorbed at the Au(111) surface next to each other, in a checkerboard-like structure (Scheme 4.1b). For higher coverages, IL molecules adsorb onto this closed interface layer and thus exhibit higher BE values resulting in broadened XPS signals that are shifted to higher BEs. Interestingly, there is one peak that behaves differently as it is illustrated in detail in Fig. 4.5 for three selected coverages.

While the C_{anion} peak at 292.2 eV and the C_{hetero} peak at 285.8 eV show no shifts up to 0.5 ML, the C_{alkyl} peak remains unshifted up to 0.4 ML, but thereafter, upon increasing the coverage to 0.5 ML, displays a shift from 284.0 to 284.3 eV.

Table 4.5 Comparison of BE values of thick evaporated (5.4 ML) and ex-situ deposited, macroscopically thick $[C_8C_1Im][Tf_2N]$ films with the 0.4 ML PVD film; Δ-values in brackets are the resulting differential shifts. For details, see text

System	Binding energy position/eV				
	C_{alkyl}	C_{hetero}	C_{anion}	N_{cation}	N_{anion}
Thick, evaporated	285.82	287.60	293.63	402.56	399.87
Sub-ML (0.4 ML)	284.00	285.76	292.19	401.09	398.59
	($\Delta = 1.82$)	($\Delta = 1.84$)	($\Delta = 1.44$)	($\Delta = 1.47$)	($\Delta = 1.28$)
Thick, ex-situ	285.47	287.28	293.31	402.46	399.82
Sub-ML (0.4 ML)	284.00	285.76	292.19	401.09	398.59
	($\Delta = 1.47$)	($\Delta = 1.52$)	($\Delta = 1.12$)	($\Delta = 1.37$)	($\Delta = 1.23$)

[a]Used as BE reference in text and Ref. [1]
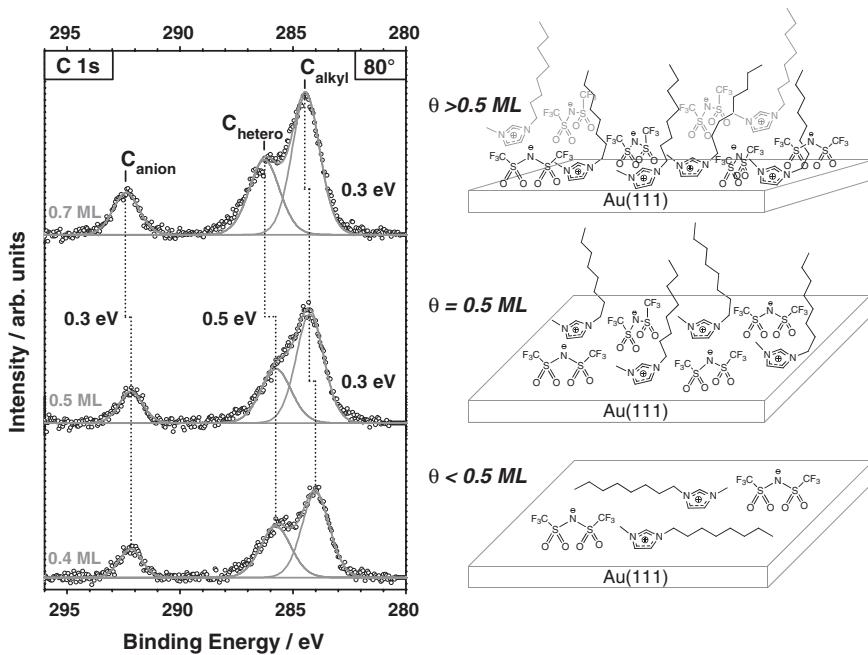
Fig. 4.5 Fit analysis of the C 1s region of ultrathin [C$_8$C$_1$Im][Tf$_2$N] films (*left*) and sketches of ion orientation (*right*) for coverages below, at and above 0.5 ML (*right*). Between 0.4 and 0.5 ML, only the C$_{alkyl}$ peak shifts (by ~0.3 eV). For higher coverages all peaks shift to higher BE as the additionally adsorbed ions are not in contact with the gold surface and thus exhibit a higher BE. The sketch depicts the arrangement of [C$_8$C$_1$Im][Tf$_2$N] on Au(111) at the corresponding coverages: at very low coverages the anions are adsorbed in cis-conformation, while the cations adsorb with the imidazolium ring parallel to the surface. The alkyl side chains are in contact with the substrate as well, in order to maximize dispersive interactions. At ~0.5 ML, the alkyl chains reorient and start point towards the vacuum, allowing further adsorption of IL ion pairs, which are bonded via their charged headgroups to the gold surface. At coverages >0.5 ML further IL molecules (*grey*) adsorb on top of the interface layer (*black*)

Above 0.5 ML further differential shifts and peak broadening are observed for all peaks. As the C$_{alkyl}$ peak does not shift in parallel with the C$_{hetero}$ peak, even a change in shape can be observed in the C 1s core level spectra. This change is most pronounced at a total coverage of 0.5 ML and 0.6 ML (see also Fig. 4.3), where the energy separation between the C$_{hetero}$ and the C$_{alkyl}$ peak is only 1.5 eV compared to ~1.8 eV for most other coverages.

In light of our interpretation for the observed BE shifts in the 0–2 ML coverage range, a shift of C$_{alkyl}$ towards higher BE indicates a larger distance between the octyl chain and the gold surface (see also discussion for [C$_1$C$_1$Im][Tf$_2$N]). Consequently, the observed BE changes for the C$_{alkyl}$ signal in the low coverage regime are the following: For coverages up to 0.4 ML the alkyl chains are in direct contact with the gold surface together with the polar headgroups of the cation

and the $[Tf_2N]^-$ anions as depicted in the scheme in Fig. 4.5, in order to maximize attractive interactions with the substrate. For higher IL coverages (threshold between 0.4 and 0.5 ML), it becomes energetically more favourable for the nonpolar octyl chains to point away from the surface towards the vacuum, thereby allowing additional adsorption of incoming IL moieties in direct contact with the gold surface (middle scheme in Fig. 4.5). This situation with the nonpolar alkyl chain pointing towards the vacuum is similar to that for self-assembled monolayers such as alkane thiols adsorbed on gold [73]. Further IL deposition then leads to the formation of "bulk" IL layers on top of this interface layer similar to the situation for $[C_1C_1Im][Tf_2N]$ on Au(111).

If this scenario was correct, the existence of a well-ordered interface layer with the octyl chains oriented towards the vacuum should be clearly seen by intensity changes in ARXPS. Indeed, a closer look at the relative intensities of the cation-related signals strongly supports this interpretation. In Fig. 4.6 intensity ratio changes for C_{hetero}/C_{alkyl} are shown as a function of film thickness, as derived from the surface sensitive spectra at 80°. While under bulk sensitive conditions at 0° the stoichiometric ratio of $5 : 7 = 0.71$ is measured, an enhancement of C_{alkyl} at the IL-vacuum interface leading to a ratio of 0.46 is observed for a macroscopically thick IL film at 80°, as it was reported earlier [55, 58]. For the thin films, at coverages below 0.3 ML, the 80° ratio is nearly stoichiometric, indicating that the whole cation is lying flat on the surface.

For thicknesses of ~0.5 and ~0.6 ML a significant drop in the C_{hetero}/C_{alkyl} ratio is found, which is a clear indication for presence of the alkyl chains at the outer surface, leading to a damping of the C_{hetero} atoms of the imidazolium ring.
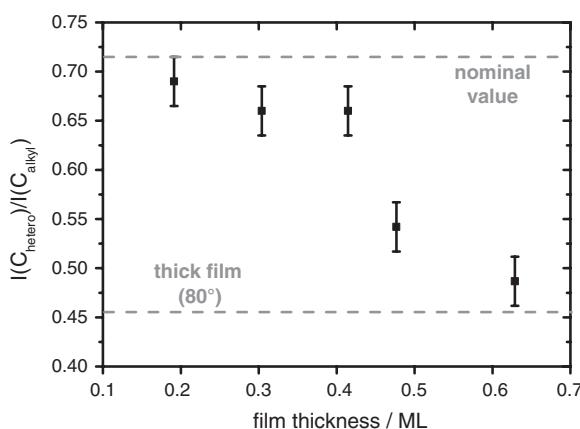
Fig. 4.6 Ratio of C_{hetero}/C_{alkyl} (mean relative error: ±0.05), measured at 80° emission, as a function of coverage. The horizontal line indicates the nominal stoichiometric ratio of $5:7 = 0.714$, which within the error bars has been measured for the thick film under 0° emission. Also indicated is the value of 0.46 measured at 80° emission for thick films, which is significantly smaller due to surface enrichment for the octyl chain [55]

Hence, the findings from the intensity changes corroborate our interpretation discussed above for the BE shifts in the low coverage regime. To summarize, at coverages below 0.4 ML, the peak ratios reveal a nearly equal distribution of anions, cation headgroup and cation alkyl chains on the gold surface. As the surface becomes filled and the molecules move closer together, the alkyl chains start to lose the contact to the surface and point towards the vacuum. This is most likely due to the fact that the attractive dispersive forces between the alkyl chains and the substrate are weaker than those between the ionic headgroups and the gold surface. After a closed complete interface layer is formed at around 0.5 ML coverage, further IL deposition leads to IL layers that are already similar to the bulk in terms of BE positions and surface enrichment of the octyl chains. It is worth noting that the arrangement of the polar headgroups in the interfacial layer on Au(111) seems to be less ordered for $[C_8C_1Im][Tf_2N]$ than for $[C_1C_1Im][Tf_2N]$, at low coverages. For the latter, the analysis of ARXP spectra of the <0.5 ML films indicates that the N and the CF_3 groups of the anion are located further away from the surface than the atoms of the imidazolium ring (see Fig. 4.1 and Table 4.4). In contrast, in the same coverage range for $[C_8C_1Im][Tf_2N]$ on Au(111) this effect is not observed to the same extent (e.g., for the 0.2 and 0.3 ML films the anion-to-cation ratio of the corresponding nitrogen and carbon signals for 80° are close to the stoichiometric value of 0.5 and 0.4, respectively, whereas for the 0.4 and 0.5 ML films a slight increase is observed, indicating a slight increase of order), as is evident from Table 4.6. This difference is most likely related to the octyl chains that introduce an additional degree of disorder into the $[C_8C_1Im][Tf_2N]$ films and thus hinder an optimum molecular packaging of ionic head groups compared to $[C_1C_1Im][Tf_2N]$. Nevertheless, it is likely that most of the imidazolium rings are also adsorbed parallel on the surface and the anion is adsorbed via the oxygen atoms of the SO_2 groups as was deduced in the case of $[C_1C_1Im][Tf_2N]$, which is further corroborated by the differential BE shifts of ~0.3–0.4 eV between anion and cation, similar to those observed for $[C_1C_1Im][Tf_2N]$.

Table 4.6 Anion-to-cation ratios for $[C_8C_1Im][Tf_2N]$ sub-ML films and the thick reference films (5.4 ML PVD and macroscopically thick film). Also denoted are the nominal values

System investigated	C_{anion}/C_{hetero}	N_{anion}/N_{cation}	C_{hetero}/C_{alkyl}
0.2 ML	0.40	0.53	0.69
0.3 ML	0.37	0.50	0.66
0.4 ML	0.45	0.58	0.66
0.5 ML	0.45	0.59	0.55
Thick, evaporated	0.39	0.55	0.47
Thick, ex-situ	0.41	0.54	0.46
Nominal	0.40	0.50	0.71

4.3.1.3 [C$_4$C$_1$Pyrr][Tf$_2$N] on Au(111)

The third example of ultrathin IL films deposited on Au(111) is [C$_4$C$_1$Pyrr][Tf$_2$N], which—in contrast to the other two ILs—possesses a different cationic headgroup and atom distribution. Therefore, before proceeding to the results obtained for the thin films, the key features and differences of [C$_4$C$_1$Py][Tf$_2$N] shall be discussed briefly in the following. Compared to the aromatic imidazolium ring, where the positive charge is rather evenly distributed over the entire cationic headgroup (see also Sect. 3.2), the five-membered ring of the pyrrolidinium moiety is solely composed of sp^3 carbons. Therefore, the positive charge is significantly more localized at the nitrogen atom, which is also represented in the spectral features observed in the C 1s and N 1s regions of [C$_4$C$_1$Pyrr][Tf$_2$N], as illustrated in Fig. 4.7. Although the cation is structurally different from the [C$_8$C$_1$Im]$^+$ cation, the C 1s and N 1s XP spectra show features similar to imidazolium-ILs, which are accordingly classified into C$_{hetero}$, C$_{alkyl}$, C$_{anion}$, N$_{anion}$ and N$_{cation}$, too. While for imidazolium-based ILs the C$_{hetero}$ feature is broader due to the slightly different chemical environment of atoms assigned to C$_{hetero}$, the four C$_{hetero}$ atoms (labelled with "1" in Fig. 4.7) of [C$_4$C$_1$Pyrr][Tf$_2$N] are more or less chemically equivalent. For fitting of the spectra, the fwhm value of the C$_{hetero}$ feature is found to be smaller than the fwhm of C$_{alkyl}$ (see experimental section for details) and also the peak separation between C$_{hetero}$ and C$_{alkyl}$ is not as pronounced as for imidazolium ILs ([C$_4$C$_1$Im]$^+$: 1.62 eV, [C$_4$C$_1$Pyrr]$^+$: 1.36 eV). For the N 1s region two peaks are observed, which, compared to the imidazolium-based ILs, also exhibit a larger peak separation (3.2 eV as opposed to 2.7 eV for [C$_8$C$_1$Im][Tf$_2$N]). The higher BE signal is assigned to N$_{cation}$, which in comparison to the imidazolium-ILs, exhibits a higher BE value due to the somewhat more localized positive charge at the quaternary nitrogen centre. A detailed 0° emission XPS study of [C$_n$C$_1$Pyrr]$^+$ ILs was recently published by Men et al., who, with respect to electronic structure and Coulomb interactions (i.e., reduced charges for small and basic anions), found striking similarities to the [C$_n$C$_1$Im]$^+$-based ILs investigated in Sect. 3.1 [74].

While for imidazolium-based ILs surface enrichment of the alkyl chain was found for n ≥ 4, in the case of [C$_4$C$_1$Pyrr][Tf$_2$N] no such enrichment can be deduced from the 80° emission data (see Fig. 4.7c and d and Table 4.7 for elemental composition). In Table 4.7 the nominal and experimental elemental compositions are compiled, clearly indicating that for [C$_4$C$_1$Pyrr][Tf$_2$N] no preferential arrangement of the alkyl chain takes place. However, SFG studies of [C$_4$C$_1$Pyrr][Tf$_2$N] suggest that the alkyl chain does point towards the vacuum at an average tilt-angle of 60° with respect to the surface normal and that the pyrrolidinium ring is oriented parallel to the surface plane [75]. Such a surface arrangement is not corroborated by our ARXPS data. Even considering the fact that the C$_{alkyl}$ feature not only originates from the three terminal carbon atoms of the C$_4$ alkyl chain, but also comprises the two alkyl carbons in the five-membered ring, signal enhancement is expected to be less pronounced than for [C$_4$C$_1$Im][Tf$_2$N]. Regardless, for a surface structure as proposed by Aliaga et al., C$_{alkyl}$ enhancement should be observed in our 80° emission ARXP spectra. Furthermore, in such a decided
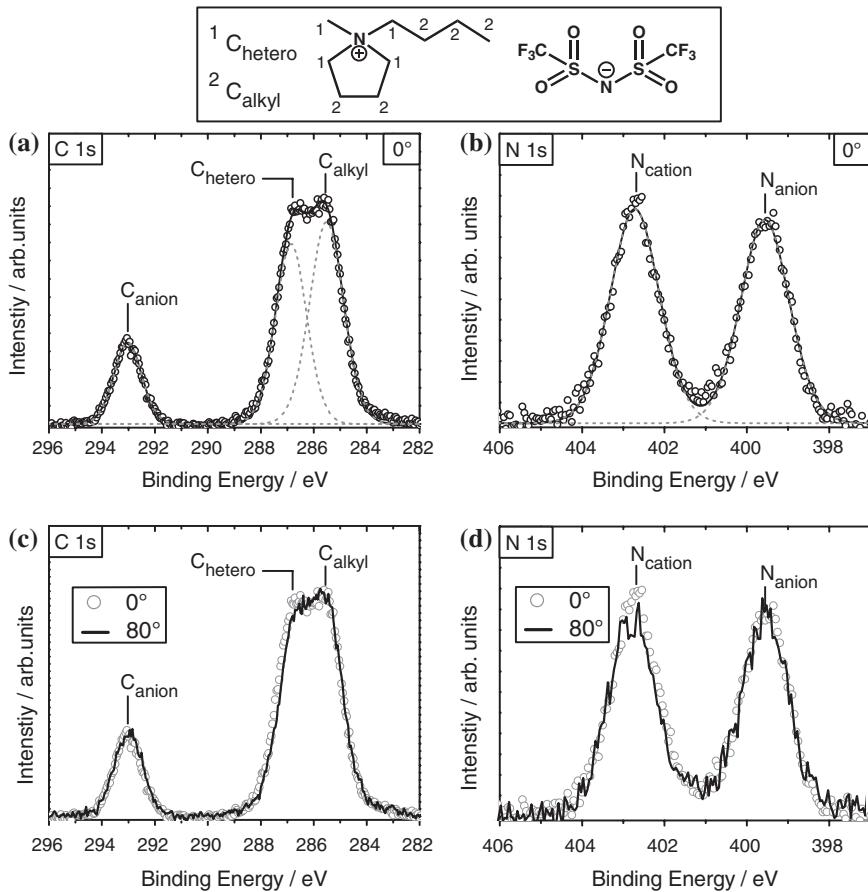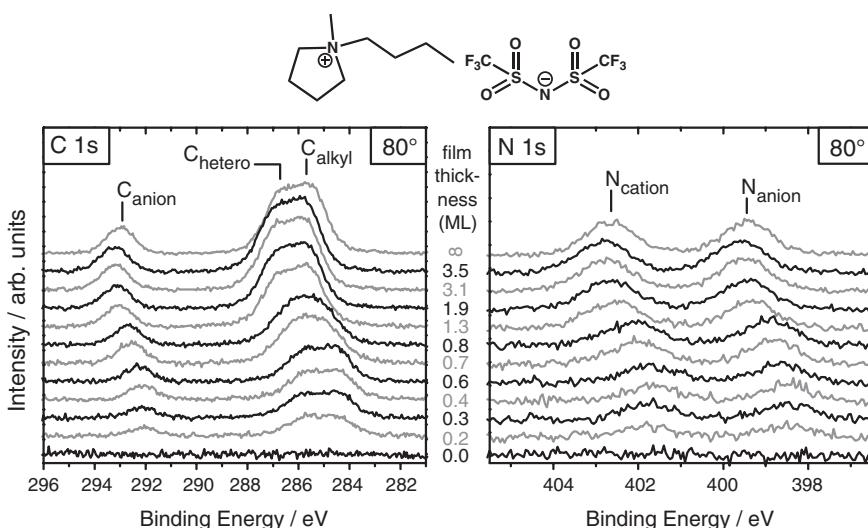
Fig. 4.7 C 1s and N 1s core level spectra of a macroscopically thick film of [C$_4$C$_1$Pyrr][Tf$_2$N]. **a** and **b** shows the 0° emission spectra with corresponding fits, while in **c** and **d** the 0° and 80° emission data are compared. Note, that 80° emission data have been normalized using a geometry factor to allow for visual comparison, see Ref. [63] for details

Table 4.7 BE values and elemental composition of a macroscopically thick film of [C$_4$C$_1$Pyrr][Tf$_2$N]

Core level	BE/eV	Elemental composition		
		Nominal value	Bulk sensitive (0°)	Surface sensitive (80°)
N$_{cation}$ 1s	402.7	1	1.0	0.9
N$_{anion}$ 1s	399.5	1	0.9	0.9
C$_{anion}$ 1s	293.0	2	1.7	1.8
C$_{hetero}$ 1s	286.9	4	4.2	4.0
C$_{alkyl}$ 1s	285.5	5	5.2	5.3
F 1s	689.0	6	5.8	6.1
O 1s	532.8	4	3.9	3.5
S 2p	169.2	2	2.3	2.4

arrangement as proposed by SFG, anion-related signals should be damped by the alkyl chains protruding into the vacuum. As no such damping is deduced from our ARXPS results, it seems to be more likely that no pronounced surface order is present at the [C$_4$C$_1$Pyrr][Tf$_2$N] surface. Further evidence for rather randomly distributed surface layers comes from the thin film experiments of [C$_4$C$_1$Pyrr] [Tf$_2$N] presented below, where no preferential ordering similar to that observed for [C$_1$C$_1$Im][Tf$_2$N] or the C$_8$ alkyl chain of [C$_8$C$_1$Im][Tf$_2$N] takes place. All in all, clarity regarding the somewhat contradicting results could be gained by studying the chain length dependence of [C$_n$C$_1$Pyrr][Tf$_2$N] using ARXPS, similar to our earlier work on imidazolium-based ILs [55].

In the following, the spectra of the C 1s and the N 1s region taken under 80° emission (Fig. 4.8) will be discussed and compared to the findings of the IL-PVD experiments of [C$_1$C$_1$Im][Tf$_2$N] and [C$_8$C$_1$Im][Tf$_2$N] on Au(111). Focusing first on BE positions, again similar observations are made: the IL signals of thin films up to a coverage of about 0.5 ML exhibit a BE shift of about 1.1–1.3 eV to lower values (again slightly depending on the ion, see discussion below) with respect to the reference thick film. Further increase of film thickness results in a simultaneous shift towards higher BEs of all observed peaks accompanied by signal broadening in the coverage regime between 0.6 and 2 ML. The total energy shift is about 1.2 eV up to the thickest deposited IL film (~3.5 ML), which again is at about ~0.2 eV higher BE compared to the signals of the macroscopically thick IL film. The shifts resemble the observations made for the two imidazolium ILs in both, magnitude and coverage-dependence and fully agree with the interpretations

Fig. 4.8 Waterfall plots of PVD films of [C$_4$C$_1$Pyrr][Tf$_2$N] on Au(111) with different thicknesses starting from the clean substrate up to macroscopic films. Depicted are the C 1s and N 1s core level spectra for 80° emission. For details see text

given in the previous chapters. Consequently, the main interpretation of the observed phenomena is as follows: for $[C_4C_1Pyrr][Tf_2N]$ a closed layer (i.e., a checkerboard-like structure) is formed at 0.5 ML, where both cations and anions are adsorbed directly at the gold surface resulting in lower BE values compared to the bulk IL. This interface layer is maintained during deposition of the next IL layer, which already exhibits BE values close to the bulk values. The superposition of signals from both layers result in an overall shift to higher BEs and a spectral broadening in the intermediate coverage range (from 0.6 to 2 ML). Once film thicknesses equal or larger to the information depth at 80° (in the range of 1–1.5 nm, corresponding to 1.5–2 ML) are achieved, the broadening diminishes and the BE value saturates at the "bulk value"; the somewhat higher value of the thickest evaporated film with respect to the ex-situ deposited thick reference film is again assigned to different work functions at the Au(111)/IL interface.

Apart from this generally similar behaviour with respect to initial surface wetting and final state screening of the first adsorbed IL (half)layer, the ARXPS spectra of the $[C_4C_1Pyrr][Tf_2N]$ film reveal some differences compared to the imidazolium thin films discussed in the previous sections. First, the differential BE shifts between anion- and cation-related species in direct contact with the Au surface are not very pronounced; in fact, as is evident from Table 4.8, only C_{anion} shows a minor differential BE shift (−0.14 eV) relative to the other IL signals, which—within the margins of error—exhibit the same shift towards lower BE (1.14 ± 0.04 eV) with respect to the reference film.

Secondly, the anion-related C_{anion} signal shifts towards lower BE in the $[C_4C_1Pyrr][Tf_2N]$ films, which is in strong contrast to the imidazolium systems, where anion-related species were found to exhibit minor BE shifts compared to the cation-related signals. For the imidazolium-based systems it was concluded that the N_{anion} and C_{anion} moieties are located further away from the surface and are therefore less susceptible to efficient screening through the Au electrons, resulting in a smaller low-BE shift with respect to the reference film. We therefore conclude for $[C_4C_1Pyrr][Tf_2N]$, that N_{anion} and C_{anion} do not favour such preferential arrangement at the Au(111) interface, but are more or less randomly oriented and in equally close contact with the surface as the cations.

Table 4.8 Comparison of BE values of thick evaporated (3.5 ML) and ex-situ deposited, macroscopically thick $[C_4C_1Pyrr][Tf_2N]$ films with the 0.4 ML PVD film; Δ-values in brackets are the resulting differential shifts. For details, see text

System	Binding energy position/eV				
	C_{alkyl}	C_{hetero}	C_{anion}	N_{cation}	N_{anion}
Thick evaporated[a]	293.24	287.07	285.79	402.82	399.61
Sub-ML (0.4 ML)	292.11	285.91	284.50	401.66	398.51
	($\Delta = 1.13$)	($\Delta = 1.16$)	($\Delta = 1.28$)	($\Delta = 1.17$)	($\Delta = 1.10$)
Thick layer ex-situ	293.00	286.80	285.53	402.65	399.44
Sub-ML (0.4 ML)	292.11	285.91	284.50	401.66	398.51
	($\Delta = 0.89$)	($\Delta = 0.90$)	($\Delta = 1.02$)	($\Delta = 0.99$)	($\Delta = 0.93$)

[a]Used as BE reference in text

Further proof for such a rather disordered interface layer comes from the anion-to-cation ratios observed for thin [C$_4$C$_1$Pyrr][Tf$_2$N] layers on Au(111), compiled in Table 4.9. For the [C$_4$C$_1$Pyrr][Tf$_2$N] films below 0.5 ML coverage, the atomic cation-to-anion ratios of all species remain constant, within the margins of error, and are at 80° emission close to the nominal ratios. Therefore, an ordered interface layer for the 0.5 ML film similar to that found for [C$_1$C$_1$Im][Tf$_2$N] (i.e., cation in close proximity to the gold surface and the anion slightly further away due to the bonding with the SO$_2$ groups in *cis*-conformation) can be ruled out.

For thick [C$_4$C$_1$Pyrr][Tf$_2$N] films, apart from a slight enhancement of the CF$_3$ groups, no preferential arrangement of the ions at the IL/vacuum interface can be deduced from our data. For the ultrathin IL layers investigated here, no enhancement of either the alkyl chain or parts of the anion (as observed for [C$_1$C$_1$Im][Tf$_2$N]) are found.

Whether this unordered structure is related to the additional symmetry-breaking character of the butyl chain or due to the more bulky character of the pyrrolidinium cation (i.e., sp^3-hybridized nitrogen in pyrrolidinium vs. sp^2 hybridized nitrogen in the flat imidazolium) is unclear. We would like to refrain from further discussion because the data basis for pyrrolidinium-based IL is insufficient at this stage (especially if compared to imidazolium ILs).

To summarize this section, initial growth, arrangement and electronic interaction was investigated for [C$_4$C$_1$Pyrr][Tf$_2$N] films on an Au(111) single crystal. Similar to the other two ILs investigated earlier, [C$_4$C$_1$Pyrr][Tf$_2$N] initially grows in a layer-by-layer fashion on top of an interface IL layer (nominal thickness 0.5 ML) in which anions and cations both cover the gold surface and form a checkerboard-like arrangement. For sub-monolayer coverages, where the IL molecules are in direct contact with the Au surface, and also for thicker IL films, no enrichment/orientation effects were observed. Hence, the cations and anions are equally distributed and randomly oriented within the first adsorption layer, which is different to the two imidazolium ILs discussed previously.

While thus far the initial wetting behaviour and subsequent IL growth was deduced by the differential shifts of IL-related signals within the first adsorption layer and the subsequent signals broadening for higher coverages, in the following

Table 4.9 Anion-to-cation and C$_{hetero}$/C$_{alkyl}$ ratios for [C$_4$C$_1$Pyrr][Tf$_2$N] sub-ML films on Au(111), a thick evaporated film and the manually deposited thick film, along with the nominal values. Ratios are derived from surface sensitive measurements in 80° emission

System investigated	C$_{hetero}$/C$_{alkyl}$	N$_{anion}$/N$_{cation}$	C$_{anion}$/C$_{hetero}$
0.2 ML	0.76	0.91	0.48
0.3 ML	0.74	0.96	0.45
0.4 ML	0.74	0.94	0.53
0.6 ML	0.72	0.98	0.47
Thick evaporated	0.70	1.00	0.45
Thick ex-situ	0.75	1.01	0.45
Nominal	0.8	1	0.5

chapter the IL growth mechanisms of the three IL are analysed based on the substrate signal (Au 4f; $E_{kin} \sim 1400$ eV) damping, which allows for a detailed analysis of the IL growth beyond the first adsorption layer up to film thicknesses in the range of the information depth of XPS (~7–9 nm for Au 4f photoelectrons at 0° emission).

4.3.1.4 IL Growth Mode on Au(111)

After having focused mainly on the adsorption behaviour of the first layer ($0 \leq \theta \leq 0.5$ ML) at the substrate/IL interface, we now address the growth behaviour of thicker IL films on the Au(111) substrate. For this purpose, the attenuation of the Au 4f peak was used. In the following, the data for $[C_8C_1Im][Tf_2N]$ are analysed in detail; while the growth behaviour of $[C_4C_1Pyrr][Tf_2N]$ is analysed in the same way as $[C_8C_1Im][Tf_2N]$, for $[C_1C_1Im][Tf_2N]$ a somewhat different evaluation was carried out, yet leading to identical conclusions.

In Fig. 4.9a, the attenuation of the Au 4f signals measured under 0° and 80° are shown, with the data at 80° displaying a significantly steeper exponential decrease due to the higher surface sensitivity. The data for the two emission angles can both be fitted with Eq. (2.4), using an inelastic mean free path of $\lambda = 3$ nm. Thereby, the 80° fit curve only differs from the the 0° fit parameters by the factor of cos(80°) accounting for the reduced information depth in 80° emission. The good agreement for both angles is an unambiguous indication for a two-dimensional
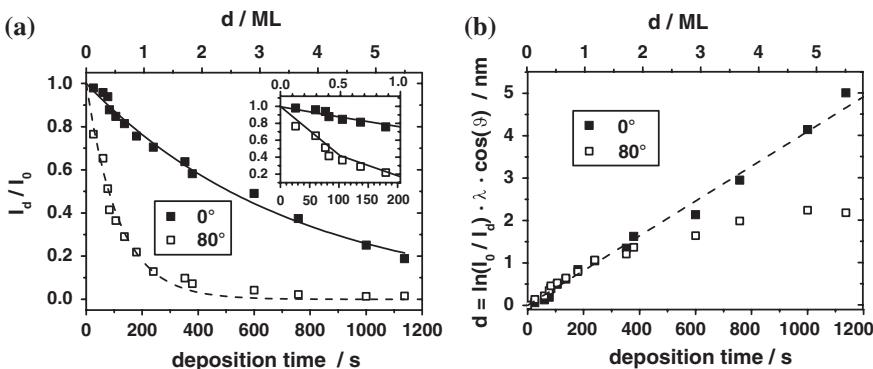

Fig. 4.9 a The exponential decay of the Au 4f substrate signal in dependence on the deposition time and thus on the amount of IL deposited. The curves are fits to the data using Eq. (2.4) with an inelastic mean free path λ of 3.0 nm and the corresponding detection angles. The insert shows that the polygon-like fit expected for strict layer-by-layer growth yields the same level of agreement with the experimental data. **b** The thickness of the deposited $[C_8C_1Im][Tf_2N]$ films, calculated from the damping of the Au 4f signal using Eq. (4.1), plotted vs. the deposition time. After about 200 s, a coverage of 1 ML is reached. The deviation of 80° emission data is assigned to elastic scattering effects

layer-by-layer growth mode. In more detail, for strict layer-by-layer growth the decrease of the substrate signals should evolve in a section-wise linear fashion during completion of each layer (i.e., a full completion of a layer is achieved before a new layer starts to grow on top; for a general discussion on growth mode studies using XPS or Auger electron spectroscopy, see e.g., Ref. [76]). Therefore, also plotted in the insert in Fig. 4.9a are linear sections for the first two molecular layers, assuming that each molecular layer adsorbed in a checkerboard geometry corresponds to a coverage of 0.5 ML. Apparently, the number of data points and the statistics are not good enough to unequivocally resolve slope changes between adjacent straight sections (note that each investigated layer was prepared separately). However, the good agreement of the data points with the exponential behaviour unequivocally points towards a two-dimensional growth mode for both emission angles.

The layer-by-layer growth is also evident from the increase of film thicknesses with evaporation time in Fig. 4.9b, calculated with Eq. (4.1) from the damping of the Au 4f signal: It clearly shows a linear increase up to 5.4 ML for the normal emission measurements. The data for 80° show perfect agreement up to ~2 ML. For higher coverages a deviation from the straight line towards lower values is observed; this is also evident from the data for >400 s in Fig. 4.9a, which slightly lie above the fit. The deviation in 80° for the thicker films is not unexpected because elastic scattering effects that mainly contribute for grazing photoelectron detection come into play, leading to higher substrate intensities and therefore to lower film thicknesses [77]. Another reason could be minor signal contributions from the sample edge, which are difficult to suppress completely at 80°. In summary, the 0° and 80° data in Fig. 4.9a and b independently clearly indicate a layer-by-layer growth mode of $[C_8C_1Im][Tf_2N]$ on Au(111).

It should be noted that similar attenuation characteristics of the Au 4f signals were also measured for the deposition of $[C_1C_1Im][Tf_2N]$ on Au(111), indicating two dimensional growth characteristics for this IL, too. However, during the deposition experiments conducted with $[C_1C_1Im][Tf_2N]$, evaporation rates were not as stable as for the experiments using $[C_8C_1Im][Tf_2N]$ and $[C_4C_1Pyrr][Tf_2N]$. Therefore, a plot similar to that in Fig. 4.9 is not possible due to the erroneous values of deposition times (x-axis). However, evidence for the conclusion that $[C_1C_1Im][Tf_2N]$ also grows in a layer-by-layer structure is provided in Fig. 4.10, where the calculated thickness d(80°) derived from the attenuation of the 80° Au 4f intensities is plotted versus d(0°) for both $[C_8C_1Im][Tf_2N]$ and $[C_1C_1Im]$ $[Tf_2N]$, documenting excellent agreement between the growth characteristics of the two ILs, therefore providing an indirect proof for layer-by-layer growth of $[C_1C_1Im][Tf_2N]$.

The findings discussed so far for the imidazolium-ILs can be transferred without reservations to the behaviour observed for $[C_4C_1Pyrr][Tf_2N]$, as is detailed in Fig. 4.11. Again, very good agreement of the 0° and 80° emission data with the expected exponential damping behaviour is found for low IL coverages, whereas only for the 80° curves deviations are observed, in analogy to the findings for $[C_8C_1Im][Tf_2N]$. Note that in both evaporation series the deviation of the 80°
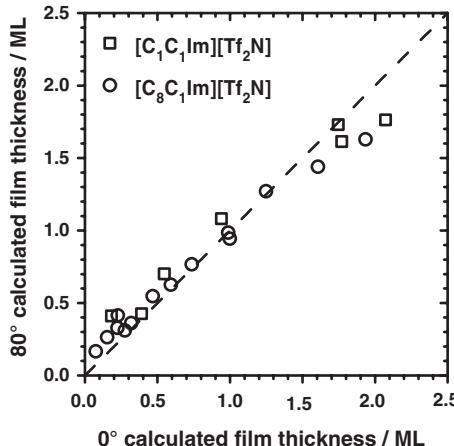
Fig. 4.10 Thickness of [C$_1$C$_1$Im][Tf$_2$N] and [C$_8$C$_1$Im][Tf$_2$N] layers, as calculated from the damping of the Au 4f signals. The data for 0° and 80° have been independently determined from Eq. (4.1) using the same inelastic mean free path of 3.0 nm. For both ILs the data fall right onto the *dashed line*, indicating perfect agreement of the analysis based on the 0 and 80° data set. The behaviour is strong evidence for two-dimensional growth of both ILs

curve from a linear behaviour starts at an overall IL film thickness of ~1.5 nm, independent of the IL used. In summary, the attenuation behaviour of the substrate signals and the calculated film thicknesses shown in Fig. 4.11a and b clearly indicate a layer-by-layer growth of [C$_4$C$_1$Pyrr][Tf$_2$N] on the Au(111) single crystal similar to that observed for the two imidazolium ILs on gold.

Interestingly, the results of two-dimensional growth for all three ILs on Au(111) differ from the growth behaviour found for [C$_2$C$_1$Im][Tf$_2$N] on glass where only for the first layer two-dimensional growth is found, followed by three dimensional growth of IL islands [49]. This is possibly related to the adsorption behaviour and molecular orientation in the first layer, where on glass a double layer formation with the anions above the cations was reported, whereas on Au(111) the checkerboard arrangement with anions and cations both in contact to the substrate was found.

4.3.1.5 Radiation Damage

As the investigation of ultrathin IL films by XPS requires sufficiently long measurement time in order to obtain reasonable signal-to-noise ratios, the influence of radiation-induced spectral changes has to be addressed. In the following this issue is discussed for [C$_1$C$_1$Im][Tf$_2$N]; however, the derived conclusions also apply to the other two [Tf$_2$N]$^-$ ILs [C$_8$C$_1$Im][Tf$_2$N] and [C$_4$C$_1$Pyrr][Tf$_2$N] on Au(111).

In Fig. 4.12, F 1s, N 1s and C 1s core level spectra of a 0.5 ML [C$_1$C$_1$Im] [Tf$_2$N] film (closed layer of anions and cations in direct contact with the substrate,
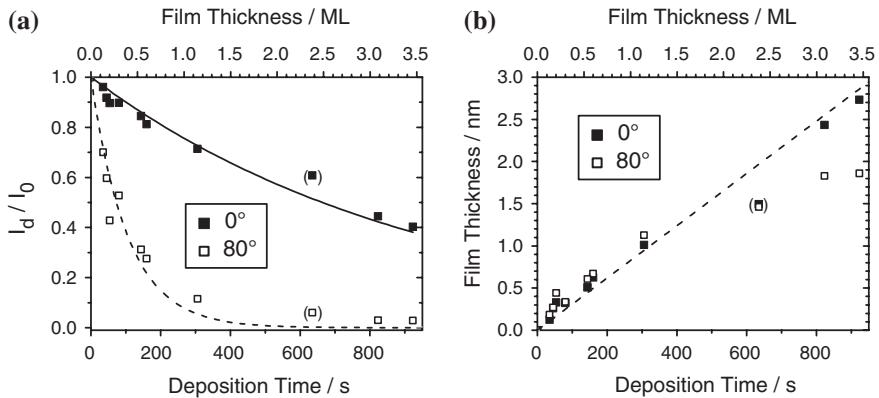
Fig. 4.11 Growth analysis of [C$_4$C$_1$Pyrr][Tf$_2$N] thin films; **a** Damping of the Au 4f signal plotted against the deposition time, black data points are 0° emission, while open symbols are measured in 80° emission. The *black line* shows the fit to the 0° data, while the dashed line represents the damping estimated from the solid 0° emission fit line according to Eq. (2.4). **b** Thickness values derived from 0° emission data (*black*) show a linear increase, while the 80° emission values (*open symbols*) increase linearly up to a film thickness of about 1.5 nm. At higher coverages, the 80° values show an apparent tend towards lower values which is assigned to elastic scattering effects. The data points in brackets are outliers and were not included in the fit
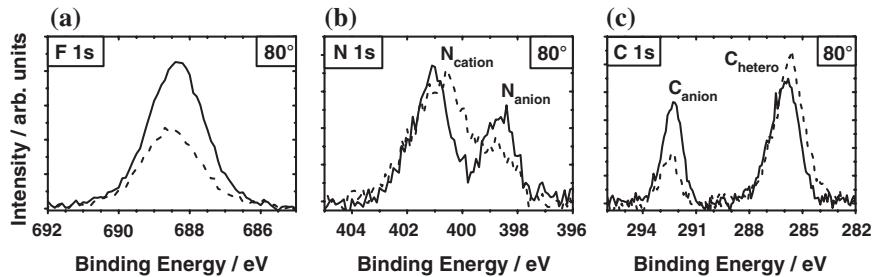

Fig. 4.12 The development of XP spectra of a 0.5 ML PVD film of [C$_1$C$_1$Im][Tf$_2$N] over time during irradiation with Al-K$_\alpha$ radiation. The spectra shown are recorded under 80° emission and were taken after 1 h (*solid line*) and after 9 h (*dashed line*) total exposure time. The F 1s signal of the anion **a** decreases during the 9 h irradiation to about one half. In the nitrogen region **b** a similar decrease is observed for the N$_{anion}$ peak whereas the N$_{cation}$ peak hardly changes its intensity; between the two peaks, a new component arises at about 400 eV, with the total intensity in the N 1s region remaining constant. The C 1s region **c** reveals a decrease in intensity of the C$_{anion}$ peak whereas the C$_{hetero}$ peak slightly increases in intensity and shifts to lower BEs

see Scheme 4.1b) are shown, as measured at 80° at a mean X-ray exposure of 1 h (= typical measuring time, solid line) and after 9 h (dashed line). After 9 h, an intensity loss of the C$_{anion}$ 1s and the F 1s peaks of about 50 % compared to the 1 h spectra is observed; this clearly indicates that about half of the CF$_3$ groups of the anion have disappeared from the IL film. The N$_{anion}$ peak at ~398.8 eV decreases by roughly a factor of two, and concomitantly, the change in the shape

of the N 1s spectra indicates the formation of a new nitrogen species between the N_{cation} and N_{anion} peak, i.e. at ~400 eV. Since the total N 1s intensity remains constant, the radiation-induced decomposition indicates a stoichiometric conversion of the anion to a new nitrogen species adsorbed at the gold surface. The C_{cation} signal slightly increases by about 20 % and shifts towards lower BE by ~0.2 eV, with the peak width remaining nearly the same.

To investigate the influence of film thickness on beam damage, several $[C_1C_1Im][Tf_2N]$ films between 0.5 and 5 ML thickness were measured at 0° emission (bulk sensitive geometry), after a prolonged exposure time of 3 h for each layer. From these spectra, the ratio C_{hetero}/C_{anion} is determined and is plotted in Fig. 4.13. This ratio can be taken as a measure for the degree of beam damage in the studied layers: For a stoichiometric film a ratio of 5:2 = 2.5 is predicted (indicated as dashed line) and for a loss of CF_3 groups due to beam damage a deviation to larger values is expected. This is indeed observed, with the effect being pronounced for the thin films and approaching the expected value at high film thicknesses. Obviously, the radiation-induced decomposition process occurs more efficiently (faster) for lower film thicknesses, with the effect strongest for molecules in direct contact with the gold surface (coverage below 0.5 ML), i.e. at the gold/IL interface.

In order to explain the intensity changes in the XP spectra of the thin $[C_1C_1Im]$ $[Tf_2N]$ films on Au(111), we propose the following scenario: For the 0.5 ML film (Fig. 4.12) the simultaneous loss of F 1s and C_{anion} intensity after X-ray exposure clearly indicates the decomposition of anions adsorbed at the gold surface with the formed CF_x-containing species desorbing into the gas phase; thus, these species are no longer observed in XPS. The residual anion fragment is still present in the film and is characterized by the new N-containing species with the N 1s BE of ~400 eV. Measurements performed on an a ~7 nm thick film show a
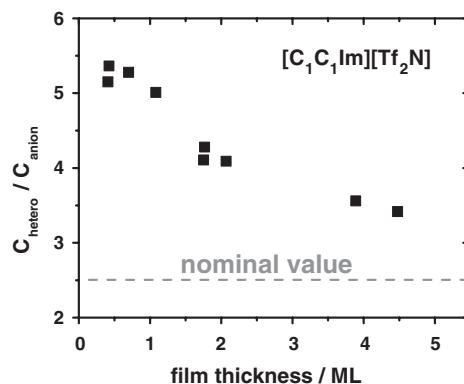
Fig. 4.13 Ratio of C_{hetero}/C_{anion} plotted versus film thickness for the 0° emission spectra after prolonged (3 h) exposure to Al-K_α radiation. The *dashed line* indicates the nominal ratio of 5:2 for stoichiometric composition, which is observed for shorter exposure times. With increasing film thickness the ratio approaches the nominal value
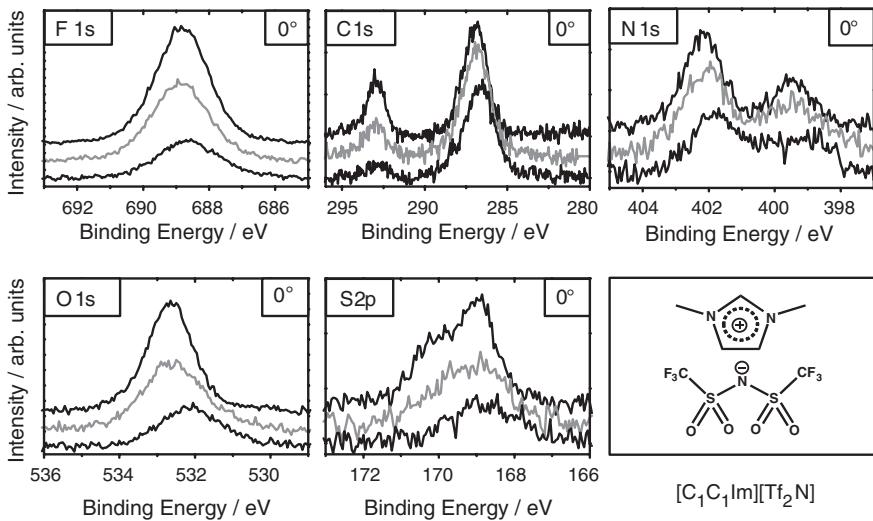
Fig. 4.14 Time-development of radiation damage of a 7 nm $[C_1C_1Im][Tf_2N]$ film measured at $0°$ emission. Shown are spectra taken after a mean exposure of 1 h (*top*), 6 h (*middle*), and >12 h (*bottom*). Core level scans of all IL regions are shown. Anion-related signals C_{anion} 1s, F 1s, S 2p and O 1s show a concomitant decrease over time, while C_{hetero} 1s and the overall nitrogen signal retains the same intensity. From this behaviour it is concluded that radiation damage mainly occurs at the anion cleaving the S–N bond. While volatile S–O–C–F fragments leave the sample, the remaining new N-containing species has a different BE at ~400 eV. Spectra are offset for clarity

concomitant decrease of O 1s and S 2p signals, as depicted in Fig. 4.14. Together with the decrease of the CF_3-related signals this suggests that the anion is most likely cleaved at the N–S bond. The large peak shift of the imide nitrogen of about 1 eV to higher BE in the remaining fragment is in line with the formation of a new anionic (or neutral) nitrogen species.

The increase of the C_{hetero} signal in Fig. 4.12 by 20 % after exposure of the 0.5 ML film to X-rays for 9 h (Fig. 4.12) is attributed to damping effects. As discussed in the introduction of Sect. 3.2, for $[C_1C_1Im][Tf_2N]$, damping of the cation-related signals (N_{cation} and C_{hetero}) by the more bulky anions occurs at $80°$ (surface sensitive geometry). When the $[Tf_2N]^-$ anion is destroyed by radiation-induced fragmentation, the attenuation of cation-related XPS signals is reduced, which results in the observed moderate intensity increase of the C_{hetero} signal.

The higher degree of beam damage for the thinner layers indicates that the gold surface plays an important role for the decomposition process the $[Tf_2N]^-$ anions. Since secondary electrons from the substrate with low kinetic energies have a much larger penetration depth than the film thickness, it is most likely that the direct proximity of the surface is crucial for the decomposition, meaning that either long-lived intermediate states are stabilized or that the gold surface acts as a kind of catalyst for the anion decomposition.

4.3.1.6 Conclusions

The results presented in this chapter are the first results on the adsorption of ILs on a well-defined metal single crystal surface, namely $[C_1C_1Im][Tf_2N]$, $[C_8C_1Im]$ $[Tf_2N]$ and $[C_4C_1Pyrr][Tf_2N]$ on Au(111), under UHV conditions. Ultrathin IL films of increasing thickness were prepared in situ by physical vapour deposition (IL-PVD), a technique, which was recently introduced by our group [49]. In particular, the molecular arrangement and orientation of the ILs at the IL/metal interface and their successive growth were investigated using quantitative angle resolved X-ray photoelectron spectroscopy (ARXPS).

From the attenuation of the Au 4f signals with increasing IL coverage measured under 0° and 80° emission, layer-by-layer growth characteristics are unequivocally derived for all three ILs, up to thicknesses ~15 ML (~9 nm).

For $[C_1C_1Im][Tf_2N]$, pronounced chemical shifts towards lower BEs are observed for all IL-derived signals in the initial growth phase up to ~0.5 ML (corresponding to a closed layer of IL molecules). These shifts unambiguously indicate that both cations and anions are in direct contact with the Au surface, most likely in a checkerboard-like arrangement to guarantee charge neutrality. The cations are adsorbed in a flat geometry, i.e., with the imidazolium ring parallel to the surface, and the more bulky anions are preferentially adsorbed in a *cis*-configuration with the SO_2-groups pointing towards the gold substrate and the CF_3-groups towards the vacuum. In the case of $[C_8C_1Im][Tf_2N]$, with the additional octyl chain at the cation, a similar adsorption configuration within the first molecular layer ($\leq$0.5 ML coverage) is found, but with a slightly lower degree of order than for $[C_1C_1Im][Tf_2N]$. Around the completion of the first layer at 0.5 ML, a change in adsorption geometry occurs. Up to 0.4 ML coverage, a first layer has formed with anions and cations, including the alkyl chain, directly attached to the substrate. Between 0.4 and 0.5 ML, the neutral alkyl chains start to point away from the surface, providing space for additional cations and anions with their charged headgroups in direct contact with the surface. Also for $[C_4C_1Pyrr][Tf_2N]$, similar initial IL growth and formation of a checkerboard-like adsorption layer is found, where both ions are in direct contact with the surface and form a closed layer at 0.5 ML. However, for this IL no preferential vertical arrangement of the ions at the Au surface is observed, indicating a lesser degree of order within the interface layer as compared to the imidazolium ILs.

For all three ILs, at thicknesses above 0.5 ML, the BEs of the IL-related signals shift to higher values, which is attributed to the loss of direct interaction with the substrate and probably also due to reduced final state screening in the molecular layer as compared to the situation within the first (half)layer which is in direct contact to the Au substrate.

The two-dimensional growth characteristics of all three ILs on the Au(111) surface are quite different to results found for a similar IL ($[C_2C_1Im][Tf_2N]$) on amorphous silica substrates (glass) discussed in Chap. 5, where three dimensional film growth and different molecular arrangements at the interface (bi-layer with the cation preferentially adsorbed at the glass side) was observed [49]. This very

different behaviour clearly indicates a strong influence of the substrate surface on the bonding interactions leading to different growth modes of ILs.

Finally, beam damage induced effects were studied in detail as a function layer thickness. These studies show that (1) beam damage takes place in ultrathin films at prolonged exposure to the X-rays, (2) the effect is most pronounced in direct vicinity to the gold surface, and (3) decomposition predominantly occurs for the anion most likely by breaking S–N bonds and loss of smaller fragments (particularly CF_3-groups) to the vacuum.

To expand our knowledge of the IL/metal interface and to gain an understanding of the role of the support material, results obtained for $[C_1C_1Im][Tf_2N]$ thin films deposited on a Ni(111) surface are presented in the following section.

4.3.2 The Ionic Liquid/Nickel Interface

To gain a more detailed insight into the fundamental aspects of IL/metal interfaces and to increase the presently very small data base, in this section the adsorbate/substrate interaction, the molecular arrangement and orientation, the growth behaviour and the thermal evolution of $[C_1C_1Im][Tf_2N]$ on clean, oxygen-precovered and oxidized Ni(111) single crystal surfaces is investigated. The Ni(111) surface was chosen for multiple reasons. One main aspect is that it was found by the Wasserscheid group that when Raney nickel is treated with an IL layer, a drastic reduction in pyrophoric character is achieved, while the catalytic activity of the compound is not affected [20]. Secondly, for a surface science approach, Ni(111) is perfectly suited as it is a well-defined and relatively well understood system. Furthermore the reactivity of this surface towards oxygen under UHV conditions (oxidation takes places at mild temperature and low oxygen partial pressures) allows for reactivity studies and therefore opens up an approach to investigate the effect of IL impregnation on the reactivity of the system.

In this study IL growth characteristics are discussed first, followed by a detailed analysis of the ultrathin films addressing the interfacial arrangement of the ions and their electronic interaction with the surface. These results are compared with findings for ultrathin $[C_1C_1Im][Tf_2N]$ films on the Au(111) single crystal surface discussed previously (Sect. 4.3.1). In a second part the interactions of $[C_1C_1Im]$ $[Tf_2N]$ with an oxygen-precovered and an oxidized NiO surface are analysed and the thermal desorption behaviour of the IL from the different surfaces is investigated. Furthermore, the reactivity of the clean Ni(111) surface towards molecular oxygen is probed as a function of IL coverage on the surface.

It is shown that for coverages well below one monolayer, anions and cations are preferentially adsorbed in a sandwich structure on Ni(111), with the cation in direct contact with the Ni surface, while the anion sits on top pointing towards the vacuum. With increasing coverage a reorientation of the ions to a checkerboard-like structure is observed, similar to that found on Au(111). An overall preference for a checkerboard-type adsorption behaviour, i.e., anion and cation adsorbed

next to each other, is found on the oxygen-precovered O($\sqrt{3}$x$\sqrt{3}$)R30° Ni(111) surface. The thermal stability of adsorbed IL layers on these surfaces and on a fully oxidized Ni(111) surface was studied by heating the layers to elevated temperatures. For clean Ni(111), reversible adsorption takes place. For the oxidized surface, however, only cation-related moieties desorb, starting at ~450 K, while anion-related signals remain on the surface up to much higher temperatures. When exposing IL-precovered Ni(111) surfaces to molecular oxygen, it is found that for sub-monolayer coverages of increasing thickness a successive inhibition of the surface reactivity takes place. At this point it is necessary to mention that most experiments on Ni(111) have been carried out at lower temperatures compared to the Au(111) studies (note that the LN$_2$ cooled manipulator is vital for preparation of the clean Ni(111) surface as fast cooling rates are necessary after annealing of the sputtered crystal to avoid surface segregation of impurities). Thus, the thermal mobility of the adsorbed [C$_1$C$_1$Im][Tf$_2$N] molecules at the Ni surface was to some extend smaller than on Au(111). However, several IL films of different thickness were heated in control experiments up to room temperature which did not reveal significant changes in ARXPS; hence, it is safe to assume that the lower adsorption and measuring temperature of the Ni sample around 220 K is not a decisive factor for the results discussed in the following.

4.3.2.1 [C$_1$C$_1$Im][Tf$_2$N] Adsorption on Ni(111)

IL growth mode

Upon deposition of [C$_1$C$_1$Im][Tf$_2$N] on the Ni(111) surface (at 220 $\pm$ 20 K) a decrease of the Ni substrate signal (Figure 4.15a) is observed at 0°, due to attenuation by the adsorbed IL molecules. At 80° the decrease is much faster, due to the increased surface sensitivity. Assuming layer-by-layer growth, the data at 0° (solid squares) are fitted with a sectionwise linear decay (red solid lines in Fig. 4.15a) with each section ending on the exponential curve according to Equation (4.3) for a full layer; note that at normal emission the observed behaviour virtually cannot be distinguished from a continuous exponential decay (blue dotted line). Using an inelastic mean free path of $\lambda = 1.6$ nm for the Ni 2p$_{3/2}$ electrons with a kinetic energy of ~630 eV (see Experimental section) [60], a deposition rate of approximately 1.2 Å/min, corresponding to 0.16 ML/min, is deduced from the fit. Based on this rate, the behaviour at 80° (open diamonds), expected for perfect two-dimensional growth, is calculated and is also included in Fig. 4.15a (straight red lines ending at the green dotted curve for each completed layer). For the first layer, the corresponding linear decrease is in perfect agreement with the experimentally observed data at 80°, which confirms the assumption of two-dimensional growth of the first layer. While the 0° data are consistent with the expectation of layer-by-layer growth up to the highest investigated coverage of ~5 ML, the 80° data deviate from the expected behaviour already in the second layer, i.e., the data points lay above the predicted straight line segments. This deviation can partly be attributed to elastic scattering

effects, which come into play at high emission angles, but is, most likely, due to non-ideal layer-by-layer growth of $[C_1C_1Im][Tf_2N]$ films on Ni(111), starting in the second layer. In comparison, for the growth of $[C_8C_1Im][Tf_2N]$ films on Au(111) the attenuation of the substrate signals at 0° and 80° revealed a more perfect two-dimensional growth behaviour [1]. It should be noted at this point that the uncertainty in the absolute IMFP value ($\pm$ 10 %), as estimated from literature [60], leads to an uncertainty of identical magnitude in the calculated absolute film thickness values, but otherwise would not change the derived conclusions.

The Ni $2p_{3/2}$ intensities at a given deposition time did not show any changes after heating the sample from 220 K (i.e., the deposition temperature) to room temperature, indicating that the growth behaviour at these two temperatures is the same and that no dewetting, i.e., formation of three-dimensional islands, occurs at this temperature. This is particularly noteworthy as the original growth temperature is well below the melting point of the IL (T_m = 299.1 K, see Ref. [78]), where one could imagine a very low mobility. This observed behaviour is in agreement with findings by Souda *et al*., who deduced quasi-liquid layers for thin $[C_2C_1Im][Tf_2N]$ films on Ni(111) from their TOF-SIMS data at temperatures as low as 200 K [79].

Apart from the attenuation of the nickel signals as shown in Fig. 4.15a, additional information on the growth behaviour of $[C_1C_1Im][Tf_2N]$ on Ni(111) can be derived from the IL-derived C 1s, N 1s, and F 1s spectra taken at 80° emission angle (S 2p and O 1s spectra at 80° were not measured to minimise beam damage in the ultrathin layers; also, spectra of the IL-derived peaks at 0° were not measured. As changes in orientation from a bilayer (sandwich) arrangement to a checkerboard arrangement occur within the first layer, which go along with changes of the relative intensities of the anion- and cation-derived peaks (Figures 4.16 and 4.17), the sum of the C 1s signals and the sum of the N 1s signals are plotted in Figure 4.15b as a function of deposition time in order to average out these effects. For perfect two-dimensional growth, the IL intensities should increase sectionwise linearly, with the interceptions (intensities at complete successive layers) following Equation (4.4). Up to completion of the first layer, the C1s and N1s data agree with the red straight line in Figure 4.15b, which was obtained using an averaged IMFP for the C1s and N1s electrons of 2.6 nm. This behaviour is in very good agreement with the proposed two-dimensional growth of the first layer. The F1s data lie slightly above the blue straight line, obtained using the corresponding IMFP of 1.9 nm. While this difference is just above the error bars, it qualitatively fits due to the enrichment of the CF_3 groups at the outer surface (see Scheme 4.3a). For coverages above 1 ML, the experimental C 1s, N 1s and F 1s data lie below the corresponding straight lines, indicative of a deviation from perfect two-dimensional growth at these coverages. This observation is in line with the conclusion drawn from the damping of the Ni $2p_{3/2}$ signal in Fig. 4.15a.

Arrangement of ions at the Ni(111) surface and electronic interactions

Information on the arrangement of the IL ions at the Ni(111) surface can be derived from the C 1s and N 1s spectra in Fig. 4.16, collected at 80° emission: With increasing thickness of the IL layer, an overall increase of the peak intensities
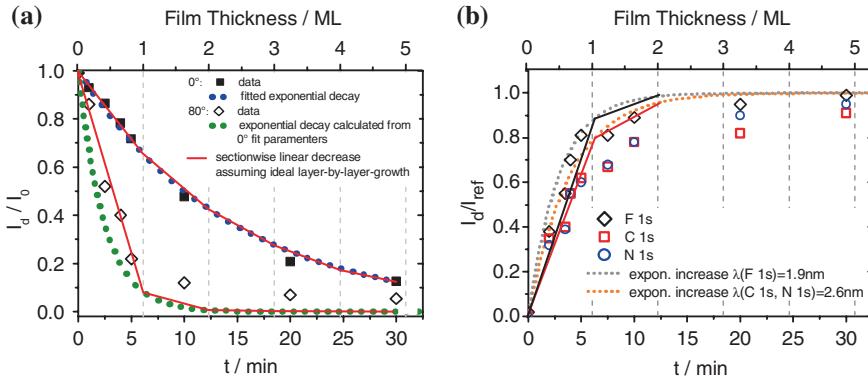
Fig. 4.15 **a** Decay of the Ni 2p$_{3/2}$ substrate signal as a function of deposition time and, thus, of the amount of IL deposited, for emission angles of 0° (solid squares) and 80° (open diamonds) with respect to the surface normal. The dotted blue line represents an exponential fit to the 0° data according to Equation (4.3), while the dotted green curve is calculated from the 0° fit parameters taking the additional factor cos 80° into account. An ideal two-dimensional layer-by-layer growth should follow along the red straight sections **b** 80° emission intensities of all measured IL-related signals (sum of all C 1s, red squares; sum of all N 1s, blue circles; F 1s, black diamonds), as a function of deposition time. The dotted lines follow an exponential increase according to Equation (4.4) taking different IMFP values into account. An ideal two-dimensional layer-by-layer growth should follow along the red (for C 1s and N 1s) and black (for F 1s) straight sections. (for details, see text)

is observed, as expected (see also Figure 4.15b). Concomitantly, the positions of the cation-related signals considerably shift towards higher BE values, whereas the anion related signals remain constant within ± 0.1 eV (as guide to the eye, the binding energy positions of the macroscopic reference film and the thin film for cation-related signals are indicated by dashed lines in Fig. 4.16). Also, relative intensity changes between the anion- and cation-derived signals are observed in Fig. 4.16 as will be thoroughly discussed below. Both effects suggest a distinct preferential arrangement of the IL at the interface. Also note that in the C 1s region a shoulder is observed at the low BE side of the C$_{cation}$ peak (~285 eV) for sub-ML coverages, due to a signal contribution from coadsorbed species (most likely CO and/or adventitious carbon C$_{adv}$) adsorbed at vacant sites of the Ni surface. This additional C 1s signal was accounted for by fitting an additional peak at 285.2 eV labelled "C$_{adv}$" (BE for CO on Ni(111), see Ref. [80]), as can be seen in Fig. 4.17.

In a first step we analyse the BE shifts observed for the IL layer in direct contact with the Ni surface, relative to those of the macroscopically thick film, which was deposited in-situ on the Ni(111) (as opposed to ex-situ preparation in the case of Au(111), see Ref. [1]): In Figure 4.17 spectra of three ultrathin films (0.15, 0.40 and 0.84 ML) are shown along with the spectrum of the thick film. Inspection of the C 1s and N 1s spectra reveals that the cation-related C$_{hetero}$ and N$_{cation}$ signals of the ultrathin layers (≤ 1 ML) are shifted to lower BE by 0.50 ± 0.10 eV relative to the thick layer, whereas the C$_{anion}$ and N$_{anion}$ signals do not display a significant shift (0.05 ± 0.10 eV). The preferential shifts of the cation-related signals to lower
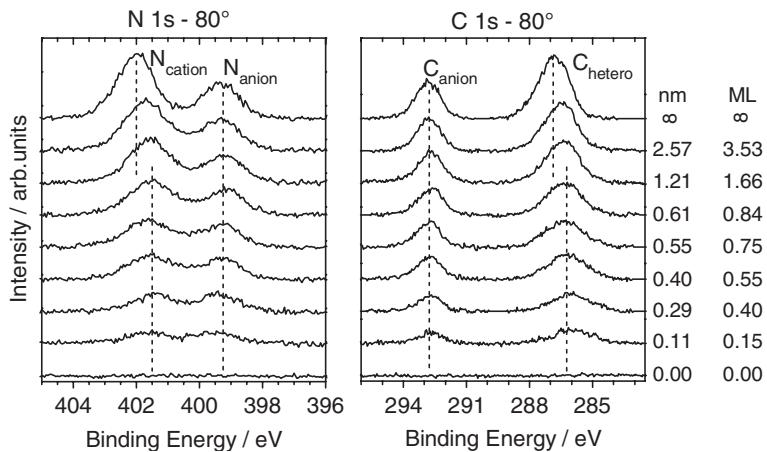
Fig. 4.16 Waterfall plots of N 1s and C 1s spectra of ultrathin [C₁C₁Im][Tf₂N] films deposited on Ni(111) at 220 K substrate temperature using IL-PVD, as a function of layer thickness. The topmost spectra represent a macroscopically thick IL film deposited in UHV. The spectra have been measured using Al-Kα radiation, at an emission angle of 80° with respect to the surface normal. The dashed lines serve as guide to the eye to analyse the BE shifts for cation-related signals N_{cation} and C_{hetero}
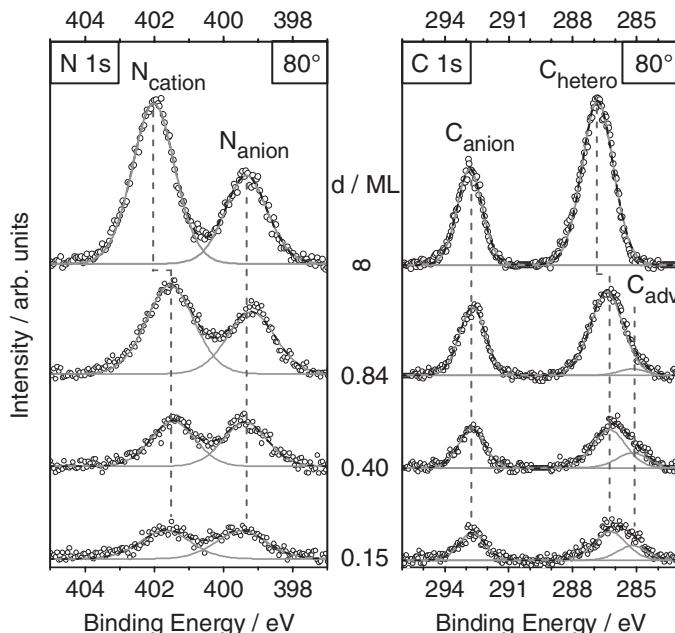
Fig. 4.17 Detailed analysis of three ultrathin IL films (selected spectra from Figure 4.16) and the macroscopic thick reference film. For details of the peak fitting, see text. The peak labelled "C_{adv}" at 285.2 eV in the C 1s region accounts for coadsorbed CO species

BE could be seen as a hint towards a specific electronic interaction of the cation with the substrate. However, since the shift is rather small compared to BE shifts observed in other IL/metal systems (see below) and as up to 1.66 ML no shifts are observed within the margin of error, such an argument has to be treated with caution. Alternatively, the differential shift between the cation- and anion-derived signals could also be due to differential screening of the doubly positively charged cation and the neutral anion after photoionization by the metal electron as a pure final state effect; however, this interpretation is speculative and requires theoretical support.

At this point it is interesting to compare the results for Ni(111) to those found for Au(111) at 0.4 ML [C_1C_1Im][Tf_2N] coverage [1]; there, considerably larger shifts to lower BE (relative to a thick IL layer) were found: 1.4 and 1.2 eV for C_{hetero} 1s and N_{cation} 1s, respectively, and 1.0 eV and 0.9 eV for C_{anion} 1s and N_{anion} 1s, respectively (see Table 4.10). Obviously, the electronic interaction for IL molecules in direct contact with Au(111) is different to adsorbed IL ions on the Ni(111) surface, as reflected by these differences in absolute BE positions. Notably, the relative (=differential) change of the BE difference between C_{hetero} 1s and C_{anion} 1s and the BE difference between N_{cation} 1s and N_{anion} 1s of the 0.4 ML film and the reference film on Au(111) amounts to 0.35 ± 0.10 eV. This relative BE shift is similar to the differential BE shifts of 0.45 ± 0.10 eV observed for Ni(111). For gold, the large overall shifts of all IL core levels (and the analysis of the relative intensities measured in ARXPS) led us to the conclusion that both anion and cation are adsorbed in a checkerboard arrangement next to each other at the Au(111) surface for coverages below 0.5 ML, resulting in a fully covered surface at $\theta = 0.5$ ML. The smaller shift for the anion-related C 1s and N 1s peaks was attributed to a geometry of the [Tf_2N]$^-$ anion in cis-configuration with the O atoms pointing towards the surface and the CF_3 groups towards the vacuum, namely being a result of the larger distance of C_{anion} and N_{anion} from the surface [1].

Detailed information on the adsorption geometry on Ni(111) and the mutual location of ions comes from the intensity ratios of the anion- and cation-related species. As was demonstrated for ultra thin IL layers on Au and for macroscopic IL films, the measuring geometry at emission angles of 80° is highly surface sensitive, so that

Table 4.10 BE values for selected thin [C_1C_1Im][Tf_2N] films in direct contact with the respective surface andfor the corresponding thick films. The thick Ni film was manually deposited in the UHV system (see experimentalsection for details), while the thick IL film on gold was evaporated

| System	Binding energy position/eV			
	C_{hetero}	C_{anion}	N_{cation}	N_{anion}
Ni: thick layer, in situ deposited	286.84	292.84	402.02	399.34
Ni: submonolayer[1]	286.35 ($\Delta = 0.49$)	292.75 ($\Delta = 0.09$)	401.55 ($\Delta = 0.47$)	399.30 ($\Delta = 0.04$)
Au: thick layer, evaporated[2]	287.09	293.09	402.19	399.44
Au: 0.4 ML	285.68 ($\Delta = 1.41$)	292.12 ($\Delta = 0.97$)	401.01 ($\Delta = 1.18$)	398.57 ($\Delta = 0.87$)

[1]Average value of 5 layers with coverages below 1 ML (± 0.10 eV); [2]Used as BE reference in Ref. [1]

surface enhancement of parts of the ions (i.e., alkyl chains or CF3 groups) can be identified by intensity analysis (see also Chapters 3.2 and 4.3.1) [55, 58, 66, 1].

For the ultrathin $[C_1C_1Im][Tf_2N]$ layers of up to 0.40 ML on Ni(111), a pronounced enhancement (by a factor of ~2) of the anion-related signals is observed in Figure 4.18 (note that the additional C 1s intensity at ~285 eV originating from the mentioned coadsorption of CO from the background pressure has been subtracted before the analysis): For N_{anion}/N_{cation} a ratio of about 1.03 ± 0.05 is found instead of the nominal value of 0.5 and for C_{anion}/C_{hetero} a ratio of 0.83 ± 0.05 instead of the nominal value of 0.4. At ~0.8 ML, both ratios have decreased significantly, and at higher coverages they approach the values of 0.55 (N 1s) and 0.47 (C 1s), which are measured for the reference bulk IL.

The strongly enhanced (by a factor of ~2) anion-to-cation-ratio up to 0.4 ML is attributed to a damping of the cation-related signals by $[Tf_2N]^-$ anions sitting on top of the cation in a sandwich arrangement as shown in Scheme 4.1 (bottom row, right) and Scheme 4.3a; this pronounced attenuation of the cation signal also implies that the imidazolium ring is lying flat, i.e., parallel to the surface plane. This sandwich or bilayer adsorption geometry at the IL/Ni interface is different to the adsorption behaviour found for $[C_1C_1Im][Tf_2N]$ on Au(111) at the same coverage (0.4 ML), where a N_{anion}/N_{cation} ratio of 0.62 and a C_{anion}/C_{hetero} ratio of 0.66 were found. There, it was concluded that the ions adsorb next to each other and form a checkerboard-like structure resulting in a surface completely covered with alternating anions and cations already at a nominal coverage of 0.5 ML (see Scheme 4.1 (bottom row, left) and Scheme 4.3b) [1].

For the macroscopically thick IL film on Ni(111) an almost stoichiometric anion-to-cation ratio is observed in the surface sensitive geometry of 80°, with values of
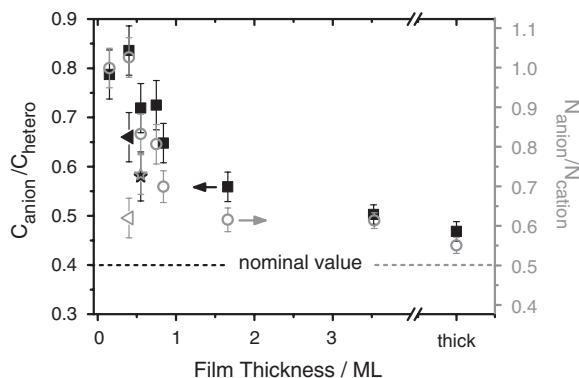
Fig. 4.18 Ratios of C_{anion}/C_{hetero} (*black symbols*) and N_{anion}/N_{cation} (*red symbols*): Ratios as a function of film thickness for $[C_1C_1Im][Tf_2N]$ on Ni(111) are plotted as solid black squares (carbon) and as solid red circles (nitrogen); data are derived from the XP spectra shown in Figs. 4.2 and 4.3. The black and red crosses are the 0.55 ML values observed for $[C_1C_1Im][Tf_2N]$ on the O-precovered $O(\sqrt{3} \times \sqrt{3})R30°$ surface and open black and red triangles are values for a 0.4 ML film of $[C_1C_1Im][Tf_2N]$ on Au(111) (error bars are omitted for clarity)

0.55 (nominal: 1:2 = 0.50) for N_{anion}/N_{cation} and 0.47 (nominal: 2:5 = 0.40) for C_{anion}/C_{hetero}; this is evident from Fig. 4.18, where the corresponding ratios are plotted vs. film thickness (slight enhancement of the C_{anion} signals due to the CF_3 groups pointing towards the vacuum side has been observed before—see Ref. [66]).

The N_{anion}/N_{cation} and C_{anion}/C_{hetero} ratios of the different systems are summarized in Table 4.11 and the deduced arrangements are illustrated in Scheme 4.3: for Au(111) the ions adsorb next to each other with the $[Tf_2N]^-$ anion in cis configuration leading to a geometry, where the CF_3 groups point towards the vacuum and therefore to a small C_{anion}/C_{hetero} enhancement. Also, a slight enhancement of N_{anion}/N_{cation} is observed as the anion is located slightly further away from the surface. These effects are most pronounced for 0.4 ML, i.e., a coverage around one closed layer of ions on the surface. For the Ni(111) surface, a different picture can be drawn: For coverages up to 0.4 ML the N_{anion}/N_{cation} and C_{anion}/C_{hetero} ratios are much larger than on Au(111), which is attributed to damping of the cation signals by the on-top sitting anions in a sandwich structure (note, that in such a sandwich structure the surface is fully covered at 1 ML as opposed to 0.5 ML in case of a checkerboard arrangement), see Scheme 4.1.

At higher coverages the intensity ratios decrease to values similar to the ones found for Au(111) at 0.4 ML, indicating that at these coverages the sandwich

Table 4.11 Relative intensities of anion- and cation-related species measured under 80° emission. Deviationsfrom the nominal values are a measure for the surface enhancement of one species, in this case of anion-relatedspecies. Values for the Au(111) single crystal are taken from Ref. [1]

System investigated	C_{anion}/C_{hetero}	N_{anion}/N_{cation}
0.4 ML on Ni(111)	0.83	1.03
0.4 ML on Au(111), see Ref. [1]	0.66	0.62
0.55 ML on Ni(111)	0.72	0.83
0.55 ML on O($\sqrt{3} \times \sqrt{3}$)R30° on Ni(111)	0.58	0.73
Thick film on Ni(111)	0.47	0.55
Thick film on Au(111)	0.47	0.55
Nominal	0.40	0.50
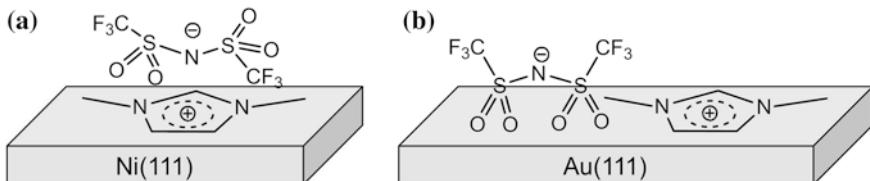
Scheme 4.3 Schematic sketch of the arrangement of $[C_1C_1Im][Tf_2N]$ on the Au(111) and Ni(111) surfaces. For Au(111) the ions adsorb next to each other in a checkerboard arrangement, while on Ni(111) a bilayer (sandwich) structure is found for low coverages up to ~0.4 ML. With increasing coverage the bilayer structure on Ni(111) changes into a checkerboard arrangement, which is attributed to increasing repulsive coulomb interactions with neighbouring ion pairs at smaller intermolecular distances

geometry is energetically no longer favourable and that a transition towards a checkerboard-like structure with alternately oriented ion pairs occurs. The driving force could be repulsive dipole-dipole interactions between neighbouring ion pairs with the same orientation at higher coverages (which are even enhanced by the image dipoles induced on the metal substrate). In contrast to that, the lateral interactions in the checkerboard arrangement are attractive, as all nearest neighbours have an opposite orientation of the dipole. In the sandwich arrangement, the repulsive lateral interactions increase with increasing coverage (hence, decrease in next neighbour distance), so that at a certain critical coverage the overall situation becomes unfavourable and a change towards a checkerboard arrangement occurs. At this point it is interesting to note that a sandwich arrangement at low coverages was also found for $[C_2C_1Im][Tf_2N]$ deposited on a glass sample, as will be discussed in Chap. 5[49].

4.3.2.2 $[C_1C_1Im][Tf_2N]$ Adsorption on Oxygen Precovered Ni(111) and on NiO

To investigate electronic interaction and ion arrangement at the oxygen-precovered Ni surface, a freshly prepared Ni(111) surface was exposed to O_2 (300 K, 1×10^{-8} mbar O_2, 10 min, ~6 L), until the LEED pattern of the well-known $(\sqrt{3} \times \sqrt{3})$ R30° superstructure was observed [82]. The Ni $2p_{3/2}$ and O 1s XP spectra of the clean Ni(111) and both oxygen-treated surfaces along with the LEED images are shown in Fig. 4.19. In addition, an oxidized NiO/Ni sample was prepared by exposing the Ni(111) crystal to a much higher oxygen dose (300 K, 1×10^{-6} mbar O_2, 5 min, ~300 L), resulting in a closed but not atomically flat oxide film [83]. The Ni $2p_{3/2}$ peak (topmost Ni spectrum in Fig. 4.19) exhibits the characteristic BE and shape of a pure Ni(II) species, i.e., NiO. From the intensity of metallic Ni(0) at 0° (i.e., in the bulk sensitive geometry, not shown), the oxide layer thickness is roughly estimated to ~1–2 nm. In the O 1s region two peaks are found, which are assigned to NiO (529.5 eV) and a hydroxyl species (531.0 eV) terminating the surface, in agreement with literature [84].

The comparison of the XP spectra obtained after dosing 0.55 ML of $[C_1C_1Im]$ $[Tf_2N]$ onto the clean Ni(111) surface and the oxygen-precovered Ni(111) surface is shown in Fig. 4.20, where the IL-derived peaks can be clearly observed in the C 1s, N 1s, F 1s and O 1s regions. The damping of the Ni $2p_{3/2}$ and O_{ads} signals is similar, indicating that the oxygen adlayer is not affected by the adsorbed IL. Furthermore, the Ni $2p_{3/2}$ and O_{ads} 1s signals remain at the same BE after IL exposure. On the oxygen-precovered surface, all IL-related signals display a uniform shift by ~0.7 eV to lower BE as compared to the clean surface. This uniform shift indicates a change in reference level for the adsorbate, due to the increased work function of the oxygen-precovered layer. The magnitude of the shift fits well to the reported work function increase of 0.7–0.8 eV upon oxygen chemisorption on Ni(111) [85–87], indicating a weak interaction (physisorption) of the IL with the substrate.

The analysis of the C 1s and N 1s peak ratios of the 0.55 ML IL on the oxygen-precovered surface reveals values of 0.58 for C_{anion}/C_{hetero} and 0.73 for N_{anion}/N_{cation},
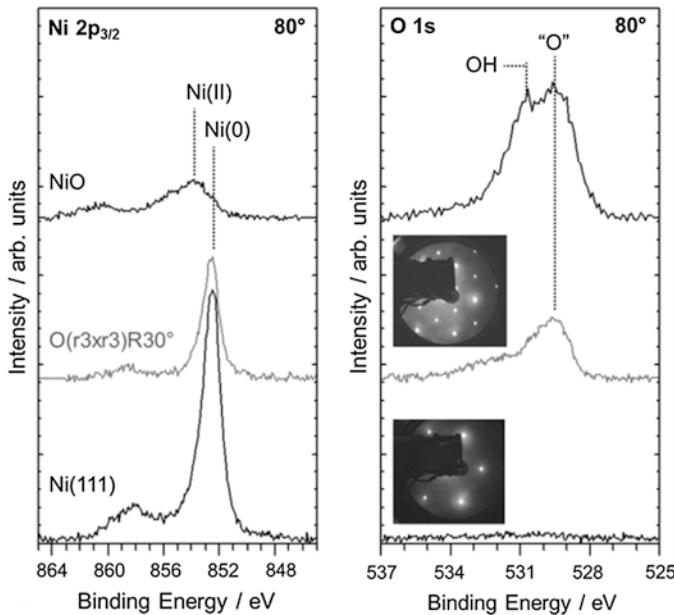
Fig. 4.19 Ni $2p_{3/2}$ and O 1s spectra of clean Ni(111), O-precovered O($\sqrt{3} \times \sqrt{3}$)R30° Ni(111) and a fully oxidized Ni surface before IL deposition. The spectra were measured using Al-K$_\alpha$ radiation, at an emission angle of 80° with respect to the surface normal. LEED pictures were taken at $E_{kin} = 114$ eV for O-precovered Ni(111) and $E_{kin} = 110$ eV for Ni(111). For preparation and spectral details, see text

which are lower than the corresponding values observed for a 0.55 ML film on Ni(111); see also Fig. 4.18. The values fall in the range of values found for Au(111) at the same IL coverage and for Ni(111) at higher IL coverages (see Table 4.11), indicating a preferential checkerboard-type arrangement for [C$_1$C$_1$Im][Tf$_2$N] on the O($\sqrt{3} \times \sqrt{3}$)R30° Ni(111) surface at this coverage.

We next address IL adsorption on the thin NiO layer: After deposition of nominally 0.75 ML [C$_1$C$_1$Im][Tf$_2$N] (estimated from the deposition time of 5 min), the IL-related peaks in Fig. 4.20 show up in the C 1s and N 1s spectra, as expected, and the substrate related Ni and O signals decrease due to damping by the IL. All IL signals are slightly shifted to lower BE (by 0.4 eV), as compared to deposition onto clean Ni(111), somewhat less than found on the chemisorbed oxygen layer (see above). Note that the true coverage could be smaller than the nominal value of 0.75 ML due to slight morphology changes (surface roughening) during oxidation. We refrain from extracting detailed information on adsorption geometries at the interface from the cation/anion intensities measured at 80° emission angle due to the unknown morphology of the underlying NiO surface. Nevertheless, for sake of completeness, it is mentioned that for the 0.75 ML film on NiO, an anion-to-cation ratio similar to the oxygen-precovered case is found.
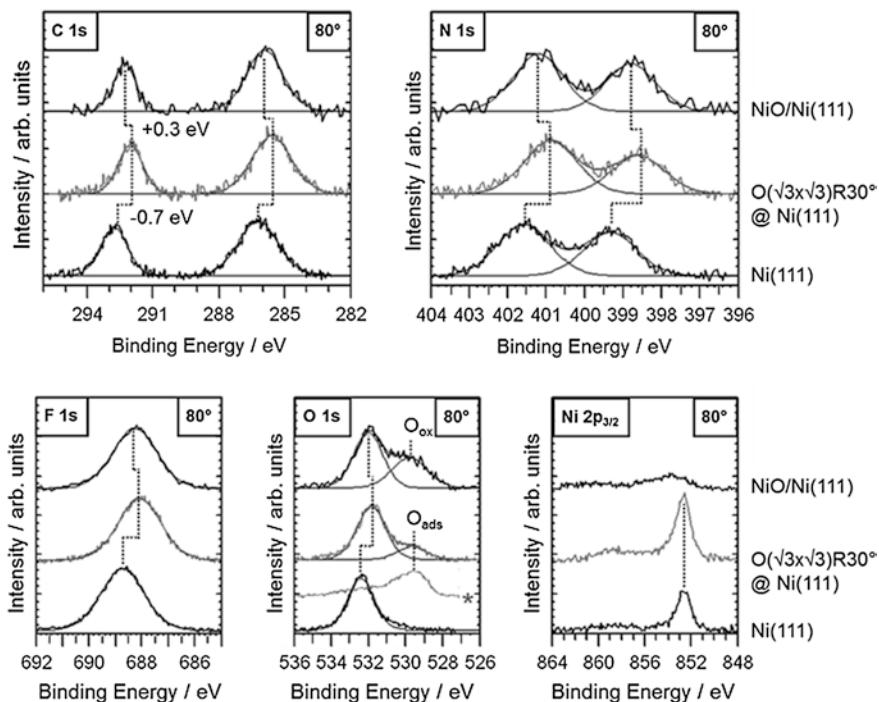
Fig. 4.20 Comparison of XP spectra after deposition of 0.55 ML [C$_1$C$_1$Im][Tf$_2$N] on Ni(111) (*bottom black spectra*), 0.55 ML IL on the O-precovered O($\sqrt{3} \times \sqrt{3}$)R30° surface (*middle grey spectra*) and 0.75 ML IL on the NiO surface (*top black spectra*); the O 1s spectrum labelled with an asterisk stems from the O-precovered O($\sqrt{3} \times \sqrt{3}$)R30° surface before IL deposition. The spectra were measured using Al-K$_\alpha$ radiation, at an emission angle of 80° with respect to the surface normal

4.3.2.3 Thermal Evolution of [C$_1$C$_1$Im][Tf$_2$N] on Ni(111) and on NiO

From the differences in adsorption behaviour and electronic interaction of [C$_1$C$_1$Im][Tf$_2$N] on Ni(111) and NiO one could envisage also differences in the thermal stability. To study the thermal evolution, two IL films with coverages of ~0.75 ML were prepared on Ni(111) and NiO/Ni(111) at 220 K and then heated to 400 K and thereafter to higher temperatures in 50 K steps (at each temperature the sample was held for 5 min); XP spectra were recorded after each heating step. This procedure was repeated until no IL signals remained. The results are summarized in Figs. 4.21 and 4.22.

For Ni(111), it is found that already after heating the sample to 400 K (which is 40 K below the evaporator temperature during IL deposition), all IL-related signals have almost vanished completely (Fig. 4.21). This is a strong indication that the IL desorbed intact from the surface, already at this rather mild temperature. Based on parallel decrease of both anion- and cation-related signals and the rather
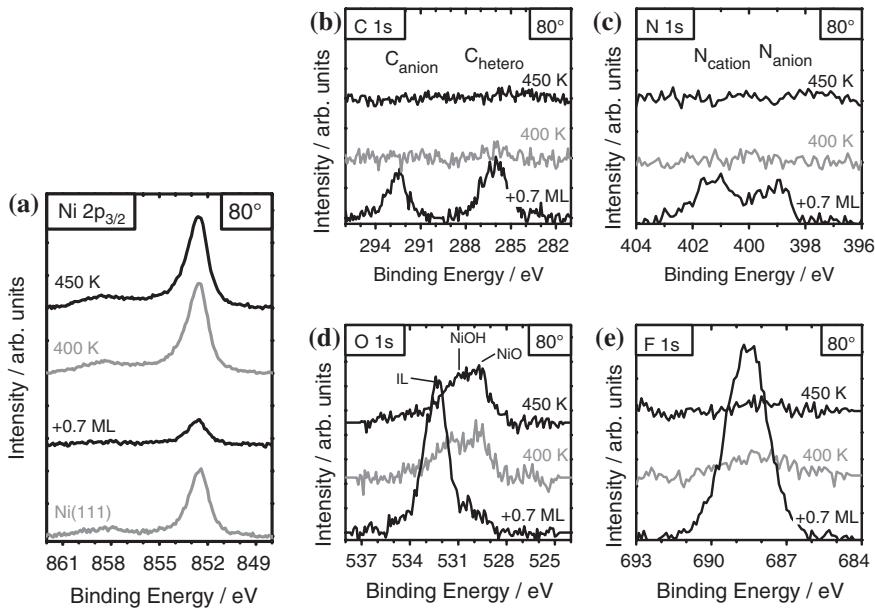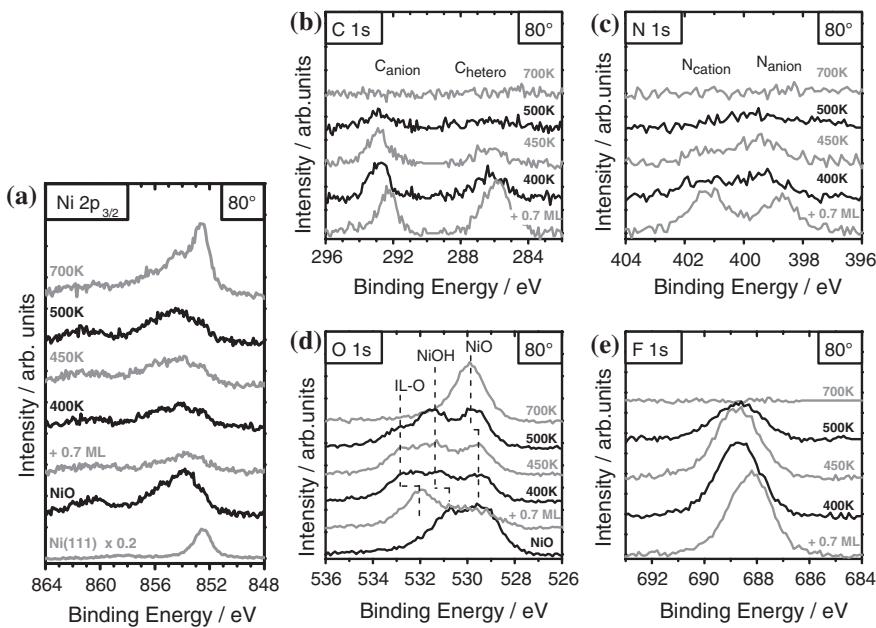
Fig. 4.21 XP spectra collected before and after heating 0.75 ML of [C₁C₁Im][Tf₂N] on Ni(111); the sample was heated in 50 K steps, until no IL signals were observed; only selected spectra are shown. The spectra were measured using Al-Kα radiation, at an emission angle of 80° with respect to the surface normal

low desorption temperature we propose that [C₁C₁Im][Tf₂N] desorbs in the form of NIPs. Further annealing to 450 K leads to desorption of the remaining minor IL signals leaving behind the bare Ni(111) surface. The remaining small O 1s signals (which were already present at 400 K) are assigned to small amounts of surface oxide (or chemisorbed O) and hydroxyl species due to dissociation of residual H_2O or O_2 on the liberated Ni(111) adsorption sites.

The situation on NiO is completely different (Fig. 4.22). After heating to 400 K, the cation-related signals (C_{hetero} and N_{cation} in Fig. 4.22b and c) do not disappear, but decrease to about 40 % of the initial intensity, and shift slightly to higher BE by ~0.5 eV. The anion-derived signals show a much smaller decrease to ~70 %, but significant broadening and a shift to higher BEs of 0.55 eV. Interestingly, also, the oxygen signal at 531 eV due to NiOH groups shows a shift to higher BE. Upon further annealing, the cation signals diminish at 500 K, while the anion-related signals remain visible (~50 %), but disappear at higher temperatures, too. Finally, after annealing to 700 K, all IL signals are gone. However, at this temperature, also, the NiO has already started to decompose, as is evident from the increasing metallic Ni(0) peak at 852 eV in the Ni 2p spectra in Fig. 4.22a, an effect which is known to occur for T > 550 K [88].

From the observed behaviour we conclude that [C₁C₁Im][Tf₂N] does not desorb from NiO as neutral ions pairs. On the other hand, there are no indications for

Fig. 4.22 XP spectra collected before and after heating 0.75 ML of [C$_1$C$_1$Im][Tf$_2$N] on an oxidized Ni(111) surface (see text for experimental details); the sample was heated in 50 K steps to 500 K and then to a final temperature of 700 K, only selected spectra are shown. The spectra were measured using Al-K$_\alpha$ radiation, at an emission angle of 80° with respect to the surface normal

chemical decomposition of either cation or anion, since the ratios of both cation-(N$_{cation}$/C$_{hetero}$) and anion-related (C$_{anion}$/N$_{anion}$/F) signals remain unchanged with temperature, indicating intact desorption of the respective ions. For the imidazolium cation one could imagine the following possible scenario: the cation can pair up with the OH groups terminating the NiO surface to form [C$_1$C$_1$Im][OH] which will further react to H$_2$O and the corresponding carbene [89]. At elevated temperatures, these neutral molecules would leave the surface immediately upon formation. In this scenario, the anion initially remains on the surface pairing with the vacant Ni ion and would then, at higher temperatures, desorb either together with some other cationic species or as a neutral molecule (after some further reaction). At this point this proposed mechanism has to be considered as speculative. Additional information on the mechanism of this complex desorption behaviour could be gained using temperature programmed desorption (TPD) techniques, which are not available in our experimental setup.

4.3.2.4 Reactivity of IL-Precovered Ni(111) Towards Molecular Oxygen

Systematic investigations (currently performed by the Wasserscheid group) of Raney nickel catalyst (RNC) impregnated with different hydrophobic ILs shows

a dramatic reduction of pyrophoric character when IL-coated RNC is exposed to air, whereas its catalytic activity remains intact and even enhanced selectivity is reported [20, 90]. Therefore, Ni(111) was used as a model substrate for investigating surface passivation effects after IL impregnation. From the previous chapter it has become evident that the Ni(111) surface is a rather reactive surface, which reacts with oxygen under quite mild conditions (RT, 10^{-6} mbar O_2) to form NiO layers, and is therefore ideally suited to perform in situ investigations on the effects of IL impregnation on the reactivity of the surface.

In Fig. 4.23, a comparison of two different preparation protocols is shown. First, the Ni(111) surface was treated with O_2 (300 K, 1×10^{-6} mbar O_2, 5 min, ~300 L) followed by deposition of ~0.75 ML IL (this system will be referred to as IL/O_2/Ni and serves mainly as a reference measurement for the following system). In a second experiment, an identical IL film was deposited on the freshly prepared clean Ni(111) followed by exposing the sample to the same amount of oxygen (this system is referred to as O_2/IL/Ni in the following). The Ni 2p and O 1s spectra of the system IL/O_2/Ni are shown in Figs. 4.23a and b, while the corresponding O_2/IL/Ni spectra are shown in Figs. 4.23c and d. The comparison of IL-related C 1s and N 1s signals of both systems is compiled in Fig. 4.23e and f.

The oxidized surface (grey spectra labelled O_2/Ni in Fig. 4.23a and b) has already been discussed in detail in Sect. 4.3.2.2. After IL deposition the NiO-related signals are damped by the IL overlayer and in the O 1s region an additional feature assigned to the $[Tf_2N]^-$-oxygen appears at 532 eV, which, as well as the other IL-related signals, is slightly shifted to lower BE (~0.4 eV) with respect to the BE position found for IL on clean Ni(111). This shift is, as discussed in Sect. 4.3.2.2, assigned to work function changes of the oxidized Ni surface. In summary, for the system IL/O_2/Ni the Ni(111) surface is first fully oxidized to a OH-terminated NiO overlayer, onto which the IL is deposited and stays intact. The system IL/O_2/Ni serves as a reference for the system of interest discussed in the following, where the reactivity of an IL-precovered surface towards molecular oxygen is investigated.

For the O_2/IL/Ni system displayed in Fig. 4.23, largely different observations are made; when IL is deposited on the clean Ni(111) surface, the substrate signal is damped and the IL BEs observed are according to the values discussed in Sect. 4.3.2.1 (i.e., BE of $[C_1C_1Im][Tf_2N]$ adsorbed directly at the Ni(111)). When this IL/Ni system is exposed to O_2, the Ni signal remains virtually unchanged and, thus, no appreciable bulk oxidation occurs, while in the O 1s region a minor shoulder at low BE emerges which is in the BE range of physisorbed oxygen (indicated by an arrow in Fig. 4.23d). Further insights can be gained from a comparison of C 1s and N 1s spectra of the systems IL/Ni, O_2/IL/Ni and IL/O_2/Ni as is shown in Fig. 4.23e and f. While the C 1s and N 1s BE positions for IL/Ni and O_2/IL/Ni are identical, a slight low BE shift of ~0.4 eV (see above) is detected for the IL/O_2/Ni system, which is assigned to work function changes of the oxidized surface. This observation is valuable as this low-BE shift can be taken as an indicator for the case where surface oxides build up upon O_2 exposure. The fact that for the O_2/IL/Ni system the IL signals remain at their initial BE indicates that no (or only
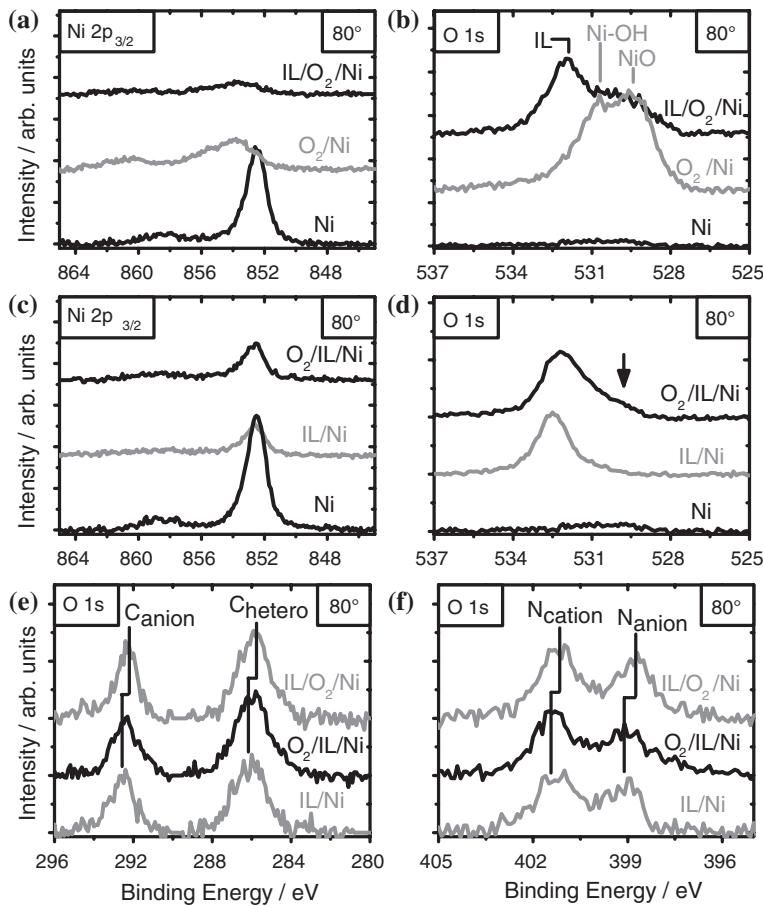
Fig. 4.23 Comparison of Ni 2p and O 1s spectra of two different preparation protocols IL/O$_2$/Ni **a**, **b** and O$_2$/IL/Ni **c**, **d** surface reactivity with and without IL deposition. **e** and **f** show the C 1s and N 1s regions of 0.75 ML films on Ni(111) before (IL/Ni) and after (O$_2$/IL/Ni) O2-treatment and an 0.75 ML film deposited on oxidized Ni(111) (IL/O$_2$/Ni). Spectra are recorded at electron emission angles of 80°

very little, see below) intercalation of atomic oxygen at the Ni/IL interface occurs, i.e. that the IL molecules mainly remain in direct contact with Ni(111) surface. However, upon close inspection of C 1s and N 1s spectra of the system O$_2$/IL/Ni a slight shoulder/broadening of the signals (more pronounced for anion-related signals C$_{anion}$ and N$_{anion}$) at the low BE side is observed, along with the small additional oxygen signal already mentioned above (indicated by arrow in Fig. 4.23d). Whether these minor spectral changes are a result of oxygen coadsorption/intercalation or are even an indication for some kind of reaction of the IL with oxygen from the gas phase, is not yet known. Nevertheless, considering that an intercalated O-layer would be subject to signal damping by the IL overlayer, a low BE

shoulder of the size as observed in Fig. 4.23d would roughly correspond to one full layer of intercalated oxygen (compare O_{ads} signal of IL/O($\sqrt{3} \times \sqrt{3}$) surface in Fig. 4.20, where 0.55 ML were deposited), which then should result in a low BE shift of *all* IL signals. Therefore, we interpret the slight shoulder (mainly present for anion-related signals O 1s, C_{anion} 1s and N_{anion} 1s) at low-BE to a direct interaction of gas phase oxygen with the IL. To gain further insights into possible surface passivation effects by preadsorbed IL layers, the surface oxidation dependent on IL coverage is discussed in the following.

For that purpose, in a further set of experiments the O_2/IL/Ni system was investigated in more detail by depositing increasing amounts of IL (0.15, 0.45 and 0.75 ML) on clean Ni(111), followed by exposure to the same oxygen dose as in the previous experiments. The corresponding spectra are shown in Fig. 4.24. While for the substrate-related Ni $2p_{3/2}$ and O 1s regions, the spectra for the bare oxidized surface are included for better comparison, in the IL-related C 1s and N 1s regions a spectrum of the 0.15 ML film before oxygen exposure is displayed (grey lines). First, in the case of the smallest coverage (0.15 ML), a more or less full oxidation of the Ni surface is observed (evident from the Ni 2p and O 1s spectra), while surprisingly the IL signals are broadened and decreased in intensity to such an extent that they can no further be identified as such. These findings indicate that—in contrast to the 0.75 ML case described above—for very low IL coverage IL decomposition seems to occur during the exposure to oxygen. It is known from the literature that oxidation of the Ni(111) surface proceeds from the step edges and propagates from there [91]. The fact that for such low coverages both IL decomposition and full oxidation of the Ni surface is observed, is tentatively assigned to the availability of non-IL-occupied reactive Ni sites (such as step edges and kinks), promoting highly reactive oxygen species, leading to both Ni-oxidation and IL decomposition.

For the oxygen-treated 0.45 ML film, largely different observations are made. Most importantly, the Ni $2p_{3/2}$ signal shows no significant signs of oxidation and also much less oxygen is observed in the O 1s region. Furthermore, the IL signals are clearly visible but are considerably shifted to lower BE, and also show a slight decrease and broadening for the anion-related signals. From the Ni 2p and O 1s spectra the conclusion can be drawn that even this partially covered surface completely inhibits the oxidation of the Ni surface, similar to the observation made for the 0.75 ML case. However, upon close inspection of IL-related signals (Figs. 4.24c and d) it becomes evident that the low BE shift observed for the cation (~0.49 ± 0.02 eV) and the anion (~0.93 ± 0.04 eV) signals is—according with our previous findings—attributed to IL adsorbed on O-precovered Ni(111). This implies that oxygen adsorbed at vacant Ni adsorption sites must be able to intercalate between the Ni and the IL adlayer resulting in an O interface layer that changes the work function and, therefore, leads to low BE shifts of IL signals. The low-BE shifts of IL-related signals as well as the conclusions drawn from the Ni $2p_{3/2}$ and O 1s spectra, i.e., that no mentionable bulk oxidation of Ni(111) occurs (as would be the case for the clean Ni(111) surface under similar oxygen exposure), indicate that only an O-intercalation-layer (chemisorbed atomic
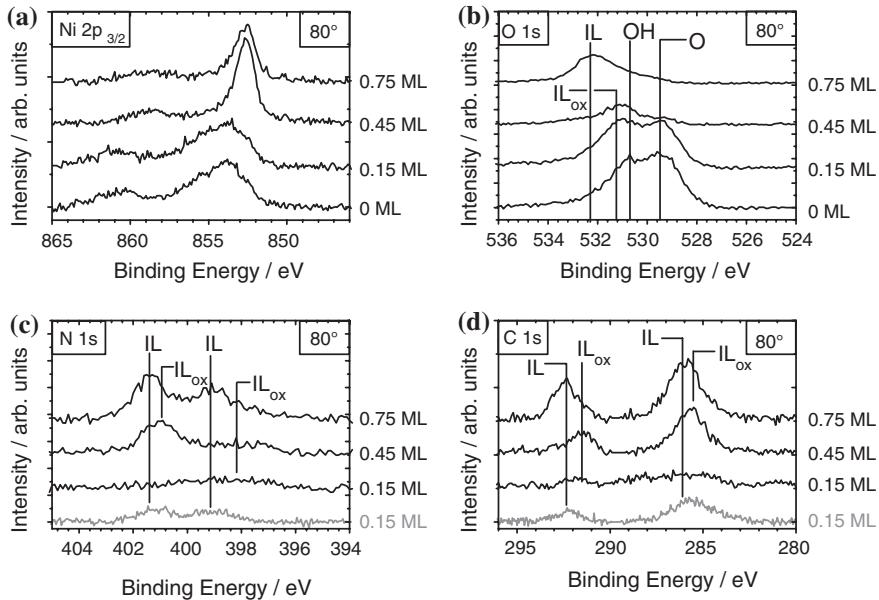
Fig. 4.24 Surface reactivity depending on IL coverage. The IL films of 0.15, 0.45 and 0.75 ML thickness were exposed to oxygen (for experimental details, see text). In the substrate related Ni $2p_{3/2}$ (**a**) and O 1s (**b**) regions the spectra of the bare oxidized substrate are included (labelled '0 ML'), while for the IL-related N 1s (**c**) and C 1s (**d**) regions the 0.15 ML film before oxygen treatment is shown (*grey spectra* labelled '0.15 ML')

oxygen) develops. Finally, for the 0.45 ML, the decrease in anion-related signals (N_{anion} and C_{anion}), accompanied by their more pronounced low-BE shift compared to the cation-related species, indicates additional O-induced decomposition effects similar to the oxidation of the 0.15 ML/Ni(111) system; in this case mainly the $[Tf_2N]^-$ anion seems to be affected.

Finally, as discussed previously, at a coverage of 0.75 ML, no changes in the Ni $2p_{3/2}$ spectra are observed while only a small shoulder in the O 1s emerges (already mentioned and partly discussed when comparing the systems $IL/O_2/Ni$ and $O_2/IL/Ni$), which one would intuitively attribute to intercalated oxygen as was discussed for an IL coverage of 0.45 ML. However, for the 0.75 ML film the BE values of the IL signals remain at the values observed for IL directly adsorbed at the Ni surface, indicating that O-intercalation does not take place (see detailed discussion above).

4.3.2.5   Conclusions

A detailed ARXPS study addressing the initial growth, the molecular arrangement and reactivity of ultrathin $[C_1C_1Im][Tf_2N]$ layers on clean, oxygen-precovered and

oxidized Ni(111) single crystal surfaces is presented in this chapter. IL films of increasing thickness were deposited on the clean Ni(111) surface using physical vapour deposition in ultra-high vacuum from a Knudsen cell. The results are compared to previous studies for the same IL on a glass substrate and on an Au(111) single crystal surface.

On the clean Ni(111) surface, IL growth was found to proceed in a two-dimensional fashion. The comparison to the behaviour on Au(111) showed some deviations from a perfect layer-by-layer growth after the completion of the first layer. From the detailed analysis of the BEs and intensities of the various IL-derived core-level peaks, and by comparison to the corresponding signals for a bulk IL film, information on the electronic interactions and on the molecular arrangement at the IL/solid interface was derived. Analysis of BEs revealed small differential BE shifts of the cation-related signals with respect to the thick film reference, while no such shifts were observed for the anion-related peaks. These findings are in contrast to the results on Au(111), where in addition to a similar differential BE shift a uniform shift of ~1 eV to lower BEs was found, which was assigned to an overall stronger coupling to the Au surface. The analysis of the XP spectra in the surface sensitive geometry, i.e., at an emission angle of 80°, shows for low IL coverages (up to 0.4 ML) a considerable enhancement of anion-related signals, indicating that the ions are arranged in a bilayer (or sandwich) structure, with the cation in direct contact with the Ni(111) surface and the anion sitting on top of the imidazolium ring. This finding strongly differs from the adsorption geometry found on Au(111) at the same coverage, where the ions adsorb next to each other in direct contact to the surface, in a checkerboard-like arrangement. Interestingly, the low-coverage bilayer structure on Ni(111) transforms into a checkerboard-like structure when increasing the IL surface coverage. The driving force for this transformation could be related to repulsive dipole–dipole interactions between neighbouring ion pairs with the same orientation, which increase due to the lower intermolecular distances at higher surface coverage; at a certain critical coverage the arrangement in a checkerboard-like structure, with attractive interactions of next neighbour ion pairs, becomes energetically favourable. Upon heating the sample the IL was found to desorb intact at temperatures as low as 400 K, which demonstrates rather weak interaction with the Ni(111) surface and is in agreement with the weak electronic coupling observed between $[C_1C_1Im][Tf_2N]$ and Ni.

For sub-ML IL films deposited onto an oxygen-precovered Ni(111) surface with a well-defined $O(\sqrt{3} \times \sqrt{3})R30°$ superstructure, all IL-derived signals are found to shift uniformly to lower BE by ~0.7 eV, which is attributed to a work function change due to the chemisorbed oxygen. This again indicates no (or only very little) electronic interaction between IL and substrate. In the 80° measurements, the enhancement of the anion-related species was found to be less pronounced than for the clean Ni(111) surface, but comparable to an IL film of similar thickness on Au(111), indicating a checkerboard-like arrangement of the IL.

$[C_1C_1Im][Tf_2N]$ adsorption on an oxidized Ni(111) surface also showed a uniform shift of the IL-derived peaks, which is again assigned to work function changes. Upon heating, a complex reaction/desorption behaviour of IL-related

species was found, in strong contrast to the reversible low-temperature desorption found for the IL/Ni(111) system. While the cation-related signals disappeared at relatively low temperature, the anion-related signals were found to remain on the surface up to temperatures above 500 K. As a tentative reaction pathway, a reaction between the imidazolium cations and hydroxyl groups terminating the NiO is proposed, where H_2O and carbene are formed and desorb as neutral molecules. The $[Tf_2N]^-$ anion pairs up with the remaining positive Ni centre and remains on the surface until oxide decomposition takes place.

When IL-precovered Ni(111) was exposed to molecular oxygen under conditions where normally considerable surface oxidation takes place, upon increasing IL coverage a significant inhibition of surface reactivity was observed with increasing IL layer thickness. The question to what extent the IL layer itself can be used to influence surface reactivity and selectivity will be subject to further investigations. In the future, the application of additional experimental methods such as temperature programmed reaction spectroscopy (TPRS) and STM experiments of thin IL films, and also theoretical investigations, are expected to be beneficial in order to obtain complementary information to the spectroscopic results presented in this work.

4.4 Summary

In this chapter ultrathin IL films were deposited on Au(111) and Ni(111) surfaces. To the best of our knowledge, these studies represent the first detailed investigations of thin IL films on well-defined single crystal surfaces under UHV conditions. They provide significant information on the interaction of the IL molecules with the substrate surface, the molecular arrangement at the interface and growth characteristics of ILs on different support materials, demonstrating the strong influence of the substrate properties on electronic and chemical interaction between IL and substrate and also on molecular orientation at the interface, on growth and on chemical reactivity.

In the course of these, studies the general growth behaviour of the ILs investigated turned out to be relatively similar for Au(111) and Ni(111), exhibiting a general trend of two-dimensional growth (more or less perfect layer-by-layer growth for Au(111) and slightly mixed growth for Ni(111)). Yet, both substrates prove to behave completely different with respect to electronic interaction and molecular arrangement at the interface. On Au(111), the ions adsorb next to each other directly at the old surface in a checkerboard-like arrangement exhibiting pronounced electronic interaction with the substrate. This arrangement leads to a fully covered surface at a nominal coverage of 0.5 ML. For the Ni(111) surface, completely different observations are made; here, for very low coverages, a pronounced bilayer structure is observed, where the cation is in direct contact with the Ni surface and the anion sits on top of the cation and is not in direct contact with the surface. Furthermore, electronic interactions between the Ni and the IL molecules are found to be rather weak.

From comparing three different ILs on Au(111), information on the influence of the IL nature could be derived; for $[C_1C_1Im][Tf_2N]$, a rather well ordered interface layer is found, with the cation lying flat on the surface and the anion adsorbed in a *cis*-conformation with the SO_2 groups in close proximity to the Au(111) and the CF_3 groups pointing towards the vacuum. A similar, yet slightly less ordered structure was found for $[C_8C_1Im][Tf_2N]$. In addition, the alkyl chain of the cation interacts with the Au surface for low coverages but—due to the lower interaction strength—detaches upon formation of one close IL layer (0.5 ML) to liberate adsorption sites for further ionic headgroups. In contrast to the two imidazolium ILs, no indications for an ordered interface layer is found for $[C_4C_1Pyrr][Tf_2N]$.

The reactivity of the Ni(111) towards oxygen under relatively mild conditions allows for IL deposition on differently oxygen-terminated surfaces (well-ordered $O(\sqrt{3} \times \sqrt{3})R30°$ superstructure and oxidized NiO surface), for which a more checkerboard-like adsorption geometry was deduced for the first adsorption layer, similar to the findings on Au(111). Furthermore, IL desorption experiments showed that the IL is relatively weakly adsorbed on Ni(111), resulting in stoichiometric IL desorption at relatively low temperatures. For the NiO surface, a complicated reaction with preferential desorption of cation-related species was deduced and is tentatively attributed to a reaction between terminal hydroxyl groups stabilising the NiO surface and the imidazolium ring. Finally, it is shown that the surface reactivity towards molecular oxygen is greatly reduced upon increasing IL layer thickness.

In the following chapter ultrathin IL films deposited on amorphous glass (Sect. 5.3.1) and ultra-pure fused silica (Sect. 5.3.2) samples are investigated in the context of the so-called "Nanolab" concept. The focus of these investigations lies in the molecular arrangement and IL growth behaviour of imidazolium-based IL on these support materials, and in approaches to modify the surfaces to obtain good substrate wetting and more uniform IL films.

References

1. T. Cremer, M. Stark, A. Deyko, H.-P. Steinrück, F. Maier, Langmuir **27**, 3662 (2011)
2. T. Cremer, L. Wibmer, S.K. Calderon, A. Deyko, F. Maier, H.-P. Steinrück, Phys. Chem. Chem. Phys. **14**, 5153 (2012)
3. P. Wasserscheid, T. Welton, *Ionic Liquids in Synthesis*, 2nd edn. (Wiley-VCH, Weinheim, 2008)
4. H. Weingärtner, Angew. Chem. Int. Ed. **47**, 654 (2008)
5. S. Werner, M. Haumann, P. Wasserscheid, Ann. Rev. Chem. Biomol. Eng. **1**, 203 (2010)
6. J.L. Anderson, D.W. Armstrong, G.T. Wei, Anal. Chem. **78**, 2892 (2006)
7. P. Sun, D.W. Armstrong, Anal. Chim. Acta **661**, 1 (2010)
8. J. Dupont, J.D. Scholten, Chem. Soc. Rev. **39**, 1780 (2010)
9. O. Höfft, F. Endres, Phys. Chem. Chem. Phys. **13**, 13472 (2011)
10. T. Fukushima, A. Kosaka, Y. Ishimura, T. Yamamoto, T. Takigawa, N. Ishii, T. Aida, Science **300**, 2072 (2003)
11. S. Baldelli, Acc. Chem. Res. **41**, 421 (2008)
12. W. Xu, C.A. Angell, Science **302**, 422 (2003)

13. P. Hapiot, C. Lagrost, Chem. Rev. **108**, 2238 (2008)
14. F. Endres, O. Höfft, N. Borisenko, L.H. Gasparotto, A. Prowald, R. Al-Salman, T. Carstens, R. Atkin, A. Bund, S.Z. El Abedin, Phys. Chem. Chem. Phys. **12**, 1724 (2010)
15. M. Forsyth, W.C. Neil, P.C. Howlett, D.R. Macfarlane, B.R.W. Hinton, N. Rocher, T.F. Kemp, M.E. Smith, Appl. Mater. Interf. **2009**, 1 (1045)
16. P. Riisager, R. van Hal Wasserscheid, R. Fehrmann, J. Catal. **219**, 452 (2003)
17. P. Mehnert, R.A. Cook, N.C. Dispenziere, M. Afeworki, J. Am. Chem. Soc. **124**, 12932 (2002)
18. Y.L. Gu, C. Ogawa, J. Kobayashi, Y. Mori, S. Kobayashi, Angw. Chem. Intl. Ed. **45**, 7217 (2006)
19. U. Kernchen, B. Etzold, W. Korth, A. Jess, Chem. Eng. Technol. **30**, 985 (2007)
20. M. Ehrig, D. Gerhard, M. Medved, K. Obert, P. Wasserscheid, US Patent 2008254971, 2008
21. Y. Gu, G. Li, Adv. Synt. Catal. **351**, 817 (2009)
22. R. Hayes, G.G. Warr, R. Atkin, Phys. Chem. Chem. Phys. **12**, 1709 (2010)
23. R. Atkin, N. Borisenko, M. Druschler, S.Z. El Abedin, F. Endres, R. Hayes, B. Huber, B. Roling, Phys. Chem. Chem. Phys. **13**, 6849 (2011)
24. M. Mezger, S. Schramm, H. Schroder, H. Reichert, M. Deutsch, E.J. De Souza, J.S. Okasinski, B.M. Ocko, V. Honkimaki, H. Dosch, J. Chem. Phys. **131**, 094701 (2009)
25. M. Mezger, H. Schroder, H. Reichert, S. Schramm, J.S. Okasinski, S. Schoder, V. Honkimaki, M. Deutsch, B.M. Ocko, J. Ralston, M. Rohwerder, M. Stratmann, H. Dosch, Science **322**, 424 (2008)
26. C. Pinilla, M.G. Del Popolo, R.M. Lynden-Bell, J. Kohanoff, J. Phys. Chem. B **109**, 17922 (2005)
27. S. Pensado, A.A.H. Pádua, Angew. Chem. Int. Ed. **123**, 8842 (2011)
28. S.A. Kislenko, I.S. Samoylov, R.H. Amirov, Phys. Chem. Chem. Phys. **11**, 5584 (2009)
29. R.M. Lynden-Bell, M.G. Del Popolo, T.G.A. Youngs, J. Kohanoff, C.G. Hanke, J.B. Harper, C.C. Pinilla, Acc. Chem. Res. **40**, 1138 (2007)
30. S. Bovio, A. Podesta, P. Milani, P. Ballone, M.G. Del Popolo, J. Phys.: Condens. Matter **21**, 424118 (2009)
31. L. Liu, S. Li, Z. Cao, Y.X. Peng, G.R. Li, T.Y. Yan, X.P. Gao, J. Phys. Chem. C **111**, 12161–12164 (2007)
32. N. Sieffert, G. Wipff, J. Phys. Chem. C **112**, 19590–19603 (2008)
33. M.L. Sha, F.C. Zhang, G.Z. Wu, H.P. Fang, C.L. Wang, S.M. Chen, Y. Zhang, J. Hu, J. Chem. Phys. **128**, 134504 (2008)
34. B.A. Fitchett, J.C. Conboy, J. Phys. Chem. B **108**, 20255 (2004)
35. J.B. Rollins, B.D. Fitchett, J.C. Conboy, J. Phys. Chem. B **111**, 4990 (2007)
36. C. Romero, S. Baldelli, J. Phys. Chem. B **110**, 6213 (2006)
37. C. Romero, H.J. Moore, T.R. Lee, S. Baldelli, J. Phys. Chem. C **111**, 240 (2007)
38. C. Aliaga, S. Baldelli, J. Phys. Chem. C **112**, 3064 (2008)
39. C. Aliaga, S. Baldelli, J. Phys. Chem. B **110**, 18481 (2006)
40. S. Rivera-Rubero, S. Baldelli, J. Phys. Chem. B **108**, 15133 (2004)
41. W. Zhou, S. Inoue, T. Iwahashi, K. Kanai, K. Seki, T. Miyamae, D. Kim, Y. Katayama, Y. Ouchi, Electrochem. Commun. **12**, 672 (2010)
42. Y.Z. Su, Y.C. Fu, J.W. Yan, Z.B. Chen, B.W. Mao, Angew. Chem. Int. Ed. **48**, 5148 (2009)
43. D. Borissov, C.L. Aravinda, W. Freyland, J. Phys. Chem. B **109**, 11606 (2005)
44. G.-B. Pan, W. Freyland, Chem. Phys. Lett. **427**, 96 (2006)
45. S. Perkin, L. Crowhurst, H. Niedermeyer, T. Welton, A.M. Smith, N.N. Gosvami, Chem. Commun. **47**, 6572 (2011)
46. S. Bovio, A. Podesta, C. Lenardi, P. Milani, J. Phys. Chem. B **113**, 6600 (2009)
47. J.P. Armstrong, C. Hurst, R.G. Jones, P. Licence, K.R.J. Lovelock, C.J. Satterley, I.J. Villar-Garcia, Phys. Chem. Chem. Phys. **9**, 982 (2007)
48. T. Cremer, Diplom Thesis, Friedrich-Alexander University Erlangen-Nuremberg, 2008
49. T. Cremer, M. Killian, J.M. Gottfried, N. Paape, P. Wasserscheid, F. Maier, H.-P. Steinrück, Chem. Phys. Chem. **9**, 2185 (2008)

50. M. Sobota, I. Nikiforidis, W. Hieringer, N. Paape, M. Happel, H.-P. Steinrück, A. Görling, P. Wasserscheid, M. Laurin, J. Libuda, Langmuir **26**, 7199 (2010)

51. M. Sobota, M. Schmid, M. Happel, M. Amende, F. Maier, H.-P. Steinrück, N. Paape, P. Wasserscheid, M. Laurin, J.M. Gottfried, J. Libuda, Phys. Chem. Chem. Phys. **12**, 10610 (2010)

52. M. Sobota, M. Happel, M. Amende, N. Paape, P. Wasserscheid, M. Laurin, J. Libuda, Adv. Mater. **23**, 2617 (2011)

53. T. Waldmann, H–.H. Huang, H.E. Hoster, O. Höfft, F. Endres, R.J. Behm, Chem. Phys. Chem. **12**, 2565 (2011)

54. L. Tamam, B.M. Ocko, H. Reichert, M. Deutsch, Phys. Rev. Lett. **106**, 197801 (2011)

55. K.R.J. Lovelock, C. Kolbeck, T. Cremer, N. Paape, P.S. Schulz, P. Wasserscheid, F. Maier, H.-P. Steinrück, J. Phys. Chem. B **113**, 2854 (2009)

56. A. Deyko, K.R.J. Lovelock, J.-A. Corfield, A.W. Taylor, P.N. Gooden, I.J. Villar-Garcia, P. Licence, R.G. Jones, V.G. Krasovskiy, E.A. Chernikova, L.M. Kustov, Phys. Chem. Chem. Phys. **11**, 8544 (2009)

57. C. Kolbeck, J. Lehmann, K.R.J. Lovelock, T. Cremer, N. Paape, P. Wasserscheid, A.P. Fröba, F. Maier, H.-P. Steinrück, J. Phys. Chem. B **114**, 17025 (2010)

58. T. Kolbeck, K.R.J. Cremer, N. Lovelock, P.S. Paape, P. Schulz, F. Wasserscheid, H.-P. Maier, J. Steinrück, Phys. Chem. B. **113**, 8682 (2009)

59. M. Keppler, T. Himmerlich, M. Ikari, E. Marschewski, O. Pachomow, W. Höfft, F. Maus-Friedrichs, S. Endres, Krischok. Phys. Chem. Chem. Phys. **13**, 1174 (2011)

60. S. Tanuma, C.J. Powell, D.R. Penn, Surf. Interf. Anal. **21**, 165 (1994)

61. D.C. Jackson, T.E. Gallon, A. Chambers, Surf. Sci. **36**, 381 (1973)

62. R.F. Roberts, D.L. Allara, C.A. Pryde, D.N.E. Buchanan, N.D. Hobbins, Surf. Interf. Anal. **2**, 5 (1980)

63. J.M. Gottfried, F. Maier, J. Rossa, D. Gerhard, P.S. Schulz, P. Wasserscheid, H.-P. Steinrück, Z. Phys, Chem. **220**, 1439 (2006)

64. C. Kolbeck, M. Killian, F. Maier, N. Paape, P. Wasserscheid, H.-P. Steinrück, Langmuir, **24**, 9500 (2008)

65. F. Maier, J.M. Gottfried, J. Rossa, D. Gerhard, P.S. Schulz, W. Schwieger, P. Wasserscheid, H.-P. Steinrück, Angw. Chem. Intl. Ed **45**, 7778 (2006)

66. T. Cremer, C. Kolbeck, K.R.J. Lovelock, N. Paape, R. Wölfel, P.S. Schulz, P. Wasserscheid, H. Weber, J. Thar, B. Kirchner, F. Maier, H.-P. Steinrück, Chem. Eur. J. **16**, 9018 (2010)

67. F. Maier, T. Cremer, C. Kolbeck, K.R.J. Lovelock, N. Paape, P.S. Schulz, P. Wasserscheid, H.-P. Steinrück, Phys. Chem. Chem. Phys. **2010**, 12 (1905)

68. S.Z. El Abedin, A.Y. Saad, H.K. Farag, N. Borisenko, Q.X. Liu, F. Endres, Electrochim. Acta **52**, 2746 (2007)

69. F. Endres, Z. Phys, Chem. **218**, 255 (2004)

70. R. Neubauer, C.M. Whelan, R. Denecke, H.-P. Steinrück, Surf. Sci. **507**, 832 (2002)

71. H. Koschel, G. Held, P. Trischberger, W. Widdra, H.-P. Steinrück, Surf. Sci. **437**, 125 (1999)

72. J.N.C. Lopes, K. Shimizu, A.A.H. Padua, Y. Umebayashi, S. Fukuda, K. Fujii, S.I. Ishiguro, J. Phys. Chem. B **112**, 1465 (2008)

73. F. Schreiber, J. Phys.: Condens. Matter **16**, 881 (2004)

74. S. Men, K.R.J. Lovelock, P. Licence, Phys. Chem. Chem. Phys. **13**, 15244 (2011)

75. G.A. Aliaga, S. Baker, J. Baldelli, Phys. Chem. B **112**, 1676 (2008)

76. G.E. Argile, Rhead. Surf. Sci. Rep. **10**, 277 (1989)

77. W.S.M. Werner, Surf. Interf. Anal. **31**, 141 (2001)

78. H. Tokuda, K. Hayamizu, K. Ishii, M. Susan, M. Watanabe, J. Phys. Chem. B **109**, 6103 (2005)

79. R. Souda, J. Phys. Chem. B **112**, 15349 (2008)

80. E. Fischermeier, T. Fauster, Poster Presentation, DPG Spring Meeting 2011

81. G. Held, J. Schuler, W. Sklarek, H.-P. Steinrück, Surf. Sci. **398**, 154 (1998)

82. T. Narusawa, W.M. Gibson, E. Törnqvist, Phys. Rev. Lett. **47**, 417 (1981)

83. T. Okazawa, T. Nishizawa, T. Nishimura, Y. Kido, Phys. Rev. B **75**, 033413 (2007)

84. J. Knudsen, L.R. Merte, G. Peng, R.T. Vang, A. Resta, E. Lægsgaard, J.N. Andersen, M. Mavrikakis, F. Besenbacher, ACS Nano **4**, 4380 (2010)
85. S. Evans, J. Pielasze, J.M. Thomas, Surf. Sci. **55**, 644 (1976)
86. S. Yamagishi, S.J. Jenkins, D.A. King, Surf. Sci. **543**, 12 (2003)
87. F. Mitchell, M.J. Graham, Surf. Sci. **114**, 546 (1982)
88. N. Kitakatsu, V. Maurice, P. Marcus, Surf. Sci. **411**, 215 (1998)
89. H. Rodriguez, G. Gurau, J.D. Holbrey, R.D. Rogers, Chem. Commun. **47**, 3222 (2011)
90. P. Wasserscheid, Erlangen, 2011, Personal communication
91. S. Hildebrandt, C. Hagendorf, T. Döge, C. Jeckstiess, R. Kulla, H. Neddermeyer, T. Uttich, J. Vac. Sci. Technol. A **2000**, 18 (1010)

Chapter 5
The Ionic Liquid/Glass Interface and the Nanolab Concept

Parts of the results in this chapter have been published in the following publications [1, 2]:

Chemical and (photo)- catalytical transformations in photonic crystal fibres [1].
Physical vapor deposition of [EMIM] [Tf$_2$(sub)N)]: A new approach to the modification of surface properties with ultrathin films [2].

The interface between ILs and silica is of great interest to the SCILL and, in particular, to the SILP concept introduced earlier. In these catalytic materials silica is used as a structural support for the IL/catalyst coatings due to its high surface area and porous structure. The interaction between the IL and the silica surface determines a number of performance-relevant properties such as wetting behaviour and IL growth characteristics, which are highly dependent on the chemical nature of both support material and IL. For these systems, the desired properties of the resulting IL films on the support material are such that a thin, uniform IL film is formed, thereby yielding the highest-possible surface area and short diffusion pathways through the IL. Such aspects are not only relevant to the SILP and SCILL systems, but also to research fields such as tribology (see Ref. [3] and references therein). It has, for example, been shown recently that ultrathin IL films on hydroxyl- and amino-terminated silicon surfaces can be prepared using a dip-coating procedure; these films have mean film thicknesses below ten nanometres and display outstanding lubrication characteristics [4].

The so-called "Nanolab" concept, which is a collaborative project within the Erlangen "Cluster of Excellence – Engineering of Advanced Materials", is an extension of the SILP concept. The inside walls of a light-guiding photonic crystal fibre (PCF) are modified according to the SILP-premises to obtain a reactor of μl volume (typical PCF dimensions: 0.1 mm in diameter and 1 m in length), which exhibits high catalytic activity and allows for in situ optical spectroscopy of reactants and products, or—in the best case—detection of transient species. For such a system, uniform IL films are not only a desired advantage leading to better performance, but are mandatory: irregular IL-film morphologies lead to IL-droplets and, consequently, to closures obstructing gas flow through the fibre core. Moreover, film inhomogeneity will lead to scattering effects of the guided light, reducing the optical performance of the PCF.

It was shown in the previous chapter that the combination of IL-PVD and ARXPS is a powerful tool in the study of interactions between the IL and a given support material and in the analysis of the wetting behaviour and initial growth phase of IL films. To investigate the IL wetting and growth behaviour on silica particles and inside the PCF walls, flat model substrates were used to deposit ultrathin IL films, followed by ARXPS measurements. In the course of these studies, non-ideal growth behaviour (three-dimensional growth and droplet formation) was observed for native, unmodified samples, leading to further investigations on surface modification and functionalization to yield more homogeneous IL coatings.

5.1 General Description of the Nanolab Concept and the Surface Science Approach

Based on the SILP technology, where a thin IL layer with a dissolved catalyst covers a high surface area support, the "Nanolab" approach presents an interesting and promising expansion. The main idea is the design of a sensor/nanoreactor within a light-guiding capillary channel (the PCF) with a SILP layer covering the inner walls of the channel(s). A schematic drawing of this approach is shown in Scheme 5.1. PCFs are light-guiding glass fibres (high purity fused silica with very low OH content), containing axial capillary channels, and can be tuned in a wide range with respect to both structure and light-guiding properties [5]. The light can be guided in both the hollow core (e.g., in a "Kagome" fibre) [6], and also within the silicate material of a solid core fibre (e.g., in a "Mercedes" fibre) [7], where the evanescent field allows for quantitative broadband sensing of species inside the hollow cladding of the fibre [8]. The PCF cross sections and SEM images of a hollow core and a solid core fibre, along with the corresponding intensity profiles, is shown in Fig. 5.1. Furthermore, it has previously been shown by our collaborating group of Philip Russel of the Max Planck Institute for the Science of Light, in
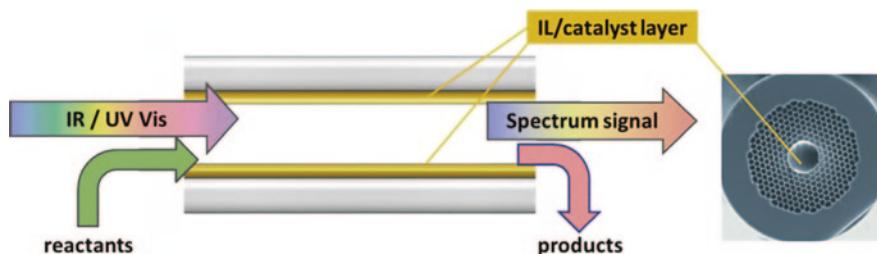
Scheme 5.1 Sketch of the Nanolab approach. The inside wall of a photonic crystal fibre is modified with a supported ionic liquid phase, i.e., an IL film with a dissolved catalyst. This setup will allow for in situ reaction monitoring, of reactants, products or even detection of reaction intermediates. Note that in case of the hollow-core fibre shown on the right the coating should be restricted to the walls of the inner core channel of the PCF, i.e., the area where most of the light is confined
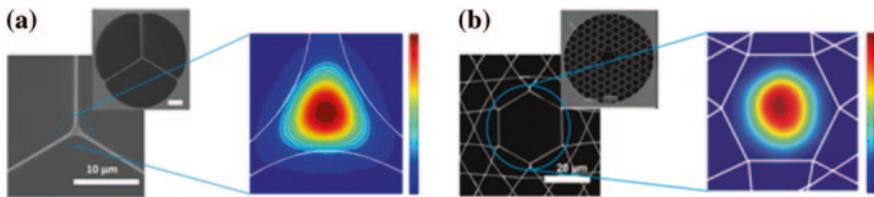
Fig. 5.1 Overview over two different PCF cross sections; **a** "Mercedes" fibre, where the light is guided in the solid core in the middle of the fibre, and **b** "Kagome" fibre, which is a hollow core band gap fibre, in which the light is guided in the hollow cavity of the fibre. For details, see Ref. [5]

Erlangen, that reaction monitoring is principally possible in PCFs; Chen et al. followed a photobleaching process in PCFs [9], while Cubillas et al. have expanded this concept to liquid phase photocatalytic reactions in a very recent study [1].

An operational setup for a Nanolab reactor requires the immobilization of the IL films along the fibre walls in a way that no droplet formation and/or clogging of the fibre occurs. In a typical SILP coating procedure, the IL films are prepared by impregnating the support with an IL dissolved in a volatile solvent, followed by evaporation of the volatile component [10]. As access to the PCF capillaries is only possible through the end of the fibre, a similar wet-chemical approach is also the most promising way to achieve fibre coating. In the best case, the inner wall of the fibre is covered completely with a homogeneous IL film, while the dissolved catalyst is enriched at the IL/gas interface. However, early experiments showed that it is extremely difficult to form uniform IL layers on the native glass surface along the whole fibre and that, in most cases, droplet formation and clogging of the fibre occurs. Possible reasons for the droplet formation will be thoroughly discussed in light of our own investigations presented below.

A promising approach to solve this problem is to introduce an interface functionalization layer, in which a functionalized IL is attached to the glass surface either by covalent bonding or through coulombic interactions. The resulting functionalized IL layer is then expected to beneficially influence the wetting behaviour of the IL. Both approaches utilize the availability of hydroxyl groups terminating the SiO_2 surface to anchor the IL molecules to the surface. Chi et al. have introduced the concept of attaching triethylsilylether functionalities to the side chain of the imidazolium cation (N-3-(3-triethoxysilylpropyl)-3-methyl imidazolium, $[TESIm]^+$), which react with terminal OH groups on the surface to form a covalently bonded IL layer (see Scheme 5.2a) [11]. A second approach is the coulombic attachment of an imidazolium cation to anionic silanolate groups, which is achieved by using a zwitterionic IL (1,3-dimethylimidazolium-2-carboxylate) as introduced by Holbrey et al. for halide-free IL synthesis [12], and adapted by Lungwitz et al. for surface modification [13]; see Scheme 5.2b for details. To allow for a high surface coverage of such a functionalization layer, the surface has to be pre-treated to minimize contaminations and exhibit a high number of hydroxyl groups.

For an understanding of the wetting behaviour, which is determined by the interaction of IL with the (modified) glass substrate, the characterisation of
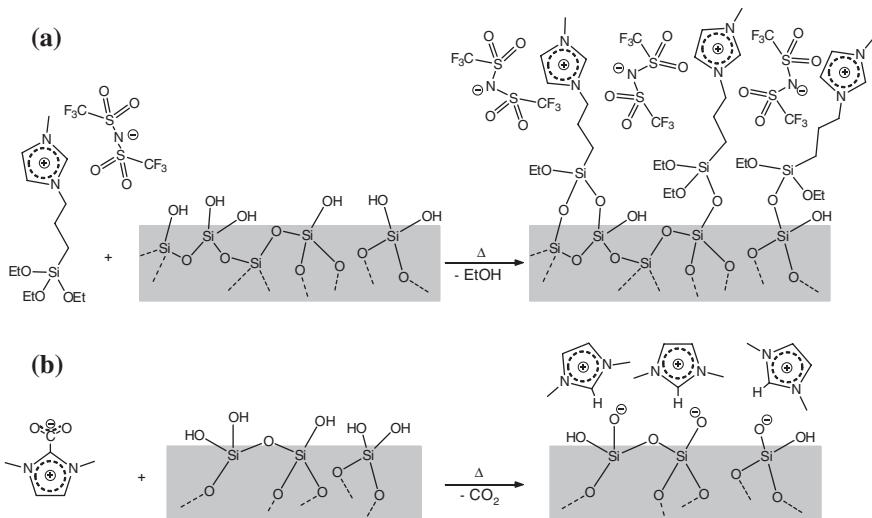
Scheme 5.2 Reaction schemes for IL functionalization of the Suprasil surface: After pre-treatment of the surface to achieve highest-possible density of surface hydroxyle groups, **a** covalent bonding of a [TESIm][Tf$_2$N], or **b** coulombic attachment of [C$_1$C$_1$Im]$^+$ moieties to anionic silanolate groups is achieved

ultrathin IL films on SiO$_2$ substrates is necessary. As the investigation of the interior of the PCF fibre is impossible with ARXPS, planar fused silica glass slides (referred to as "Suprasil", see below) were used as a model substrate for ARXPS investigations of IL thin film growth for the Nanolab approach. Hence, ultrathin films of [C$_1$C$_1$Im][Tf$_2$N] were prepared on pristine, etched and IL-functionalized Suprasil glass by IL-PVD and were investigated by means of ARXPS.

After discussing relevant experimental aspects in Sect. 5.2, we investigate the initial growth stages and molecular arrangement of [C$_2$C$_1$Im][Tf$_2$N] at the interface of a native untreated glass sample in Sect. 5.3.1. Section 5.3.2 deals with the effect of surface etching and IL-functionalization of Suprasil samples on the IL growth. Molecular arrangement effects of the ions at the interface will only be briefly discussed where necessary.

5.2 Experimental Aspects

Sample preparation: For the experiments conducted in Sect. 5.3.1 a standard microscope slide (10 × 10 × 1 mm^3), was carefully cleaned by ultrasonic treatment for 1 h in ultra-pure water at 80 °C prior to its introduction into the UHV system. XPS analysis of the glass surface showed the expected Si and O signals with some residual carbon contamination (~0.3 ML).

"Suprasil 300" is the trade name for ultrapure fused silica glass with an extremely low bulk OH-content below 1 ppm, low bulk contamination levels, and

very high optical transmission ranging from near IR to UV. All Suprasil samples were cut down to dimensions of $15 \times 12 \times 1$ mm^3. This was followed by thorough cleaning with acetone and isopropanol in an ultrasonic bath and storing in an oven at 70 °C until further use. Subsequent surface modifications were performed as follows (summarized in Table 5.3, Sect. 5.3.2):

Soft-etched Suprasil: The samples were immersed for 10 min in a 60 °C pH 10 buffer solution of H_3BO_3, KCl and NaOH (VWR 32040.298). After extensive rinsing with ultra-pure water, the samples were dried in a drying cabinet at 60 °C for at least 1 h. Hydroxide treatment of silica leads to hydroxylation and eventually to dissolution of the solid material, as illustrated in Scheme 5.3:

This leeching indeed led to surface morphology changes (i.e. formation of nanopores), which could be deduced from the ARXPS data after $[C_1C_1Im][Tf_2N]$ deposition onto the sample (spectra are compiled in the Appendix in Fig. A2). Due to these pronounced morphology changes it was impossible to obtain unambiguous information on the wetting behaviour, so this approach of surface hydroxylation was abandoned.

Strong-etched Suprasil: The samples were immersed in a 60 °C pH 14 NaOH solution ($c = 1$ mol/L) and stirred for 1 h. This was followed by thoroughly rinsing the samples with ultra-pure water and drying in a drying cabinet for at least 1 h. This preparation protocol was quickly abandoned, as the dissolution process was so fast that in the Mercedes-PCF, breakdown of the struts supporting the solid core was observed. Nevertheless, one set of experiments (i.e., characterisation using ARXPS and investigation of IL growth) was performed for a strong-etched Suprasil sample, the spectra of which are compiled in the Appendix in Fig. A3.

Piranha-etched Suprasil: For preparing a fresh Piranha solution (1:3 mixture of 10 % aqueous H_2O_2 solution and conc. H_2SO_4) about 30 mL of conc. H_2SO_4 were placed in a thoroughly pre-cleaned and dried beaker and stirred at moderate speed. Then, 10 mL of H_2O_2 solution were slowly added. After heating the mixture to 80 °C, the Suprasil samples were immersed into the reaction mixture and stirred for 40 min. Afterwards, the samples were thoroughly cleaned by rinsing with ultra-pure water (aqua ad iniectabilia), blow-dried in Argon atmosphere and immediately used for the next preparation step (or introduced into the UHV
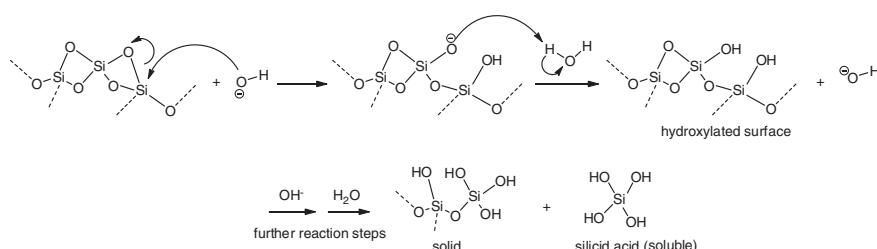

Scheme 5.3 Reaction mechanism of OH$^-$-induced hydroxylation and dissolution of silica. In contrast to acidic treatment, the etching process is a catalytic process and is able to dissolve the bulk glass due to silicid acid formation which is soluble in alkaline solution

system). The reaction mechanism for the generation of atomic oxygen and OH radicals for silica hydroxylation is as follows:

$$H_2SO_4 + H_2O_2 \rightarrow H_3O^+ + HSO_4^- + O\bullet$$

$$O \bullet + H_2O \rightarrow 2 \bullet OH$$
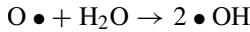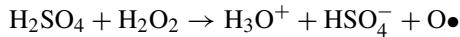
Ozone-treated Suprasil: The pre-cleaned samples were placed on a sample holder in an "ozone-box" composed of a UV lamp and a Petri dish filled with ultra-pure water. After sealing the box, the samples were kept in the reaction chamber for a minimum of 5 h or until further use. The reaction mechanism for the generation of •OH radicals is as follows:

$$3O_2 + h\nu(UV) \rightarrow 2 O_3$$

$$O_3 + H_2O \rightarrow O_2 + 2 \bullet OH$$
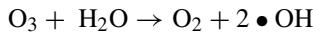
IL functionalization with [TESIm][Tf$_2$N]: The samples were prepared by covering a pre-treated, hydroxylated sample with a thick film of *N*-3-(3-triethoxysilylpropyl)-3-methyl imidazolium bis(trifluoromethylsulfonyl)imid ([TESIm][Tf$_2$N]) and reacted for 24 h at 60 °C in a drying cabinet. Afterwards the excess IL was removed by rinsing the sample with acetone (please see Scheme 5.2a for the reaction pathway and the resulting surface modification). The XP spectra of a macroscopically thick [TESIm][Tf$_2$N] film are shown in the Appendix, Fig. A5.

IL functionalization with C$_1$C$_1$Im-CO$_2$: The samples were prepared by covering an ozone-treated sample with a droplet of a 1,3-dimethylimidazolium-2-carboxylate/water mixture and reacted for 24 h at 100 °C in a drying cabinet. During the reaction time the solid on top of the sample was regularly re-immersed in a droplet of water. Afterwards, the excess IL was removed by rinsing the sample with acetone. For the reaction pathway and the resulting surface modification, please see Scheme 5.2b. This approach led to a distinct modification of the Suprasil surface. However, in the course of this study it was not possible to thoroughly investigate the IL growth behaviour on this surface. The available preliminary data are compiled in the Appendix, Fig. A4.

Finally, the samples were mounted on a sample holder using tantalum strips as shown in Ref. [14], and introduced into the UHV system.

Thin film preparation: For the experiments presented in Sect. 5.3.1 the ultrathin IL films were produced by controlled thermal evaporation from a well-defined IL reservoir, consisting of a planar gold foil (10 × 10 mm^2) covered with a thick [C$_2$C$_1$Im][Tf$_2$N] film. This IL reservoir was introduced into the UHV chamber (base pressure 1 × 10^{-9} mbar) via a load lock system. For deposition, the reservoir temperature was raised to the evaporation temperature of 320 K and held at this temperature for half an hour prior to the evaporation/re-condensation process, in order to ensure stable and clean conditions (background pressure

6×10^{-9} mbar). Evaporation of $[C_2C_1Im][Tf_2N]$ was then carried out with the sample at room temperature sitting face to face to the IL reservoir at a distance of 1 cm. The IL films were deposited in three successive evaporation steps.

For the experiments using the Suprasil glass, thin film preparation was carried out in analogy to the IL-PVD experiments performed in Chap. 4 using the TECTRA WKC3 Knudsen cell; please see Sect. 4.2 for detailed information. The base pressure during evaporation was ~1×10^{-9} mbar. The evaporation temperatures for $[C_1C_1Im][Tf_2N]$ were in the range of 430–440 K, depending on the deposition rate. The latter were monitored by QCM measurements in order to guarantee constant IL fluxes. Film thicknesses d were determined by analysis of the damping of the substrate Si 2p levels by Eq. (4.1) according to the detailed discussion in Chap. 4, while nominal film thicknesses and mean deposition rates were determined from reference measurements on Au(111), for which ideal layer-by-layer growth is observed and therefore Eq. (4.1) is strictly valid.

In accordance to Sect. 4.2, the film thickness is given in monolayers (ML), where 1 ML of IL is referred to as one closed layer of ion pairs, vertically arranged on top of each other; possible arrangements of the ion pairs which are consistent with this definition are illustrated in Scheme 4.1a. According to this definition, one closed layer of ions covering the surface in a checkerboard arrangement, as shown in Scheme 4.1b, corresponds to a coverage of 0.5 ML, while for a bilayered structure all adsorption sites are occupied at a coverage of 1 ML (Scheme 4.1c) For the $[C_2C_1Im][Tf_2N]$ IL used in Sect. 5.3.1 the height h of 1 ML was estimated to 0.75 nm, see Table 4.1. However, in the analysis in Sect. 5.3.1 a value of 0.7 nm is used, accounting for a certain amount of void volume (using a value of 0.75 nm would not change any of the conclusions drawn from this data). For the Suprasil experiments using $[C_1C_1Im][Tf_2N]$, the same value as in Chap. 4, namely h = 0.73 nm, was used.

XPS measurements and data analysis: For the experiments in Sect. 5.3.1, the measurements were performed with an ESCALAB 200 CHA and Al-K_α radiation generated by the original ESCALAB 200 X-ray gun at a power of 75 W. The spectra were recorded with a pass energy of 20 eV, yielding an overall energy resolution of 0.9 eV. The denoted intensity scale is the same for all levels studied and corresponds to the counts for one single sweep with a dwell time of 0.1 s. For all spectra shown, five sweeps were accumulated. Measurements at 0° emission probe the near-surface region of an organic compound with an information depth of ~7–9 nm ("bulk"-sensitive), whereas measurements at 70° probe only the topmost layers (~2–3 nm, "surface sensitive") [15]. To correct for reduced overall transmission at 70° detection angle, the corresponding ionic liquid spectra were multiplied by an empirical factor determined individually for each sample holder. After this correction, for a homogeneous distribution of the various elements in the investigated sample, identical signals are expected in both geometries. For the Suprasil experiments presented in Sect. 5.3.2 the SCIENTA R3000 analyser was used, with identical settings of pass energy used in Chap. 4.

Data analysis was performed using Origin 7.5 for the experiments conducted in Sect. 5.3.1, employing Gaussian fit functions. For the Suprasil experiments Casa

XPS was used and, in analogy to the detailed discussion given in Sect. 4.2, a G:L (70:30) lineshape was employed.

The native glass and the Suprasil samples are insulating materials and, therefore, charging of the sample is observed during XPS. To allow for visual comparison of the spectra, a BE calibration was employed, as explained below. It should be noted that information on absolute BE position is not possible due to the absence of a reliable reference level and therefore, throughout Chap. 5, we refrain from discussing differential BE shifts between different IL layer thicknesses, and absolute BE position are used only to refer to a certain peak observed in a given figure. To account for this sample charging effect, all spectra were shifted, so that the BE of O 1s and Si 2p signals roughly matched literature values for the respective samples. In Sect. 5.3.1, BE values of 103.8 eV (Si 2p) and 532.5 eV (O 1s) were used for calibration, by adapting literature values from Ref. [16] as discussed in Ref. [17], while in Sect. 5.3.2 the spectra were referenced to values of ~103 eV for Si 2p and ~532 eV for O 1s obtained for pure quartz materials from Ref. [16].

5.3 Results and Discussion

5.3.1 $[C_2C_1Im][Tf_2N]$ on Native Glass

In this section a first in situ study of ultrathin $[C_2C_1Im][Tf_2N]$ films on a native, untreated glass substrate is presented. The sample was chosen, because the investigation of ultrathin ionic liquid films on silicate surfaces is of fundamental and technological interest, e.g., for the development and understanding of supported ionic liquid phase (SILP) materials [10]. Thereby, the main interest was to investigate a "real" sample, i.e. one that resembles a real silica surface in terms of residual carbon contamination and amount of OH groups. For evaporation, the IL $[C_2C_1Im][Tf_2N]$ was selected because of its comparably high vapour pressure and its high thermal stability [18]. To investigate $[C_2C_1Im][Tf_2N]$ thin films on a glass substrate, films of increasing average thickness were prepared by successive deposition (total deposition times: 0, 10, 25, and 55 min), while each deposition step was followed by taking ARXP spectra. In addition, a thick IL film was prepared by prolonged deposition (estimated mean thickness larger than 100 nm). In Fig. 5.2, the XP spectra of the deposited IL films are depicted along with the spectra of the IL reservoir. To obtain a detailed overview, all IL- and substrate-related regions are shown for normal emission (0°) and grazing emission (70°).

Depending on the deposition time, and, consequently, the thickness of the IL layer, shifts of the XP spectra were observed, which are attributed to charging of the insulating glass substrate. The magnitude of this shift depends on the emission angle and on the deposition time (e.g., at 0° a shift of 9.2 eV is found for the bare glass substrate as compared to 0.4 eV for the thick IL film on the glass substrate). To correct for this charging and for better comparison, the spectra have been shifted to align the peaks in Fig. 5.2 (the mean values of these shift are denoted
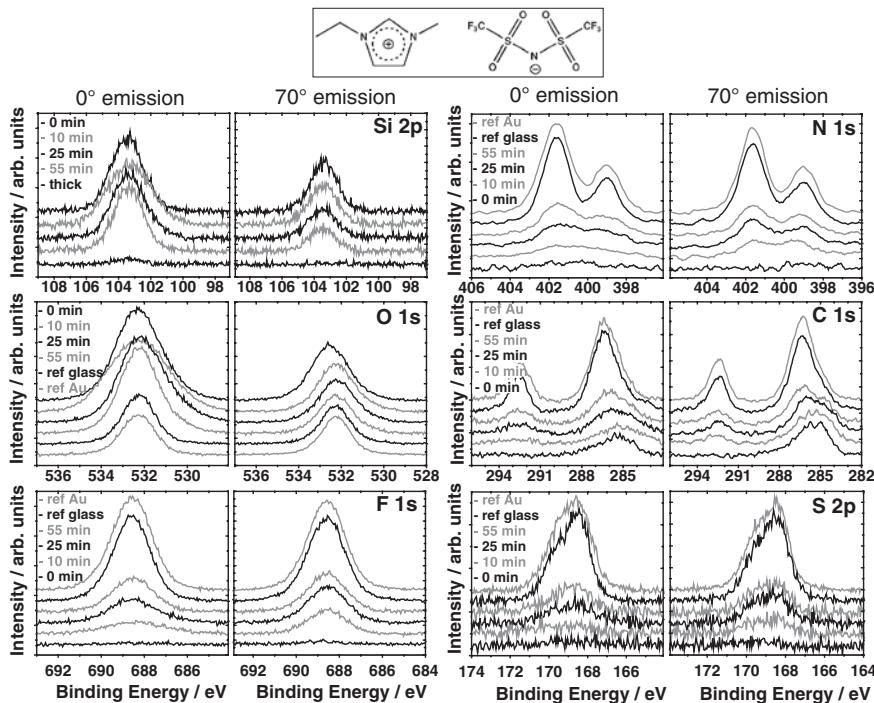
Fig. 5.2 Si 2p, O 1s, F 1s, N 1s, C 1s and S 2p XP spectra of [C₂C₁Im][Tf₂N] (schematic drawing shown at the *top*), deposited on a glass substrate, at emission angles of 0° (*left*) and 70° (*right*). Spectra are shown for deposition times of 0, 10, 25, and 55 min and for a thick layer ("ref glass"); also shown are the corresponding spectra of the IL in the reservoir ("ref Au"). For the IL films on the glass substrate charging is observed. To compensate for that and to allow comparison of the different layers, the spectra have been shifted uniformly to lower BE (with maximum deviations of ±0.5 eV) by the following values (0°/70°): 0 min: 9.2/6.9 eV, 10 min: 8.7/7.0 eV, 25 min: 9.2/7.1 eV, 55 min 8.5/6.6 eV, thick: 0.5/0.4 eV. Note that the N 1s and C 1s spectra have been smoothed

in the figure caption), as stipulated in Sect. 5.2. As a consequence, throughout Chap. 5, BE values should not be regarded as "real" or "true" values. Furthermore, no comparison of differential BE shifts between thin film and bulk IL values, e.g., similar to those observed for the IL/Au interface, is possible. Accordingly, the conclusions drawn are mainly based on the damping of substrate signals and relative intensity changes of IL-related signals. The C 1s spectra of the glass surface prior to deposition show a peak at ~285.6 eV, which is attributed to a contamination of the surface with small amounts of carbon (estimated to ~0.3 ML by comparing the Si 2p damping in 0° and 70° emission).

As a first step of analysis, the spectra for the thick evaporated IL film on glass are compared to those of the reservoir (i.e., a macroscopically thick IL film on gold). This comparison yields identical peak intensities for both normal and grazing emission within ±5 %. This agreement indicates that the chemical composition and

statistical distribution of anions and cations of the deposited film is identical to that of the source IL, and that the evaporation process leaves the IL intact. Furthermore, for all IL-related core levels of the thick film, no significant changes of intensity with increasing emission angle were observed, indicating a homogeneous distribution of the elements within the near-surface region. It also rules out pronounced preferential vertical orientation of IL molecules. This finding is in accordance with our ARXPS investigations on $[C_nC_1Im][Tf_2N]$, in which surface segregation of the alkyl chains was observed for $n \geq 4$, whereas for $n \geq 4$ the ions are more or less randomly oriented [19]. Table 5.1 shows the quantitative evaluation of the XPS signals of the thick film in 70° geometry, where the signals from the glass substrate totally vanish. For this film, the surface composition is, within the margins of error, in excellent agreement with the nominal stoichiometry and the reference macroscopically thick IL film before deposition. The N 1s and the C 1s spectra of the thick IL film on glass (and also of the IL reservoir) show two well-separated peaks at 401.7/399.0 eV and 286.4/292.5 eV, respectively. They are attributed to the corresponding atoms in the cation and anions. Their intensity ratios of 2:1 for N 1s and 6:2 for C 1s fit perfectly to the nominal composition. Furthermore, the peak positions and peak shapes of the thick IL film are in good agreement with XP spectra of $[C_2C_1Im][Tf_2N]$ published by other groups (e.g., see Ref. [20–22]).

After demonstrating that the IL remains intact upon vapour deposition, we investigated the initial growth stages of ultrathin IL layers. With increasing deposition time (0, 10, 25, and 55 min), the Si 2p signals of the glass substrate (Fig. 5.2) show the expected decrease in intensity, and the IL-related signals (F 1s, N 1s, C 1s and S 2p) show a concomitant increase due to the increasing IL film thickness. The degree of charging, i.e., the denoted uniform shifts of the spectra, is reduced with increasing deposition time (note that the spectrum for 10 min deposition time at 0° is also considerably broadened, which is not fully understood but tentatively assigned to experimental aspects rather than being of physical significance).

It is noteworthy for the following discussion, that the derived conclusions are not very sensitive to the exact inelastic mean free path (i.e., 3 nm) or the estimated thickness of the monolayer (i.e., 0.7 nm). From the decrease of the Si 2p signals of the glass substrate, information on the layer thickness and on the growth mode can be obtained, according to the procedure used in Chap. 4. In Fig. 5.3, the relative Si 2p intensity is plotted versus evaporation time for both emission angles. Assuming

Table 5.1 Elemental compositions of IL core levels of $[C_2C_1Im][Tf_2N]$ macroscopically thick film, thick IL-PVD film and the corresponding nominal composition

System	Elemental composition of IL core levels				
	N 1s	C 1s	O 1s	F 1s	S 2p
Reference[a]	3.2	7.7	4.1	6.0	2.0
Thick evaporated	2.9	8.3	4.1	5.7	2.0
Nominal	3	8	4	6	2

Experimental values are derived from measurements at 70° emission angle
[a]Macroscopically thick, ex-situ deposited

two-dimensional growth within the first layer, a linear decrease of the substrate signals is expected for both emission angles; the data for the first two deposition steps (10 and 25 min) in both experimental geometries are indeed consistent with such a linear decrease. Using Eq. (2.4), from the damping of the Si 2p signal the completion of 1 ML is estimated to be achieved at a deposition time of 31 and 34 min for 0° and 70° emission, respectively, resulting in a mean value of 32.5 min (see Fig. 5.3).

The solid lines represent the fits to both geometries, using the average value of 32.5 min for the completion of the first layer. The observed very good agreement for the two geometries (within the margin of error of ±3 min) is a strong indication that the growth mode is two-dimensional up to one closed layer of ion pairs. If the growth of the IL film did occur in a three-dimensional fashion, the decrease of the Si 2p signal with deposition time would be slower, in particular when measured at 70°. As one possible scenario, the behaviour expected for the growth of islands with uniform height of two IL layers (i.e., 1.4 nm) is plotted in Fig. 5.3 (dotted lines). The smaller negative slope, in particular for 70°, is immediately evident (note that this effect becomes even more pronounced when growth in islands of larger thickness occur; in other words, the higher the islands, the greater the similarity of the slopes at 70° and 0° emission). As the deviation from the experimental data points is well outside the margins of error, three dimensional growth can be ruled out. At this stage of analysis, we conclude that the first layer of IL ion pairs grows two-dimensionally. Conclusions for the growth on top of this first layer are tentative as only one more data point at 55 min is available. However, from the fact that its intensities for both 0° and 70° are above the values expected for completion of
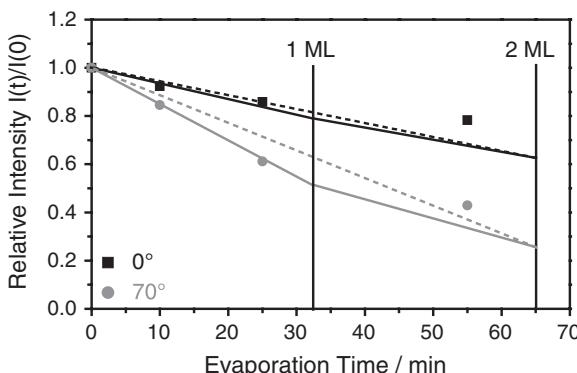

Fig. 5.3 Relative intensity of the Si 2p levels at 0° (*black squares*) and 70° (*grey circles*) as function of evaporation time. The size of the symbols corresponds to the mean error bars. The vertical line at 32.5 min indicates the time (average value determined from the data at 0 and 70°) needed for the completion of the first complete IL layer, as determined from the linear decrease of the signals at both emission angles, an estimated thickness of 0.7 nm and an inelastic mean free path of 3 nm (for details see text). The *solid lines* represent the linear decrease assuming two-dimensional IL islands (with the height of one IL layer) using the average value of 32.5 min for the completion of the first layer. The *dashed lines* show the expected decrease for the growth of islands with uniform height of two IL layers (i.e., 1.4 nm)

two layers, growth in three dimensional islands is likely. More evidence for a non-ideal growth behaviour, i.e. formation of 3D islands, comes from investigations in Sect. 5.3.2, where thicker IL layers were deposited on an untreated Suprasil sample.

In the following, the IL-related signals shown in Fig. 5.2 are discussed in more detail: With increasing deposition time, the F 1s, N 1s, and S 2p and the C_{anion} 1s peak show the expected increase in signal intensity, whereas for the O 1s peak and the C_{cation} 1s peaks the situation is more complex due to the superimposed signal from the glass substrate and the carbon contamination, respectively (note that the O 1s BE of oxygen in glass and in the IL are nearly identical). The comparison of the data for the two emission angles after 10 and 25 min deposition time shows a significantly higher intensity for 70° compared to 0°. This behaviour is consistent with the two-dimensional film growth of the first monolayer, which has been proposed above, indicating a complete wetting of the glass substrate by the IL film. After 55 min deposition, the F 1s, N 1s, S 2p and C 1s spectra are nearly identical for both angles, but are still significantly smaller than for the thick film obtained after extensive deposition. These observations and the fact that the Si signal of the substrate is still clearly visible after 55 min (see above) indicate three-dimensional island growth on top of the first layer; for an evaporation time of 55 min only parts of the surface are covered by these islands. An influence of the small carbon contamination on the observed growth mode cannot be completely ruled out. In fact, evidence for a rather pronounced influence of C_{adv} comes from experiments presented in Sect. 5.3.2.

A more thorough discussion is needed for the N 1s spectra at 10 and 25 min deposition times, where additional information on the orientation of the ions in the ultrathin IL films can be derived. From the stoichiometry of the IL, an intensity ratio of 0.5 is expected for N_{anion}/N_{cation}. This ratio is indeed observed for the thick IL layer on glass (and also on Au), as can be seen in Fig. 5.4, where the N 1s spectra are plotted along with fits of the two components. Inspection of the N 1s spectra for deposition times of 10 and 25 min shows ratios of $[Tf_2N]^-$: $[C_2C_1Im]^+$ significantly smaller than 2 : 1 (0° spectra: 1.3 : 1 at 10 min and 1.6 : 1 at 25 min, respectively; for 70°, even smaller values of 1.1 : 1 and 1.5 : 1 are observed as shown in Fig. 5.4 and Table 5.2). This behaviour can be understood if we assume that the anions and cations within the first adsorption layer are not randomly distributed, but form a bilayer structure with the $[C_2C_1Im]^+$ in direct contact to the surface and the $[Tf_2N]^-$ at the vacuum side, as shown in the Scheme embedded in Table 5.2. In this geometry, the $[C_2C_1Im]^+$-derived N 1s signals are damped by the $[Tf_2N]^-$ half-layer sitting on top of it. This damping should be more pronounced at grazing emission, as is indeed observed (note that in 0° emission near-stoichiometric values should be observed, however, the statistics are not good enough in 0° emission to make unequivocal statements). Although the higher N_{anion}/N_{cation} ratio is unequivocal from the experimental spectra, we refrain from further detailed quantitative analysis since the positions of the N atoms in the bilayer, the thickness of the bilayer, and the mean free path of the electrons are not known with sufficient accuracy. Furthermore, the relatively low count rate restricts a more detailed interpretation of the data. Also, for higher film thicknesses, radiation-induced changes may have an impact on the anion-to-cation ratio due to prolonged X-ray exposure.
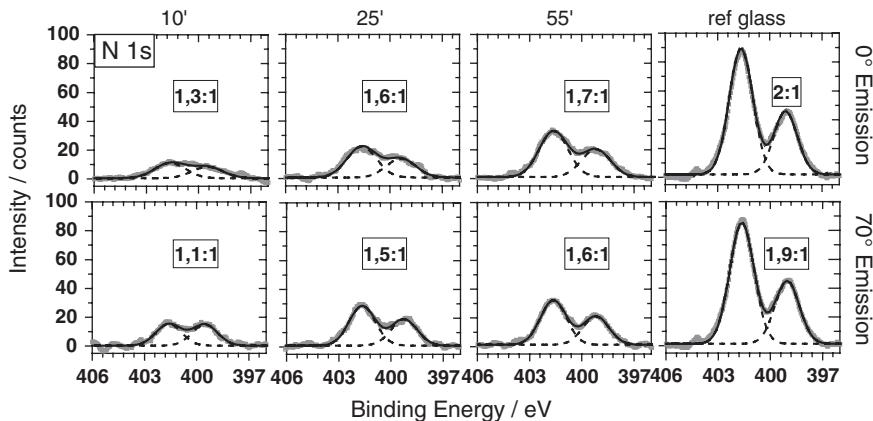
Fig. 5.4 N 1s XP spectra of [C$_2$C$_1$Im][Tf$_2$N] deposited on glass, at emission angles of 0° (*top*) and 70° (*bottom*). Spectra are shown (from *left* to *right*) for deposition times of 10, 25, and 55 min, and for a thick layer ("ref glass"). In addition to the spectra, fits are shown in order to determine the relative contributions of the cation- (~401.7 eV) and anion-related (~399.0 eV) N 1s signals. The resulting intensity ratios are denoted

Table 5.2 N_{anion}/N_{cation} ratios of thin (10, 20 and 55 min) and thick (ref glass) IL-PVD films on glass, along with a sketch of the arrangement of [C$_2$C$_1$Im][Tf$_2$N] for very low coverages within the first adsorption layer adsorbed on glass, with the [C$_2$C$_1$Im]$^+$ cation in contact with the substrate and the [Tf$_2$N]$^-$ anion at the vacuum side

Evaporation time (film thickness)[a]	N_{anion}/N_{cation}		Scheme of sub-ML arrangement
	0°	70°	
10 min (0.30 ML)	0.77	0.91	
20 min (0.78 ML)	0.63	0.67	
55 min (1.68 ML)	0.59	0.63	
Thick, evaporated	0.5	0.53	

[a]Film thicknesses are derived from the damping of the Si 2p signals using Eq. (4.1) and might, due to the imperfect growth behaviour, deviate from the real deposited amount (i.e. the nominal thickness)

The bilayer structure at the IL/glass interface is now briefly compared to the findings on Ni(111) (Sect. 4.3.2); for very low coverages a bilayered structure is observed, however, upon approaching a thickness of 1 ML, a reorientation towards a checkerboard-like structure takes place. A similar scenario can be envisioned for the IL/glass system investigated here, because the N_{anion}/N_{cation} ratio is most pronounced for very low coverages, whereas for higher film thicknesses the values slowly approach the nominal values. However, the effects observed on the glass surface are not as clear cut as for the Ni(111) surface, which can be attributed to the limited number of data points. Also, on the glass surface, the films were deposited on top of each

other, so that signal contributions due to onset of radiation damage cannot be fully excluded (see Sect. 4.3.1.5 for a detailed discussion of radiation damage effects).

From proposing a bilayer structure within the first adsorption layer, an imminent question is that of the orientation of the imidazolium ring. From the findings in Chap. 4, where for Au(111) and Ni(111) the imidazolium ring was found to lie flat on the surface, it is tempting to speculate that the imidazolium ring is also oriented parallel to the surface, in accordance with the pronounced anion enrichment found in the 70° emission N 1s spectrum. However, results from SFG spectroscopy contradict such an interpretation; for systems, in which the SiO_2 surface is covered by a macroscopically thick IL film, a more upright orientation of the imidazolium ring at the interface is suggested [23]. Moreover, it was found that both the anions and the cations are located at the silicate surface [24]. Although it is important to compare the results and to note that there is conflicting evidence, the two systems are quite different. Therefore, a detailed comparison of findings from bulk-IL/solid interfaces with the thin layers investigated here has to be done with great caution, and further experimental data will help elucidate the extent to which data from bulk and thin film can be compared.

With respect to the stability of the deposited ultrathin IL films it is interesting to note that after bringing the 55 min deposited film to ambient conditions (air) over 2 h virtually no differences were observable by subsequent XPS measurements. This finding demonstrates the practical usefulness of hybrid materials covered by an ultrathin ionic liquid film, which acts as a protection layer [25]. Only in cases, where the ultrathin film was kept in vacuo (pressure at 10^{-9} mbar) at room temperature for extended periods of time (10 h), was a considerable decrease of IL signals measured due a non-negligible evaporation rate at room temperature, i.e., the reversibility of the physical vapour deposition process.

To conclude, it is shown in this first study that for ultrathin films of $[C_2C_1Im]$ $[Tf_2N]$ on a native untreated glass sample the initial growth of the IL film occurs via the formation of a closed first layer followed by three-dimensional island growth. In the very first adsorption layer, a preferential distribution of the ions is observed, with the $[C_2C_1Im]^+$ cations preferring direct contact to the glass surface and the $[Tf_2N]^-$ anions at the vacuum side, similar to the results presented in Sect. 4.3.2, where a bilayer structure was found for sub-ML coverages of $[C_1C_1Im][Tf_2N]$ on Ni(111). The study presented here provides an excellent starting point for thin film studies of high purity glass samples presented in the next section. As uniform IL films (i.e., good wetting behaviour) are of paramount importance for the Nanolab concept, the subsequent chapter deals with approaches for SiO_2 surface modification to achieve more uniform films morphologies.

5.3.2 Surface Modification and $[C_1C_1Im][Tf_2N]$ Growth on Suprasil

As evident from the previous investigation, on untreated glass IL growth proceeds in a Stranski–Krastanov-type fashion, i.e., three-dimensional growth (droplet

formation) on top of a wetting layer. Hence, to achieve better IL wetting, different surface modification procedures were tested: Firstly, a hydroxylated and contamination-free surface was prepared in order to implement an IL-functionalization of the glass surface. Such IL-functionalization can be achieved either by covalent attachment of functionalized imidazolium cations to the SiO_2 surface or by bonding an imidazolium moiety by coulombic interactions to surface silanolate groups. The preparation step, in which procedures were tested to obtain hydroxyl-terminated surfaces, is referred to in the following discussion as "sample etching", while the reaction step between IL-moieties and the surface OH groups is referred to as "IL-functionalization". In the etching step, a number of protocols were tested, ranging from strongly alkaline 1 M NaOH solution ("strong etched"), slightly basic pH 10 buffer solution ("soft etched"), over a conc. H_2SO_4/H_2O_2 mixture ("piranha etched"), to an ozone/H_2O/UV gas phase treatment ("ozone-etched"). While the exact etching protocols are specified in the experimental section in Sect. 5.2, the parameters are again summarized in Table 5.3, along with a short summary of the results in terms of surface morphology and reduction in carbon contamination. As mentioned in the experimental section, only the results from piranha-/ozone-etched and [TESIM][Tf$_2$N]-functionalized samples are discussed in detail, while the data obtained for the other systems are compiled in the Appendix.

In terms of XPS measurements of SiO_2 samples, a direct quantification of surface modification in terms of hydroxylation is not possible, due to the similar O 1s BE values for bulk SiO_2 and SiOH. Furthermore, it is not possible to draw any meaningful conclusions concerning the amount of surface hydroxyl from changes in Si/O ratio in ARXPS, as is exemplified in Table 5.4 for an untreated (pristine) and a hydroxylated (Piranha-etched) Suprasil sample. The only substrate XPS signal that can be analysed and quantified to a certain extent from ARXP spectra taken before and after etching, is the amount of residual carbon contamination

Table 5.3 Overview over different etching (hydroxyl-termination) and IL-functionalization protocols

Label	Active species	pH	T [°C]	Time	Effect on surface
Strong etch[*]	OH^- in NaOH	14	60	60 min	Dissolution of SiO_2 on a macroscopic scale (i.e., disintegration of struts of Mercedes PCF)
Soft etch[*]	OH^- in H_3BO_3/ KCl/NaOH	10	60	10 min	Dissolution of SiO_2 on a nanoscale (i.e., formation of nanopores)
Piranha etch	Acidic/OH radicals	<1	80	60 min	Surface hydroxylation, reduction of adventitious surface carbon
Ozone etch	OH radicals	–	RT	>5 h	Surface hydroxylation, reduction of adventitious surface carbon
[TESIm][Tf$_2$N]	Silyl-ether group	–	70°	>24 h	Covalent attachment of cation to surface –OH
C_1C_1Im-CO_2^*	CO_2 group	–	80°	>24 h	Coulombic bond of $[C_1C_1Im]^+$ to surface Si–O^-

[*]Systems marked with an asterisk are not discussed in detail in this chapter, but available data is compiled in the Appendix

Table 5.4 Relative abundance of oxygen and silicon in Suprasil glass measured in 0° and 80° emission. Values match the nominal composition of the bulk value of SiO_2 of 1:2 within the margins of error (± 5 %)

System	Relative abundance in 0° emission		Relative abundance in 80° emission	
	O (%)	Si (%)	O (%)	Si (%)
Pristine	62.5	37.5	62	38
Piranha etched	66	34	65	35
nominal	66.7	33.3	66.7	33.3

on the surface. For the experiments conducted in this work, however, this value is afflicted with a relatively large experimental scatter due to the ex-situ sample preparation. As a rough guideline most C_{adv} was found on untreated, pristine samples, while the piranha and ozone-etched samples showed the least amount of residual surface carbon.

Therefore, to assess the effect that the etching protocols might have on the surface morphology and on the IL growth behaviour in general, we deposited ultrathin IL films on the differently prepared sample surfaces followed by analysis with ARXPS (note that from this analysis morphology changes could be deduced for the alkaline-etched samples, see Appendix). In the following sections, IL deposition was performed on three selected systems, namely pristine, Piranha-/ozone-etched and [TESIm][Tf₂N]-functionalized Suprasil (Piranha- and ozone-etching leads to identical results and are therefore not discussed separately). These different systems are compared with respect to their IL wetting behaviour, and the corresponding IL growth characteristics are compared to the results on Au(111), for which ideal layer-by-layer growth has been unambiguously derived (see Sect. 4.3.1) [26].

For all following experiments the film thicknesses are given in values of "nominal thickness", as calculated from reference measurements on Au(111). Therefore, for growth characteristics which diverge from ideal layered growth (i.e. a de-wetting of the surface), the IL-covered parts will exhibit higher coverages than the nominal value (e.g., if 50 % of the surface is de-wetted, at a nominal coverage of 1 ML the remaining IL-covered surface will be covered by 2 ML of IL).

5.3.2.1 [C₁C₁Im][Tf₂N] on Pristine Suprasil

For the investigation of [C₁C₁Im][Tf₂N] growth on pristine Suprasil, a native untreated sample was introduced into the UHV system and characterized prior to IL deposition, followed by multiple evaporation steps amounting to nominal thicknesses up to ~10 ML. In Fig. 5.5 the core-level spectra of the "clean" surface (= prior to IL deposition) and the first three subsequent IL evaporation steps (with nominal coverages of 1, 2 and 3 ML as derived from reference measurements on Au(111)) are shown. From the Si 2p spectra, it becomes evident that
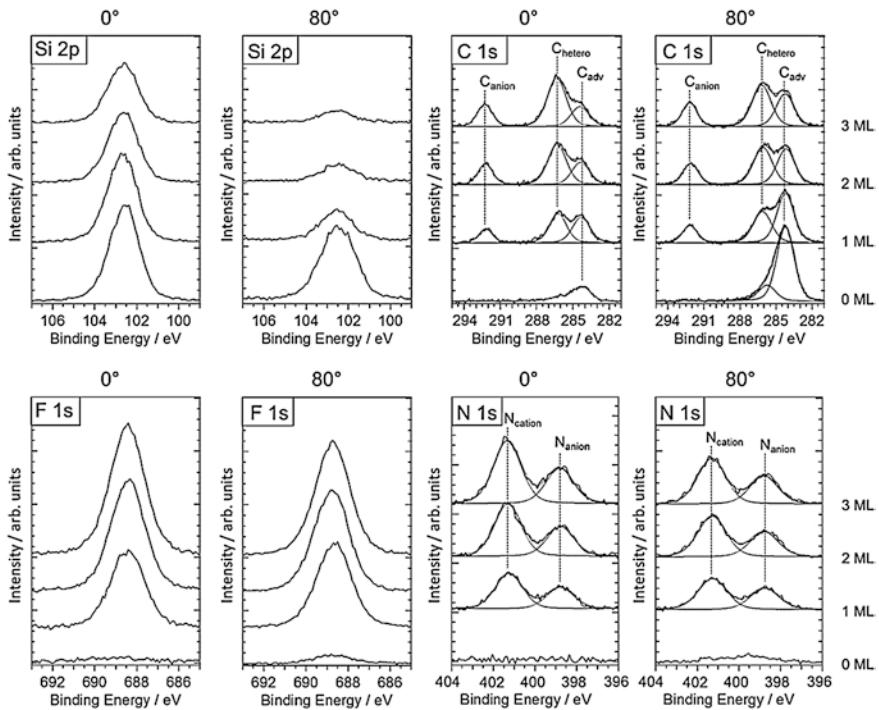
Fig. 5.5 Si 2p, C 1s, F 1s and N 1s ARXP spectra of initial stages of $[C_1C_1Im][Tf_2N]$ growth on a pristine Suprasil sample. Shown are the sample before IL deposition (0 ML) and three consecutive evaporation steps with nominal thicknesses of 1, 2 and 3 ML. The spectra are plotted with identical y-axis without further correction for reduced overall transmission in 80° emission

with increasing IL film thickness the substrate signal is attenuated. The damping characteristics are more pronounced in 80° emission, which is expected from the enhanced surface sensitivity in this geometry (for a flat surface morphology). Comparing the substrate signal damping to the case where the same IL with similar coverage was deposited on the Au reference sample, it becomes obvious that the damping found on the pristine Suprasil is much less pronounced (see Fig. 5.9 in Sect. 5.3.2.4, where a detailed comparison of the growth behaviour of differently terminated Suprasil surfaces is made). Although a thorough discussion of the growth behaviour will be given in Sect. 5.3.2.4, it should be pointed out at this stage that from the damping of the substrate signals an imperfect (= mixed 2D/3D) growth behaviour can unambiguously be deduced. This is particularly noteworthy because strong indications for an imperfect growth due to dewetting of the IL from carbon-contaminated surface areas are deduced from the analysis of the C 1s region discussed in the following paragraph.

Moving on to the IL-related C 1s, F 1s and N 1s regions, a simultaneous increase in signal intensity is observed in the 0° emission spectra up to 3 ML film thickness, while for the 80° spectra signal saturation is observed for the 2 ML

film (corresponding to a film thickness of ~1.5 nm, which is in the range of the maximum information depth at 80° emission). As indicated above, particularly important conclusions with respect to the IL wetting behaviour can be drawn from analysing the C 1s region: In the experiments presented in Sect. 5.3.1, the methyl group of the C_2 side chain showed a significant BE overlap with the adventitious carbon contamination C_{adv} on the surface, making a detailed analysis of the C 1s region extremely difficult. This disadvantage was circumvented in this study by using $[C_1C_1Im][Tf_2N]$, whose C_{hetero} BE value (~286.3 eV) is well separated from C_{adv} (~284.2 eV), therefore allowing for an unambiguous interpretation of the features in the C 1s region. On the pristine surface, a prominent C_{adv} signal is observed which is greatly enhanced in 80° emission, indicating that this feature is indeed a surface contamination (in case of a bulk contamination the Si/C_{adv} ratio should not change in grazing emission). The amount is roughly estimated to ~0.3 ML and is therefore in the range of that observed for the $[C_2C_1Im][Tf_2N]/$ glass system investigated in Sect. 5.3.1. Upon IL deposition the IL signals C_{anion} and C_{hetero} increase with increasing amount of IL, while in both emission angles the C_{adv} feature remains visible as a prominent feature. This observation is especially surprising for the 80° emission data, because for film thicknesses of 2 and 3 ML the damping should be similar to that observed in the Si 2p region, where a strong decrease is observed in 80° emission. Also in normal emission, the C_{adv} feature is not as efficiently damped as the corresponding Si 2p signal. From this behaviour it is concluded that the IL preferably adsorbs on uncontaminated areas of the SiO_2 surface, thereby efficiently damping the silicate Si 2p and O 1s substrate signals, whereas the contaminated surface areas (most likely agglomerated patches of C_{adv}) seem not to be significantly wetted by the IL. It seems very likely that the non-homogeneous distribution of surface carbon on native glass surfaces is one of the reasons (or even the most important reason) for the observed mixed growth behaviour of the IL on this substrate.

In Sect. 5.3.1 a preferential arrangement of the ions at the IL/glass interface was deduced from analysing the nitrogen region, i.e. the intensity ratios of the N_{anion} and N_{cation} signals. From a close inspection of the N 1s region it becomes evident that the nominal ratio of 2:1 is observed for all coverages in both bulk- and surface-sensitive geometries, indicating a random distribution of the ions already at nominal coverages of 1 ML. For the 1 ML film, this observation at first sight contradicts the results presented in Sect. 5.3.1, where for $[C_2C_1Im][Tf_2N]$ on a native glass sample significant enhancement of anion-related signals was observed even for coverages close to one ML. However, a nominal thickness of 1 ML is too thick to unambiguously determine preferential arrangement at the IL/solid interface, and therefore, we refrain from further discussing preferential arrangement at this stage and refer instead to Sect. 5.3.2.2, where it is shown in experiments on Piranha-etched Suprasil that for low coverages (0.2 ML) of $[C_1C_1Im][Tf_2N]$ a bilayered arrangement is observed, in agreement with our findings from Sect. 5.3.1.

To summarize the growth behaviour of $[C_1C_1Im][Tf_2N]$ on pristine, untreated Suprasil samples, non-ideal (dewetting and/or islanding) growth behaviour is observed. From a close analysis of the C 1s region, it was deduced that surface

areas covered by an adventitious carbon contamination are significantly less coated by IL molecules. This finding corroborates the tentative statement on a possible influence of the carbon contamination made in Sect. 5.3.1, where the C 1s region could not be analysed due to the signal overlap between that of the terminal methyl group of the ethyl side chain of the $[C_2C_1Im]^+$ cation and C_{adv}.

In the following, the effect of surface modification procedures, i.e., a Piranha-etched Suprasil sample, are investigated with respect to the IL wetting behaviour. For the piranha-etched sample, it will become evident that the reduced amount of surface contamination in combination with surface hydroxylation is beneficial for the IL wetting behaviour.

5.3.2.2 $[C_1C_1Im][Tf_2N]$ on Hydroxyl-Terminated Suprasil

Piranha-etched and ozone-treated Suprasil: Before moving on to the results of thin film deposition on Piranha-etched samples, the chemical reaction of a Piranha solution (and ozone treatment) with silicate surfaces and residual carbon contaminations will be briefly discussed. Piranha solution is usually used in applications where not only a hydroxyl termination is required (treatment with a strong acid would be sufficient), but where the surface has to be clean and free of residual carbonaceous materials. It was shown in the experimental section that in a Piranha solution atomic oxygen and also hydroxyl radicals are formed. These highly reactive species can react with carbonaceous contaminations, where even pure sp^2-carbon materials, i.e., char or graphite, can be broken down according to the following reaction pathway:

Oxygen radicals successively break the C=C bonds by inserting oxygen, eventually leading to CO_2 and water-soluble compounds, leaving behind the clean, hydroxylated surface. The ozone treatment has a similar effect on residual carbonaceous surface contaminations, but has the advantage that the reaction takes place in the gas phase, therefore being promising for applications in PCFs. Qualitatively, the Piranha etching method and the ozone treatment lead to similar results regarding the IL wetting behaviour. Therefore, examples from both systems are used for the discussion of hydroxylated Suprasil surfaces; the results presented in the following are obtained from a Piranha-etched Suprasil sample, while the results for the growth comparison of the three different samples made in Sect. 5.3.2.4 were obtained on ozone-etched samples.

In Fig. 5.6, the spectra of the clean sample and three successive evaporation steps with nominal film thicknesses of 0.2, 1 and 2 ML are shown. In analogy to the findings for the pristine Suprasil sample in the Si 2p region, considerable damping of the substrate signal is observed with increasing film thickness.
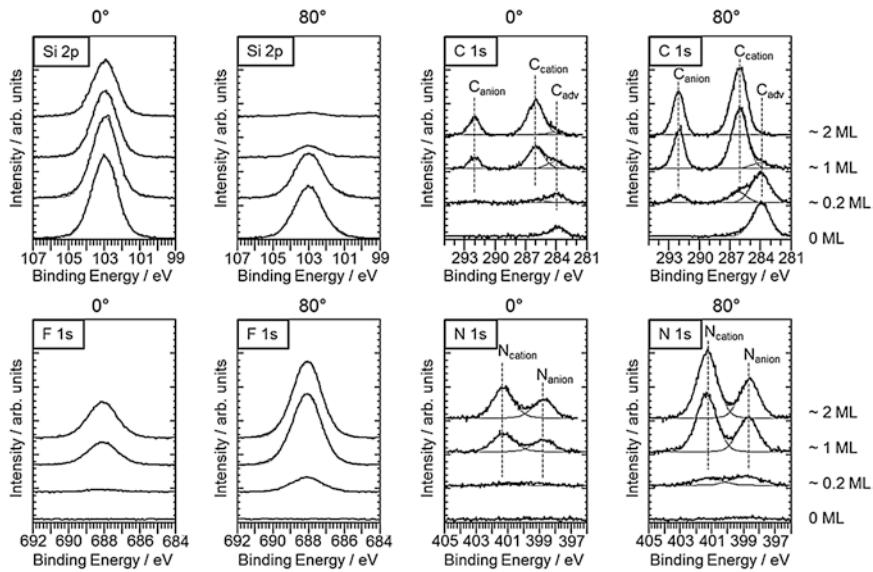
Fig. 5.6 Si 2p, C 1s, F 1s and N 1s ARXP spectra of initial stages of [C$_1$C$_1$Im][Tf$_2$N] growth on Piranha-etched Suprasil. Shown are the sample before IL deposition (0 ML) and three consecutive evaporation step with nominal thicknesses of 0.2, 1 and 2 ML. 0° and 80° spectra are plotted using the same scale (y-axis) without further correcting for reduced transmission in 80° measurements

However, upon close inspection of the 80° emission spectra, it becomes evident that for the 2 ML film the Si 2p signal is considerably more damped than in the case of the 3 ML film on the pristine sample, indicating a better wetting behaviour. The carbon contamination, which is—in comparison to the pristine sample—much smaller (<0.1 ML), is very efficiently damped by the IL overlayer in both 0° and 80° emission, similar to the damping observed in the Si 2p region. This observation stands in strong contrast with the findings on the pristine sample, for which inhomogeneous growth behaviour was assigned to a de-wetting from contaminated areas of the surface (evident from the persistence of the C$_{adv}$ signal, even at coverages, at which the Si 2p signals are significantly damped). This observation is attributed to the chemical modification of the carbonaceous material apparently resulting in a better IL wetting behaviour (Piranha and ozone treatment introduces oxygen and hydroxyl species into C$_{adv}$, thereby rendering it more polar). In contrast to the untreated Suprasil, the general IL growth behaviour of Piranha-etched and ozone-treated samples is similar to the 2D layered growth behaviour observed on Au(111), as evident from Fig. 5.9.

Before summarizing and moving on to the next system, a closer look is taken at the N 1s region of the 0.2 ML film, which, in 80° emission, shows a considerably different anion-to-cation ratio than for the higher coverages: The anion signal is dramatically enhanced with respect to the N$_{cation}$ signal, similar to our findings

for $[C_1C_1Im][Tf_2N]$ on Ni(111) and $[C_2C_1Im][Tf_2N]$ on glass (Sects. 4.3.2 and 5.3.1, respectively). The N_{anion}/N_{cation} value of 1.2 ± 0.2 deviates even more pronounced from the nominal value of 0.5 than that of $[C_1C_1Im][Tf_2N]$ on Ni(111); one should note that for the glass measurements the signal-to-noise ratio is worse due to relatively short measuring times to prevent radiation damage (see experimental section, Sect. 5.2), leading to relatively large error bars. An analysis of the C 1s region yields a value of $C_{anion}/C_{hetero} = 0.7$ (instead of $2:5 = 0.4$), which is also indicative for a remarkable anion enhancement, i.e., a bilayered structure. From the 0° emission data no conclusions can be drawn as the signals are too small.

To briefly summarize, for thin $[C_1C_1Im][Tf_2N]$ films on Piranha-etched (and ozone-treated) Suprasil, a considerable reduction of surface contamination by adventitious carbon can be achieved. As a consequence, an overall better wetting of the IL is found, and remarkably, also the carbon contamination is significantly damped by overlaying IL. This observation is in strong contrast to the finding on untreated Suprasil and is assigned to the fact that both ozone and Piranha treatment lead to a O-functionalization of the carbonaceous species, therefore becoming more "IL-o-philic". Furthermore, for very low IL coverages the anion signals are enhanced with respect to the cation signals, indicating a bilayered structure for sub-ML coverages, in accordance with the findings in Sect. 5.3.1.
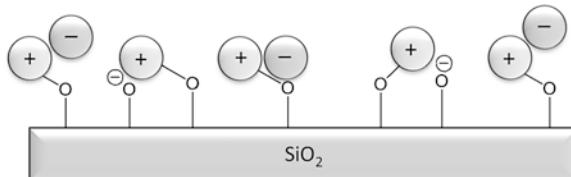
5.3.2.3 $[C_1C_1Im][Tf_2N]$ on $[TESIm][Tf_2N]$-Functionalized Suprasil

To obtain an IL-functionalized surface, an ozone-treated sample was reacted with $[TESIm][Tf_2N]$ according to the procedure stipulated in Sect. 5.2. For a successfully functionalized surface it is expected that $[TESIm][Tf_2N]$-related signals can be detected prior to $[C_1C_1Im][Tf_2N]$ deposition. As shown in Fig. 5.7, in all IL-related regions, additional cation and anion-related signals are observed for the 0 ML sample.

In the C 1s region a prominent, broad feature consisting of C_{hetero} and C_{alkyl} is observed. In comparison to the reference spectrum of pure $[TESIm][Tf_2N]$ (see Fig. A5), the C_{alkyl} feature is more intense due to additional intensity from surface carbon (C_{adv}) resulting from the ex-situ functionalization step. The C_{anion} feature at ~292 eV is not very pronounced and also the other anion-related signals, i.e., N_{anion} and F, are of relatively low intensity. The N_{anion}/N_{cation} ratio shows a value of ~1:3 in normal emission and ~1:2 in 80° emission. This indicates that in general more cationic species are present on the surface, but also that the anion—being slightly enhanced in 80° emission—is on average located slightly above the cationic headgroup. The lower overall anion signal intensities are tentatively assigned to some kind of ion exchange, where vacant surface hydroxide groups deprotonate and act as the counter ion (leading to a different stoichiometry for $[TESIm]^+$ and $[Tf_2N]^-$), as depicted in Scheme 5.4. From the overall $[TESIm][Tf_2N]$-related signal intensity in comparison with the sum intensity of 1 ML $[C_1C_1Im][Tf_2N]$ on Au(111) film, a $[TESIm][Tf_2N]$ surface coverage of ~0.6 ML is estimated.
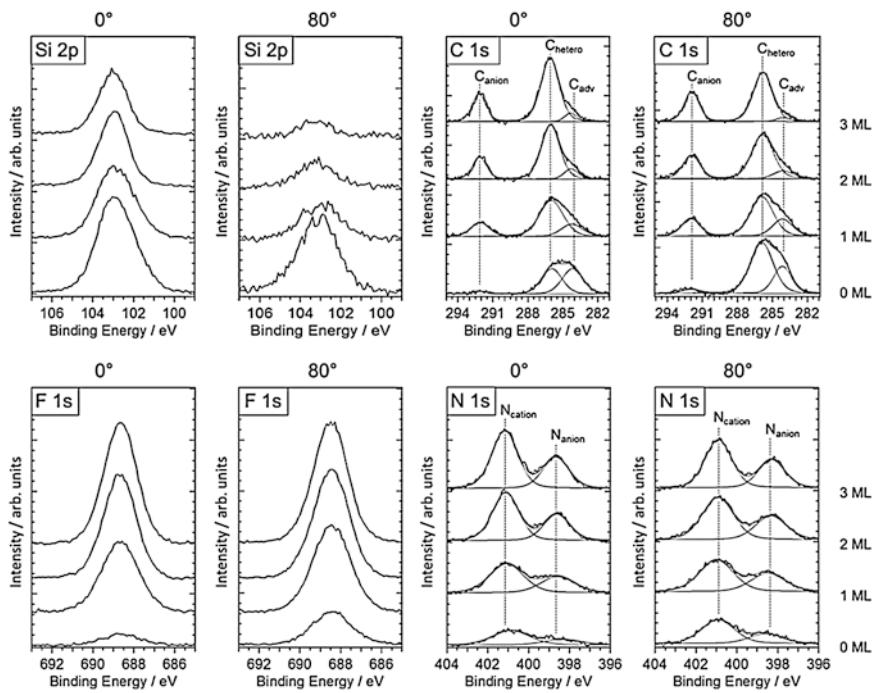
Fig. 5.7 Si 2p, C 1s, F 1s and N 1s ARXP spectra of initial stages of [C₁C₁Im][Tf₂N] growth on [TESIm][Tf₂N]-functionalized Suprasil. Shown are the sample before deposition (0 ML), and three consecutive evaporation steps (1, 2 and 3 ML). 0° and 80° spectra are plotted using the same scale (y-axis) without further correction for reduced transmission in 80° measurements

Scheme 5.4 Sketch of the [TESIm][Tf₂N]-functionalized Suprasil surface, as indicated by the ARXPS measurements. Covalently attached cations pair up with anionic silanolate groups on the surface, therefore leading to reduced amounts of [Tf₂N]⁻ anions. The anions present are on average located slightly above the cation

Upon IL deposition, again, a significant decrease of substrate signals is observed, similar to the observations made for the ozone-treated sample. Also for this sample, the $C_{hetero}/C_{alkyl}/C_{adv}$ is subject to significant damping by the deposited IL, again indicating layered growth behaviour in the initial stages of IL film growth.

To summarize, on the IL-functionalized surface [TESIm][Tf$_2$N] related signals are found, not at stoichiometric values, but with less anion-related signals. This is assigned to a partial pairing of [TESIm]$^+$ moieties with surface silanolate groups. IL growth on top of this functionalized layer, leads to significant damping of all surface-related signals and therefore indicates a good wetting behaviour, at least in the initial stages of IL film growth.

In the following chapter, the growth characteristics of the three different systems investigated are discussed by analysis of the damping behaviour using Eqs. (2.4) and (4.1). The results are compared to reference measurements on Au(111), where—as was shown in Sect. 4.3.1—perfect layer-by-layer growth is observed.

5.3.2.4   Comparison of [C$_1$C$_1$Im][Tf$_2$N] Growth on Different Suprasil Surfaces

The 80° emission C 1s spectra of IL films deposited on the three different Suprasil surfaces discussed in detail in the previous sections are depicted in Fig. 5.8. In contrast to the spectra shown before, also spectra of higher IL coverages, i.e. 4 ML and also 6 ML (ozone-treated and IL-functionalized Suprasil) and 10 ML (pristine Suprasil) films are shown. From the direct comparison of the 1 ML film it becomes immediately evident that for the pristine sample the C$_{adv}$ feature is significantly less damped compared to the other two samples. While for the ozone-treated and the IL-functionalized samples exclusively IL signals are observed for the 4 ML film, C$_{adv}$ still remains as a prominent feature in the case of the pristine sample. Even for a nominal coverage of 10 ML the C$_{adv}$ feature is still visible, while in the modified samples already at 4 ML coverage the bulk IL spectrum is observed. These characteristics, in combination with more efficient damping of the Si 2p signal as compared to the C$_{adv}$ feature, led to the conclusion that the IL shows preferential adsorption on clean, uncontaminated regions of the surface, while dewetting occurs on the carbon-contaminated surface areas. While the majority of the surface is covered by a homogeneous IL layer, leading to significant damping of the substrate signal, remaining intensity is still observed from the Si located below the contaminated areas.

In the following, the IL growth will be discussed in more detail by analysing the attenuation behaviour of the Si 2p substrate signal. In Fig. 5.9 the relative decrease in Si 2p signals (I/I$_0$) as measured in 0° geometry is plotted against evaporation time. The curves for the hydroxylated (squares) and the IL-functionalized (triangles) surface agree well, within the experimental accuracy of evaporation rates, with the damping behaviour observed for the reference film on Au(111) (circles), where the attenuation of the Au 4f signal was used. The pristine sample, however, shows considerable deviation towards higher values, which is a strong indication for non-ideal growth behaviour. This finding corroborates the interpretation that, for the pristine sample, a de-wetting of contaminated surface regions takes place. When the calculated film thickness is plotted against the deposition
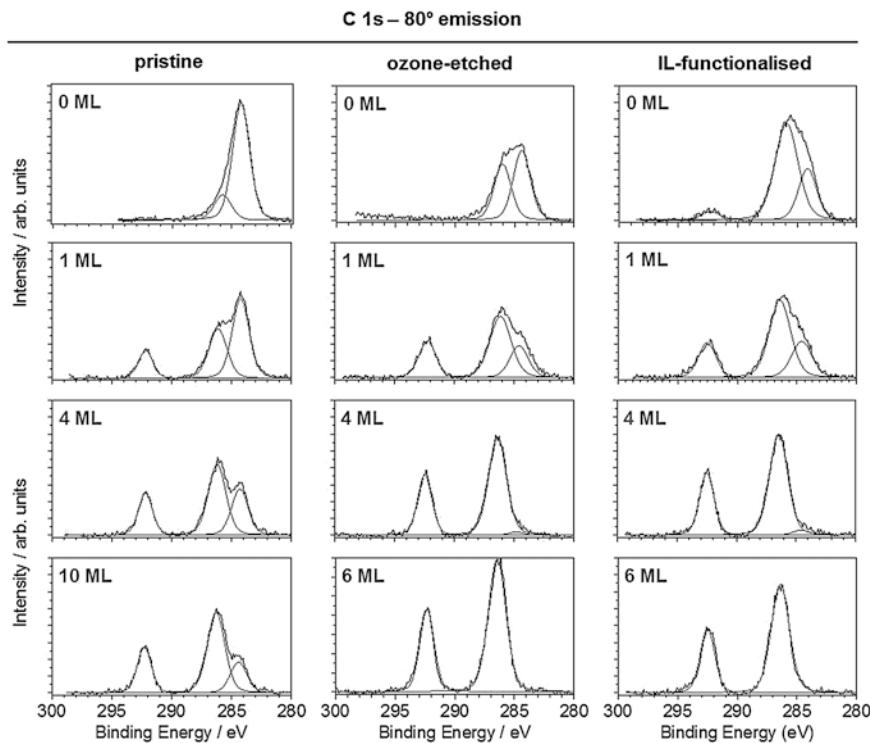
Fig. 5.8 80° emission C 1s spectra of three different Suprasil samples (pristine, *left*; ozone-treated, *middle*; IL-functionalized, *right*) with increasing IL layer thickness. All spectra are scaled to the same intensity
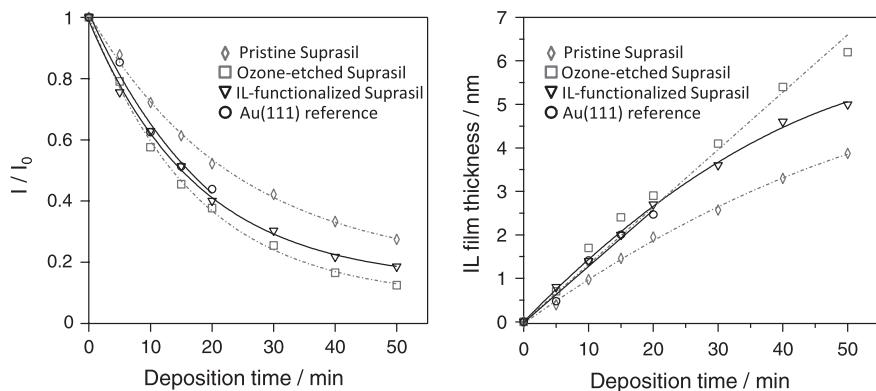
Fig. 5.9 *Left* Attenuation of the substrate Si 2p signal for three different Suprasil samples (pristine, *diamonds*; ozone-treated, *squares*; IL-functionalized, *triangles*) and the Au 4f signal of the reference system (Au(111), *circles*) from the 0° XP spectra; *Right* Calculated IL film thickness as a function of IL deposition time for the same systems

Table 5.5 Contact angles of $[C_1C_1Im][Tf_2N]$ on three different quartz glass samples, namely untreated (pristine), ozone-etched and IL-functionalized silica glass

Suprasil Type	Contact Angle	Comment
Pristine	$36.6° \pm 2°$	–
Ozone-etched	$18.3° \pm 5°$	–
IL-functionalized	$23° (\downarrow 20°)$	Contact angle decreases over time

time, a linear increase in film thickness is observed for the ozone-treated sample, whereas the IL-functionalized sample shows slight deviations to lower values at relatively high coverages. Again, the pristine sample is an outlier and shows considerably lower values for the calculated film thickness due to the formation of 3D IL islands and/or dewetting effects as discussed before.

The findings of IL wetting behaviour of the different Suprasil samples are corroborated on a macroscopic level by contact angle measurements, summarized in Table 5.5. The contact angle of the pristine sample shows the highest value, and the ozone-treated sample shows greatly reduced contact angle (about 50 %), and therefore the best wetting behaviour on a macroscopic level, in agreement with the nanoscale results obtained from the ARXPS data. For the IL functionalized sample an initial contact angle of 23° was observed; however, this value changes over the course of ~20 min, to eventually reach a value of ~20°.

To summarize the results, it is shown that IL growth on untreated, carbon-contaminated samples proceeds in a way that after formation of an initial wetting layer, IL island formation occurs, leading to an inhomogeneous growth of the IL film, even for coverages beyond 10 ML. For cleaned, hydroxylated SiO_2 surfaces, however, a layered IL growth comparable to that on Au(111) is observed, and IL-functionalization of the hydroxylated surface does not lead to any further improvement. The results obtained on a molecular level by ARXPS match well the macroscopic contact angle measurements.

5.4 Conclusions

In this chapter, the growth behaviour and molecular arrangement of $[C_nC_1Im]$ $[Tf_2N]$ (n = 1, 2) on silicate-based surfaces was investigated. From investigating untreated, pristine glass and ultrapure fused silica samples for the first adsorption layer of $[C_nC_1Im][Tf_2N]$, a bilayer structure similar to that on Ni(111) was observed. Resulting from the relatively large amounts of adventitious carbon present on the sample surface, non-ideal (dewetting and island formation) growth behaviour could unambiguously be deduced for coverages exceeding values of 1 ML. For samples cleaned with Piranha solution or a $H_2O/O_3/UV$ gas phase treatment, reduced amounts of adventitious carbon contamination were observed, and IL growth was found to proceed in a layer-by-layer fashion, similar to that observed on Au(111). By adding a functionalization layer using a task-specific IL,

which is covalently attached to the terminal hydroxyl groups of the silica samples, no further improvement of the wetting behaviour and subsequent IL growth could be deduced. Moreover, contact angle measurements of $[C_1C_1Im][Tf_2N]$ on the differently modified samples showed that the smallest contact angle was achieved on the ozone-treated sample.

Our investigations clearly demonstrate that important information on the initial stages of IL growth and the wetting behaviour on silicate surface can be obtained by ARXPS investigations of such thin IL films. However, the limited applicability for this class of materials in surface science experiments should be kept in mind. Firstly, sample charging is an issue, and the necessary referencing procedure leads to a relatively high inaccuracy of the BE values, therefore obstructing the strength of XPS to derive detailed information on electronic interactions between the IL and the adsorbate. Furthermore, for samples as investigated in this chapter, standard UHV techniques available for sample cleaning cannot be employed, and due to the—in most cases indispensable—ex-situ sample preparation, a certain amount of adventitious carbon contamination will always be introduced. The investigation of silicate (and also aluminate) systems under better-defined conditions using standard UHV preparation methods such as sputtering techniques or in situ oxide growth, should provide more detailed information and a deeper understanding of the processes occurring at the IL/dielectric interface.

References

1. M. Cubillas, M. Schmidt, M. Scharrer, T. G. Euser, B. J. M. Etzold, N. Taccardi, P. Wasserscheid, P. S. J. Russell, Chem. Eur. J. **18**, 1586 (2012)
2. T. Cremer, M. Killian, J.M. Gottfried, N. Paape, P. Wasserscheid, F. Maier, H.-P. Steinrück, Chem. Phys. Chem. **9**, 2185–2190 (2008)
3. H. Kamimura, T. Kubo, I. Minami, S. Mori, Tribol. Int. **40**, 620 (2007)
4. M. Zhu, J. Yan, Y. Mo, M. Bai, Tribol. Lett. **29**, 177 (2008)
5. P.S.J. Russell, J. Lightwave Technol. **24**, 4729 (2006)
6. T.G. Euser, G. Whyte, M. Scharrer, J.S.Y. Chen, A. Abdolvand, J. Nold, C.F. Kaminski, P.S.J. Russell, Opt. Express **16**, 17972 (2008)
7. S. Webb, F. Poletti, D.J. Richardson, J.K. Sahu, Opt. Eng. **46**, 010503 (2007)
8. T.G. Euser, J.S.Y. Chen, M. Scharrer, P.S.J. Russell, N.J. Farrer, P.J. Sadler, J. Appl. Phys. **103**, 103108 (2008)
9. J.S.Y. Chen, T.G. Euser, N.J. Farrer, P.J. Sadler, M. Scharrer, P.S.J. Russell, Chem. Eur. J. **16**, 5607 (2010)
10. R. Riisager, M. Fehrmann, P. Haumann, Wasserscheid. Top. Catal. **40**, 91 (2006)
11. Y.S. Chi, J.K. Lee, S.-g. Lee, I.S. Choi, Langmuir, **20**, 3024 (2004)
12. J.D. Holbrey, W.M. Reichert, I. Tkatchenko, E. Bouajila, O. Walter, I. Tommasi, R.D. Rogers, Chem. Commun. **28** (2003)
13. R. Lungwitz, T. Linder, J. Sundermeyer, I. Tkatchenko, S. Spange, Chem. Commun. **5903** (2010)
14. M. Stark, Master Thesis, Friedrich-Alexander-University Erlangen-Nuremberg, 2010
15. R.F. Roberts, D.L. Allara, C.A. Pryde, D.N.E. Buchanan, N.D. Hobbins, Surf. Interf. Anal. **2**, 5 (1980)
16. D. Wagner, D.E. Passoja, H.F. Hillery, T.G. Kinisky, H.A. Six, W.T. Jansen, J.A. Taylor, J. Vac. Sci. Technol. **21**, 933 (1982)

17. T. Cremer, Diplom Thesis, Friedrich-Alexander University Erlangen-Nuremberg, 2008
18. J.P. Armstrong, C. Hurst, R.G. Jones, P. Licence, K.R.J. Lovelock, C.J. Satterley, I.J. Villar-Garcia, Phys. Chem. Chem. Phys. **9**, 982 (2007)
19. K.R.J. Lovelock, C. Kolbeck, T. Cremer, N. Paape, P.S. Schulz, P. Wasserscheid, F. Maier, H.-P. Steinrück, J. Phys. Chem. B **113**, 2854 (2009)
20. S. Krischok, M. Eremtchenko, M. Himmerlich, P. Lorenz, J. Uhlig, A. Neumann, R. Ottking, W.J.D. Beenken, O. Höfft, S. Bahr, V. Kempter, J.A. Schäfer, J. Phys. Chem. B **111**, 4801 (2007)
21. E.F. Smith, F.J.M. Rutten, I.J. Villar-Garcia, D. Briggs, P. Licence, Langmuir **22**, 9386 (2006)
22. O. Höfft, S. Bahr, M. Himmerlich, S. Krischok, J.A. Schäfer, V. Kempter, Langmuir **22**, 7120 (2006)
23. A. Fitchett, J.C. Conboy, J. Phys. Chem. B **108**, 20255 (2004)
24. C. Aliaga, C.S. Santos, S. Baldelli, Phys. Chem. Chem. Phys. **9**, 3683 (2007)
25. K.H. Maier, T. Cremer, H.-P. Steinrück, P. Wasserscheid, Neuartige Hybridmaterialen, 2008, (pending patent application 10 2008 2015 2015.2000)
26. T. Cremer, M. Stark, A. Deyko, H.-P. Steinrück, F. Maier, Langmuir **27**, 3662 (2011)

Chapter 6
Summary and Outlook

In this thesis, ionic liquid (IL) bulk properties, the IL/vacuum interface and the IL/ solid interface were investigated, primarily using angle-resolved X-ray photoelectron spectroscopy (ARXPS) under ultrahigh vacuum (UHV) conditions. ILs represents a class of materials with unique physico-chemical properties leading to a myriad of potential applications. Many of these take advantage of the extremely low vapour pressure, in particular of aprotic ILs, to fabricate permanent, non-volatile liquid coatings of solid materials. The research carried out herein focused on issues related to thin IL coatings, in particular concerning new catalytic concepts such as the supported ionic liquid phase (SILP) and solid catalyst with ionic liquid layer (SCILL) systems. In addition to ion–ion interactions within the IL film, IL/gas and IL/solid interfaces have been shown to significantly contribute to the overall performance of these catalytic materials. Well-defined UHV conditions and in situ preparation methods were used to investigate first IL-film model systems and address the following fundamental questions on a molecular level: How does the chemical structure of IL molecules influence the intermolecular forces within the IL bulk? To what extent does the anion influence the structure formation in the near-surface region of ILs? How do properties such as the electronic interaction between IL and solid, the growth behaviour, and the molecular arrangement at the IL/solid interface depend on the choice of IL or support material?

As a first step, the electronic structure of ten 1-methyl-3-octylimidazolium ($[C_8C_1Im]^+$)-based ILs with different anions was investigated, focusing on anion-cation interactions. Through a cooperative effort using ARXPS as well as nuclear magnetic resonance (NMR) spectroscopy and density-functional-theory (DFT) calculations, distinct interaction schemes between anion and cation were derived. The hydrogen bonding strength was found to increase when smaller and more-strongly coordinating anions are used. Moreover, first experimental evidence of orbital mixing leading to reduced net charges could be deduced from the chemical shifts found in XPS, corroborated by DFT results. For the same set of ILs, the IL/vacuum interface was investigated by ARXPS concerning both surface composition and enrichment effects. It was demonstrated that the cation octyl chains

preferentially terminate the IL/vacuum phase boundary. This alkyl chain surface enrichment increases with decreasing size and coordination strength of the anion, due to a denser packing and a higher degree of order in the chains resulting from inter-chain van-der-Waals forces. These findings on bulk properties formed the basis the first detailed ARXPS investigations of the IL/solid interface, which represent the main part of this thesis.

To access the so far largely unexplored IL/solid interface, a physical vapour deposition process (IL-PVD), developed in the author's preceding diploma thesis, was used to deposit ultrathin IL layers on the substrates of interest. This approach, in combination with ARXPS, enabled the investigation of: (1) the electronic interactions between the IL and the support material, (2) the arrangement of ions at the IL/solid interface, and (3) the growth characteristics of ultrathin IL films on a given support material.

Addressing well-defined IL/metal interfaces, ultrathin IL films of various thickness were investigated on the (111) surfaces of Au and Ni. On Au(111), IL films of 1-alkyl-3-methylimidazolium bis(trifluoromethylsulfonyl)imide ($[C_nC_1Im][Tf_2N]$ with n = 1, 8) and 1-butyl-1-methylpyrrolidinium bis(trifluoromethylsulfonyl) imide ($[C_4C_1Pyrr][Tf_2N]$) were deposited and analysed using ARXPS. The main results are: For all three ILs, both anion and cation preferentially adsorb directly on the gold surface in a checkerboard-like arrangement. With increasing IL coverage, the IL films grow in a layer-by-layer fashion. For the octyl-imidazolium cation, the alkyl chains disconnect from the surface upon completion of one closed layer of IL molecules and start pointing towards the vacuum, thereby liberating adsorption sites for additional ionic headgroups which interact more strongly with the metal surface. Furthermore, for imidazolium ILs, the first IL-interface layer exhibits a high degree of molecular orientation: the imidazolium ring lies flat on the surface and the $[Tf_2N]^-$ anion adopts a *cis*-type configuration with the SO_2 groups in contact with the gold surface and the CF_3 groups pointing towards the vacuum. Interestingly, no indications for such a well-ordered interface arrangement were found for the pyrrolidinium-based IL, where a rather random orientation of the molecules was observed.

On the more reactive Ni(111) surface, thin layers of $[C_1C_1Im][Tf_2N]$ were deposited, exhibiting a less perfect layer-by-layer growth behaviour than on Au(111). For IL coverages well below a full molecular layer, a bilayered structure of ions was deduced from a pronounced enhancement of anion-related signals in the surface-sensitive geometry of the ARXPS measurements. This bilayered structure at the IL/Ni interface, with the cation in direct contact with the surface and the anion positioned on top terminating the surface towards the vacuum, differs from the checkerboard-like arrangement found on Au(111). Investigations of the adsorption behaviour on oxygen-precovered and oxidised Ni(111) surfaces indicated a loss in film ordering in comparison to clean Ni(111). Isothermal heating experiments provided first insights into reactions between the IL film and the surface; on a clean Ni(111) surface the IL cations and anions desorb intact upon heating, whereas on a fully oxidised Ni surface preferential desorption of cation-related species revealed a thermally induced surface reaction. The investigations using

model Ni(111) surfaces concluded with highly application-relevant considerations such as IL-induced surface passivation and reduction of pyrophoric character. In these experiments, an unambiguous lowering of the Ni reactivity towards oxygen was observed with increasing IL coverage.

In addition to well-defined IL/metal-interfaces, also the IL/silicate-interface was investigated. This system is of paramount interest for SILP and SCILL cataly-sis and is also closely related to the so-called "Nanolab" project, where uniform IL films are essential for optimum device performance. It was shown that on native, untreated glass substrates—in contrast to the metallic materials—ILs form a wet-ting layer followed by three-dimensional growth (i.e., droplet formation). As such behaviour is disadvantageous for the above-mentioned applications, the silicate support was subjected to different surface modification procedures (i.e., surface hydroxylation and IL-functionalization layers), which were shown to positively influence the IL growth. Furthermore, it was demonstrated that the residual surface carbon contamination present on untreated silicate materials is the main reason for non-ideal IL growth.

In conclusion, this thesis documents fundamental research addressing IL bulk properties, the surface composition of macroscopically thick IL films, and the IL/solid interface in the context of IL-coated solids. The presented results contribute to a large number of IL-related research fields. In particular the studies concern-ing ultrathin IL films on solids mark the starting point for an exciting and broad field of material research. Furthermore, the detailed understanding of the IL/solid interface at a molecular level is expected to be beneficial for various research areas such as heterogeneous catalysis, electrochemistry, energy storage devices (i.e., electric double layer capacitors and batteries), solar cells, tribology and coating technologies.

Main directions for future thin film research include: (1) expanding the funda-mental knowledge base by investigation of well-defined model systems; (2) IL thin film research focussed on less well-defined, but application-relevant systems; and (3) use of functionalized, task specific ILs.

In order to expand the knowledge base on well-defined IL/solid interfaces, ARXPS investigations of other single crystalline metal surfaces, single-crystal oxide supports, or well-ordered carbonaceous materials (highly ordered pyrolytic graphite (HOPG) or graphene) are recommended. In addition, the application of complementary methods dedicated primarily to structure determination of highly ordered surfaces and adsorbate systems such as scanning tunnelling microscopy (STM), electron diffraction, or synchrotron-based techniques (e.g., near-edge X-ray adsorption fine structure (NEXAFS)), will contribute to a more thorough understanding of IL boundaries. Concomitantly, theoretical approaches such as DFT calculations and molecular dynamic (MD) simulations are required for an atomistic understanding of IL/solid interfaces.

The examination of less well-defined—but highly application-relevant—systems can also contribute significantly to various aspects of IL research, as shown by the results obtained from investigating the IL/silicate interface. Such studies are partic-ularly important for coating and surface modification technologies, where a better

understanding of the interface region may help improve existing systems and aid in developing new materials.

Finally, interesting results are expected from further study of thin films with task-specific ILs, where functional groups attached to the IL backbone allow for specific interactions between the IL and the surface. In addition to the presented IL-PVD-methods, new deposition techniques allowing the use of less-thermally-stable ILs will need to be developed, in order to achieve this.
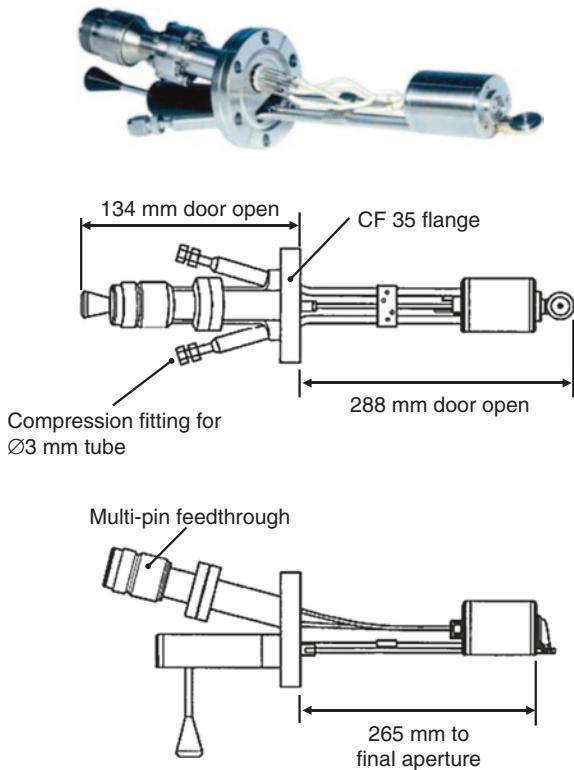
Appendix

A.1 Modifications to the XPS Chamber

In the course of this thesis, a number of major modifications were made to the Escalab 200 apparatus. In 2009, the chamber was equipped with a detachable IL-evaporator, discussed in detail in Chap. 4. Also, a new Scienta R3000 electron analyser installed was installed, as described in detail in Ref. [67]. Finally, a new X-ray gun (Specs XR50) and a new, custom-build sample holder system were fitted to the system in 2011. The specifications and drawing of relevant parts of the IL-evaporator and the sample holder system are compiled in the following.

A.1.1 IL-Evaporator

Tectra WKC3 high temperature Knudsen Cell:

134 mm door open

CF 35 flange

Compression fitting for
∅3 mm tube

288 mm door open

Multi-pin feedthrough

265 mm to
final aperture

Specifications differing from the standard version:

- Type K thermocouple
- Custom length: 450 mm (distance flange-orifice), effective distance when mounted on z-transfer: d (flange-orifice) = 265 mm
- Z-transfer: 300 mm (485–185 mm); Brand: Mewasa
- Custom made aperture (outer Ø: 12 mm, inner Ø: 5 mm; thickness: 2 mm)
- "Sledge" for head of evaporator (assures smooth gliding through flange region): The sledge was cut from stainless steel foil and fixed to the water pipes by bending the 6 mm wide side strips around the water pipes followed by spot welding the resulting loop.

Sledge dimensions
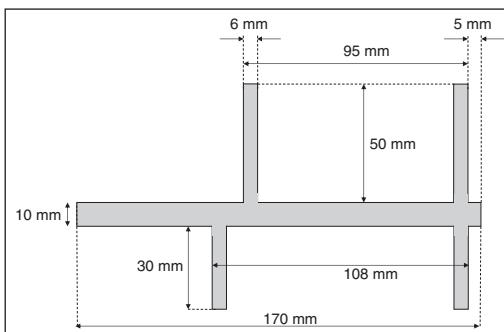
Front view of sledge fixation
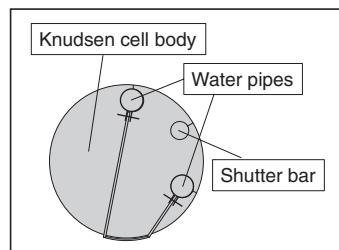
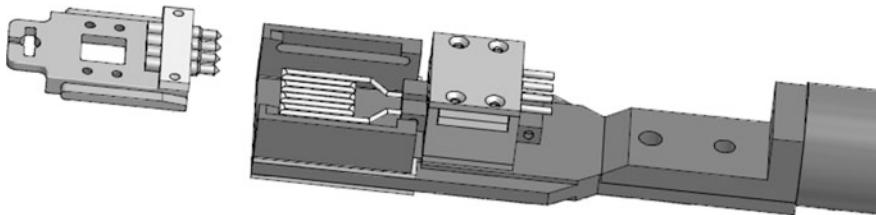Side view of sledge fixation
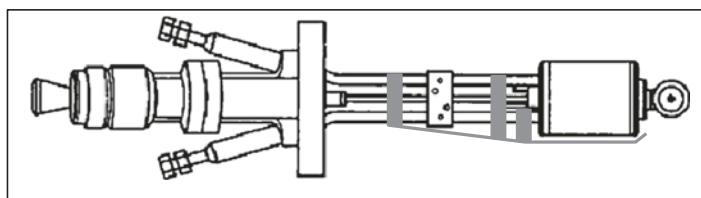
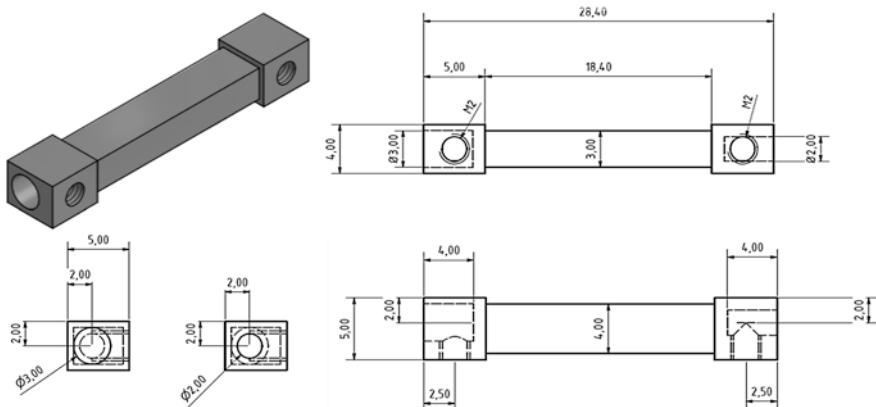- four-membered CF40 flange cross:

Top view
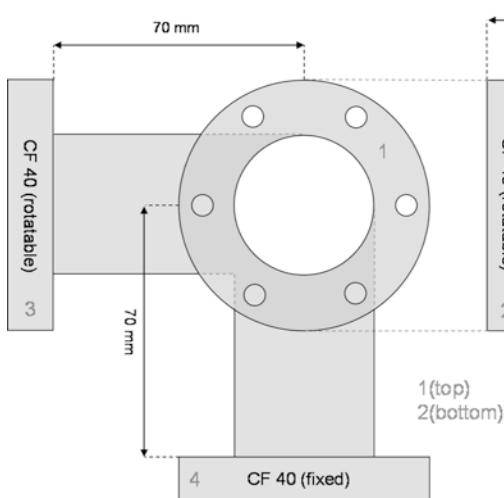
Side view
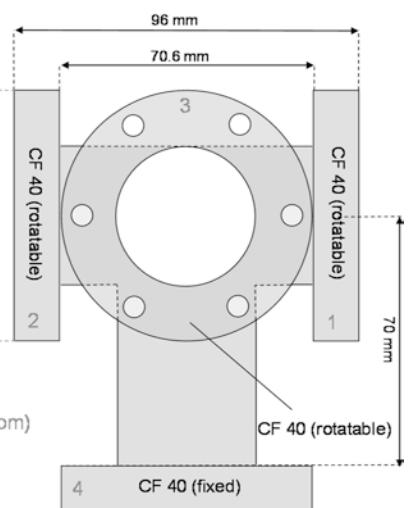
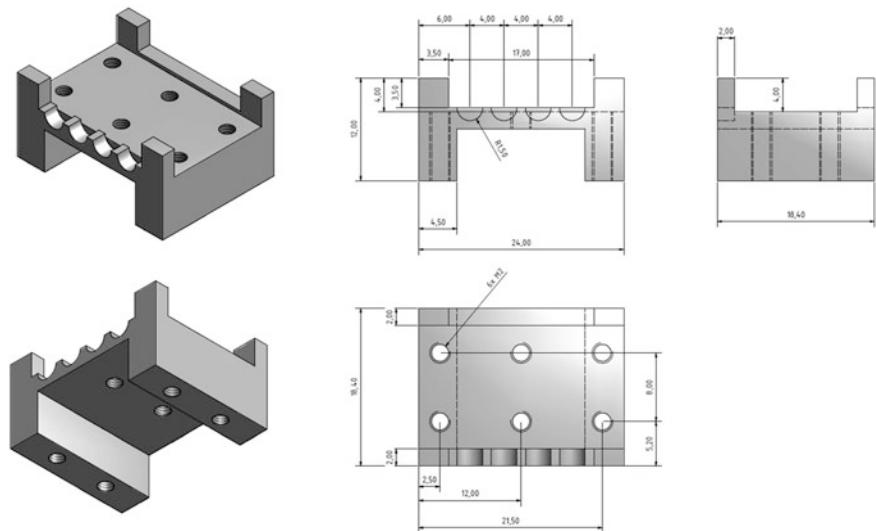## *A.1.2   Sample Holder System*
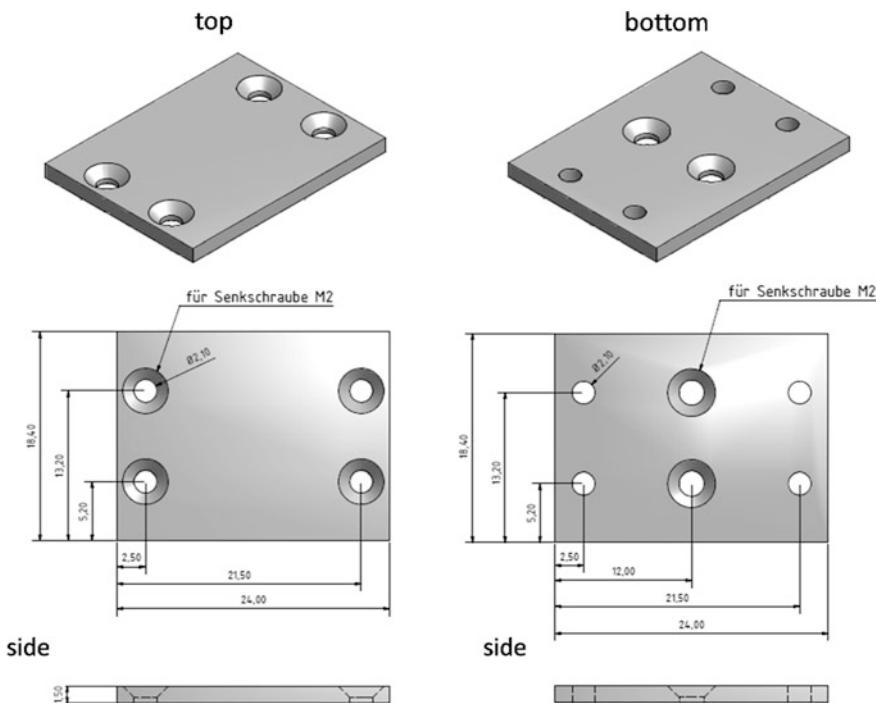
- Sample Holder, assembled
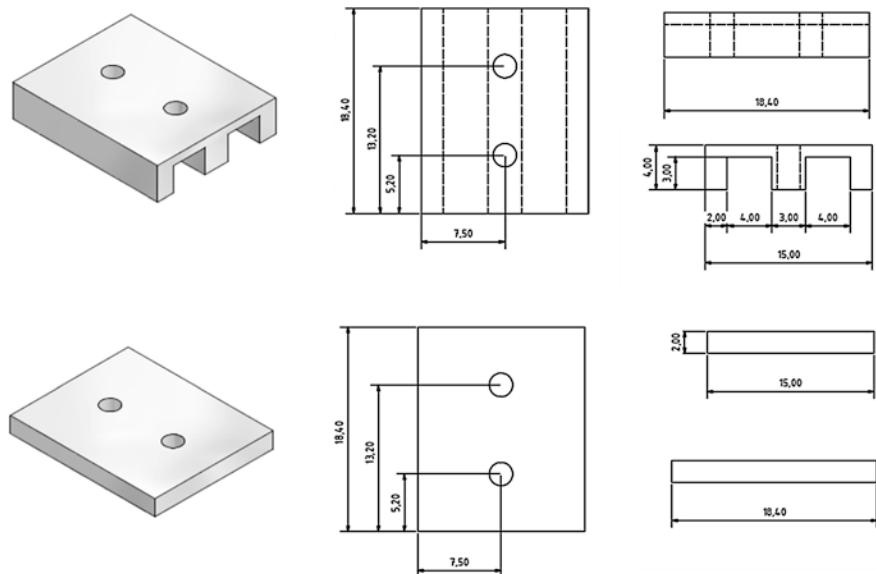

- Filament connector; material: copper

- Holder for thermocouple connector; material: stainless steel
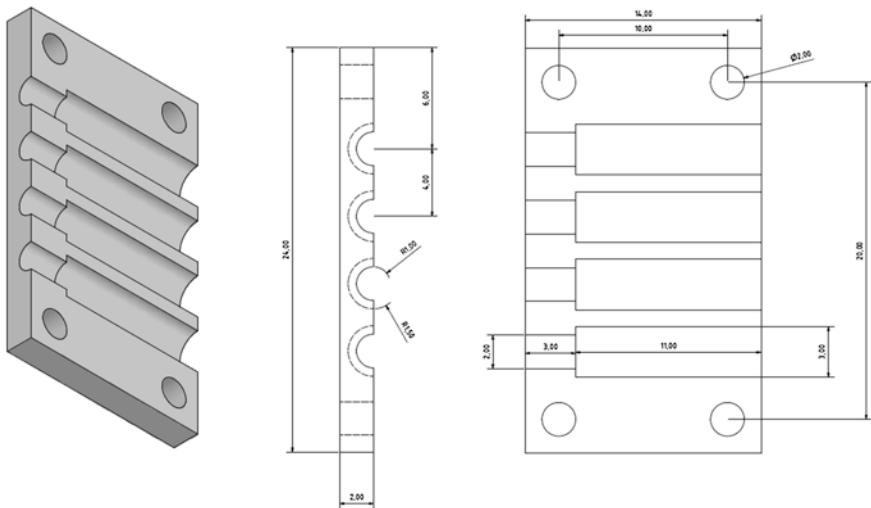
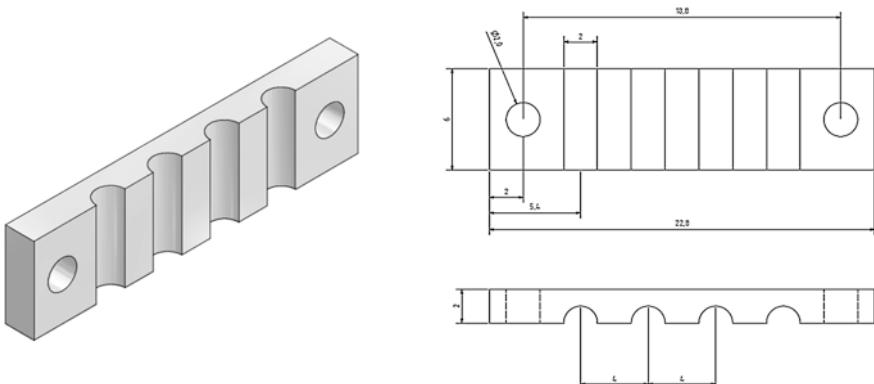- Plates for thermocouple connector; material: stainless steel

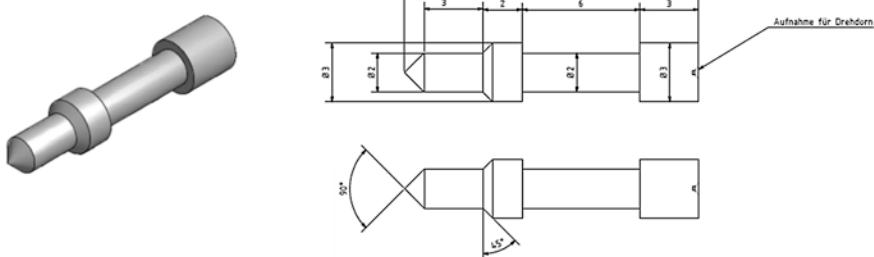- Insulator for filament connector; material: macor

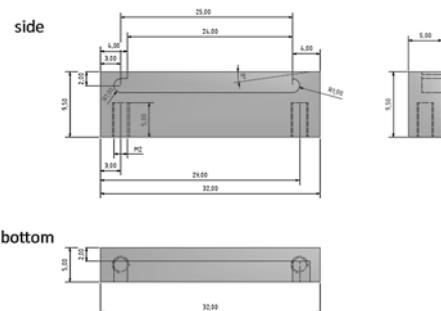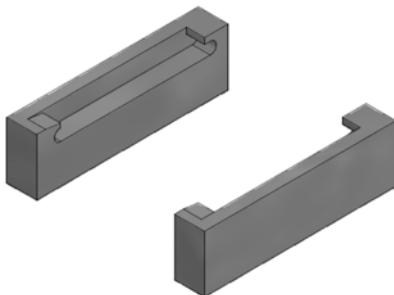- Ceramic for thermocouple feed through; material: sapphire

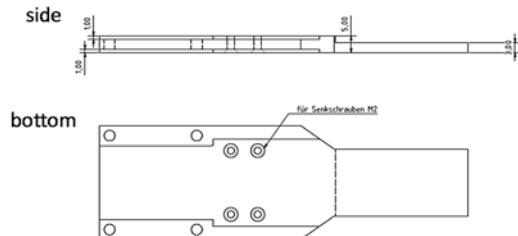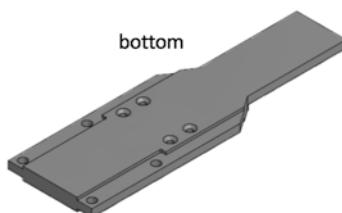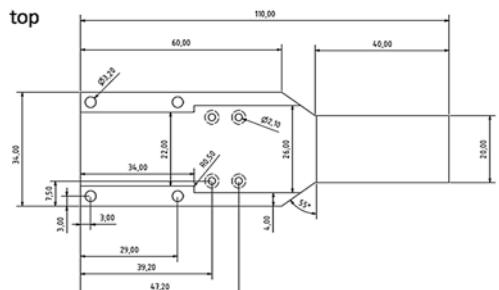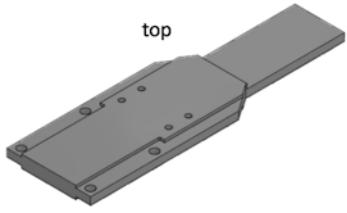- Ceramic for thermocouple pins; material: sapphire

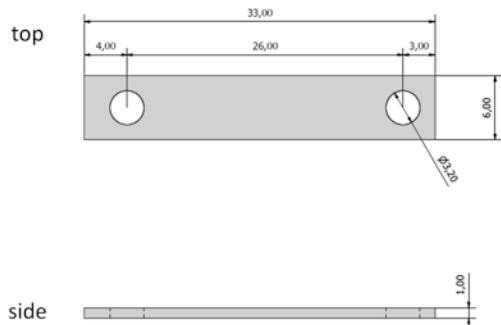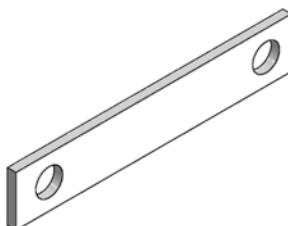- Thermocouple pins; material: type-K thermocouple material

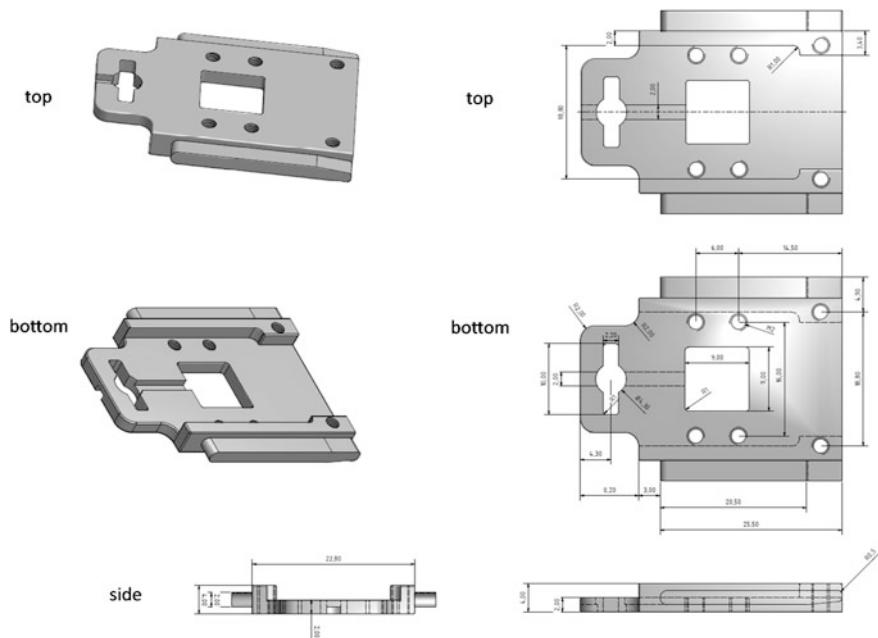- Brackets for sample holder; material: copper

- Base plate; material: copper

- Insulating plate; material: sapphire

• Sample holder; material: molybdenum or tantalum

A.2   Tables

See Tables A.1, A.2 and A.3.

Table A.1 Quantitative analysis of the XP spectra of [C$_8$C$_1$Im]X

IL		Cation			Anion	
[C$_8$C$_1$Im]Cl	Element	C 1s (hetero)	C 1s (alkyl)	N 1s (ring)	Cl 2p	
	ASF	0.205	0.205	0.350	0.550	
	Position peak maxima (eV)	286.4	285.0	401.5	197.0	
	Nominal	5	7	2	1	
	0°	4.8	7.3	1.9	1.0	
	70°	4.0	8.6	1.6	0.8	
	80°	3.2	10.0	1.2	0.7	
[C$_8$C$_1$Im]Br	Element	C 1s (hetero)	C 1s (alkyl)	N 1s (ring)	Br 3d	
	ASF	0.205	0.205	0.350	0.550	
	Position peak maxima (eV)	286.5	285.0	401.8	67.4	
	Nominal	5	7	2	1	
	0°	4.9	7.1	1.9	1.0	
	70°	4.2	8.2	1.6	1.0	
	80°	3.2	9.8	1.2	0.8	
[C$_8$C$_1$Im]I	Element	C 1s (hetero)	C 1s (alkyl)	N 1s (ring)	I 5d	
	ASF	0.205	0.205	0.350	5.61	
	Position peak maxima (eV)	286.5	285.0	401.9	618.7	
	Nominal	5	7	2	1	
	0°	5.0	7.1	2.0	1.0	
	70°	4.2	8.6	1.5	0.7	
	80°	3.5	9.5	1.3	0.7	
[C$_8$C$_1$Im][NO$_3$]	Element	C 1s (hetero)	C 1s (alkyl)	N 1s (ring)	O 1s	N 1s
	ASF	0.205	0.205	0.350	0.58	0.350
	Position peak maxima (eV)	286.6	285.0	401.8	532.1	406.5
	Nominal	5	7	2	3	1
	0°	5.1	7.5	1.8	2.8	0.9
	70°	4.2	9.4	1.5	2.3	0.6
	80°	3.4	11.3	1.1	1.7	0.5

(continued)

Table A.1 (continued)

[C₈C₁Im][BF₄]

IL		Cation			Anion	
	Element	C 1s (hetero)	C 1s (alkyl)	N 1s (ring)	F 1s	B 1s
	ASF	0.205	0.205	0.350	1.000	0.115
	Position peak maxima (eV)	286.7	285.0	402.0	686.1	194.2
	Nominal	5	7	2	4	1
	0°	5.1	7.1	1.9	3.9	1.0
	70°	4.8	8.1	1.8	3.5	0.9
	80°	4.1	9.9	1.5	2.8	0.8

[C₈C₁Im][PF₆]

IL		Cation			Anion	
	Element	C 1s (hetero)	C 1s (alkyl)	N 1s (ring)	F 1s	P 2p
	ASF	0.205	0.205	0.350	1.000	0.300
	Position peak maxima (eV)	286.8	285.0	402.1	686.9	136.7
	Nominal	5	7	2	6	1
	0°	5.1	7.0	1.9	6.0	1.0
	70°	4.9	8.1	1.7	5.2	1.1
	80°	4.2	10.0	1.5	4.4	0.9

[C₈C₁Im][TfO]

IL		Cation			Anion			
	Element	C 1s (hetero)	C 1s (alkyl)	N 1s (ring)	F 1s	C 1s (CF₂)	O 1s	S 2p
	ASF	0.205	0.205	0.350	1.000	0.205	0.580	0.400
	Position peak maxima (eV)	286.8	285.0	402.1	688.8	292.6	532.2	168.4
	Nominal	5	7	2	3	1	3	1
	0°	5.0	7.0	2.0	2.9	1.0	3.2	1.0
	70°	4.8	8.0	1.7	2.6	1.0	2.9	1.0
	80°	4.0	9.6	1.5	2.7	0.8	2.5	0.9

Table A.1 (continued)

[C₈C₁Im][Tf₂N]

	Cation			Anion					
Element	C 1s (hetero)	C 1s (alkyl)	N 1s (ring)	F 1s	C 1s (CF₂)	O 1s	S 2p	N 1s	C 1s (CF₃)
ASF	0.205	0.205	0.350	1.000	0.205	0.580	0.400	0.350	0.205
Position peak maxima (eV)	286.8	285.0	402.2	689.1	293.0	532.8	169.0	399.5	293.7
Nominal	5	7	2	6	2	4	2	1	2
0°	5.1	7.0	2.1	5.9	2.0	3.9	2.1	1.0	2.0
70°	5.0	8.1	1.9	5.6	1.9	3.5	2.0	1.0	2.1
80°	4.4	9.7	1.6	5.7	1.7	3.1	1.8	0.9	2.1

[C₈C₁Im][Pf₂N]

	Cation			Anion					
Element	C 1s (hetero)	C 1s (alkyl)	N 1s (ring)	F 1s	C 1s (CF₂)	O 1s	S 2p	N 1s	C 1s (CF₃)
ASF	0.205	0.205	0.350	1.000	0.205	0.580	0.400	0.350	0.205
Position peak maxima (eV)	286.9	285.0	402.3	689.3	291.1	532.9	169.0	399.6	293.7
Nominal	5	7	2	10	2	4	2	1	2
0°	5.5	7.5	2.2	9.8	1.4	3.8	1.9	1.1	2.0
70°	5.0	7.9	2.0	9.9	1.5	3.7	2.0	1.1	2.1
80°	4.3	9.1	1.7	10.2	1.4	3.4	1.9	0.9	2.1

[C₈C₁Im][FAP]

	Cation			Anion				
Element	C 1s (hetero)	C 1s (alkyl)	N 1s (ring)	F 1s (CFₓ)	F 1s (PF)	C 1s (CF₂)	P 2p	C 1s (CF₃)
ASF	0.205	0.205	0.350	1.000	1.000	0.205	0.300	0.205
Position peak maxima (eV)	287.0	285.0	402.3	688.5	686.8	290.0	135.0	293.1
Nominal	5	7	2	15	3	3	1	3
0°	5.3	7.1	2.0	14.9	3.0	2.8	1.0	3.0
70°	4.9	8.1	1.8	15.0	2.7	2.6	0.9	2.8
80°	5.0	10.0	1.7	13.6	2.2	2.5	1.0	2.9

The nominal and the experimentally determined composition in number of atoms are given for the various elements constituting the ILs; the experimental values are derived from XP spectra at 0, 70 and 80°. The atomic sensitivity factors (ASF) taking the transmission function of our electron analyser into account are taken from Ref. [37]

Table A.2 Nominal versus measured elemental composition of the ten [C$_8$C$_1$m]$^+$-based ILs investigated in Chap. 3.

ASF [37]	Core levels for respective ILs	C1s [a,b,c,d] 0.205	N1s [e,f] 0.350	O1s 0.580	S2p 0.400	F1s 1.000	Cl2p 0.550	Br2p 0.550	I3d$_{5/2}$ 5.610	B1s 0.115	P2p 0.300
[TfO]⁻	Nominal	–/1/5/7	2/–	3	1	3	–	–	–	–	–
	Experimental	–1.0/5.0/6.9	2.0/–	3.2	1.1	2.9	–	–	–	–	–
[Tf₂N]⁻	Nominal	–/2/5/7	2/1	4	2	6	–	–	–	–	–
	Experimental	–2.0/5.1/7.0	2.1/1.0	3.9	2.1	5.9	–	–	–	–	–
[Pf₂N]⁻	Nominal	2/2/5/7	2/1	4	2	10	–	–	–	–	–
	Experimental	2.1/1.6/5.0/7.1	2.1/1.0	4.0	2.0	10.0	–	–	–	–	–
[FAP]⁻	Nominal	3/3/5/7	2/–	–	–	18	–	–	–	–	1
	Experimental	3.0/2.8/5.3/7.1	2.0/–	–	–	17.9	–	–	–	–	0.95
[PF₆]⁻	Nominal	–/–/5/7	2/–	–	–	6	–	–	–	–	1
	Experimental	–/–5.1/7.0	1.9/–	–	–	5.9	–	–	–	–	1.0
[BF₄]⁻	Nominal	–/–/5/7	2/–	–	–	4	–	–	–	1	–
	Experimental	–/–5.1/7.1	1.9/–	–	–	3.9	–	–	–	1.0	–
Br⁻	Nominal	–/–/5/7	2/–	–	–	–	–	1	–	–	–
	Experimental	–/–4.9/7.1	1.9/–	–	–	–	–	1.1	–	–	–
[NO₃]⁻	Nominal	–/–/5/7	2/1	3	–	–	–	–	–	–	–
	Experimental	–/–5.0/7.6	1.8/0.9	2.7	–	–	–	–	–	–	–
Cl⁻	Nominal	–/–/5/7	2/–	–	–	–	1	–	–	–	–
	Experimental	–/–4.8/7.3	1.9/–	–	–	–	1.0	–	–	–	–
I⁻	Nominal	–/–/5/7	2/–	–	–	–	–	–	1	–	–
	Experimental	–/–5.0/7.1	2.0/–	–	–	–	–	–	1.0	–	–

[a] Number of carbon atoms originating from anion-related peaks with a terminal CF$_3$ group ≥291.5 eV
[b] Number of carbon atoms originating from anion-related peaks with a CF$_2$ group 289 < x < 291.5 eV
[c] Number of carbon atoms originating from heteroatom-bound C-moieties with BE ≈ 286–287 eV
[d] Number of carbon atoms originating from the alkyl chain(s) BE = 285 eV
[e] Number of nitrogen atoms originating from cation heterocycle
[f] Number of nitrogen atoms originating from anion-related nitrogen species

Table A.3 Shifts applied for energy scale calibration to BE(C$_{alkyl}$) = 285.0 eV and resulting peak positions for all IL core levels

Anion	Applied shifts / eV	C1s a	C1s b	C1s c	C1s d	N1s e	N1s f	O1s	S2p$_{3/2}$	F1s	Cl2p	Br3d$_{5/2}$	I3d$_{5/2}$	B1s	P2p
								Peak position / eV (from fitted Gauss functions after energy scale calibration to BE(Calkyl= 285.0 eV))							
[FAP]⁻	0.34	293.14	290.05	287.04	285.00	402.33	-	-	-	686.87	-	-	-	-	135.03
[Tf₂N]⁻	0.30	292.97	-	286.83	285.00	402.17	399.53	532.80	168.95	689.06	-	-	-	-	-
[Pf₂N]⁻	0.36	293.66	291.07	286.83	285.00	402.14	399.50	532.78	168.90	689.18	-	-	-	-	136.74
[PF₆]⁻	0.42	-	-	286.81	285.00	402.15	-	-	-	686.94	-	-	-	-	-
[TfO]⁻	0.23	292.58	-	286.73	285.00	402.02	-	532.12	168.38	688.71	-	-	-	-	-
[BF₄]⁻	0.14	-	-	286.71	285.00	402.03	-	-	-	686.17	-	-	-	194.19	-
[NO₃]⁻	0.21	-	-	286.60	285.00	401.83	406.45	532.10	-	-	-	-	-	-	-
I⁻	0.49	-	-	286.51	285.00	401.86	-	-	-	-	-	-	618.65	-	-
Br⁻	0.18	-	-	286.48	285.00	401.81	-	-	-	-	-	67.34	-	-	-
Cl⁻	0.11	-	-	286.44	285.00	401.66	-	-	-	-	197.00	-	-	-	-

a Carbon atoms originating from anion-related peaks with a terminal CF₃ group ≥291.5 eV
b Carbon atoms originating from anion-related peaks with a CF₂ group 289 < x < 291.5 eV
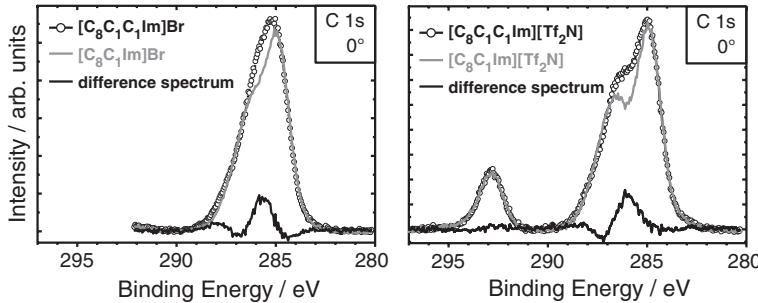c Carbon atoms originating from heteroatom-bound C-moieties with BE ≈ 286–287 eV
d Carbon atoms originating from the alkyl chain(s) BE = 285 eV
e Nitrogen atoms originating from cation heterocycle
f Nitrogen atoms originating from anion-related nitrogen species

A.3 Figures

See Figs. A.1, A.2, A.3, A.4 and A.5.

Fig. A.1 Comparison of XPS spectra of [C₈C₁C₁Im]Br and [C₈C₁Im]Br (*top*), and of [C₈C₁C₁Im][Tf₂N] and [C₈C₁Im][Tf₂N] (*bottom*). The *blue* spectra are the difference spectra and indicate the BE position of the additional CH_3 group in $[C_8C_1C_1Im]^+$ ILs
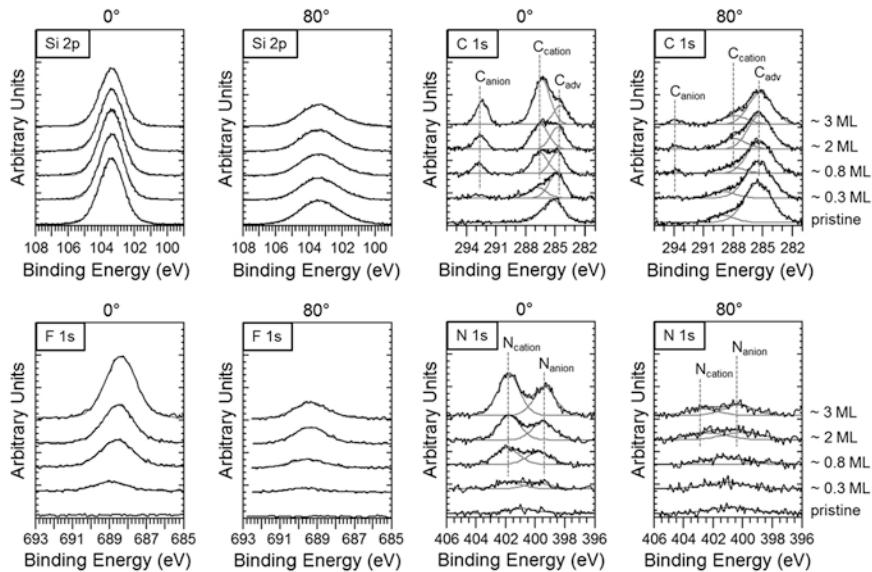

Fig. A.2 Core level spectra of thin [C₁C₁Im][Tf₂N] films deposited on soft-etched (pH 10 buffer solution, 60 °C, 10 min) Suprasil glass. In 0° emission a little decrease of Si 2p substrate signal is observed due to substrate damping by the deposited IL, while the 0° emission IL regions show increased IL signals, however at considerably lower overall intensities as compared to the p-etched sample. In 80° emission, however, the IL signals are hardly present and mainly C_{adv} is visible in the C 1s region. Furthermore, the spectra are significantly broadened, which is also observed for the 80° Si 2p spectra. 0 and 80° spectra are plotted as measured with identical y-scales for better comparison
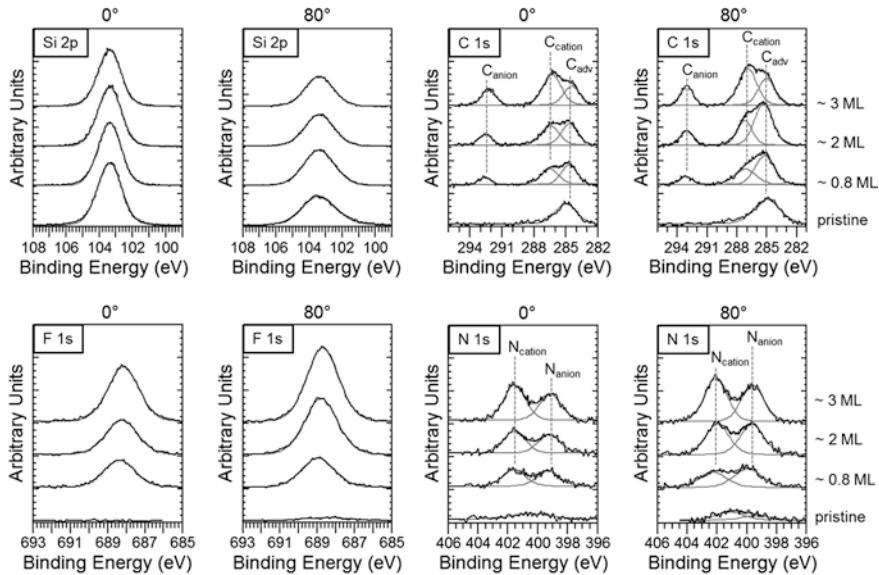
Fig. A.3 Core level spectra of thin [C₁C₁Im][Tf₂N] films deposited on strong-etched (1 M NaOH, 60 °C, 1 h) Suprasil. In both 0 and 80° emission an increase of IL-related regions is observed, however no pronounced angle-dependence is observed, indicating morphology changes (i.e. large pits), resulting in a loss of angular information. 0 and 80° spectra are plotted as measured with identical y-scales for better comparison
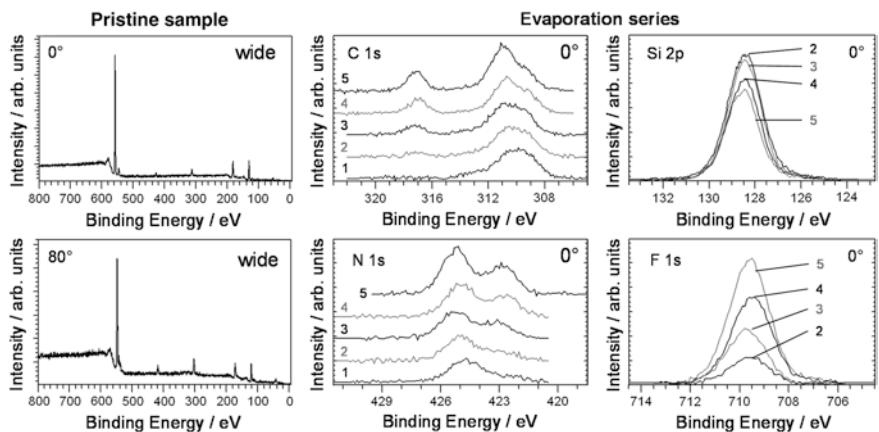
Fig. A.4 *Left column*: 0 and 80° emission wide scans of CO_2-imidazolium-functionalized Suprasil. *Middle* and *right column*: 0° emission core level spectra of an evaporation series of [C₁C₁Im][Tf₂N], recorded at 0° emission with respect to the surface normal. *1* represents the pristine sample (0 ML), *2–5* are IL deposits of increasing thickness (accumulated doses of 5, 10, 20 and 40 min at T = 450 K). Nominal thicknesses are not available due to calibration problems during the experiments
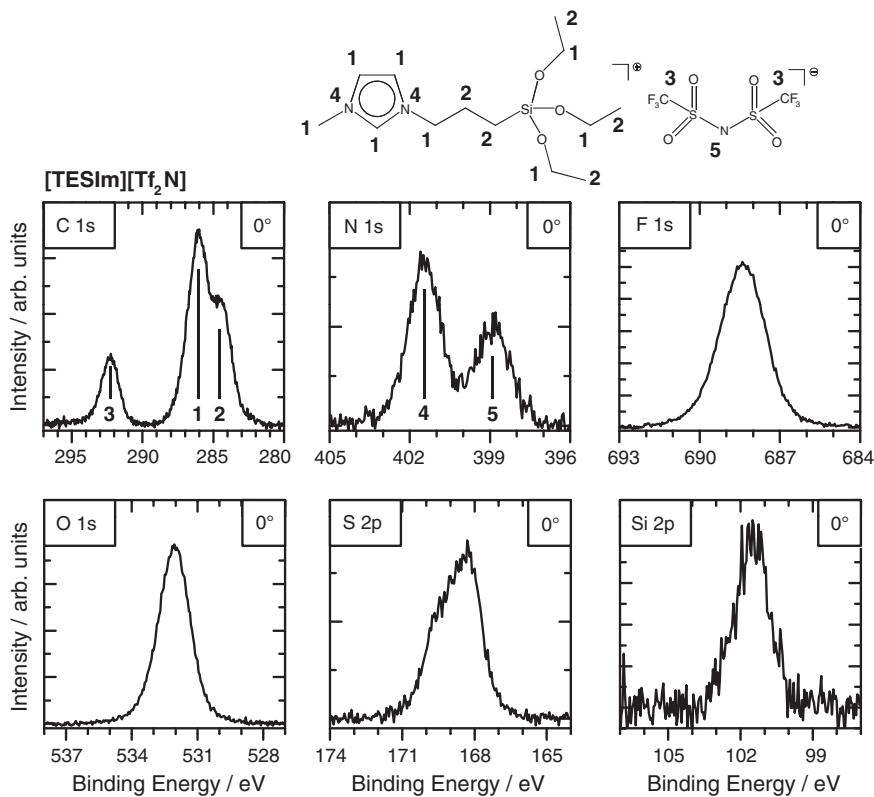
Fig. A.5 Core level spectra of a macroscopically thick film of [TESIm][Tf$_2$N], recorded at 0° emission with respect to the surface normal. In the C 1s region, three features, namely C$_{hetero}$ (*1*), C$_{alkyl}$ (*2*) and C$_{anion}$ (*3*) can be distinguished, while in the N 1s two peak attributed to N$_{cation}$ (*4*) and N$_{anion}$ (*5*) are observed. The experimental intensity ratios (not shown) match well the nominal composition of the IL